UNIVERSITY OF LEICESTER

Understanding interfacial phenomena to visualise and unravel fingerprints

Thesis submitted for the degree of

Doctor of Philosophy

at the University of Leicester

by

Annelies Voorhaar

Department of Chemistry

University of Leicester

2019

Abstract

Understanding interfacial phenomena to visualise and unravel fingerprints

Annelies Voorhaar

This research seeks to enhance the detection of fingerprints by two approaches; enhance currently used techniques using electrowetting and developing a novel detection method using molecularly imprinted polymers (MIPs).

First, electrowetting was investigated as a method to enhance fingerprint visualisation. Aiming to make fingerprint molecules better accessible for fingerprint visualisation reagents and creating a more homogeneously distributed fingerprint ridge using a flow induced by electrowetting. The electrowetting process demonstrated to be able to induce flows in droplets, but for the formation of a flow in a fingerprint several challenges such as the physical and compositional structure of a fingerprint must still be overcome. Subsequently, to define the impact of a potential on a surface, potential-driven changes of surface characteristics were investigated. Conductive polymers were investigated as a surface, demonstrating that the hydrophobicity, composition and topography (roughness) could be tuned to a small or large extent.

Second, MIPs were explored for the detection (visualisation and retrieving intelligence information) of fingerprints because of their chemical recognition characteristics and visualisation properties. By treatment of a fingerprint with fluorescent MIPs (targeted to albumin and trypsin) the fingerprint became fluorescent when the targeted molecules were present. Even tertiary level detail was observed which makes this technique promising for identification purposes. However, despite that the MIPs showed a higher affinity with their target molecule compared to other relevant molecules, it is questionable whether MIPs behave specifically under each circumstances. Possibly the accessibility and mobility of the MIPs in the fingerprint and substrate interactions affected the performance of the MIPs. This suggests that the affinity, size/shape and hydrophobicity of the MIPs as well as the viscosity, composition and physical structure of the fingerprint could be important for this application.

Acknowledgements

It would not have been possible to do this PhD without the support and encouragements of family, friends, colleagues and collaborators.

First, I would like to thank my supervisory team Prof. Karl S. Ryder, Prof. A. Robert Hillman and Prof. J. Derek Raine for all their insightful comments, suggestions and discussions.

I would also like to thank all members of the Materials Centre, both past and present, in particular Dr. Andrew D. Ballantyne, Dr. Alex Goddard, Dr. Igor Efimov, Dr. Robert C. Harris, Dr. Rachel Sapstead and Dr. Chris Zaleski for training me on the instruments, AFM-troubleshooting and the numerous ideas. Emma J. Palin and Stephen Viles for the fun in the write-up room and for providing feedback. Of course also a massive thanks to the other PhD students, especially Dr. Sahar S.M. Alabdullah (football), Omaymah Alaysuy (coffee), Dr. Ahmed Z.M. Al-Bassam (apples), Francesca Bevan (crochet), Dr. Salih Cihangir (crazy Turkish friend), Dr. Azhar Al-Murshedi (snow-woman, weekend lab-companion), Ioanna Maria 'Marianna' Pateli (evening lab-companion), Marian I. Perera (music), Shannon Stodd (sports, bikes), Stylianos 'Stelios' Spathariotis (origami, all-time lab-companion) and Wanwan Qu (positive distractor).

Also a special thanks for all the collaborators within and outside the University of Leicester. The biotechnology group, for all their help and the warm welcome in the group, in particular Dr. Antonio Guerreiro for explaining the world of MIPs, all the demonstrations and numerous ideas. Dr. Thomas S. Bedwell and Dr. Francesco Canfarotta for the support with the SPR analysis, Todd Cowen for the (maybe not so lucky) computational studies and explanations.

The atmospheric chemistry group especially Dr. Rebecca L. Cordell for all the mass spec help and for directing to the right persons, Dr Michael J. Wilde for all the explanations how to interpret and describe data and Thalassa S.E. Valkenburg as Dutch buddy, for the pancake dinners, swimming and all the "lekker directe" comments on everything.

The workshop team, Gareth Bustin, Gayle Prince and Carl Schieferstein for complying with all my requests, from building the electrowetting set-up to fixing my skate wheels and discussing all kind of possible future research ideas.

The PNACL and in particular Dr. Andrew R. Bottrill for the support with the MALDI measurements.

This PhD would not be complete without the secondments. A special thanks to Dr. Melanie J. Bailey, Dr. Gustavo Ferraz Trindade and Dr. Steven J. Hinder for their support with the ToF-SIMS analysis at the University of Surrey. Dr. Martin Jönsson-Niedziolka and Marta Podrażka for the help with the electrowetting experiments at the Institute of Physical Chemistry (Poland).

The INTREPID team, in particular Prof. Lisa Smith for coordinating the INTREPID Forensics programme which has given me the opportunities to follow several trainings of which the fire investigation might have been the most impressive. Thanks to Thomas W. Horton and Alexander Murphy for sorting out all the admin work and of course also a massive thanks to the EU for funding this project.

Last, but not least, thanks to my family and friends for all their support and encouragements. Thanks for all the visits, cards and week-ends full of activities back home. In particular, my parents for all their support, Jeroen for the never-ending stories and Saskia for all the skate-tours and kite adventures.

The research has received funding from the European Union Seventh Framework Programme (FP7/2007-2013) under grant agreement no 607930.

Contents

List of Tables

List of Figures

Figure 4.4 – Reaction mechanism for the binding of glutaraldehyde to the glass beads (R_1=silanised glass beads binding side, AH=acid, B=base).
Figure 4.5 – Reaction mechanism for coupling the template molecule to the glass beads. R_1=silanised glass beads binding side, R_2= template, AH=acid and B=base.
Figure 4.6 – Bicinchoninic acid protein test reaction equation. Step 1 (top): reduction of Cu^{2+} to Cu^{+} using a protein. Step 2 (bottom): the formation of a purple bicinchoninic acid – Cu^{+} complex.
Figure 4.7 – Free-radical polymerisation mechanism, first formation of a radical monomer using an initiator after which the polymerisation continues. R_1= monomer rest-group.
Figure 4.8 – N-(3-dimethylaminopropyl)-N-ethylcarbodiimide (EDC) coupling to the SPR chip (R_1).
Figure 4.9 – N-hydroxysuccinimide (NHS) coupling to the SPR chip (as prepared in Figure 4.8). In which R_1 is SPR chip.
Figure 4.10 - Coupling of the target molecule or MIP to the SPR chip (as prepared in Figure 4.9). In which R_1 is gold SPR chip and R_2 is the target molecule or MIP to be coupled to the SPR chip.
Figure 4.11 – Fluorescent intensity of a BSA imprinted linear MIPs solution, obtained over a range of emission wavelengths (450-600 nm) and using a range of excitation wavelengths (425 till 510 nm). Filled area is marking the lowest long-pass viewing filter wavelength.
Figure 4.12 – Percentages visualised fingerprints using albumin imprinted nano MIPs (**A**) and trypsin imprinted nano MIPs (**B**). Blue dots illustrate the percentage of fingerprints visible by eye/light microscope, red dots the percentage of fluorescent fingerprints and green dots the normalised percentage of fluorescent fingerprints.
Figure 4.13 – Percentages visualised fingerprints using albumin imprinted linear MIPs (**A**) and trypsin imprinted linear MIPs (**B**). Blue dots illustrate the percentage of fingerprints visible by eye/light microscope, red dots the percentage of fluorescent fingerprints and green dots the normalised percentage of fluorescent fingerprints.
Figure 4.14 – MALDI-MS spectra of albumin imprinted linear MIPs. The arrows indicate the proposed monomers based on mass difference between the peaks, red arrows APMA (Δm/z 142), orange arrows tBAm (Δm/z 127), green arrows acrylic acid (Δm/z 72), blue arrows acrylamide (Δm/z 71). Inset: zoom out of the main mass spectra.
Figure 4.15 – Order of monomers tentatively determined based on the MALDI-MS spectra of Figure 4.14. The colours of the connecting lines correspond to the colours of the peaks of the mass spectra. The numbers are the mass to charge ratios of the beginning/end of a proposed monomer or cluster, the latter is indicated by a square.
Figure 4.16 – Fitted sensorgram illustrating the amount of binding of albumin imprinted linear MIPs (in acetate solution) towards albumin (red) and trypsin (black). $K_{D,\ albumin\text{-}trypsin}$ = 0.2 nM. Measurements of a range of trypsin and albumin concentrations (0.59, 2.35, 9.38, 37.50 and 150 nM) were performed using the SPR Navi 220A (BioNavis).
Figure 4.17 - Sensorgram illustrating the amount of binding of albumin imprinted linear MIPs (in water) with albumin (red) and streptavidin (blue). Measurements of a range of MIP concentrations (dilutions in water: 1, 1/3, 1/9, 1/27, 1/81, 1/243) were performed using the BIACore 3000 SPR system (GE Healthcare).
Figure 4.18 – Sensorgram illustrating the affinity of BSA imprinted linear MIPs (in water) towards BSA, HSA and keratin. Measurements performed using the BIACore 3000 SPR system (GE Healthcare).
Figure 4.19 – Fitted sensorgram illustrating the affinity of a variety of concentrations albumin towards albumin imprinted MIPs (**A**; K_D=2.27 nM) and trypsin imprinted MIPs (**B**; K_D=3.23 nM), both in water. Measurements were performed using the BIACore 3000 SPR system (GE Healthcare).
Figure 4.20 – Fluorescence intensity of BSA imprinted linear MIPs solution, BSA solution and BSA plus BSA imprinted MIPs solution. Measurements were performed using an excitation wavelength of 495 nm and a range of emission wavelengths (400-650 nm).
Figure 4.21 - ToF-SIMS spectrum of a visualised fluorescent fingerprint. The peaks were tentatively assigned to the fingerprint compounds (salts, amino acids, fatty acids) and the MIPs visualisation reagent.
Figure 4.22 – Mass-selected ToF-SIMS images of a well visualised fingerprint area (**A**). The ToF-SIMS images were based on groups of fragments which were tentatively assigned to MIPs (**B**), amino acids (**C**) and fatty acids (**D**). The colour scales of the ToF-SIMS were individually adjusted to obtain optimal contrast, a high and low intensity was indicated by the yellow and red colour respectively.
Figure 4.23 – Mass-selected ToF-SIMS images of a poorly visualised fingerprint area (**A**). The ToF-SIMS images were based on group of fragments which are tentatively assigned to MIPs (**B**), amino acids (**C**) and

Abbreviations

AC	Alternating current
ACN	Acetonitrile
AFM	Atomic force microscope
APFAES	Ammonium perfluoroalkylethylsulfite
APMA	*N*-(3-aminopropyl)methacrylamide
ATR-FTIR	Attenuated Total Reflectance-Fourier Transform Infrared Spectroscopy
BIS	*N,N*-methylenebisacrylamide
BSA	Albumin from bovine serum
CA	Contact angle
$CHCl_3$	Chloroform
CS	Chondroitin sulfate
DBS(A)	Dodecylbenzenesulfonic (acid)
DC	Direct current
DCM	Dichloromethane
DESI	Desorption Electrospray Ionization
DFO	1,8-diazafluoren-9-one
DI-water	Deionised water
DNT	2,4-dinitrotoluene
DS	Dextran sulphate sodium salt
EDC	*N*-(3-dimethylaminopropyl)-N-ethylcarbodiimide
EDOT	3,4-ethylenedioxythiophene
EWOD	Electrowetting-on-dielectric
$_{BSA}$fingerprints	BSA-spiked fingerprints
$_{NAT}$fingerprints	Natural fingerprints
$_{TR}$fingerprints	Trypsin-spiked fingerprints
FPS	Frames per second
FTIR	Fourier transform Infrared
GC-MS	Gas Chromatography-Mass Spectrometry
GHB	y-hydroxybutyric
H_2SO_4	Sulphuric acid
HA	Hyaluronic acid sodium salt
HSA	Albumin from human serum
HOMO	Highest occupied molecular orbital
IPA	Isopropanol
ITO	Indium tin oxide
$K_2S_2O_8$	Potassium peroxydisulfate
KCl	Potassium chloride
LC-MS	Liquid Chromatography-Mass Spectrometry
$LiClO_4$	Lithium perchlorate
LUMO	Lowest unoccupied molecular orbital
MALDI	Matrix Assisted Laser Desorption/Ionisation
MALDI-IMS-MS/MS	Ion Mobility Tandem Mass Spectrometry Matrix Assisted Laser Desorption
MALDI-ToF-MS	Matrix-assisted laser desorption/ionization-Time of Flight-Mass Spectrometry

MCAR	Mixed cell agglutination reaction
$MgSO_4$	Magnesium sulfate
MIPs	Molecularly imprinted polymers
$_{BSA}$MIPs	BSA imprinted MIPs
$_{L}$MIPs	Linear MIPs
$_{N}$MIPs	Nano MIPs
$_{TR}$MIPs	Trypsin imprinted MIPs
MISPE	Molecular-imprinted solid-phase extraction
MNT	Mononitrotoluene
MPTMS	(3-Mercaptopropyl)trimethoxysilane
MCT	Mercury cadmium telluride
NaCl	Sodium chloride
$NaHCO_3$	Sodium hydrogen carbonate
NH_4ClO_4	Ammonium perchlorate
NHS	*N*-hydroxysuccinimide
Ninhydrin	1,2,3-indantrione
NIPAm	*N*-isopropylacrylamide
OX	Oxidised
PBS	Phosphate buffered saline
PEDOT	Poly(3,4-ethylenedioxythiophene)
PET	Polyethyleneftalate
pNaSS	Poly-(sodium 4-styrenesulfonate)
PNMP	Poly(N-methylpyrrole)
PS	Polystyrene
PSS	Poly(styrene sulfonate)
PSSS	Poly(sodium 4-styrenesulfonate)
pTS	Sodium para-toluenesulfonate
PVC	Polyvinylchloride
QCM	Quartz crystal microbalance
RDX	Trinitrohexahydro-1,3,5-triazine,
RED	Reduced
SPE	Solid phase extraction
SPR	Surface plasmon resonance
tBAm	*N*-tert-butylacrylamide
TBAP	Tetrabutylammonium perchlorate
TEAPFOS	Tetraethylammonium perfluoreooctanesulfonate
THC	Tetrahydrocannabinol
THF	Tetrahydrofuran
TLC	Thin Layer Chromatography
TNT	2,4,6-trinitrotoluene
ToF-SIMS	Time of Flight Secondary Ion Mass Spectrometry
UV light	Ultraviolet light

Introduction 1

Chapter 1.

It is widely acknowledged that every person has a unique fingerprint, even identical twins. [1] Together with the fact that the most commonly found fingerprints on crime scenes are not yet visible to the naked eye [2] makes the fingerprint visualisation process of high importance for the identification of the donor of a fingerprint.

This research will seek to enhance the detection of fingerprints by two different approaches; enhance currently used techniques and develop a novel detection method. Molecularly imprinted polymers (MIPs) were explored for the detection (visualisation and retrieving intelligence information) of fingerprints because of their chemical recognition characteristics and visualisation properties. By treating a surface/fingerprint with MIPs (targeted to a specific molecule), the fingerprint becomes fluorescent when the targeted molecules are present. In addition, electrowetting was investigated as a technique to create a flow in a (simulated) fingerprint, aiming to make the molecules in a fingerprint better approachable by currently used fingerprint visualisation reagents and forming more homogenous distributed fingerprint ridges resulting in more/better visualised fingerprints. Subsequently the effect of a potential on a surface was investigated by the analysis of potential driven changes in composition, hydrophobicity, morphology and topography (roughness) of conductive polymer films.

This chapter will provide an overview of the mentioned subjects and used techniques; fingerprints, MIPs, electrowetting, conductive polymers, contact angle measurements, electrochemical, mass spectrometry, microscopy and spectroscopy techniques.

1.1. Fingerprints

A fingerprint is an impression of a collection of friction ridges, also present on the palms, toes, heels and soles. Although the development of the ridges is not completely understood, it is assumed that they are developed during the embryonic stage, probably influenced by physical stress caused by changes in the volar pad (size and symmetry) and growth of the epidermis. The differences in environment (physical stresses and cellular distribution) of each finger imparts a unique pattern of ridges. [3, 4]

The uniqueness of fingerprints make fingerprints, as well as DNA, the well-established methods for identification; whereby DNA profiling is based on the chemical structure, fingerprint identification is based on the physical structure. After the first recording of fingerprint ridges by Nehemiah Grew in 1684 and report about fingerprint ridge features by Joannes Purkinje in 1823, the main foundation for fingerprint identification was laid by the discoveries of the permanence of fingerprints and their uniqueness. Sir William Herschel established that fingerprints remain the same over time (over the period 1860-1890) and introduced the use of fingerprints for identification purposes by identifying inmates. Sir Francis Galton recognised the unique nature of fingerprints in 1892 and introduced a classification system for fingerprint ridge detail (loop, arches and whorls) which is still used nowadays. [1]

1.1.1. Fingerprint composition

A fingerprint is an impression of the pattern of a fingertip, which is created by the release of sweat when the finger comes into contact with a surface. The composition of fingerprint residue depends on the characteristics of the donor and is subjected to the environment. Except contaminated substances such as cosmetics, lubricants and dirt, components of fingerprint residue originate from three secretion glands; the eccrine, sebaceous and apocrine glands. In a hand (fingers and palm) are only eccrine glands present, but because of contact between hands and other body parts, fingerprint residue also consists of components of the sebaceous and apocrine glands which both secrete through hair follicles. Apocrine glands are located at the peripheral and axillary areas and produce mainly proteins, carbohydrates and cholesterol. Sebaceous glands are mostly present on the scalp and face and secrete oily and waxy molecules such as

squalene, wax esters and triglycerides. The eccrine secretion is believed to consist mainly of water (ca. 98%) although the review of Kent [5] showed that the water content might be no more than 20%. In addition, eccrine secretion contains inorganic and organic molecules such as amino acids which are crucial for several visualisation methods. [6] An overview of the fingerprint composition based on the literature is outlined in the Appendix (Section A.1).

The change in fingerprint composition, focussed on lipid content, with time has been investigated in several studies. Generally a decrease in lipid content [7] has been observed. In addition, the influence of bacteria on the degradation process [6], sunlight exposure on the squalene content [8] and the age of the fingerprint donor on the composition and corresponding stability such as a higher cholesterol content in children's fingerprints and wax ester/glycerides content in adults fingerprints [7] has been demonstrated.

1.1.2. Fingerprint patterns

Fingerprints can be used for identification purposes due to their unique ridge pattern. Since Galton's publication in 1892, fingerprints are classified in three main groups: loops, whorls and arches. After the determination of these primary level characteristics, the fingerprint is further analysed on secondary level characteristics such as bifurcations, dots and ridge endings and tertiary level characteristics such as pores (Figure 1.1).

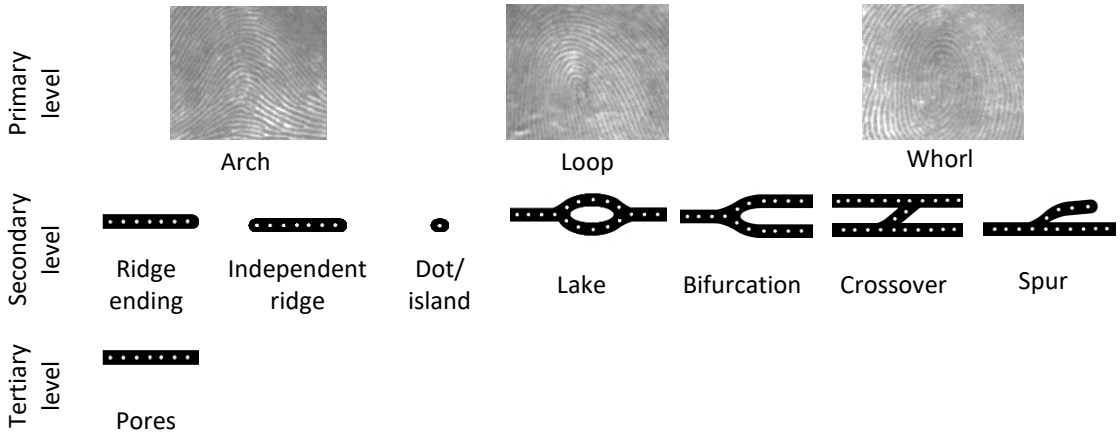

Figure 1.1 – Illustration of fingerprint ridge detail of three levels: primary (top), secondary (middle) and tertiary (bottom) level characteristics. [9]

In the identification process, fingermarks recovered from a crime scene are analysed on the presence and location of the above mentioned characteristics, and compared to fingerprints of suspects and/or databases. As discussed above, impressions of the fingertip can be called fingermarks, referred to traces found on the crime scene, or fingerprints, referred to traces deposited under controlled circumstances. In this thesis above mentioned definitions were used, although the definitions are not ambiguous, e.g. fingermarks could also be defined as latent fingerprints or as traces originating from an unknown donor as well as both terms have been used interchangeably. [10, 11]

1.1.3. Fingerprint techniques/methodologies

Three types of fingerprints can be recovered from the crime scene: patent, impressed and latent fingerprints. Patent and impressed fingerprints can be recovered directly from the crime scene by lifting, casting and photographing, while latent fingerprints or in other words fingerprints not visible to the naked eye, require a visualisation process.

There are several fingerprint visualisation reagents currently available, both based on physical and chemical interactions with the fingerprint residue. The choice of method depends on the nature of the surface (porosity, colour) and/or environmental induced changes (wetting).

Non-porous dry surfaces, such as glass, metals and plastics can be treated with powders, based on the physical adhesion of powders to the fingerprint residue. To address a wide range of coloured surfaces, luminescent, magnetic and coloured powders are available. [12] Alternatively fingerprints can be visualised using cyanoacrylate fuming; cyanoacrylate, also known as superglue, is evaporated at 120 ^{o}C with a humidity of ca. 80% [13] and adheres to the fingerprint residue resulting in a white film. To enhance the contrast, the surface can subsequently be sprayed with colouring agents such as crystal violet, Basic Yellow 40 and safranine or cyanoacrylate modified reagents such as Lumicyano [14] and PolyCyano UV [15] could be used instead of cyanoacrylate. [16] Vacuum metal deposition could also be used to visualise fingerprints on non-porous surfaces, commonly performed by diffusion of gold in the fingerprint and zinc on top. Vacuum metal deposition and to a lesser extent cyanoacrylate showed potential to be

used on fabrics. [17] In comparison to cyanoacrylate, vacuum metal deposition showed higher sensitivity on aged marks but requires also more specialist knowledge to operate. [1, 18]

The enhancement of fingerprints on porous dry surfaces are often performed by a sequence of techniques: 1,8-diazafluoren-9-one (DFO) or 1,2-indanedione followed by indane-1,2,3-trion (ninhydrin) and physical developer. The visualised fingerprints will be recorded after each treatment. DFO and 1,2-indanedione react with amino acids present in the fingerprint till a yellow fluorescent image using green/blue laser excitation and orange/red viewing filter. Ninhydrin reacts with amino acids present in the fingerprint, forming a purple deposit which is also known as Ruhnemann's purple. Physical developer is a silver-based reagent which attaches to the hydrophobic molecules in a fingerprint, producing a grey deposit which is visible using white light. Although physical developer is expensive, time-consuming and the reagent has a short life-time, it is the preferred technique for wetted porous surfaces as amino acids are water soluble. [1, 19]

Besides the above discussed established techniques, research has been performed to use nanoparticles and quantum dots for the visualisation of fingerprints. [20-22] Nanoparticles could also be combined with antibodies to provide specific binding and to obtain intelligence information about the behaviour/characteristics of the donor of the fingerprint or to confirm a certain scenario. Antibodies have also shown to have potential to be used in conjugation with a fluorophore for the detection of fingerprints. [23] Additionally, a wide range of spectrometric and spectroscopic techniques has been used to detect drugs of abuse, non-controlled substances, cosmetics and explosives in fingerprints, as well as information about condom brands/types and personal characteristics has been revealed out of fingerprints. A brief overview of possible detectable substances is given in Table 1.1.

Table 1.1 – Overview of intelligence information detected in fingerprints. Substances: DNT=2,4-dinitrotoluene, GHB=γ-hydroxybutyric, MNT=mononitrotoluene, RDX=trinitrohexahydro-1,3,5-triazine, THC=tetrahydrocannabinol and TNT=2,4,6-trinitrotoluene. Techniques: ATR-FTIR= attenuated total reflectance-fourier transform infrared spectroscopy, DESI=desorption electrospray ionization, GC-MS=gas chromatography-mass spectrometry, LC-MS=liquid chromatography-mass spectrometry, MALDI=matrix assisted laser desorption/ionisation, MALDI-IMS-MS/MS=ion mobility tandem mass spectrometry matrix assisted laser desorption, MCAR=mixed cell agglutination reaction and TLC=thin layer chromatography.

Type	Detected substance/characteristic	Technique	Reference
Behaviour	Caffeine, aspirin, paracetamol, starch and talc	Raman spectroscopy	[24]
Behaviour	Caffeine	LC-MS	[25]
Behaviour	Cotinine	Antibody nanoparticle conjugation	[26]
Behaviour	Nicotine	GC-MS	[27]
Characteristics	Gender	MALDI	[28]
Characteristics	Gender	Ridge density	[29]
Characteristics	Age	TLC	[30]
Characteristics	Age	TLC, photodensitometry	[31]
Characteristics	Blood group	MCAR	[32]
Cosmetics	Face cream, foundation, body lotion, body butter, serum cream and lip gloss	ATR-FTIR	[33]
Cosmetics	Foundation	GC-MS	[27]
Drugs	Cocaine, benzoylecgonine and methylecgonine	DESI, MALDI-IMS-MS/MS	[34]
Drugs	Cocaine and heroin	LC-MS/MS	[35]
Drugs	Cocaine and Δ9-THC,	DESI	[36]
Drugs	Codeine phosphate, cocaine hydrochloride, amphetamine sulphate, barbital and nitrazepam	Raman spectroscopy	[24]
Drugs	GHB	ATR-FTIR	[33]
Drugs	THC and methadone	Antibody magnetic particle conjugation	[37]
Explosives	RDX	DESI	[36]
Explosives	TNT, DNT and MNT	Optical catapulting with laser induced breakdown spectroscopy	[38]
Supplementary information	Condom brand/type	MALDI MSI, MS/MS, Raman spectroscopy and ATR-FTIR	[39]

1.2. Molecularly Imprinted Polymers

Molecularly imprinted polymers (MIPs) attract large interest because of their recognition abilities, stability and low costs of manufacturing compared to their biological equivalents (antibodies). In molecular imprinting the target molecule functions as template around which the monomers polymerise in the form of a shell, followed by the removal of said template. This results in a target-shaped cavity containing specific recognition sites which allow the MIPs to recognize and specifically re-bind to their target molecule. This principle is similar to the lock-and-key or antigen-antibody principle, therefore the MIPs are also called synthetic or plastic antibodies.

The origin of MIPs goes back to 1931 when Polyakov discovered that the structure and surface area of silica polymers was influenced by the solvent. Subsequently, the study of Dickey in 1949 showed that sodium silicate polymers synthesised in the presence of a dye (functioning as template), bind specifically to that dye after removal of the template. [40] The next breakthrough was the introduction of organic solvents [41] and discovery of the increase in adsorption capacity by restricting the mobility of polymer chains using cross-linkers, [42] both in 1972. Opposed to the covalent approach of Wulf *et al.* [41], whereby as the name implies the MIPs and target molecule bind covalently, Arshady and Mosbach [43] introduced in 1981 the non-covalent approach, or also called the self-assembly approach. [44] The self-assembly approach leads to higher simplicity of manufacturing while the covalent approach results in more well defined binding sites and a higher stability. [45] As shown in Figure 1.2, the amount of publications increased significantly from ca. 1997, which could be due to the publication in 1995 by Andersson *et al.* [46] describing the use of aqueous buffers for MIPs synthesis instead of the so far used organic solvents. This breakthrough resulted in the possibility to use this technique also in biological contexts. Additionally, in 1995 the semi-covalent approach was developed by Whitcombe, consisting of covalent binding during polymerisation and non-covalent rebinding. This approach relies on the introduction of a spacer group which got released when the template is removed. [47] However, the noncovalent approach is still the most widely used method, possibly due to the development of stoichiometric monomer/template methods. [45] In 2002 and 2008 the increase in

publications stopped, which could be caused by the start of the recession and the European economic crises in the early 2000s and 2007 respectively.

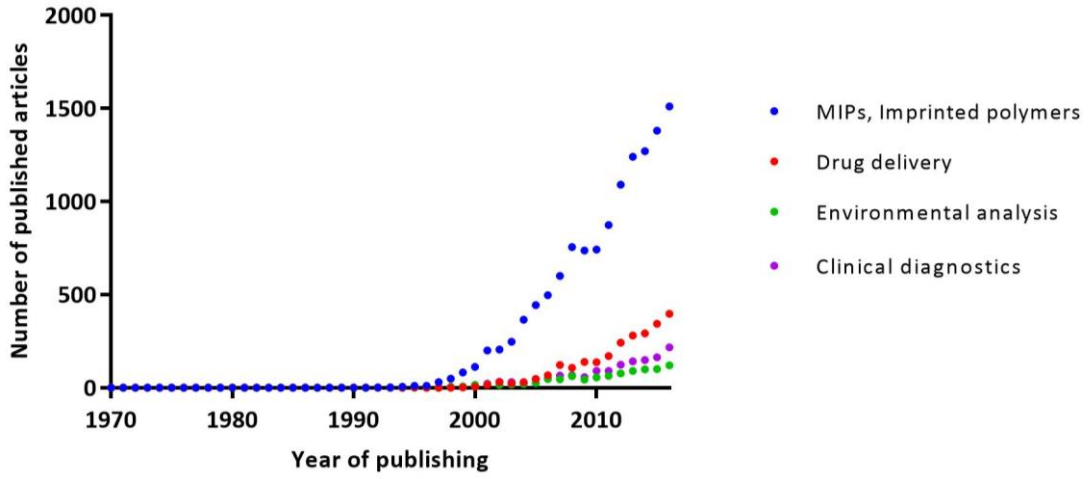

Figure 1.2 – Amount of MIPs articles published over time (search term in google scholar: MIPS "imprinted polymers" + specific term).

Currently, MIPs are seen as synthetic antibodies and receptors and are therefore of growing interest for a wide variety of applications such as for drug delivery [48], environmental analysis/extractions [49] and clinical diagnostics [50] as shown in Figure 1.2 and discussed in more detail in Section 1.2.2. In contrast to antibodies, MIPs show a higher stability, could be used in both aqueous and organic matrices and there is no need for test animals. However, for the synthesis of the MIPs the target molecule has to be available, although fragments or analogues could also be used instead of the target molecule. [50, 51]

1.2.1. Preparation of MIPs

The MIPs are synthesised by free-radical polymerisation of functional monomers, and usually cross-linkers, around a target molecule which acts as a template. Afterwards the target molecule is removed and a polymer shell remains. Due to the presence of these specific recognition sites in the polymer, the MIPs can recognise and specifically re-bind to the target molecule.

The functional groups of the monomers interact with the target molecules and the cross-linking agent functions, like the name implies, to cross-link the polymer chain. The latter are also called cross-linking monomers or cross-linkers. Depending on the target

molecule and the type of MIPs, different kinds and/or amounts of functional monomers and cross-linkers could be used to obtain optimal stiffness (enough selectivity by retaining its shape), flexibility, accessibility of the cavity, mechanical and thermal stability (for applications which require high pressure/temperature). [52] Due to the complexity and wide variety of monomers, computational studies could be performed to determine the optimal theoretical type and amount of monomers.

The functional monomers are the main components of the MIPs. To maximize the affinity between the MIPs and the target molecule, the functional groups of the monomer should match the target molecule; commonly using H-donor groups (as carboxylic acid) and H-acceptor groups (as alcohol, ether or amine). [53] The affinity could be increased by increasing numbers of monomers [54] and optimising the ratio monomer/target molecule, noting that the amount of binding in the covalent approach is determined by the target molecule only. Cross-linkers have an influence on the morphology and stability and thereby on the selectivity and flexibility of the MIPs; by increasing the amount of cross-linking, the MIPs might be more specific, but the 'cavity' could also be less accessible for the target molecule. [52, 53] This increase in amount of cross-linking can be achieved by a change in type/size of the cross-linkers and/or increase in concentration. As the latter could result in both an increase in stiffness and selectivity of the MIPs, an optimum must be sought. [54, 55] Commonly used functional monomers and cross-linkers are shown in Figures 1.3 and 1.4 respectively. [54, 56, 57]

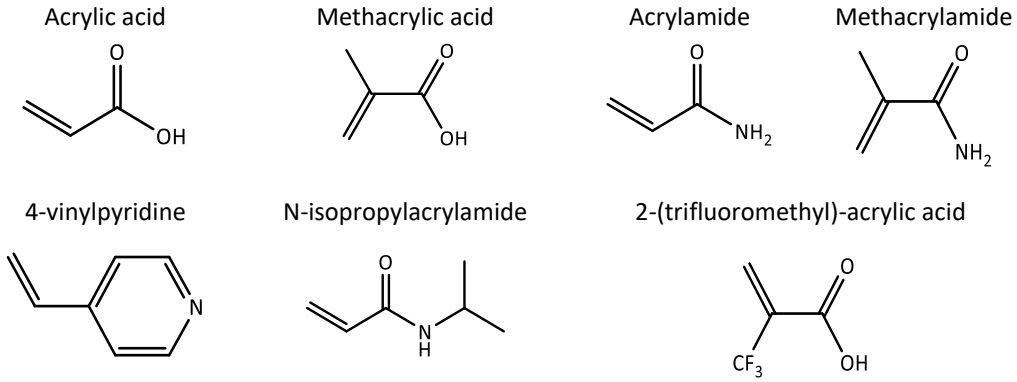

Figure 1.3 – Functional monomers commonly used in MIPs.

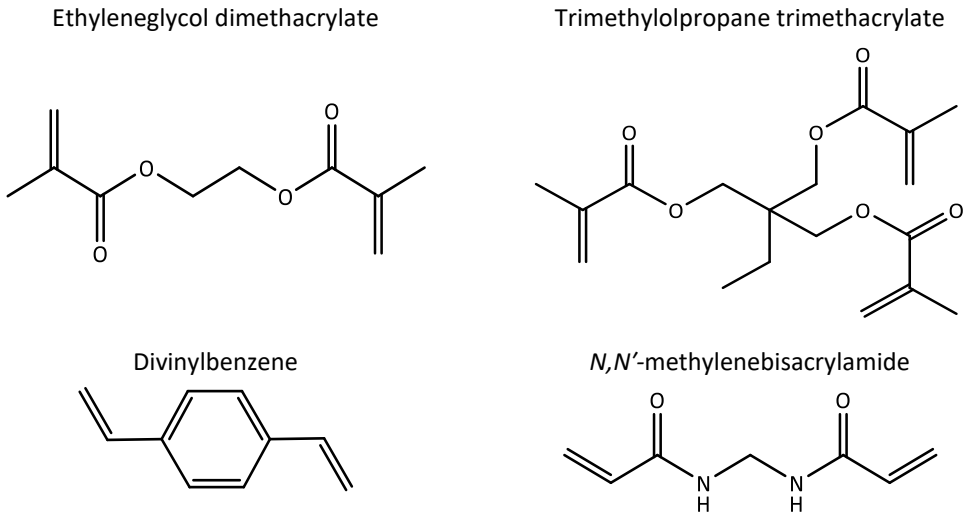

Figure 1.4 – Cross-linkers commonly used in MIPs.

The solvent is not only used to dissolve the monomers, cross-linkers and target molecules but also to create a porous morphology, therefore also called a porogen. Low polarity of the solvent could result in less interference of the H-bonding between the monomer and the target molecule and low solubility could result in larger pores and a smaller surface area due to phase-separation early in the polymerization process. [54, 58] Additionally, the selectivity could be influenced by the solvent, although to a limited extent. Ideally the solvent should not compete significantly for the same type of interactions between monomer and target molecule.

1.2.2. Applications

MIPs have shown to possess good recognition characteristic and being able to detect a wide variety of molecules in a range of environments, from pesticides in strawberries [59] to paracetamol in human serum [60]. Therefore MIPs were an obvious choice for discovering the possibilities to detect specific molecules in a fingerprint. At this time this is a very novel application based on two novel concepts, the use of non-cross-linked linear MIPs and the detection of molecules in a fingerprint using MIPs, therefore the amount of literature is very limited. However, the concept of linear MIPs was recently demonstrated in a medical context. [61] To provide more insight in the possibilities of the MIPs, three widely used and forensic relevant (regarding target molecule and/or matrix) applications were discussed in more detail below.

Similar to the research in this thesis, the detection of fingerprints using MIPs, in the drug delivery application the MIPs have to move through a medium towards their location of interest. In the fingerprint detection application, towards the target molecule and in the drug delivery application towards the drug release location. In the drug delivery application, a drug bound to a MIP is released at their target position, for instance a certain cell or organ, by applying or experiencing a stimuli. As outlined in Table 1.2, the release could be caused by e.g. a change in pH, irradiation or the presence of another molecule to which the MIPs bind. To deliver the drug at the right position and time without harming the rest of the body, a controlled, accurate and non-toxic delivery is required. The high stability, resistance and ability to change by external stimuli makes MIPs appropriate for this application. [48, 62, 63]

Table 1.2 – Overview of a variety of MIP drug delivery studies using several target molecules, drug delivery forms and release principles. NR=not reported.

Target molecule	Drug delivery form	Release principle	Ref.
Bimatoprost	Contact lenses	Release by swelling induced by pH or hydration	[64]
Doxorubicin	NR	Double imprinted MIP. Release of doxorubicin by binding to epidermal growth factor receptor	[65]
Propranol, ibuprofen, ketoprofen	Tablet form	Dissolution, stereo-selective	[66, 67] [68]
Hydrocortisone	NR	Release by hydration. The release of a similar molecule bound to the MIPs (testosterone) was accelerated in the presence of the target molecule.	[69]
Vancomycin	Albinate matrix	Diffusion and swelling	[70]
Metronidazole	Oral	pH-trigger	[71]
Mitoxantrone	NR	X-ray stimulate the MIPs/nanoparticles resulting in the generation of light and activation of the photosensitizer mitoxantrone	[72]

The application of MIPs for environmental analysis is mainly focused on the extraction of contaminants or harmful substances such as pesticides or drugs in food, (waste) water and soil matrices. The extraction is based on conventional extraction methods such as solid-phase (micro) extraction, magnetic solid-phase extraction and stir-bar sorption extraction, whereby the sorbent is replaced by a MIP sorbent, also called molecular-imprinted solid-phase extraction (MISPE). The MIPs sorbents are of interest due to their high specificity, low costs and easy preparation [73] and performed comparable or even better than conventional extraction kits. [49, 74, 75] The potential

of the use of MIPs for the extraction of a variety of compounds is not only shown by the wealth of performed research but is also emphasised by the presence of several commercially available MISPE products.

The successfulness of the extraction, defined by among others the selectivity and sorption capacity, could be influenced by the homogeneity and porosity of the MIPs sorbent. Therefore the MIPs synthesis settings, which could affect these factors, are of high importance. [49] Possible template leakage and the requirement of the target molecules during the synthesis could be a disadvantage of the MIPs compared to conventional methods. The latter can be problematic for target molecules present in very low concentrations, although this possibly can be solved by the use of fragments or analogues instead of the actual target molecule. [76]

To get a better understanding of the possibilities of the extraction using MIPs, a range of studies are outlined such as the extraction of pharmaceutical and food products as shown in Tables 1.3 and 1.4. The studies using pharmaceutical products demonstrate the possibility to extract medication in among others forensically relevant matrices such as body fluids.

Table 1.3 – Overview of pharmaceutical molecules extracted with MIPs. NR=not reported.

Target molecule	Matrix	Recovery	Reference
Adefovir (Hepatitis B, antiviral drug)	Human serum and urine	88.2-93.5% 84.3-90.2%	[77]
Oxprenolol (beta-blocker)	Urine	NR	[78]
Gastrodin (for a.o. epilepsy)	Root extract	76.6%	[79]
Hypericin (antibiotic, antiviral)	Herbal extract	82.30%	[80]
Pentamidine (PCP, AIDS-related diseases)	Urine	<89%	[81]
Peniciloic acid (allergenic impurity in penicillin)	Penicillin	76.2-88.3%	[82]
Warvarin (anticoagulant)	Urine	>95%	[83]

The studies using food products were selected because of the increasing concern of food safety. The increase in regulations and public interest resulted in a growing interest for improved and/or alternative extraction and detection methods both during and after the food processing. MIPs have been shown to be of potential interest as sorbents for the extraction of a variety of food related substances such as (trace) impurities like herbicides, pesticides and toxic substances but also additives, and resulted even in

higher selectivity than some conventional methods according to the study by Karimi *et al.* [84].

Table 1.4 – Overview of food relevant molecules extracted with MIPs. NR=not reported.

Target molecule	Matrix	Recovery	Reference
Lactose	Milk	NR	[85]
Oranophosphate (pesticide)	Strawberries	65.25-87.70%	[59]
Protocatechuic acid (reduce lactose intolerance)	Extract from Rhizoma homalomenae	82%	[86]
Sulfonamides (drug)	Chicken meat	95-99%	[84]
Synthetic colorants	Chilli spice and chilli powder	72.1-95.6% 72.1-92.3%	[87]
Diethylstilbenstrol	Fish	>87.5%	[88]

MIPs could also be used for the purpose of clinical diagnostics, to confirm the presence of medical relevant molecules such as glucose and paracetamol in serum or urine samples. [60, 89] As shown in Table 1.5, a range of sensors have been developed using MIPs as recognition elements.

Table 1.5 – Overview of a range of using MIPs detected medical relevant molecules. NR=not reported.

Target molecule	Matrix	Sensor	Reference
Caffeine	NR	QCM	[90, 91]
Nucleosides (cancer biomarkers)	Urine	Extraction	[92]
Chloroamphenicol	Serum	Optical	[93]
Clenbuterol	Bovine liver	Electrochemical	[94]
β-Estradiol	NR	Optical (fluorescence)	[95]
Glucose	Human blood serum	Electrochemical	[89]
Human Rhinovirus serotype 2, Tobacco Mosaic Virus	NR	Spectroscopy (impedance)	[96]
Morphine	NR	Electrochemical	[97]
Paracetamol	Human serum, urine	Electrochemical	[60]
Phenactin	Human serum, urine	QCM	[98]

1.3. Electrowetting

Electrowetting is a process in which the amount of wetting is modified by the application of an electrical potential. The wetting phenomenon itself was already described in 1612 by Galileo, [99, 100] after which Young [101] quantified wetting using the contact angle in 1805. Subsequently electrowetting was introduced, which principle is based on one of the most important fundamentals of fluid dynamics, the electrocapillary phenomenon. This phenomenon was first described by the French physicist and later Nobel prize winner Gabriel Lippmann in 1975. [102] He described the relation between surface energy/interfacial tension and potential by applying a potential across an electrolyte-mercury interface after which a change in capillary depression of mercury was observed. Besides the publication of the electrocapillary theory, Lippmann applied it in practise by the invention of the electrometer. In 1993 Berge [103] introduced the use of an insulator layer on top of the substrate electrode to prevent contact between the electrode and the liquid and thereby electrolysis, while the insulator layer functioned also as capacitor. This principle is currently implied in most of the research and applications, and known as electrowetting-on-dielectric (EWOD). In this research EWOD was used, therefore electrowetting without insulator/dielectric layer is not discussed in detail.

1.3.1. Operation of the electrowetting-on-dielectric process

By applying a potential, the droplet and substrate become oppositely charged resulting in the attraction of the droplet to the substrate and thereby spreading of the droplet (Figure 1.5A). The dielectric layer functions hereby as capacitor, it enables a higher electric field and reduces the electrolysis problem. The influence of several factors such as liquid composition, dielectric layer composition, potential and frequency on the electrowetting process will be discussed in Chapter 3.

To obtain electrowetting, a variety of set-ups could be used; a wire or a plate can function as top-electrode (Figure 1.5A and B) and the bottom electrode can consist of a single electrode (Figure 1.5A and B) or multiple electrodes (Figure 1.5C and D). By using interdigitated electrodes (Figure 1.5C and D) also called individually addressable electrodes, a droplet can move along a line of electrodes.

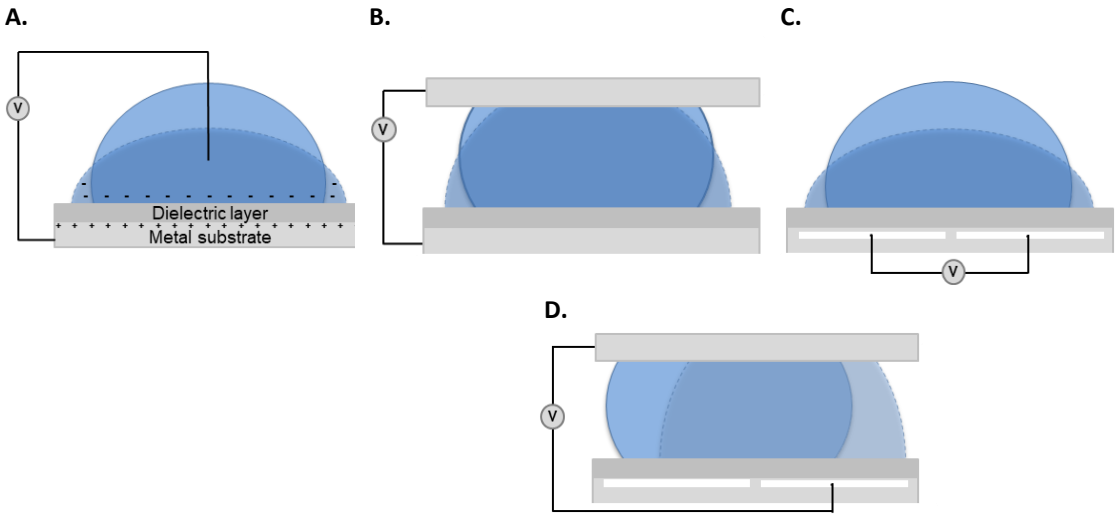

Figure 1.5 – Schematic illustration of electrowetting-on-dielectric set-ups with a wire as top electrode (**A**), plate as top electrode (**B, D**) and interdigitated electrodes in the substrate (**C, D**).

1.3.2. Formation of a flow using electrowetting

The application of a potential across a droplet and the underlying surface does not only lead to spreading of the droplet but could also induce a flow inside the droplet. This flow formation has been investigated in several studies for a variety of purposes, both by tracking of particles added to the droplet and by staining the droplet partially with a fluorescent dye. [104-110]

The electrowetting induced flow has been shown to be able to merge liquids, e.g. glycerol has been mixed with water whereby the top layer was stained with a dye to follow the movement of the dyed liquid through the rest of the droplet. [110] This study demonstrated a decrease in mixing time and symmetric distribution by increasing viscosity. Other studies were focussed on origin of the flows as outlined in Table 1.6, illustrating that flows can be divided in two groups based on the applied frequency. The low frequencies are known as the hydrodynamic frequency range whereby the droplet is able to screen the applied electric field. The formed flow in this range is probably caused by (interfacial) oscillations of the droplet/electric force acting on the three-phase contact line. [105, 108, 109] The flows in the high frequency range are believed to be an electrohydrodynamic effect and are probably dependent on the electric field distribution [104, 105] suggested by the flow formation caused by an induced electrothermal force [108] and the presence of a stronger electric field at the location where the flow appears, according to a numerical study. [105] Instead of focussing on

the bulk viscous dissipation, the study of Lu *et al.* [111] investigated the response of a droplet to frequency from a kinetic perceptive, focussing on the contact line friction and pinning force in the low frequency range (0-200 Hz). This showed a dominancy of the contact line friction and inertia over the electric and capillary force by increasing frequency, resulting in a droplet which cannot fully follow the frequency anymore at high frequencies and a completely vanished oscillation at 200 Hz. Based on the extraction/retraction time of a droplet subjected to direct current (DC) potential the response time of a droplet was determined at 15 s, suggesting the contact line of the droplet cannot follow frequencies larger than ca. 30 Hz. It should be noted that while the contact line is damped by contact line friction, the contact angle is also dependent on the oscillations of the height which depends on the inner flow and take a longer time to be damped (compared to the contact line) due to slower viscous dissipation. [111]

Table 1.6 – Literature overview of flow formation induced by electrowetting induced. NR=not reported.

Frequency	Observation/interpretation	Reference
10 Hz-15 kHz	Flow insensitive to conductivity and possibly caused by an electrical force acting on the three-phase contact line/oscillations of the complete droplet.	[105]
35-256 kHz	Flow sensitive to liquid conductivity and electrode position, probably controlled by electric field distribution.	[105]
<33 Hz	Droplet responds to the applied frequency.	[111]
200 Hz	Visible movement almost completely disappeared. By increasing frequency the contact line friction and inertia became dominant over the capillary force, the droplet cannot respond to the high frequencies.	[111]
50-310 kHz	Flow probably caused by an electrohydrodynamic effect. Despite the correlation between frequency and conductivity, and the increase in electric field with frequency, the flow velocity does not increase linearly by frequency (an optimum op 110-150 kHz).	[104]
Low (NR)	Flow attributed to oscillations of the complete droplet.	[108]
High (NR)	An electric field in the droplet results in a temperature increase. Flow is formed by an induced electoral force caused by gradients in temperature and thereby in conductivity and permittivity.	[108]
~10 Hz	Quasistatic behaviour using frequencies below the eigenfrequency.	[107]
~10 Hz - kHz	Hydrodynamic behaviour.	[107]
> kHz	Electrothermal behaviour. Electric field in the bulk of the droplet.	[107]
1 Hz	Quasistatic and complete droplet oscillation flows are dominant.	[106]
50 Hz	Steady flows in opposite direction of the electrode are dominant.	[106]

This knowledge about the influence of the frequency on the flow has been used in the research of Eral *et al.* [107] to determine the optimal conditions to suppress ring stain formation. Ring stain formation, also known as the coffee stain effect, was overcome by inducing a flow in a drying droplet using the electrowetting process. The flow inside the droplet prevents particles to adsorb on the substrate and droplet contact line pinning to the surface. [107] The flow formation has not only been of interest from a fundamental perspective but also for applications such as MALDI sample preparation. The formation of a flow in a drying sample could create more homogenously distributed and smaller sample spots due to suppression of the ring shaped stain formation, [112] which could be of use for MALDI analysis as small crystallised sample spots are preferred.

1.3.3. Applications

Besides the possibility to improve the sample preparation of MALDI, the electrowetting process can be used for a wide range of applications.

In 2003, Hayes and Veenstra [113] successfully introduced the electrowetting process in displays followed by the start of the Philips spin-off company Liquavista. This application is based on the movement of coloured oil droplets in pixels; by applying a potential between the substrate and droplet, the amount of droplet coverage and thereby colour on the pixel changes as illustrated in Figure 1.6.

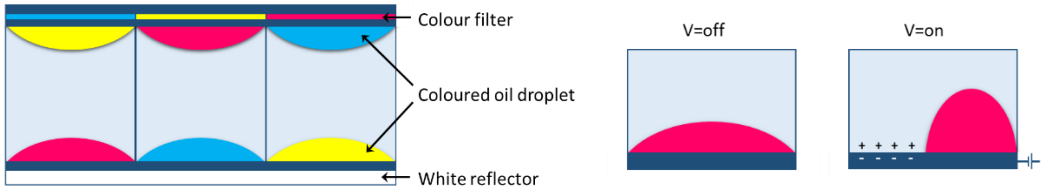

Figure 1.6 – Schematic illustration of the electrowetting display as invented by Hayes and Veenstra. [113]

In comparison with the conventional displays such as LCD screens, the electrowetting displays show brighter colours, therefore less supplementary lighting is required resulting in battery savings. The electrowetting displays also show good usage in high direct daylight conditions such as outdoor in the sun as the principle is based on reflection and there is no need for a polarisator like in the conventional emission or transmission displays. [114]

One of the oldest electrowetting applications is the lab-on-a-chip application whereby electricity is used to manipulate liquid present on a chip. The chip consists of an array of individually addressable electrodes which makes it possible to move liquid along a path to mix, merge, split and create chemical reactions as shown in Figure 1.7. Hereby a droplet is positioned on two electrodes, by addressing one of them a movement is induced as illustrated in Figure 1.7B.

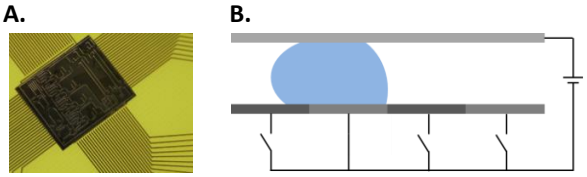

Figure 1.7 – Illustration of a lab-on-a-chip systems: a photo of a chip (**A**) and a schematic illustration of a droplet on individually addressable electrodes (**B**).

In 1979, Terry *et al.* [115] developed a miniature gas chromatography system using photolithography which is generally seen as the first lab-on-a-chip system. Subsequently, lab-on-a-chip has been used for a wide variety of purposes because of its ease of use, requirements of low volumes and short analysis time. [116] Currently used and investigated applications are medical diagnostics such as diabetes self-testing, drug screening, food analysis and ecology such as water analysis. [117]

The electrowetting process has also been of interest in the field of micro-optics, in particular to tune micro camera lenses using electrowetting. This application was first demonstrated by Berge *et al.* [118] in 2000 and further developed by Philips and Varioptic. Electrodes are positioned on both sides of the droplet and by applying a potential the shape of the droplet changes and thereby the lens properties (Figure 1.8). The advantage of the electrowetting lens to conventional lenses is that there is no need for mechanical constructions to adjust the lens which could be challenging for micro constructions.

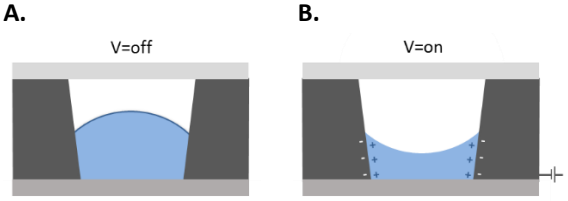

Figure 1.8 – Schematic illustration of an electrowetting lens with electrodes (dark grey) on the left and right side of the liquid (blue), without applying a potential (**A**) and by applying a potential (**B**).

1.4. Conductive polymers

Conductive polymers, also called conjugated or electroactive polymers, are polymers which can conduct electricity. However, in the beginning they were used as isolators. This radical change in properties happened in 1977 by the discovery of high conductivity by exposing polymers to a halogenic vapour (Cl, Br, I). [119] The importance of this discovery was emphasised by the receipt of the Nobel prize in Chemistry in 2000 by Heeger, MacDiarmid and Shirakawa. [120] This also led to a rapid increase in the number of applications. Based on the electrochemical reaction, the applications can be divided in two groups; ones that occur when a potential is applied and ones that produce a potential, resulting in a wide range of applications: energy storage such as rechargeable batteries, [121-124] fuel cells [125, 126] and cellulose-based devices [127-130], smart materials such as displays [131-133] and windows [134, 135] and as coatings anti-static [136, 137], anti-corrosive, [138-143] and anti-fingerprint [144]. Conductive polymers could also be integrated with molecular recognition sites functioning as sensor in which the properties of conductive polymers change by binding of the target molecule. [145] In addition, conductive polymers could be used as fingerprint visualisation reagent. [146]

This research is focussed on the behaviour of three widely studied conductive polymers; polyaniline, polypyrrole and poly(3,4-ethylenedioxythiophene)(PEDOT); these conductive polymers have the advantage of being able to be used at room temperature, [147] good redox reversibility, high conductivity and stability. [148] As shown in Figure 1.9, one of the most popular polymers, polyaniline, has been of increasing interest with time. Polyaniline was first introduced in the early 1830s by Runge [149], whereby the colour changes by oxidation/reduction got special attention. However, due to the possible formation of toxic benzidine derivatives, [150] other polymers such as polypyrrole and the polythiophenes (of which PEDOT is part of) became of interest. Polypyrrole, also called pyrrole black named after its colour in oxidative state, was one of the first heterocycle conductive polymers, first reported in 1963. [151-153] This polymer is of general interest because of its possibility to polymerise in both aqueous and organic solution. [154-156] The third polymer used in this research is PEDOT. This polymer was discovered in the late 1980s as an anti-static coating in photographic films

by researchers of Bayer. [157-160] Now-a-days PEDOT is used for a wide range of application such as displays, [161-163] transparent electrodes [164-166] and re-chargeable batteries, because of its transparency in oxidised state, high stability and moderate band-gap. [167] However, in contrast to polyaniline and polypyrrole, PEDOT has a low solubility in water and is therefore preferably polymerised in an organic solvent or in an aqueous solution with a surfactant. Alternatively, a PEDOT film can be formed using very low monomer concentrations in aqueous solutions. [168]

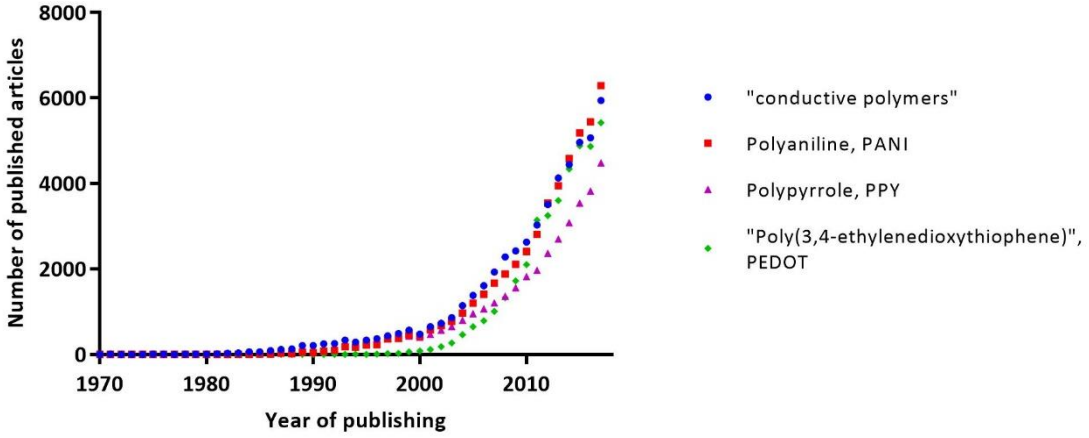

Figure 1.9 – Number of published articles about conductive polymers (based on the title as search term in google scholar).

1.4.1. The electroactivity of conductive polymers

Conductive materials owe their conductive properties to the ability to carry electricity. Due to the conjugated sp^2 backbone structure, or in other words alternating single-double bond structure of the conductive polymers (Figure 1.10), delocalised electrons can move around. [169]

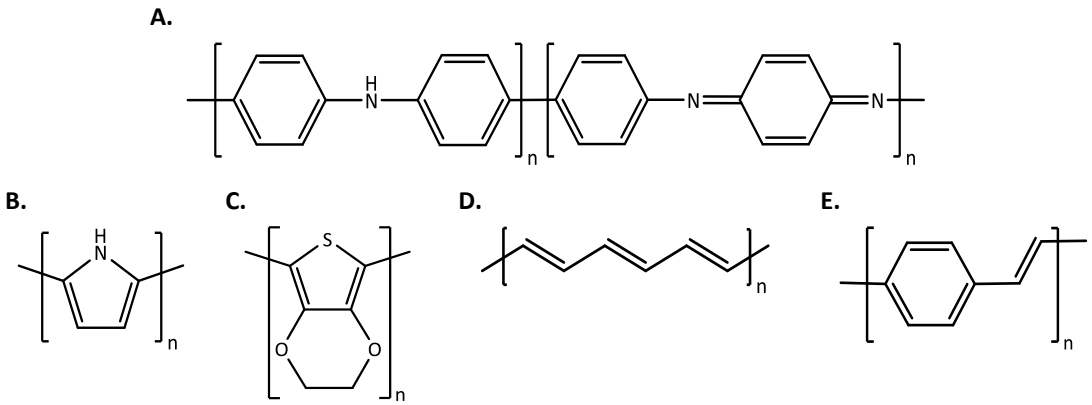

Figure 1.10 – Chemical structure of conductive polymers with aromatic cycles such as polyaniline (**A**), polypyrrole (**B**) and PEDOT (**C**), double bonds (**D**; polyacetylene) and both an aromatic cycle and double bond (**E**; poly(p-phenylenevinylene)).

As shown in Figure 1.11, in a conjugated sp^2 structure each carbon atom has three σ-bonds and one π-bond, forming a sp^2 orbital per atom (orange) and π-electron cloud (red and blue) in which the delocalised electrons move around.

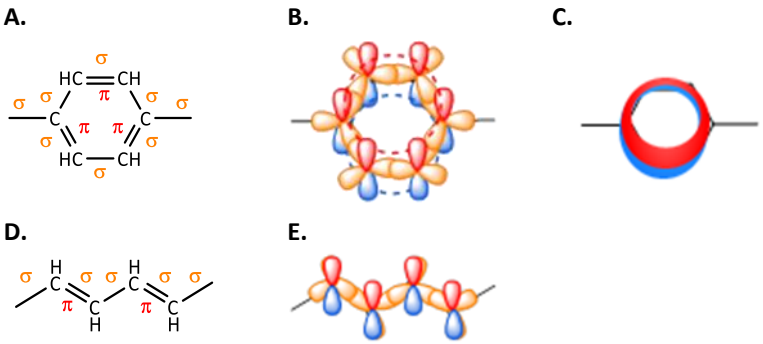

Figure 1.11 – Illustration of sp^2 backbone structures of benzene (**A, B, C**) and poly(1,3-butadiene) (**D, E**) in the form of the chemical structure (**A, D**), orbitals (**B, E**) and the formed π-electron clouds (**C**).

More precisely conductivity could be described by the movement of electrons from the valence band to the conduction band, resulting in an electron that can move around in the conduction band and an electron-free hole in the valence band which could function as mobile charge carrier. The energy band-gap defines the amount of conductivity; no band-gap in metals, bridgeable band-gap in semi-conductors and a band-gap which is too large to cross in insulators, therefore non-conductive (Figure 1.12).

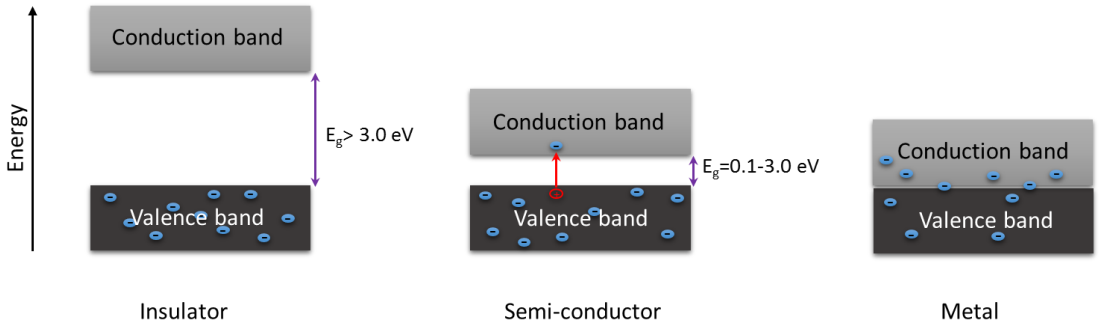

Figure 1.12 – Energy levels in insulators, conductive polymers and metals, including the energy band-gap (E_g), electrons (blue) and electron-free hole (red).

Most conductive polymers behave intrinsically as insulators/semi-conductors. However, the addition of doping can decrease the energy band-gap, resulting in an increase in conductivity. [170] During oxidation, the polymer film becomes positively charged after which an anion (dopant) could enter the film to neutralise the charge, leading to a distortion and thereby formation of a localised charge which reduces the energy band-

gap between the highest occupied molecular orbital (HOMO) and lowest unoccupied molecular orbital (LUMO), also known as polaron (Figure 1.13). [171] By increasing the amount of charge even dipolaron(s) could develop. During the reduction process the polymer film is discharged, the anion is ejected from the film and a cation can be inserted in the polymer film. [172]

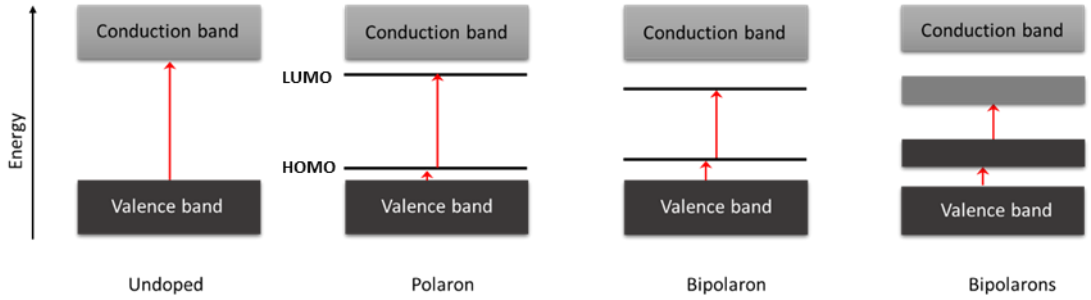

Figure 1.13 – Energy levels of conductive polymers in undoped and doped state (polaron and bipolarons).

Additionally, due to the structure of the conductive polymer chain, the energy band-gap decreases by increasing chain length (Figure 1.14). The HOMO energy level increased and LUMO energy level decreased by the formation of butadiene due to the interaction between the HOMO and LUMO of ethene. By polymerising further, the carbon chain prolongates and thereby the number of carbons (π-orbitals), resulting in a decrease in energy gap between the valence and conduction band. [173, 174]

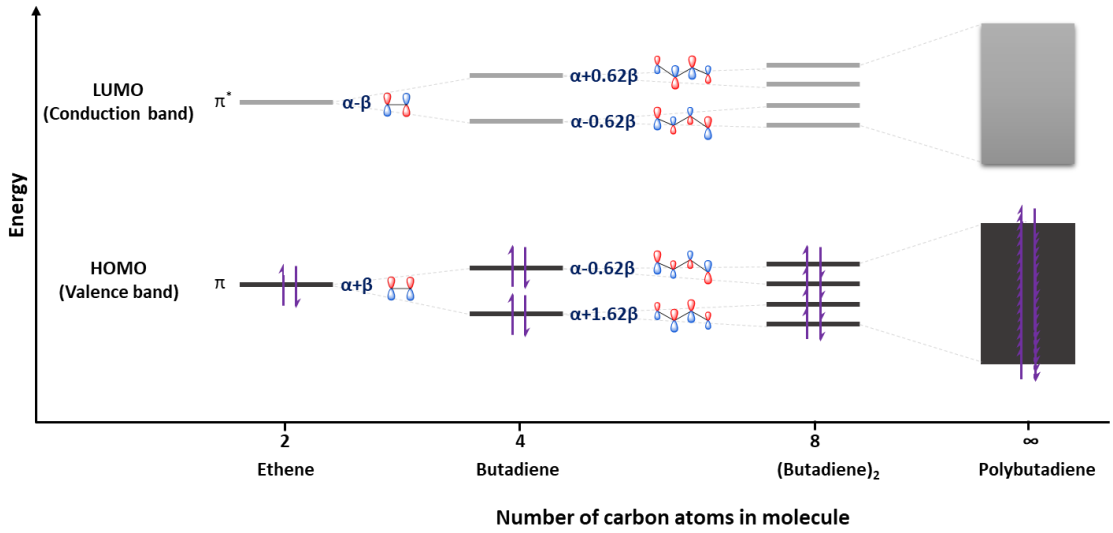

Figure 1.14 – Energy level diagram (π-type orbitals) of the formation of polybutadiene.

1.4.2. Characterisation of conductive polymer films

The chemical and physical characteristics of conductive polymer films could change during redox reaction. As this research is focussed on the potential driven changes in composition, morphology, topography (roughness) and hydrophobicity of polyaniline, polypyrrole and PEDOT films, the following overview is focussed on these aspects.

The chemical composition of the conductive polymer film can change by redox reaction, both during and after polymerisation. Although the polymerisation mechanism of conductive polymers is not unambiguous, for all the three polymers, polyaniline, polypyrrole and PEDOT the polymerisation is generally assumed to occur in three steps (Figure 1.15). A radical cation was formed by oxidation at the anode (step 1). Subsequently the monomers dimerise, resulting in a double charged dimer which will be deprotonated to form a neutral dimer (step 2). This dimer is oxidised to form a new cation (step 3) which undergoes coupling with a radical monomer to propagate the chain (repeat step 2). These oxidation and deprotonation steps could be repeated till the desired chain length/ film thickness is achieved. [175-177] To maintain electroneutrality, counter electrons present in the surrounding electrolyte solution could enter the polymer film which could result in (de)swelling of the polymer film.

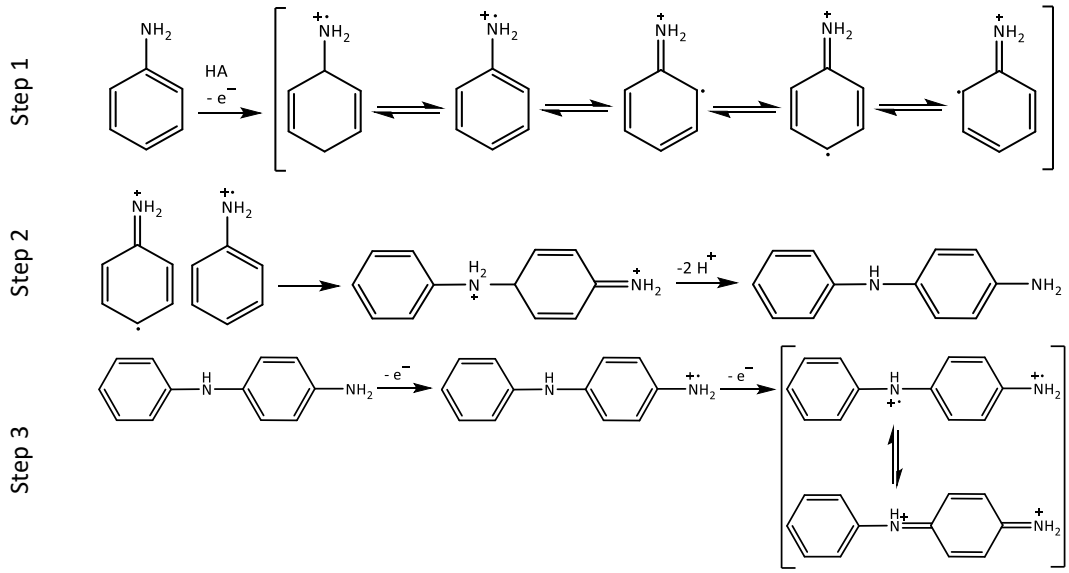

Figure 1.15 – Polymerisation mechanism of polyaniline, illustrating in three steps; formation of a radical cation (step 1), dimerization (step 2) and formation of a new cation (step 3). These steps could be repeated till the required polymer film thickness is obtained.

During the oxidation and reduction of the polymer, the change in chemical composition was accompanied by a change in colour, also called electrochromism. Therefore conductive polymers are potential materials for a range of applications such as smart windows [134, 135] and displays [131-133]. Polypyrrole is known as a two coloured state polymer, yellow/green in reduced state and blue/violet in oxidised state. However, this colour change has not always been observed, possibly caused by fading over time and/or by the absence of a colour change using thick films (>1 µm). [172] PEDOT changes colour from almost transparent to dark blue by oxidising, also called cathodic colouring. This type of colouring is typical for low energy band gaps (<1.5 eV) which in the case of PEDOT could be caused by the presence of an electron donating oxygen in the ring structure which increases the HOMO energy level. [178, 179] Polyaniline is known for its different coloured electronic states, from leucomeraldine (colourless/yellow, fully reduced form) via emeraldine (green/blue; half oxidised/ reduced form) to pernigraniline (blue/purple; fully oxidised) during oxidation and in backwards direction during reduction (Figure 1.17). Besides the three mentioned structures whereby the benzoid unit converts into a quinoid unit during oxidation (Figure 1.16), polyaniline could also convert from a base to a salt form by acid doping (Figure 1.17). [180-183] This demonstrates that the electronic and electrochromic properties of polyaniline depend on both the oxidation and protonation state.

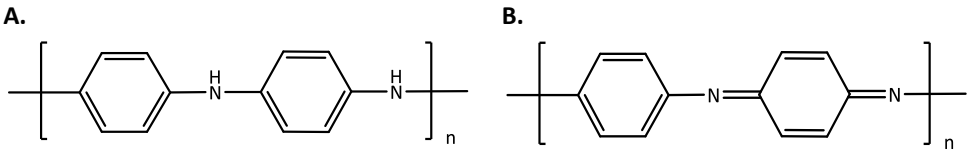

Figure 1.16 – Benzoid (**A**) and quinoid (**B**) unit of polyaniline.

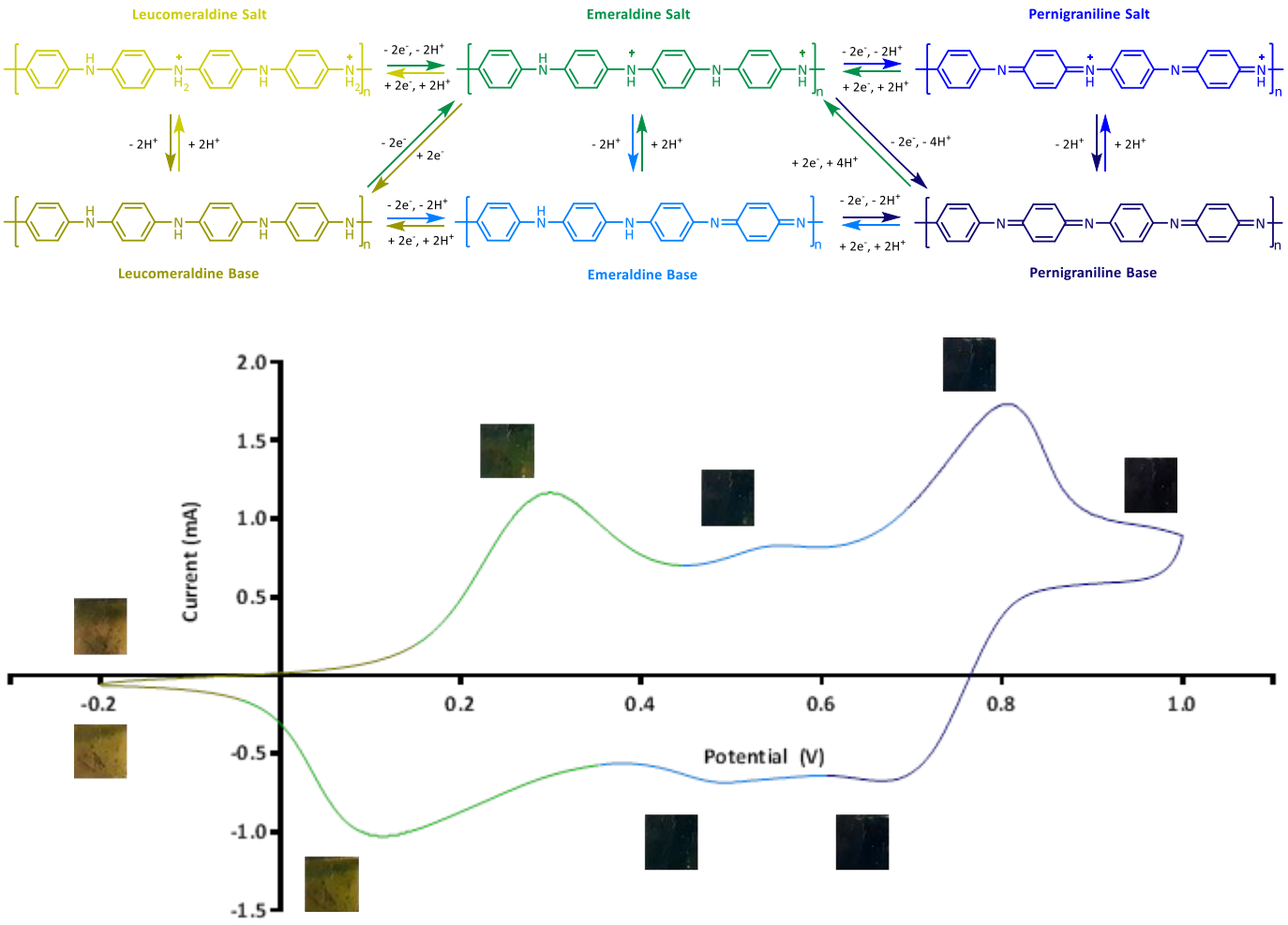

Figure 1.17 – Cyclic voltammogram of polyaniline, including their corresponding molecular structures and colours.

Studies about the hydrophobicity of conductive polymer films resulted in a wide variety of observed effects as outlined in Table 1.7, possibly due to the differences in experimental setting. This resulted in several speculations about the behaviour of the hydrophobicity of conductive polymer films as discussed below.

Reorientation of the polymer structure, caused by diffusion of the anion in the film, could possibly result in a change in hydrophobicity (Figure 1.18). [184-186] The influence of the polymer chain on the hydrophobicity was also implied by the increase in hydrophobicity with non-polarity of the polymer chain (longer alkyl-side-group). [186]

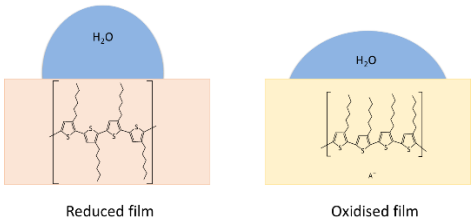

Figure 1.18 – Illustration of the possible influence of the polymer structure on the hydrophobicity of the polymer film.

The orientation of the dopant towards the droplet could possibly also affect the hydrophobicity. A relatively hydrophobic group could be oriented towards the oxidised polymer chain and reversed in reduced state (Figure 1.19A), [187] the anions could possibly also move into the droplet resulting in a change in surface tension and contact angle of the droplet (Figure 1.19B). [188] Due to the movement of the (surfactant) anions in the droplet-electrolyte interface, the surface tension of this interface could decrease. Together with a density difference of the droplet and electrolyte (and gravity), spreading of the droplet could be induced while the hydrophilic polymer film limits the spreading, resulting in an increase in contact angle of the spread droplet upon reduction, also known as the pancake shape (Figure 1.19C). [184]

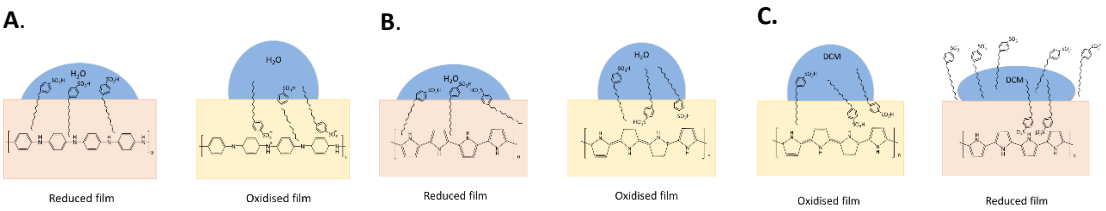

Figure 1.19 – Illustration of the possible influence of the hydrophobic chain anion pointed towards droplet (**A**), movement of anions into the droplet (**B**) and behaviour of anions at the polymer-electrolyte-droplet interface (**C**) on the hydrophobicity of the polymer film.

However, the movement of anions in the droplet might be questionable because of the possible slow movement of the anions out of the polymer film due to immobilisation and the relatively fast stabilisation of the droplet after deposition, which would make it possible to measure the contact angle of a stable droplet before anions could enter the droplet. [185]

Contrary hydrophobicities were obtained between single measurements, droplet is positioned on the polymer film in reduced or oxidised state, and continuous measurements whereby the droplet stays on the polymer film during the redox reactions. During the continuous measurements the droplet covers an area of the polymer film. This area underneath the droplet is only accessible via the droplet, via the edges of the droplet and/or via deeper layers of the polymer film, possibly causing limited movement of anions/cations into that covered area. This could result in a difference in surface tension between the covered area and the surrounding area, the latter containing anions/cations and leading to an induced motion from the low to the high surface tension area and spreading/retraction of the droplet (Figure 1.20). [185] Alternatively, due to the surface coverage the contact angle could be unaffected during further redox reactions.

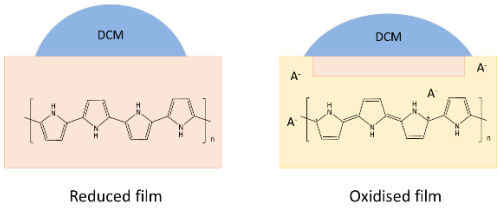

Figure 1.20 – Illustration of the possible influence of the diffusion of electrolyte in the polymer film, on the hydrophobicity of the polymer film.

The hydrophobicity of surfaces is commonly determined by depositing a droplet on the surface, which subsequently spreads until it reaches a contact angle that relates to the hydrophobicity of the film. The presence of irregularities on the polymer film could influence the amount of spreading of the droplet during the contact angle measurements and thereby the hydrophobicity. Therefore, the contact angle is not only dependent on chemical/molecular properties such as polarity of the polymer film but also on physical/macroscopic properties such as roughness.

The roughness can possibly be influenced by several factors, the type and size of the dopant as well as the electronic state and thickness of the film. [189-192] It should be noted that these influences were not observed in all studies and the roughness can also be caused by factors such as (de)swelling and drying, which might or might not have a relation with the chemical or physical properties of the film. The effect of the roughness on the contact angle could be calculated using the Wenzel, Cassie and Cassie-Baxter model as will be discussed in Section 1.5.2. In addition, in most of the studies listed in Table 1.7, the influence of roughness was not taken into consideration, therefore more research about the influence of chemical/molecular and physical/macroscopic properties on the hydrophobicity of (polymer) films would be of use.

Besides the change in roughness, the conductivity and morphology appeared also to be affected by the dopant and film formation settings. Generally, an increase in homogeneity [191, 193], grain size [191], denseness [194] and porosity [195-197] was observed by increasing anion size as well as an increase in porosity by increasing cation-size. [195] Low scan rates (ca. 50 mV/s) resulted in more amorphous, rougher and less dense films compared to fast scan rates (20 V/s), [198] although opposite trends were observed as well, such as more homogenous films using lower scan rates. [199]
As the factors morphology, roughness and hydrophobicity/contact angle measurements are not isolated, the influence of these aspects on each other must also be taken into account. For example, more compact and (electrochemically) stable PEDOT films could be obtained using aqueous plus surfactant solvents, compared to organic solvents. [184] However, the surfactant could affect the contact angle measurements and aqueous solutions without surfactant are limited to low monomer concentrations. Therefore, in this research was chosen to perform the polymerisation of EDOT in the organic solvent acetonitrile.

Table 1.7 – Overview of research about the hydrophobicity of polyaniline, polypyrrole and thiophene polymer films. NR=not reported. APFAES=Ammonium perfluoroalkylethylsulfite, CS=chondroitin sulfate A sodium salt, DBS(A)=dodecylbenzenesulfonic (acid), DS=dextran sulphate sodium salt, HA=hyaluronic acid sodium salt, $K_2S_2O_8$=potassium peroxydisulfate, $LiClO_4$=lithium perchlorate, $MgSO_4$=magnesium sulfate, NaCl=sodium chloride and TEAPFOS= tetraethylammonium perfluoreooctanesulfonate, pNaSS=poly-(sodium 4-styrenesulfonate), PNMP=poly(N-methylpyrrole), PSS=poly(styrene sulfonate), PSSS=poly(sodium 4-styrenesulfonate) and pTS=sodium para-toluenesulfonate.

Polymer	Electrolyte	In-situ or ex-situ	Droplet composition/ contact angle	Most hydrophobic	Roughness	Deposition/ analysis method	Contact angle method	Ref.
Polyaniline	HCl	In-situ	OX (50^0) < RED (75^0)	RED	NR	Cyclic voltammetry	Meniscus height	[200]
Polyaniline	DBSA (intrinsically doped)	NR	H_2O: OX (37^0) > RED (9^0)	OX	15 nm (no influence)	Spin-coated/ In-house made device	Droplet	[187]
Thiophenes	NR (intrinsically undoped)	NR	H_2O: OX (77^0) < RED (95^0)	RED	NR	Spin-coated/In-house	Droplet	[187]
Thiophenes	pNaSS, D-sorbitol, glycerol, $MgSO_4$	NR	H_2O: RED > OX	RED	NR	Spin-coated/5V potential	Droplet	[186]
Polypyrrole	PFOS	NR	H_2O: OX > RED	OX	RED < OX	Galvanostatic	Droplet	[192]
Polypyrrole	NaCl, CS, DBS, DS, HA, $LiClO_4$, PSSS, pTS	Ex-situ	H_2O: pTS > DBS > $LiClO_4$ ≥ HA ≥ DS, CS > Cl	NR	$LiClO_4$ > HA > NaCl > other	Electrochemical	Droplet	[190]
Polypyrrole	DBS	Ex-situ in-situ	H_2O: OX (72^0) > RED (18^0) DCM: OX < RED, but RED more spread than OX	OX (H_2O)	NR	Galvanostatic/cyclic voltammetry	Droplet	[184]
Polypyrrole	$(CH_3CH_2)_4NBF_4$ $LiClO_4$	In-situ	$(CH_3CH_2)_4NBF_4$: polarity/interfacial force OX> RED $LiClO_4$: unclear	RED	NR	Cyclic voltammetry/fixed potential	William balance tensiometry	[201]
Polypyrrole	$K_2S_2O_8$, APFAES (chemical deposition) $LiClO_4$, APFAES (electro-chemical deposition)	Ex-situ	H_2O: CA increased (more hydrophobic) by doping.	NR	NR	Chemical and electrochemical	Droplet (on polypyrrole pellets)	[202]
Polypyrrole	NaDBS	Ex-situ, In-situ	H_2O: OX > RED (single); DCM: OX (107^0) < RED (133^0) (single); DCM: OX > RED (continuous)	OX (single) RD (continuous)	NR	Potentiostatic/cyclic voltammetry, square pulse	Droplet	[185]
Polypyrrole	TEAPFOS, $FeCl_3$ in ACN	NR	H_2O: OX > RED More ΔCA on porous PPY film than compact PPY film.	OX	Lower roughness: less ΔCA	Galvanostatic/NR	Droplet	[203]

1.5. Contact angle measurements

The hydrophobicity of a surface could be determine using contact angle measurements, as done in this research. These measurements are performed by depositing a droplet on a surface which subsequently spreads until it reaches a certain contact angle that corresponds to the hydrophobicity of the surface.

Water droplets with a contact angle larger than 90° suggests that the surface is hydrophobic and smaller than 90° that the surface is hydrophilic, this is based on the surface energies at the three-phase interface as described by Young's equation (1.1).

$$\cos\theta_Y = \frac{\sigma_{SV} - \sigma_{SL}}{\sigma_{LV}} \qquad \textbf{Equation 1.1}$$

σ_{LV}, σ_{SL} and σ_{SV} are the surface energies at the liquid-vapour, solid-liquid and solid-vapour interface as illustrated in Figure 1.21. This three-phase interface is later referred to as the contact line.

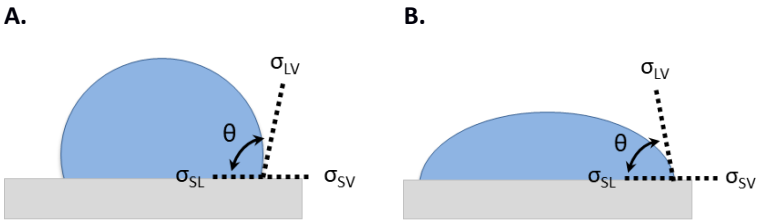

Figure 1.21 – Water droplet (in air) on a hydrophobic surface (**A**; $\theta > 90^0$) and hydrophilic surface (**B**; $\theta < 90^0$).

The contact angles were measured by photographing the droplets from the side whereby a background light source could be used to increase the contrast (Figure 1.22).

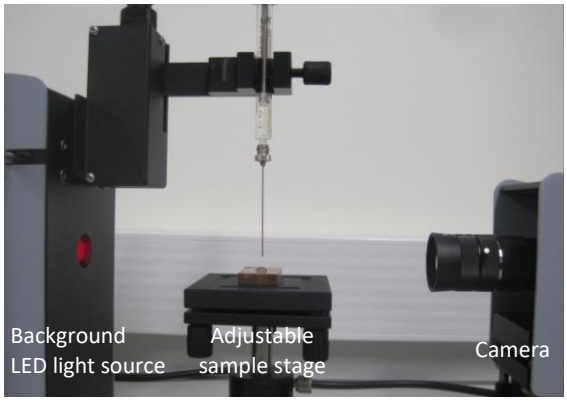

Figure 1.22 – Theta Lite Optical Tensiometer (Biolin Scientific) with the main components: the camera, sample stage and background light.

Commercial available software such as the OneAttention tensiometer software and the Image-J Drop Analysis plugins Dropsnake and LB-ADSA could be used to determine the contact angles of the recorded droplets. The DropSnake method is based on the B-spline snake algorithm in which manually positioned dots at the contour line of the droplet are connected. [204] Due to the nature of B-splines, this method is suitable for a wide range of droplet shapes. In this study the OneAttention tensiometer software and Image-J Drop Analysis plugin LB-ADSA were used, both are based on a fitting of the Young-Laplace curvature to the droplet shape. [205] Other curvatures are also available in the OneAttention software, such as polynomial and circle fitting, however were not used in this study. The Young-Laplace equation relates the curvature of the interface to the pressure difference (Δp) across an interface (e.g. liquid-vapour), due to the surface tension as shown in Equation 1.2. $\overline{\nabla} \cdot \hat{n}$ is the unit normal vector pointing outwards. This equation can be simplified, in which R_1 and R_2 are the radius of the curvature of a droplet as illustrated in Figure 1.23. Based on this fit, the contact angle is determined.

$$\Delta p = -\sigma_{LV}\overline{\nabla} \cdot \hat{n} = \sigma_{LV} \cdot \left(\frac{1}{R_1} + \frac{1}{R_2}\right) \qquad \textbf{Equation 1.2}$$

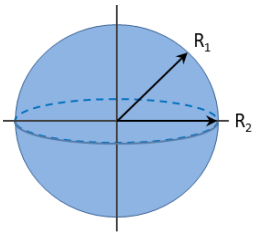

Figure 1.23 – Radius (R_1, R_2) of the curvature as used in Equation 1.2.

1.5.1. Contact angle hysteresis

A droplet can have a range of stable contact angles, also called the hysteresis phenomenon, which can be described in two ways (Figure 1.24). A droplet on a vertical surface, like a rain drop on a window, is pulled down due to gravitation forces, however because of the presence of multiple stable contact angles the droplet stays in an asymmetrical shape. By increasing droplet volume the droplet will slide down in its stable asymmetric position. The minimum and maximum stable contact angles are called the advancing and reducing contact angles which difference is defined by the contact angle hysteresis. Alternatively, a range of stable contact angles can be observed by increasing and decreasing the volume of the droplet. [206]

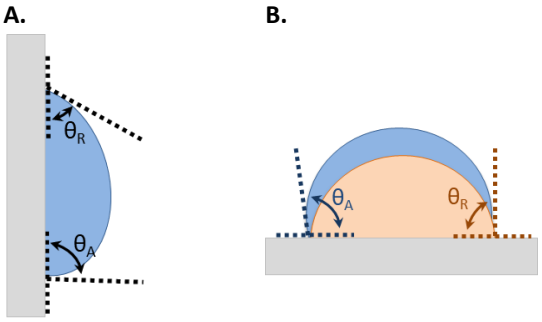

Figure 1.24 – Schematic illustration of a droplet in vertical position (**A**) and de/-increasing droplet volume (**B**), both showing the contact angle hysteresis defined by the difference between the advancing and receding contact angle (θ_A and θ_R respectively).

1.5.2. Influence of roughness on the contact angle

In the contact angle measurements, a droplet deposited on a surface spreads until it reaches a certain contact angle corresponding to the hydrophobicity of the surface. As the amount of spreading of the droplet could be influenced by irregularities on the surface, the interaction between the droplet and the roughness of the surface is of importance.

A droplet is assumed to spread in two phases, first spreading of a thin precursor film followed by the rest of the fluid on top of the precursor film (Figure 1.25). [207, 208] This suggests that irregularities only have an influence on the formed precursor film, 'the ring'. It must be noted that the precursor film was only noticed in a small fraction of the experiments.

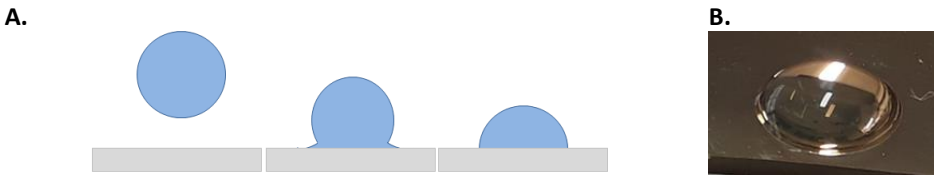

Figure 1.25 – Droplet with precursor film illustrated using a three-steps illustration of a droplet falling, precursor film formation and spreading of the rest of the droplet (**A**) and a real droplet (**B**).

The influence of roughness on the contact angle is generally described by the Wenzel, Cassie or Cassie-Baxter model. Generally assumed, the Cassie model is applicable on heterogeneous surfaces and the Wenzel and Cassie-Baxter models on homogenous surfaces. These models are limited to roughnesses smaller than 2-40 times the size of the droplet. [209, 210]

1.5.2.1. Wenzel model

The Wenzel model is based on the assumption that the droplet moves into the grooves (formed by irregularities) on the surface, resulting in an increase in contact surface area (Figure 1.26). The contact angle subjected to roughness (θ_W) could be determined by magnifying Young's contact angle (θ_Y; contact angle on an ideal smooth surface) with a surface area correction factor (R-factor) as shown in Equation 1.3. [211]

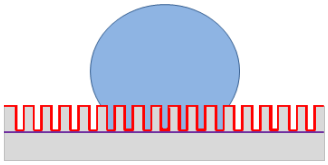

Figure 1.26 – Schematic illustration of the Wenzel model. Red line is the actual surface area (also known as the topographical area), purple line is the projected surface area as used to determine the R-factor using Equation 1.3.

$$\cos\theta_W = \text{R-factor} \cdot \cos\theta_Y = \frac{Actual\ area}{Projected\ area} \cdot \cos\theta_Y \qquad \textbf{Equation 1.3}$$

This model shows an amplification of the hydrophobicity/hydrophilicity by increasing roughness (R-factor); hydrophilic surfaces become more hydrophilic, hydrophobic surfaces more hydrophobic (Figure 1.27).

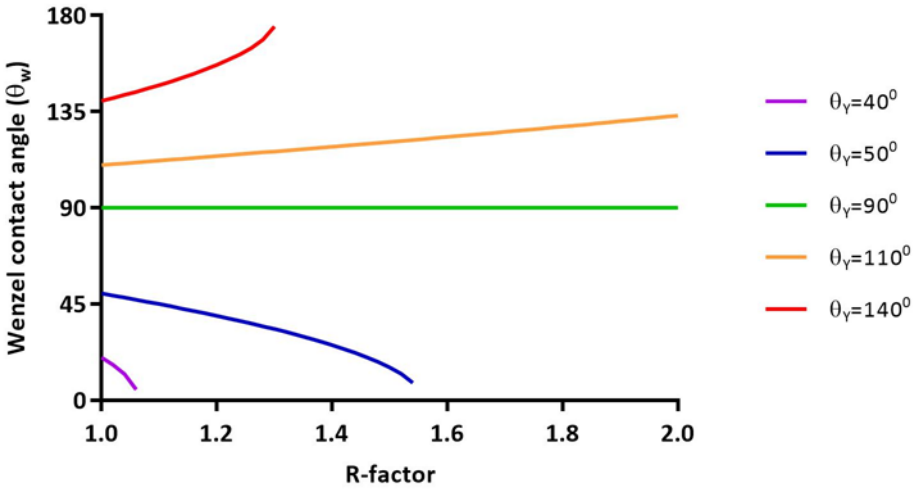

Figure 1.27 – Theoretical determination of the influence of roughness on the contact angle, where θ_Y is the contact angle on an ideal smooth surface (Young's contact angle) and θ_w the contact angle subjected to roughness.

1.5.2.2. Cassie model

On heterogeneous surfaces, the Cassie model is commonly used, whereby the contact angle (θ_Y) of each material is proportional (area fraction f_i; sum of fractions is 1) taken into account as shown in Equation 1.4. [212]

$$cos\,\theta_C = \sum_{i=1}^{n} f_i \cos\theta_{Y,i} = f_1 \cdot cos\,\theta_{Y,1} + f_2 \cdot cos\,\theta_{Y,2} + \cdots \qquad \textbf{Equation 1.4}$$

1.5.2.3. Cassie-Baxter model

The Cassie-Baxter model is based on the Cassie model, whereby air is assumed to be trapped into the grooves and both air and the solid surface are defined as two materials (Figure 1.28 and Equation 1.5).

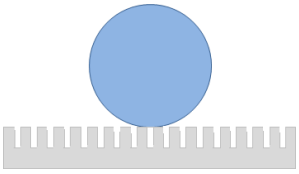

Figure 1.28 – Schematic illustration of the Cassie-Baxter model whereby air is trapped into the grooves.

$$cos\,\theta_{CB} = f_{\text{solid}} \cdot \cos\theta_{Y,solid} + f_{air} \cdot \cos\theta_{Y,air} \qquad \textbf{Equation 1.5}$$

The implementation of Young's equation (Equation 1.1) in Equation 1.5 and the assumptions that the sum of the fractions is 1, $\sigma_{SV,\text{air}}$ is 0 and $\sigma_{SL,\text{air}}$ is σ_{LV} (Step 1-3) results in Equation 1.9 which describes the Cassie-Baxter model. [213]

Step 1: $$cos\,\theta_{CB} = f_{solid} \cdot \frac{\sigma_{SV,\text{solid}} - \sigma_{SL,\text{solid}}}{\sigma_{LV}} + f_{\text{air}} \cdot \frac{\sigma_{SV,\text{air}} - \sigma_{SL,\text{air}}}{\sigma_{LV}} \qquad \textbf{Equation 1.6}$$

Step 2: $$cos\,\theta_{CB} = f_{solid} \cdot \frac{\sigma_{SV,\text{solid}} - \sigma_{SL,\text{solid}}}{\sigma_{LV}} + (1 - f_{\text{solid}}) \cdot \frac{-\sigma_{LV}}{\sigma_{LV}} \qquad \textbf{Equation 1.7}$$

Step 3: $$cos\,\theta_{CB} = f_{\text{solid}} \cdot \frac{\sigma_{SV,\text{solid}} - \sigma_{SL,\text{solid}}}{\sigma_{LV}} - (1 - f_{\text{solid}}) \qquad \textbf{Equation 1.8}$$

Step 4: $$cos\,\theta_{CB} = f_{\text{solid}} \cdot \cos\theta_{Y,\text{solid}} - (1 - f_{\text{solid}}) \qquad \textbf{Equation 1.9}$$

As illustrated in Figure 1.29, in the Cassie-Baxter model the contact angle decreases by increasing the solid fraction.

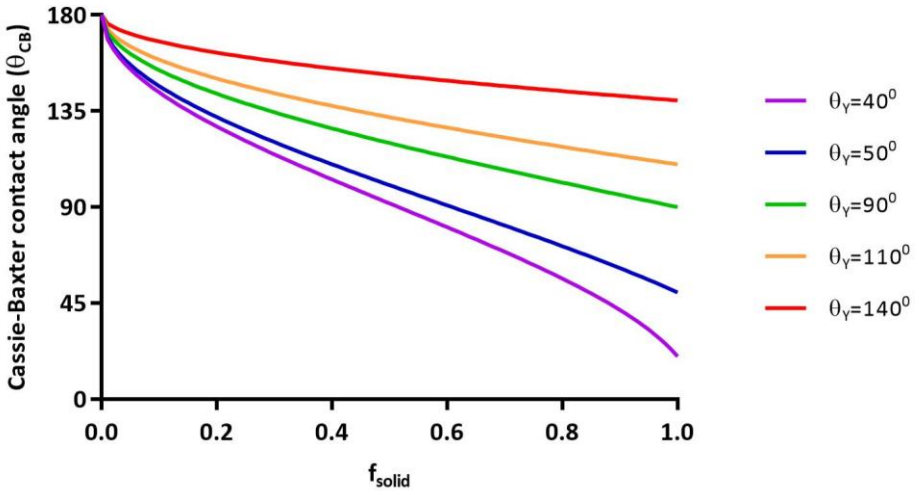

Figure 1.29 – Theoretical determination of the influence of roughness on the contact angle using the Cassie-Baxter model. In which θ_Y is the contact angle on an ideal smooth surface (Young's contact angle), θ_{CB} the contact angle subjected to roughness and f_{solid} is the fraction solid surface of the total surface.

A solid fraction of 1 corresponds to a completely solid surface, so no irregularities are present and in fractions smaller than 0.5 the air fraction is in excess. Noting that a solid fraction of 0 corresponds to a layer of air, so f-values close to 0 contain possibly barely irregularities. It has to be noted that the geography of the surface probably also has an influence on the interpretation of the f-values. Additionally, when the contact line is only located on the solid phase, air bubbles can be present in the grooves as illustrated in Figure 1.30A. When the contact line is partly located on an air compartment and partly on the solid phase, the liquid of the droplet tends to move into the grooves, resulting in the Wenzel model as shown in Figure 1.30B. [213] A reversed scenario could also occur in which air bubbles are trapped into the grooves, resulting in a transformation of the Wenzel to the Cassie-Baxter model. This indicates that the Cassie-Baxter model could only be obtained under certain roughness conditions and that besides the solid/air fraction also the location of the irregularities could have an influence on the impact of roughness on the droplet.

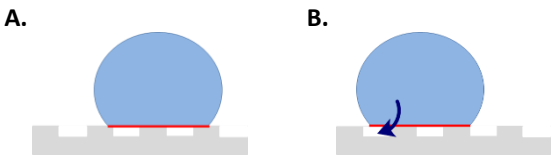

Figure 1.30 – Schematic illustration of the three-phase contact line of a droplet (red line) on top of the solid phase (**A**) and partly positioned on the solid phase and thereby falling into the groove (**B**).

1.5.2.4. Adjustments of the models.

Over the last years, the derivatisation of the Wenzel and Cassie-Baxter equations and the conditions under which these models are validated has been questioned by several researchers. [214-219] The main point of discussion was the dependency of the contact angle on the contact line only or as described in the models on the area underneath the droplet. [218] This resulted in an adjustment of the equations in which the R-factor (in Wenzel's equation) and the f-factor (in Cassie and Cassie-Baxter's equation) are no longer based on the total area underneath the droplet but on the local area at the contact line. However, on homogeneous surfaces the roughness of a small area is equal to a larger area. [216]

1.5.3. Influence of an applied potential on the contact angle

The hydrophobicity of a surface can also be adjusted by the application of a potential between the droplet and the underlying substrate (Figure 1.31A). Due to the applied potential, the droplet and substrate become oppositely charged whereby the field on the contact line of the droplet tend to push the droplet down (Figure 1.31B). This results in spreading of the droplet by the application of a potential. In the electrowetting-on-a-dielectric process, as used in this study, the metal substrate is covered by a dielectric layer which functions as capacitor, this will enable a higher electric field and limits electrolysis.

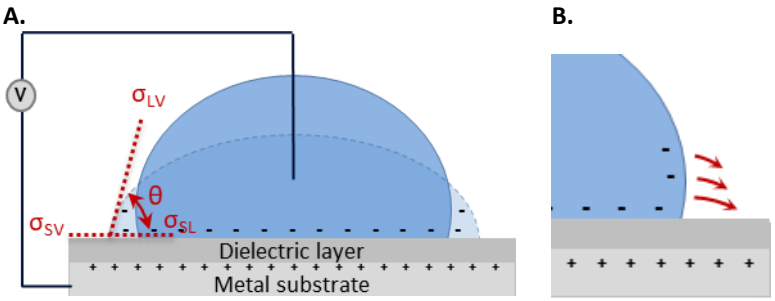

Figure 1.31 – Schematic illustration of electrowetting (**A**) including zoom-in at the 'corner of the droplet' (**B**).

The electrowetting phenomenon can be described using the Young-Lippmann equation which is based on the balance between surface tensions and a potential driven adjustment of the surface tension at the liquid-surface interface. This adjustment is based on the potential induced change in electrostatic energy (Equation 1.11). [109,

220, 221] Implementation of Equation 1.11 into Young's equation (1.10) results in the Young-Lippmann equation as shown in Equation 1.12. In these equations σ_{SL}, σ_{LV} and σ_{SV} are the surface tensions at the surface-liquid, liquid-vapour and surface-vapour interface respectively, C is the capacitance of the dielectric layer and V the applied potential. The capacity depends in the thickness of the layer (d) and the permittivity of the dielectric layer (ε_d) with respect to the permittivity in vacuum (ε_0). The influence of the potential, capacitance and liquid-vapour surface tension on the contact angle is expressed by the dimensionless electrowetting number (η), which defines the strength of the electrostatic energy compared to the surface tension (Equation 1.13). [109]

$$\cos\theta = \frac{\sigma_{SV} - \sigma_{SL}}{\sigma_{LV}} \qquad \textbf{Equation 1.10}$$

$$\sigma_{SL} = \sigma_{SL}^{0} - \frac{C \cdot V^2}{2} \qquad C = \frac{\varepsilon_d \cdot \varepsilon_0}{d} \qquad \textbf{Equation 1.11}$$

$$\cos\theta = \frac{\sigma_{SV} - \sigma_{SL}^{0}}{\sigma_{LV}} + \frac{C \cdot V^2}{2 \cdot \sigma_{LV}} \qquad \textbf{Equation 1.12}$$

$$\cos\theta = \cos\theta_Y + \eta \qquad \eta = \frac{C}{2 \cdot \sigma_{LV}} \cdot V^2 \qquad \textbf{Equation 1.13}$$

It should be noted that the Young-Lippmann equation is only valid for potentials up to the saturation potential, higher potentials have less effect on the contact angle resulting in a deviation from the equation. Currently this contact angle saturation phenomenon has not been completely understood, however the following mechanisms were proposed. [109, 222] Due to divergence of the electric field at the contact line, the local electric field will be enhanced whereby an exceeding of the insulator capacities could lead to local dielectric breakdown and charge trapping in the insulator layer. The latter could be caused by a stronger electrostatic force between the ions in the liquid and the charged substrate compared to the liquid-ion interaction force. Ions trapped in the insulator layer screen the electric field, resulting in a decrease in force acting on the contact line and thereby reduced electrowetting effect. [223] Additionally, using salty droplets, the ionisation of the air around the contact line could result in charge leakage and finally contact angle saturation. [224] The saturation phenomenon could also be explained by non-perfect behavior of the conductive liquid or dielectric such as by using a resistive liquid or substrate. [225]

1.6. Electrochemical techniques

Electrochemistry can be defined as the study of charge transfer at the interface of usually a solid electrode and reactant molecules (in electrolyte solution), either via spontaneous reactions producing a potential (galvanic system such as batteries) or by applying a potential (electrolytic system). In these reactions electrons are transferred from the oxidised species to the reduced species, also called redox reaction. In this research, an electrolytic system was used to grow a polymer film and oxidise/reduce them subsequently using the method cyclic voltammetry.

Electrochemical processes are commonly performed using a three-electrode electrochemical cell, consisting of a working electrode, counter electrode and reference electrode in an electrolyte solution (Figure 1.32):

- Working electrode: substrate of interest and used to deposit the material on top.
- Counter electrode: functions as passage to ensure that no current flows through the reference electrode and thereby influence the potential.
- Reference electrode: set the potential of the working electrode.
- Electrolyte solution: a salt/acid functioning as support to electron transfer.

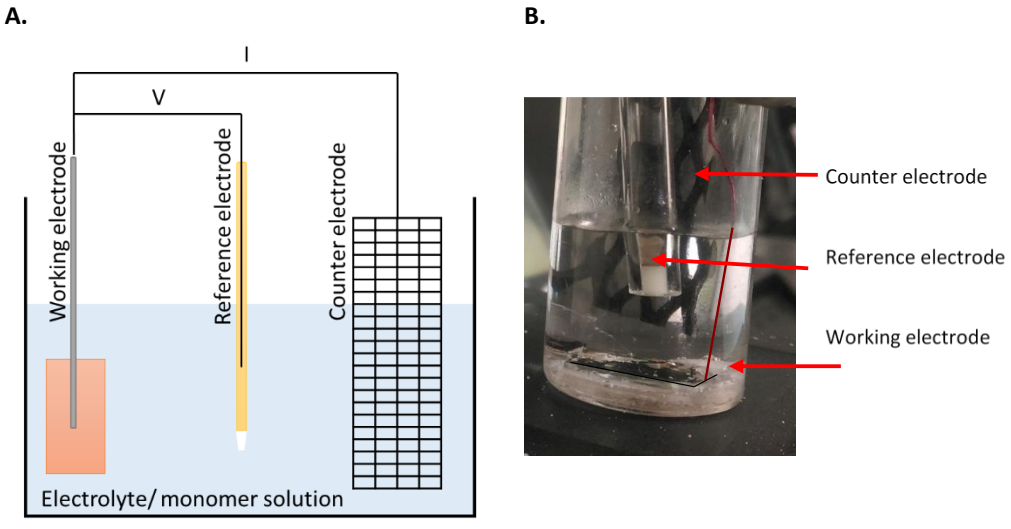

Figure 1.32 – Schematic illustration (**A**) and photo (**B**) of a three-electrode electrochemical cell containing a working, reference and counter electrode.

1.6.1. Cyclic voltammetry

Cyclic voltammetry measures current as a function of potential in the form of a voltammogram in order to provide both qualitative and quantitative information. The potential is ramped linearly over a potential window, whereby the forward and reverse motion form a cycle that can be repeated till the requested film thickness is obtained (Figure 1.33).

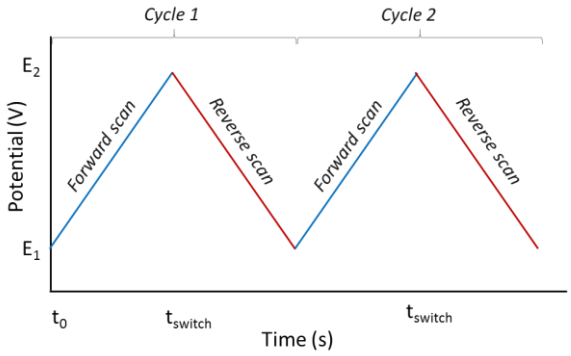

Figure 1.33 – Schematic illustration of cyclic voltammetry curves.

During the forward scan (blue curves in Figures 1.33 and 1.34) the monomers oxidises and deposits on the working electrode, followed by reduction during the reverse scan whereby the film becomes more diffusive by decreasing current (red curve). In the cyclic voltammogram of polyaniline (Figure 1.34A), the three oxidation (A-C) and reduction (D-F) peaks indicate the presence of three excitation states.

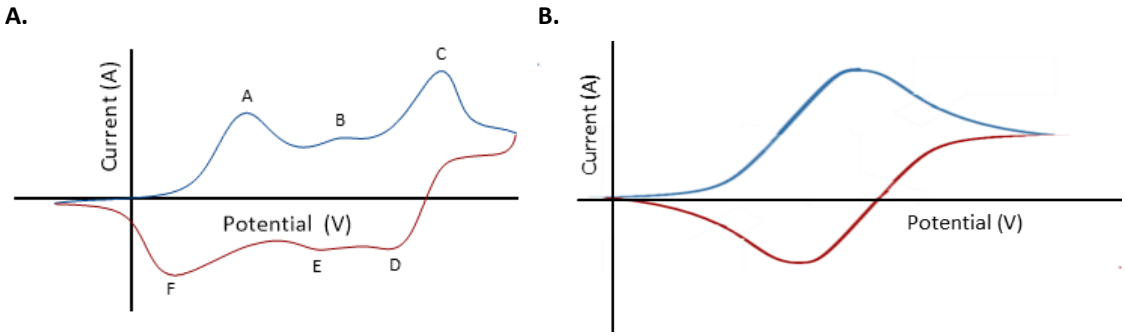

Figure 1.34 – Cyclic voltammogram of polyaniline (**A**) and a one electron transfer reaction (**B**). Blue curve shows the oxidation reaction and red curve the reduction reaction.

The cyclic voltammogram could be used to determine the thickness of the deposited film (h) using the concentration of the monomer (c) along with the molar coverage (Γ) as shown in Equation 1.14. The latter could be determined by the charge (Q), the number of transferred electrons (n), area (A) and Faraday constant (96,485 C mol^{-1}) as

shown in Equation 1.15. The charge can be established by converting the voltammogram into a current-time (I-t) plot, whereby the area behind the curve defines the charge required to form the film (Equation 1.16). The concentration of the monomer (c) can be calculated using the density (ρ) and molecular weight (MW); Equation 1.17.

$$\mathrm{h} = \frac{\Gamma}{c} \qquad \textbf{Equation 1.14}$$

$$\Gamma = \frac{Q}{n \cdot F \cdot A} \qquad \textbf{Equation 1.15}$$

$$Q = \int_0^t I(t)dt \qquad \textbf{Equation 1.16}$$

$$c = \frac{\rho}{MW} \qquad \textbf{Equation 1.17}$$

These thickness calculations are based on a few assumptions such as the formation of a homogenous film and charging of the complete film, and could therefore differentiate from the actual thicknesses.

1.6.2. Quartz Crystal Microbalance (QCM)

The QCM technique is based on the piezoelectric nature of quartz. By passing an AC potential through the crystal, the crystal oscillates at the resonant frequency which decreases by depositing material on the crystal. Therefore, QCM is a sensitive technique to determine the amount of deposited material, as done in this study to express the electrowetting effect. Depending on the application, a QCM crystal with a gold (used in this research; Figure 1.35), silver or stress-reducing alloy coating can be used.

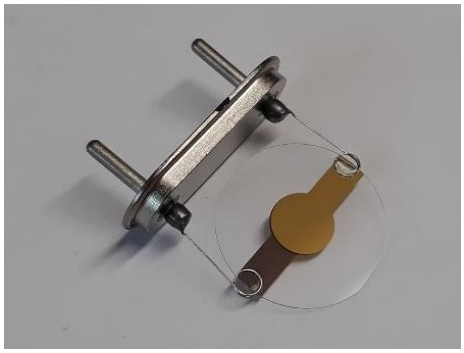

Figure 1.35 – Gold QCM crystal.

The mass of the deposited material can be calculated using the Sauerbrey equation (1.18) in which Δf is the change in frequency, f_0 is the resonant frequency, A is the area of the electrode, ρ_q is the density of the quartz crystal, v_q is the shear modulus of the quartz crystal and Δm is the mass change. [226]

$$\Delta f = -\frac{2 \cdot f_0^2}{A \cdot \sqrt{\rho_q \cdot v_q}} \cdot \Delta m \qquad \textbf{Equation 1.18}$$

The Sauerbrey equation is limited to deposited material which behaves in the same way as the quartz crystal, expressed by the peak intensity and width-at-half-height, whereby the deposited material can be seen as an extension of the crystal. As shown in Figure 1.36 an increase in mass from A to B did not result in a change in behaviour suggesting an uniform, rigid and integral mass, while an increase in mass from A to C resulted in an increase in resistance and thereby loss of energy suggesting the addition of a viscoelastic, thick, rough or solvated layer.

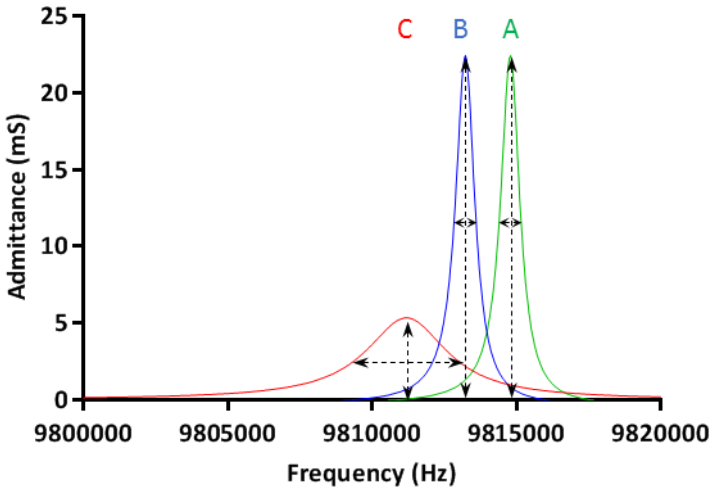

Figure 1.36 – Admittance curves illustrating an increase in deposited mass (uniform, rigid (shear stress) and integral) while the behaviour remains similar (curve **A** to **B**) and the addition of a viscoelastic, thick, rough or solvate layer causing mechanical loss (curve **A** to **C**).

The change in behaviour of the crystal deposited material can been determined by the Q-factor which describes the relation between peak intensity and width ($w_{1/2}$; width at half height) as shown in Equation 1.19.

$$Q\text{-}factor = \frac{f_0}{w_{1/2}} \qquad \textbf{Equation 1.19}$$

1.7. Mass Spectrometry techniques

Mass spectrometry is an analytical technique used for the purpose of identification or quantification of molecules present in a sample. This technique is based on the principle of ionising samples in solid, liquid or gas phase, followed by detection of the mass to charge ratio separated ions. In this research the two mass spectrometry techniques ToF-SIMS and MALDI-ToF-MS were used as discussed below.

1.7.1. Time-of-Flight Secondary Ion Mass Spectrometry (ToF-SIMS)

ToF-SIMS analysis is performed to obtain knowledge about the composition of the top monolayers of a material in the form of spectra or images. In this research MIPs, natural fingerprints and fingerprints visualised by MIPs were analysed on glass microscope slides.

The main components of a ToF-SIMS are a source, flood gun, flight tube and detector (Figure 1.37). The primary ion source (such as Ar^+, Cs^+, Bi^{n+}; 0.1-20 keV) irradiates the surface, resulting in the generation of neutral particles, electrons and secondary ions by the transfer of primary ion energy via atomic collisions (Figure 1.38). In addition to the ion source, a flood gun, which is a beam of electrons, is advised for use on non-conductive substrates to stabilise the build-up of surface charge. The secondary ions are subsequently accelerated in the flight tube and detected. [227]

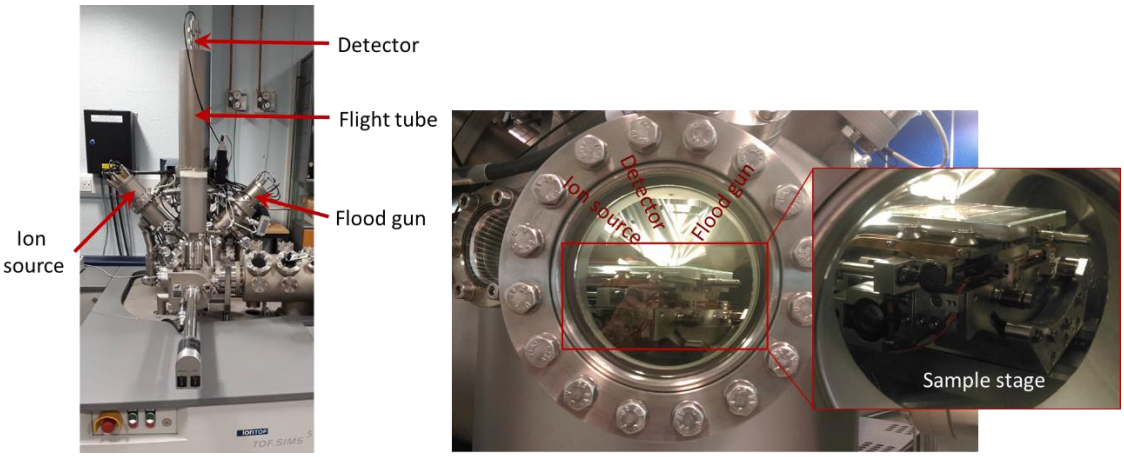

Figure 1.37– IonToF 5 ToF-SIMS instrument with their main components indicated; ion source, flood gun, flight tube and detector.

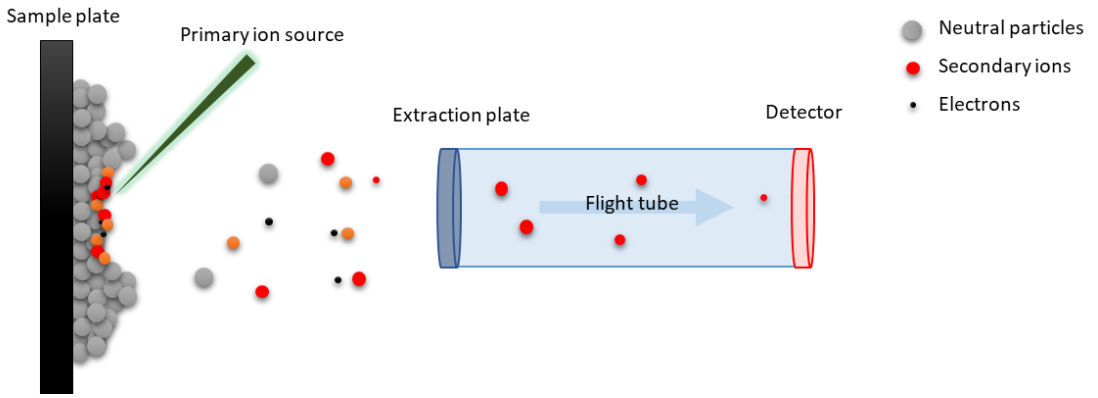

Figure 1.38 – Schematic illustration of the ToF-SIMS technique, showing the ionisation/desorption process and separation in the flight tube before detection.

1.7.1.1. Principle of Time-of-flight analyser

In Time-of-Flight mass spectrometry, the ions are accelerated by an electric field resulting in a separation based on the mass to charge ratio (Figure 1.39). The velocity of the ions with similar kinetic energies is inversely related to the mass to charge ratio (m/z), meaning ions with a lower m/z reach the detector first.

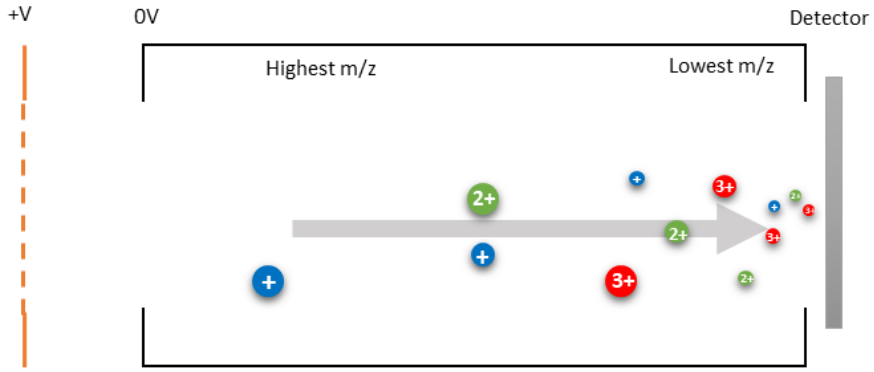

Figure 1.39 – Schematic illustration of Time-of-Flight principle, in which the size of the circles represent the mass (larger size means higher mass) and charges are illustrated by the numbers +, 2+ and 3+ and colours blue, green and red, respectively; both sizes and charges are imaginary values.

1.7.2. Matrix Assisted Laser Desorption/Ionisation Time of Flight Mass Spectrometry (MALDI-ToF-MS)

MALDI mass spectrometry is commonly used for the analysis of polymers and proteins because of its low ionisation power, therefore it allows the detection of intact polymers and proteins and could be used to determine the amino acid or monomer sequence, as done in this study.

In MALDI-ToF-MS, the sample (analyte embedded in matrix) is irradiated with a nitrogen laser (commonly 337 nm), desorbed in the form of a plume [228-230] and ionised as illustrated in Figure 1.40. The matrix functions as solvent for the analyte, absorbs the energy of the laser beam, forms a plume and transports the energy to the analyte. [228]

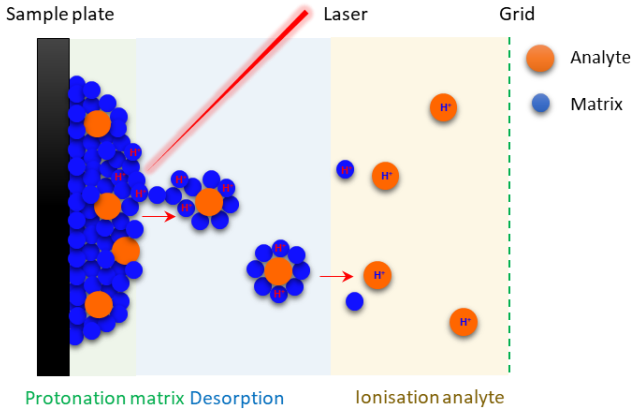

Figure 1.40 – Schematic overview of the ionisation and desorption of the matrix and analyte occurring in MALDI.

The ions are subsequently accelerated in the flight tube and detected (Figure 1.41). In the flight tube a timed ion selector, also known as a Bradbury-Neilson gate, could be used to detect only the selected masses. The detection can be performed in two modes; linear and reflection mode. In linear mode, the ions are detected directly. In reflection mode, the ions continue their path via a repulsive electric field caused by gridded ion mirrors (also known as the reflector). With respect to the linear mode, the reflection mode could result in a higher resolution, due to the longer flight length, but also in a lower intensity, as the ions are more separated and therefore less ions reach the detector at the same time.

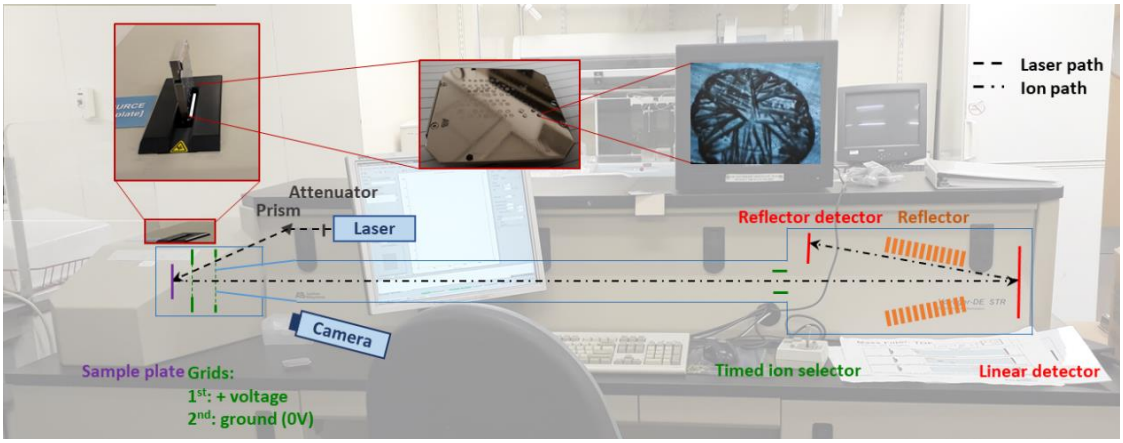

Figure 1.41 – Illustration of the MALDI-ToF-MS Voyager-DE STR (Applied Biosystems). The colour of the components corresponds to the colour of the name of the components.

1.8. Microscopy techniques

1.8.1. Atomic Force Microscope (AFM)

The AFM is capable of providing topographical information of insulating and conducting surfaces at Angström level. In this study it is used to determine the roughness of surfaces.

The AFM uses a cantilever with a sharp tip at the end which is scanned across the surface. Variations in height and forces between the cantilever and surface leads to vertical deflection of the cantilever. To monitor the movements of the cantilever, a laser is reflected off the cantilever and detected by a four quadrant photodiode detector (Figure 1.42).

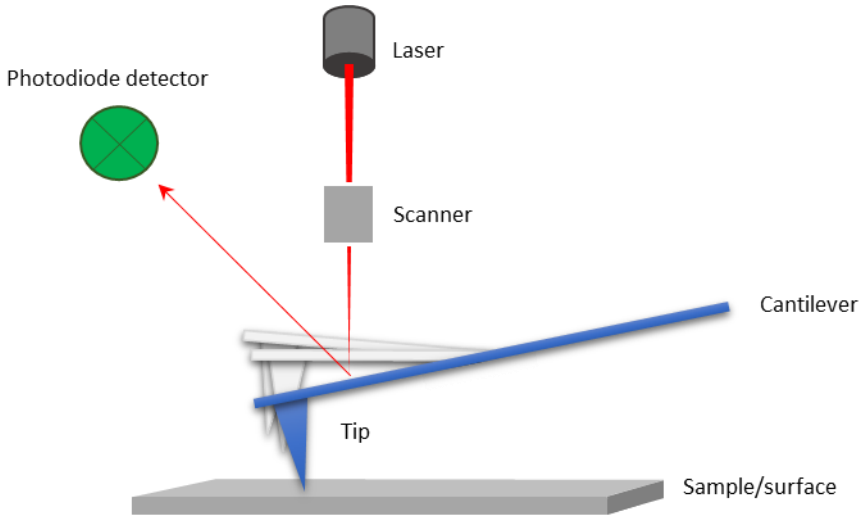

Figure 1.42 – Schematic illustration of an AFM.

The AFM can operate in three modes; contact, non-contact and tapping. In contact mode, the tip is in direct constant contact with the surface and dragged across the surface, therefore destructive. In this mode, the recorded height information is based on physical movements of the scanner, by maintaining a constant cantilever deflection and thereby constant repulsive force between tip and surface. In non-contact mode, the tip is held a small distance (typically 5-10 nm) above the surface. This mode is based on the principle of maintaining a constant oscillation frequency. Variation in oscillation frequency, caused by attractive Van der Waals forces between the tip and surface lead to adjustments of the height of the cantilever. This results in the recording of height differences based on the Van der Waals forces. The force-distance relationship might

not be simply related for each material, possibly resulting in less accurate height determinations. The tapping mode, also seen as the intermediate between the contact mode (operating at constant force) and non-contact mode (operating at constant height), is the most common used mode in which the cantilever oscillates over the surface while continually tapping the surface. As tapping the surface affects the oscillation amplitude, the latter has been recorded to obtain information about the topography of the surface. [231, 232]

1.8.2. Optical Profilometry

Optical profilometry could also be used to provide information about the topography of a surface. In this research two type of profilometric instruments were used, the Zeta-20 Optical profilometer (Zeta Instruments) based on a confocal microscope principle and the Contour GT profilometer (Bruker) based on interferometry.

1.8.3. Confocal microscope

This technique scans stepwise vertically through the surface by recording the height across a 2D surface every step. Combining the information of all the steps results in the formation of a 3D image. Depending on the step size, which depends on the number of steps and vertical height the instrument is scanning through, and the resolution of the objectives, the resolution of the measurements is determined.

In this research the Zeta optical (3D) Microscope has been used which is based on the Zdot Confocal Grid Structured Illumination technology (Figure 1.43). In contrast to conventional confocal (laser) microscopes, this microscope uses a High Brightness long-Life LED light source instead of a laser, providing true colour images instead of false coloured images. [233]

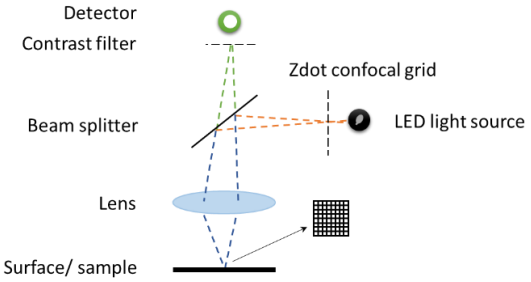

Figure 1.43 – Schematic illustration of the Zeta-20 optical (3D) microscope (Zeta Instruments).

Due to the nature of the optical technique, this technique is non-destructive but the analysis of transparent or very dark surfaces could be challenging. Depending on the height of the features, AFM or scanning electron microscopy could be a possibility for these surfaces.

1.8.3.1. Interferometry based microscope

The Contour GT profilometer (Bruker) is based on the principle of interferometry, whereby the height measurements are determined by phase differences between the sample and a reference. As shown in Figure 1.44, a white light beam is split, half is reflected on the sample and half on the reference mirror. After which both optical paths are combined, resulting in an interference pattern. Due to perfect smoothness of the reference mirror and a similar distance between the beam splitter and the sample and the beam splitter and the reference mirror, phase shifts can be assigned to irregularities on the surface of the sample.

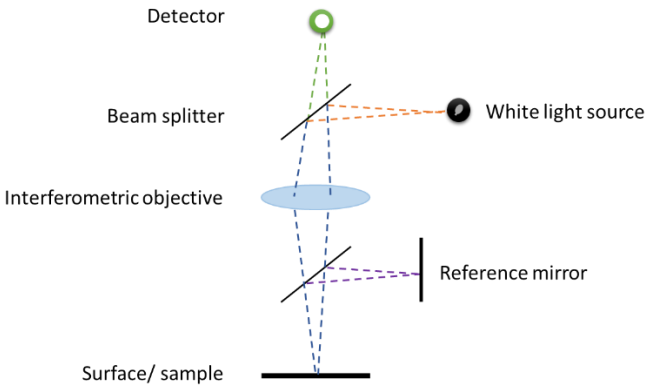

Figure 1.44 – Schematic illustration of an interferometer.

1.9. Spectroscopy techniques

1.9.1. Fourier Transform Infrared Spectroscopy

Fourier transform infrared spectroscopy (FTIR) provides a spectra of the infrared absorbance of a sample and could be used to confirm or determine the composition of a sample. By irradiating the sample with infrared radiation (~10,000-500 cm^{-1}), specific frequencies (reported in IR spectra using wavenumbers) are adsorbed by the molecules in the sample causing a change in dipole moment by stretching/bending of the bonds; Table 1.8. In practise infrared spectroscopy only differentiates between stretching and bending. [231]

Table 1.8 – Stretching and bending vibrations (plus torsion rotation) of a 4-atom containing molecule.

Stretching		**Bending**				**Torsion**
Symmetric	Asymmetric	Scissoring (in-plane)	Rocking (in-plane)	Wagging (out-of-plane)	Twisting (out-of-plane)	
						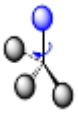

The exact wavenumbers in which the bonds are vibrating depends on the atoms and their surrounding; decreasing bond length, heavier atoms and electron withdrawing groups could result in slower vibrations and higher wavenumber as shown in Table 1.9.

Table 1.9 – IR vibration frequencies of a variety of bonds. [234]

Bond strength/length	C≡N 2260-2240 cm^{-1}	C=N 1690-1640 cm^{-1}	C-N (amine) 1410 cm^{-1}
Mass ratio	O-H (alcohol) 3525-3200 cm^{-1}	N-H (amide) 3325-3050 cm^{-1}	C-H (alkane, alkene) 3100-2800 cm^{-1}
Surrounding	C-H alkyne 3525-3250 cm^{-1}	C-H benzene/alkene 3100-3300 cm^{-1}	C-H alkane 3000-2800 cm^{-1}

The Fourier transform term in FTIR refers to the conversion of the raw frequency/absorbance data into an IR spectra using mathematical data processing.

In this research a FTIR (Frontier of Perkin Elmer) is connected to a microscope/ imaging system (Spotlight 400 of Perkin Elmer). The incident beam can be send to the microscope/imaging system or the standard detector by switching the movable mirror (Figure 1.45).

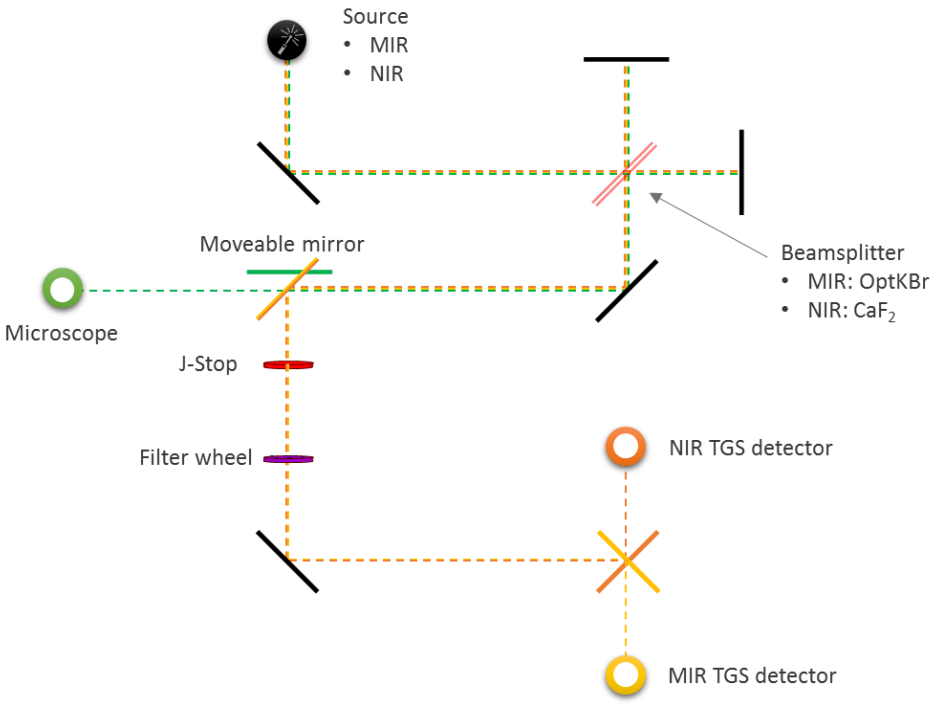

Figure 1.45 – Schematic illustration of Spotlight 400 FTIR imaging system connected to a Frontier FTIR (all Perkin Elmer). Green beam path is going towards the microscope, yellow and orange beam paths are going to the mid infrared (MIR) and near infrared (NIR) detector respectively.

Regarding the standard detector, the signal-to-noise (S/N) ratio can be controlled by decreasing/increasing the opening of the J-stop, which regulates the amount of energy passed through. The width of the opening is generally smaller for higher resolutions, resulting in the requirement of more scans/pixel to obtain the same S/N. [235]

The microscope/imaging system used in this research is a large-area microscopic imaging system coupled to a dual mode mercury cadmium telluride (MCT) detector containing a 16-elements linear array imaging detector and a single element detector. The MCT detector is a cryogenic detector and therefore requires cooling, generally using N_2 (l). These two modes make it possible to perform multiple measurements of one point or to create an image containing the entire IR spectrum for each pixel. Depending on the image size (max 10,000 μm^2), pixel size (6.25, 25 or 50 µm), scans/pixel (1-512) and spectral resolution (2-64 cm^{-1}), the image and spectra quality can be adjusted.

1.9.2. Surface Plasmon Resonance (SPR)

SPR is an optical label-free absorbance detection technique used to retrieve information about affinity, specificity and kinetics of molecular interactions. In this study it was used to determine the affinity and specificity of the MIPs towards their target molecule albumin and other relevant molecules, such as keratin, a protein present in fingerprints.

To measure the molecular interactions between a ligand and analyte, the ligand is immobilised on the gold SPR chip and the analyte passes over the immobilised ligands. The binding causes a change in mass on the gold SPR chip which is registered in the form of a sensorgram (Figure 1.46). The binding of an analyte to the ligands causes an increase in the response till a steady state has reached (analyte bind and unbind in equal amounts). Subsequently the chip is washed and the unbound or weakly bound ligand molecules are released. [236]

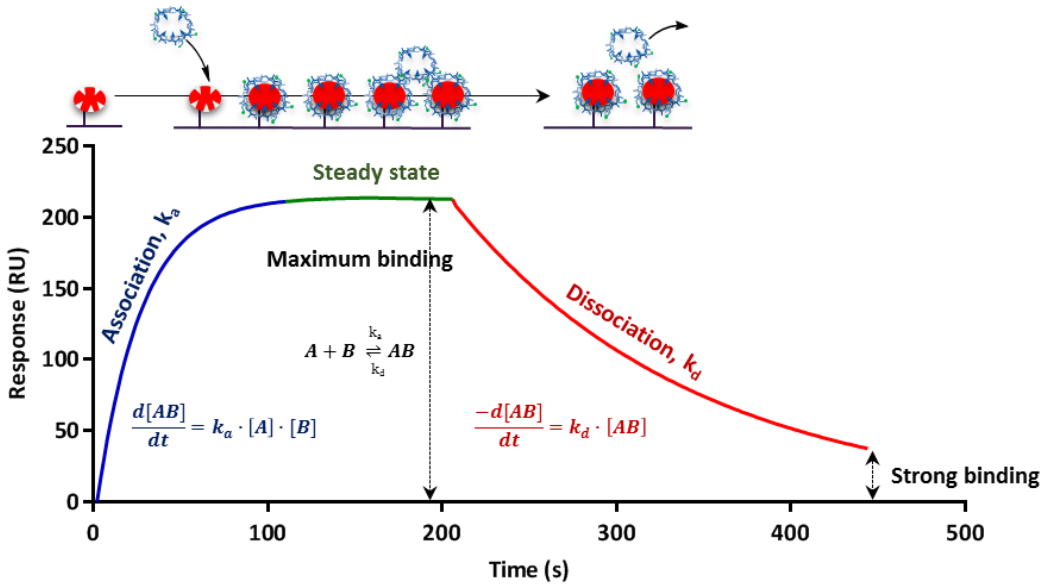

Figure 1.46 – Schematic illustration and sensorgram of the different stages during SPR.

SPR can be performed using three different configurations, the Kretschmann, grating and Otto configuration. As the Kretschmann configuration is most commonly used in commercial instruments as well as used in this research, this configuration will be discussed in most detail.

In the Kretschmann configuration, a light source produces polarised light which is sent through a prism and reflects off the backside of the SPR-chip. Certain angles of incidence create a surface plasmon wave on the SPR-chip. The excited surface plasmons reduce the intensity of the reflective light, indicated by the black line in Figure 1.47. By binding or unbinding of the analyte (which passes through the flow channel) to the ligand which is immobilised on the SPR chip, the refractive index changes slightly, resulting in a change in signal.

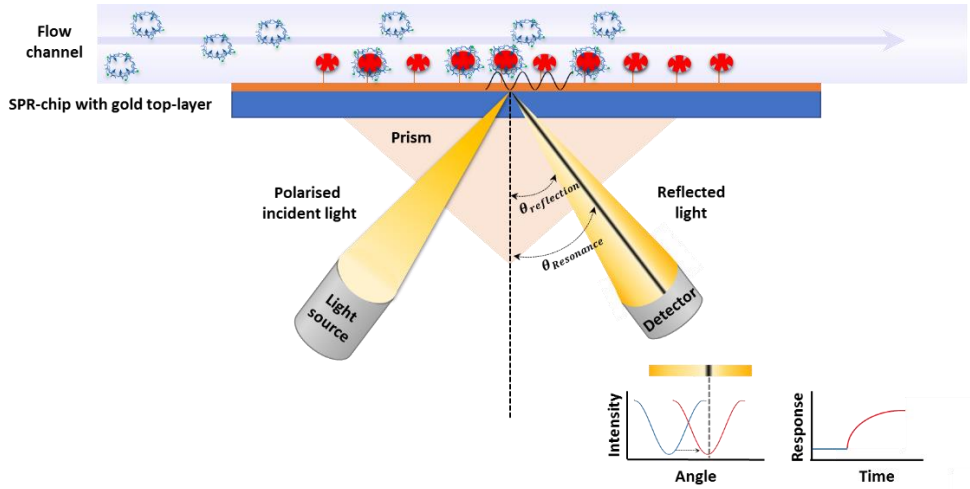

Figure 1.47 – Schematic illustration of the SPR Kretschmann configuration.

There are two different ways to form the incident beam and detect the reflective beam. First, the fixed-angle set-up in which the angle of incident is fixed. This method is the least sensitive method, but is of use for high-throughput analysis. Second, the focused beam set-up in which the beams are focussed using optics, this is currently the most commonly used set-up such as in the Biacore system. Third, the angle-scanning set-up, where by the incident light angle is adjusted by moving the light source over a variety of angles as present in the BioNavi system. [237]

In the grating configuration (Figure 1.48A), the incident light beam reaches the SPR chip via the sample solution and a grating coupler, resulting in the excitation of plasmons. It has to be noted that the reflective angle can be affected by the fact that the light is going through the sample. [236] In the Otto configuration (Figure 1.48B) there is a distance between the incident light beam and the SPR-chip, which is filled with a low refractive

index medium. Due to the decrease in efficiency, this configuration is not often used for liquid samples. However, it is very appropriate for solid samples. [236, 238]

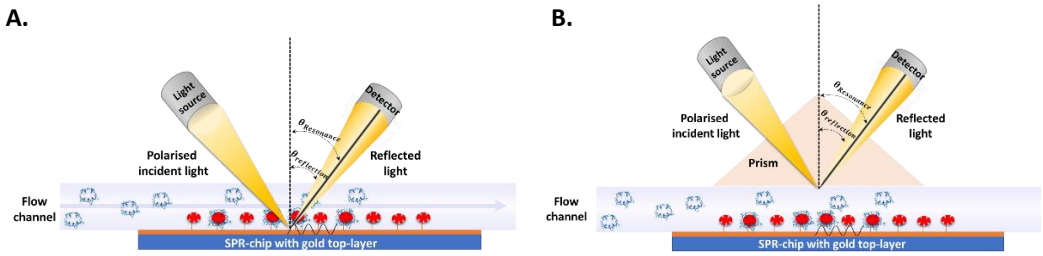

Figure 1.48 – Schematic illustration of the grating (**A**) and Otto (**B**) SPR configuration.

1.9.3. Spectrofluorometry

Fluorescence spectroscopy can provide information about the fluorescence intensity and emission/excitation wavelengths of a sample. In this study it was used to compare the fluorescence intensities of the MIP solutions.

In the fluorospectrometer, UV light of a specific excitation wavelength is first split using a beam splitter, 8% is directed to a reference photodiode to correct for light intensity variations and the rest to the sample (Figure 1.49). The irradiation of the sample results in the excitation of electrons (from ground to excited state) present in the sample. Afterwards the electrons fall back to the ground state by emittance of photons which are recorded by a photomultiplier detector. Only the emission wavelengths of interest were detected by means of an emission monochromator.

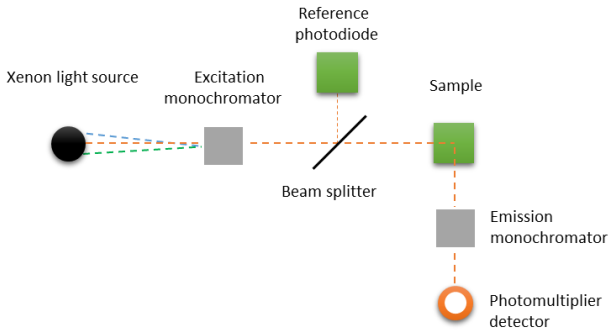

Figure 1.49 – Schematic illustration of the Fluoromax 2 fluorospectrometer (Horiba). [239]

1.10. Aims and objectives

The overarching aim of this research was to improve the detection of fingerprints by two different approaches; enhance currently used techniques by creating a flow in a fingerprint using the electrowetting process and developing a novel detection method using molecularly imprinted polymers (MIPs).

Aim: To enhance currently used techniques by creating a flow in a fingerprint using electrowetting.

The objectives for Chapter 2 are:

- Determination of the influence of an applied potential on the hydrophobicity, composition, morphology and topography (roughness) of the conductive polymer film.
- Estimation of the influence of wetting on the roughness measurements, focusing on wetting caused by a droplet (used for contact angle measurements) and by in solution film formation.
- Investigation of the influence of potential driven topographical (roughness) changes of the polymer film on the contact angle measurements.

The objectives for Chapter 3 are:

- Determine if nano gravimetric methods (QCM) and the movements inside the droplet can deliver insights into electrowetting mechanisms.
- Estimate the influence of the evaporation process with respect to the influence of the potential on the droplet shape change during the electrowetting process.
- Investigating how the electrowetting process could be influenced by the characteristics of the dielectric layer and external factors such as potential and frequency.
- Understand how the electrowetting on fingerprints application could be affected by the composition and physical structure of the fingerprint as well as the consequences on the fingerprint pattern.

Aim: Develop a novel detection method using MIPs

The objectives for Chapter 4 are:

- Determination of the most appropriate type of MIPs as well as retrieving compositional information about the MIPs.
- Understand the influence of the fingerprint composition/matrix on the behaviour of the MIPs (including false positives).
- Determination of the influence of the substrate on the detection of fingerprints using MIPs.
- Estimation of the visualisation quality of the fingerprints visualised using MIPs.
- Investigation of the scope and limitations of the detection of fingerprints using MIPs, by analytical techniques.

1.11. References

[1] H.C. Lee, R.E. Gaensslen, Advances in fingerprint technolgy, 2nd ed., CRC Press2001.
[2] R.S. Croxton, M.G. Baron, D. Butler, T. Kent, V.G. Sears, Variation in amino acid and lipid composition of latent fingerprints, Forensic Science International, 199 (2010) 93-102.
[3] K. Wertheim, A. Maceo, The critical stage of friction ridge and pattern formation, Journal of Forensic Identification, 52 (2002) 35-85.
[4] M. Kücken, A. Newell, A model for fingerprint formation, EPL (Europhysics Letters), 68 (2004) 141.
[5] T. Kent, Water content of latent fingerprints–Dispelling the myth, Forensic science international, 266 (2016) 134-138.
[6] R.S. Ramotowski, Chapter 3: Composition of latent fingerprint residue, Advances in fingerprint technology, CRC Press LLC2001.
[7] K.M. Antoine, S. Mortazavi, A.D. Miller, L.M. Miller, Chemical differences are observed in children's versus adults' latent fingerprints as a function of time, Journal of Forensic Sciences, 55 (2010).
[8] N.E. Archer, Y. Charles, J.A. Elliott, S. Jickells, Changes in the lipid composition of latent fingerprint residue with time after deposition on a surface, Forensic Science International, 154 (2005) 224-239.
[9] Fingerprint, https://en.wikipedia.org/wiki/Fingerprint, accessed: 11/3/2019
[10] Forensic Science Regulator, Information Forensic Examination - Terminology, Definitions and Acronyms FSR-I-402, 2013.
[11] R.S. Ramotowski, Lee and Gaensslen's Advances in fingerprint technology, CRC Press2013.
[12] G.S. Sodhi, J. Kaur, Powder method for detecting latent fingerprints: a review, Forensic science international, 120 (2001) 172-176.
[13] Foster and Freeman, MVC™ 1000/D2 Cyanoacrylate Fuming Chamber User Manual, 2016.
[14] Crime Science Technology SAS, Lumicyano. The one-step fluorescent cyanoacrylate fuming process., 2016.
[15] Foster and Freeman, PolyCyano UV cyanoacrylate fuming equipment user manual (Applications), 2013.
[16] C. Champod, C. Lennard, P. Margot, M. Stoilovic, Fingerprints and other ridge skin impressions (International Forensic Science Investigation), CRC Press2004.
[17] J. Fraser, P. Deacon, S. Bleay, D.H. Bremner, A comparison of the use of vacuum metal deposition versus cyanoacrylate fuming for visualisation of fingermarks and grab impressions on fabrics, Science & Justice, 54 (2014) 133-140.
[18] Home Office, Fingerprint Source Book v2.0, 2017.
[19] G.L. John, S.E. Russell, S.L. Naccarato, A comparison of physical developer formulas, (2008).
[20] A. Becue, S. Moret, C. Champod, P. Margot, Use of quantum dots in aqueous solution to detect blood fingermarks on non-porous surfaces, Forensic Science International, 191 (2009) 36-41.
[21] Y.F. Wang, R.Q. Yang, Y.J. Wang, Z.X. Shi, J.J. Liu, Application of CdSe nanoparticle suspension for developing latent fingermarks on the sticky side of adhesives, Forensic Science International, 185 (2009) 96-99.
[22] C. Wang, J. Zhou, L. Lulu, Q. Song, Rapid visualization of latent fingerprints with color-tunable solid fluorescent carbon dots, particle & particle systems characterization, 35 (2018) 1700387.
[23] A. van Dam, K.A. van Nes, M.C.G. Aalders, T.G. van Leeuwen, S.A.G. Lambrechts, Immunolabeling of fingermarks left on forensic relevant surfaces, including thermal paper, Analytical Methods, 6 (2014) 1051-1058.
[24] J.S. Day, H.G.M. Edwards, S.A. Dobrowski, A.M. Voice, The detection of drugs of abuse in fingerprints using Raman spectroscopy I: latent fingerprints, Spectrochimica acta part A, 60 (2004) 563-568.

[25] K. Kuwayama, K. Tsujikawa, H. Miyaguchi, K. T., Y.T. Iwata, H. Inoue, Time-course measurements of caffeine and its metabolites extracted from fingertips after coffee intake: a preliminary study for the detection of drugs from fingerprints, Analytical and Bioanalytical Chemistry, 405 (2013) 3945-3952.
[26] R. Leggett, E.E. Lee-Smith, S.M. Jickells, D.A. Russell, "Intelligent" fingerprinting: simultaneous identification of drug metabolites and individuals by using antibody-functionalized nanoparticles, Angewandte Chemie International Edition, 46 (2007) 4100-4103.
[27] B. Hartzell-Baguley, R.E. Hipp, N.R. Morgan, S.L. Morgan, Chemical composition of latent fingerprints by gas chromatography-mass spectrometry, Journal of Chemical Education, 84 (2007) 689-691.
[28] L.S. Ferguson, F. Wulfert, R. Wolstenholme, J.M. Fonville, M.R. Clench, V.A. Carolan, S. Francese, Direct detection of peptides and small proteins in fingermarks and determination of sex by MALDI mass spectrometry profiling, Analyst, 137 (2012) 4686-4692.
[29] A. Sánchez-Andrés, J.A. Barea, N. Rivaldería, C. Alonso-Rodríguez, E. Gutiérrez-Redomero, Impact of aging on fingerprint ridge density: anthropometry and forensic implications in sex inference, Science & Justice, (2018).
[30] P. Ramasastry, D.T. Downing, P.E. Pochi, J.S. Strauss, Chemical composition of human skin surface lipids from birth to puberty, Journal of Investigative Dermatology, 54 (1970) 139-144.
[31] M. Nazzaro-Porro, S. Passi, L. Boniforti, F. Belsito, Effects of aging on fatty acids in skin surface lipids, Journal of Investigative Dermatology, 73 (1979).
[32] I. Ishiyama, M. Orui, K. Ogawa, T. Kimura, The determination of isoantigenic activity from latent fingerprints: mixed cell agglutination reaction in forensic serology, Journal of Forensic Science, 22 (1977) 365-375.
[33] C. Ricci, S.G. Kazarian, Collection and detection of latent fingermarks contaminated with cosmetics on nonporous and porous surfaces, Surface and Interface Analysis, 42 (2010) 386-392.
[34] M.J. Bailey, R. Bradshaw, S. Francese, T.L. Salter, c. Costa, M. Ismail, R.P. Webb, I. Bosman, K. Wolff, M. de Puit, Rapid detection of cocaine, benzoylecgonine and methylecgonine in fingerprints using surface mass spectrometry Analyst, 140 (2015) 6254-6259.
[35] M. Ismail, D. Stevenson, C. Costa, R. Webb, M. de Puit, M. Bailey, Noninvasive detection of cocaine and heroin use with single fingerprints: determination of an environmental cutoff, Clinical chemistry, (2018) clinchem. 2017.281469.
[36] D.R. Ifa, N.E. Manicke, A.L. Dill, R.G. Cooks, Latent fingerprint chemical imaging by mass spectrometry, Science . 321 (2008) 805.
[37] P. Hazarika, S.M. Jickells, K. Wolff, D.A. Russell, Imaging of latent fingerprints through the detection of drugs and metabolites., Angewandte Chemie (International Edition in English), 47 (2008) 10167-10170.
[38] M. Abdelhamid, F. Fortes, M. Harith, J. Laserna, Analysis of explosive residues in human fingerprints using optical catapulting–laser-induced breakdown spectroscopy, Journal of Analytical Atomic Spectrometry, 26 (2011) 1445-1450.
[39] R. Bradshaw, R. Wolstenholme, L.S. Ferguson, C. Sammon, K. Mader, E. Claude, R.D. Blackledge, M.R. Clench, S. Francese, Spectroscopic imaging based approach for condom identification in condom contaminated fingermarks, Analyst, 138 (2013) 2546-2557.
[40] F.H. Dickey, The preparation of specific absorbents, Proceedings of the National Academy of Sciences, 35 (1949) 227-229.
[41] G. Wulff, A. Sarhan, Use of polymers with enzyme-analogous structures for resolution of racemates, Angewandte Chemie International Edition, 11 (1972) 341-344.
[42] T. Takagish, I.M. Klotz, Macromolecule-small molecule interactions - Introduction of additional binding-sites in polyethyleimine by disulfide crosslinkages, Biopolymers, 11 (1972) 483-491.

[43] R. Arshady, K. Mosbach, Synthesis of substrate-selective polymers by host-guest polymerization, Die Makromolekulare Chemie: Macromolecular Chemistry and Physics, 182 (1981) 687-692.
[44] F. Yemis, P. Alkan, B. Yenigül, M. Yenigül, Molecularly imprinted polymers and their synthesis by different methods, Polymers & Polymer Composites, 21 (2013) 145.
[45] G. Crini, P.-M. Badot, Sorption processes and pollution: conventional and non-conventional sorbents for pollutant removal from wastewaters, Presses Univ. Franche-Comté2010.
[46] L.I. Andersson, R. Mueller, G. Vlatakis, K. Mosbach, Mimics of the binding sites of opioid receptors obtained by molecularly imprinting of enkephalin and morphine, Proceedings of the National Academy of Sciences USA, 92 (1995) 4788-4792.
[47] M.J. Whitcombe, M.E. Rodriguez, P. Villar, E.N. Vulfson, A new method for the introduction of recognition site functionality into polymers prepared by molecular imprinting: synthesis and characterization of polymeric receptors for cholesterol, Journal of the American Chemical Society, 117 (1995) 7105-7111.
[48] S.A. Zaidi, Latest trends in molecular imprinted polymer based drug delivery systems, RSC Advances, 6 (2016) 88807-88819.
[49] A. Speltini, A. Scalabrini, F. Maraschi, M. Sturini, A. Profumo, Newest applications of molecularly imprinted polymers for extraction of contaminants from environmental and food matrices: A review, Analytica chimica acta, 974 (2017) 1-26.
[50] S.A. Piletsky, N.W. Turner, P. Laitenberger, Molecularly imprinted polymers in clinical diagnostics—Future potential and existing problems, Medical engineering & physics, 28 (2006) 971-977.
[51] C. Alexander, H.S. Andersson, L.I. Andersson, R.J. Ansell, N. Kirsch, I.A. Nicholls, J. O'Mahony, M.J. Whitcombe, Molecular imprinting science and technology: a survey of the literature for the years up to and including 2003, Journal of Molecular Recognition: An Interdisciplinary Journal, 19 (2006) 106-180.
[52] G. Wulff, Molecular imprinting in cross-linked materials with the aid of molecular templates—a way towards artificial antibodies, Angewandte Chemie International Edition in English, 34 (1995) 1812-1832.
[53] I. Iturralde, M. Paulis, J. Leiza, The effect of the crosslinking agent on the performance of propranolol imprinted polymers, European Polymer Journal, 53 (2014) 282-291.
[54] H. Yan, K.H. Row, Characteristic and synthetic approach of molecularly imprinted polymer, International journal of molecular Sciences, 7 (2006) 155-178.
[55] A. Biffis, N.B. Graham, G. Siedlaczek, S. Stalberg, G. Wulff, The synthesis, characterization and molecular recognition properties of imprinted microgels, Macromolecular Chemistry and Physics, 202 (2001) 163-171.
[56] D.R. Kryscio, N.A. Peppas, Critical review and perspective of macromolecularly imprinted polymers, Acta Biomaterialia, 8 (2012) 461-173.
[57] E. Turiel, A. Martín-Esteban, Molecularly imprinted polymers for sample preparation: a review, Analytica Chimica Acta, 668 (2010) 87-99.
[58] E.S. Azizi, M.N. Ahmad, A.S. Islam, D. Arbain, I. Tahir, Porogen effect towards the quality of curcumin imprinted polymer, Indonesian Journal of Chemistry, 11 (2011) 207-211.
[59] I.M. Baldim, M.C. de Oliveira Souza, J.C.J. da Cunha Souza, E.C. Figueiredo, I. Martins, Application of the molecularly imprinted solid-phase extraction to the organophosphate residues determination in strawberries, Analytical and bioanalytical chemistry, 404 (2012) 1959-1966.
[60] J. Luo, Q. Ma, W. Wei, Y. Zhu, R. Liu, X. Liu, Synthesis of water-dispersible molecularly imprinted electroactive nanoparticles for the sensitive and selective paracetamol detection, ACS applied materials & interfaces, 8 (2016) 21028-21038.
[61] A. Motib, A. Guerreiro, F. Al-Bayati, E. Piletska, I. Manzoor, S. Shafeeq, A. Kadam, O. Kuipers, L. Hiller, T. Cowen, S. Piletsky, P.W. Andrew, H. Yesilkaya, Modulation of quorum sensing

inaGram-positive pathogen by linear molecularly imprinted polymers with anti-infective properties, Anti-infective Agents, 129 (2017) 16782-16785.
[62] S.A. Zaidi, Molecular imprinted polymers as drug delivery vehicles, Drug delivery, 23 (2016) 2262-2271.
[63] B. Sellergren, C.J. Allender, Molecularly imprinted polymers: a bridge to advanced drug delivery, Advanced drug delivery reviews, 57 (2005) 1733-1741.
[64] P. Nichols, N. Mortensen, D. Tingy, A. Vasquez, J. Bates, Pharmacokinetics of molecular imprinted hydrogels as drug delivery vehicles, Biochemistry & Pharmacology, 7 (2018).
[65] F. Canfarotta, L. Lezina, A. Guerreiro, J. Czulak, A. Petukhov, A. Daks, K. Smolinska-Kempisty, A. Poma, S. Piletsky, N.A. Barlev, Specific drug delivery to cancer cells with double-imprinted nanoparticles against epidermal growth factor receptor, Nano letters, 18 (2018) 4641-4646.
[66] R. Suedee, T. Srichana, R. Chotivatesin, G. Martin, Stereoselective release behaviors of imprinted bead matrices, Drug development and industrial pharmacy, 28 (2002) 545-554.
[67] R. Suedee, T. Srichana, G.P. Martin, Evaluation of matrices containing molecularly imprinted polymers in the enantioselective-controlled delivery of β-blockers, Journal of controlled release, 66 (2000) 135-147.
[68] R. Suedee, T. Srichana, T. Rattananont, Enantioselective release of controlled delivery granules based on molecularly imprinted polymers, Drug Delivery, 9 (2002) 19-30.
[69] K. Sreenivasan, On the application of molecularly imprinted poly (HEMA) as a template responsive release system, Journal of applied polymer science, 71 (1999) 1819-1821.
[70] J. Kurczewska, M. Cegłowski, P. Pecyna, M. Ratajczak, M. Gajęcka, G. Schroeder, Molecularly imprinted polymer as drug delivery carrier in alginate dressing, Materials Letters, 201 (2017) 46-49.
[71] G. Marcelo, I.C. Ferreira, R. Viveiros, T. Casimiro, Development of itaconic acid-based molecular imprinted polymers using supercritical fluid technology for pH-triggered drug delivery, International journal of pharmaceutics, 542 (2018) 125-131.
[72] M. Bakhshizadeh, A. Sazgarnia, M. Seifi, F. Hadizadeh, G. Rajabzadeh, S. Ahmad Mohajeri, TiO2-based mitoxantrone imprinted poly (methacrylic acid-co-polycaprolctone diacrylate) nanoparticles as a drug delivery system, Current pharmaceutical design, 23 (2017) 2685-2694.
[73] X. Song, S. Xu, L. Chen, Y. Wei, H. Xiong, Recent advances in molecularly imprinted polymers in food analysis, Journal of Applied Polymer Science, 131 (2014).
[74] Y. Yang, J. Yu, J. Yin, B. Shao, J. Zhang, Molecularly imprinted solid-phase extraction for selective extraction of bisphenol analogues in beverages and canned food, Journal of agricultural and food chemistry, 62 (2014) 11130-11137.
[75] J. Yang, Z. Wang, T. Zhou, X. Song, Q. Liu, Y. Zhang, L. He, Determination of cyproheptadine in feeds using molecularly imprinted solid-phase extraction coupled with HPLC, Journal of Chromatography B, 990 (2015) 39-44.
[76] T. Kubo, K. Hosoya, Y. Watabe, N. Tanaka, T. Sano, K. Kaya, Recognition of hepatotoxic homologues of microcystin using a combination of selective adsorption media, Journal of separation science, 27 (2004) 316-324.
[77] M. Pourfarzib, R. Dinarvand, B. Akbari-adergani, A. Mehramizi, H. Rastegar, M. Shekarchi, Water-compatible molecularly imprinted polymer as a sorbent for the selective extraction and purification of adefovir from human serum and urine, Journal of separation science, 38 (2015) 1755-1762.
[78] M.G. Santos, I.M.C. Tavares, V.B. Boralli, E.C. Figueiredo, Direct doping analysis of beta-blocker drugs from urinary samples by on-line molecularly imprinted solid-phase extraction coupled to liquid chromatography/mass spectrometry, Analyst, 140 (2015) 2696-2703.
[79] W. Ji, L. Chen, X. Ma, X. Wang, Q. Gao, Y. Geng, L. Huang, Molecularly imprinted polymers with novel functional monomer for selective solid-phase extraction of gastrodin from the aqueous extract of Gastrodia elata, Journal of Chromatography A, 1342 (2014) 1-7.

[80] Z. Li, C. Qin, D. Li, Y. Hou, S. Li, J. Sun, Molecularly imprinted polymer for specific extraction of hypericin from Hypericum perforatum L. herbal extract, Journal of pharmaceutical and biomedical analysis, 98 (2014) 210-220.
[81] B. Sellergren, Direct drug determination by selective sample enrichment on an imprinted polymer, Analytical chemistry, 66 (1994) 1578-1582.
[82] Z. Luo, A. Zeng, P. Zheng, P. Guo, W. Du, K. Du, Q. Fu, Preparation of surface molecularly imprinted polymers as the solid-phase extraction sorbents for the specific recognition of penicilloic acid in penicillin, Analytical Methods, 6 (2014) 7865-7874.
[83] M. Peyrovi, M. Hadjmohammadi, Synthesis of molecularly imprinted polypyrrole as an adsorbent for solid-phase extraction of warfarin from human plasma and urine, Biomedical Chromatography, 29 (2015) 1623-1628.
[84] M. Karimi, F. Aboufazeli, H.R.L.Z. Zhad, O. Sadeghi, E. Najafi, Determination of sulfonamides in chicken meat by magnetic molecularly imprinted polymer coupled to HPLC-UV, Food Analytical Methods, 7 (2014) 73-80.
[85] F. Hadizadeh, M. Hassanpour Moghadam, S.A. Mohajeri, Application of molecularly imprinted hydrogel for the preparation of lactose-free milk, Journal of the Science of Food and Agriculture, 93 (2013) 304-309.
[86] F.F. Chen, G.Y. Wang, Y.P. Shi, Molecularly imprinted polymer microspheres for solid-phase extraction of protocatechuic acid in Rhizoma homalomenae, Journal of separation science, 34 (2011) 2602-2610.
[87] C. Long, Z. Mai, Y. Yang, B. Zhu, X. Xu, L. Lu, X. Zou, Synthesis and characterization of a novel molecularly imprinted polymer for simultaneous extraction and determination of water-soluble and fat-soluble synthetic colorants in chilli products by solid phase extraction and high performance liquid chromatography, Journal of Chromatography A, 1216 (2009) 8379-8385.
[88] X. Jiang, C. Zhao, N. Jiang, H. Zhang, M. Liu, Selective solid-phase extraction using molecular imprinted polymer for the analysis of diethylstilbestrol, Food chemistry, 108 (2008) 1061-1067.
[89] W. Zheng, H. Wu, Y. Jiang, J. Xu, X. Li, W. Zhang, F. Qiu, A molecularly-imprinted-electrochemical-sensor modified with nano-carbon-dots with high sensitivity and selectivity for rapid determination of glucose, Analytical biochemistry, (2018).
[90] T. Kobayashi, Y. Murawaki, P.S. Reddy, M. Abe, N. Fujii, Molecular imprinting of caffeine and its recognition assay by quartz-crystal microbalance, Analytica Chimica Acta, 435 (2001) 141-149.
[91] E.P. Lai, A. Fafara, V.A. VanderNoot, M. Kono, B. Polsky, Surface plasmon resonance sensors using molecularly imprinted polymers for sorbent assay of theophylline, caffeine, and xanthine, Canadian Journal of Chemistry, 76 (1998) 265-273.
[92] D. Jégourel, R. Delépée, F. Breton, A. Rolland, R. Vidal, L.A. Agrofoglio, Molecularly imprinted polymer of 5-methyluridine for solid-phase extraction of pyrimidine nucleoside cancer markers in urine, Bioorganic & medicinal chemistry, 16 (2008) 8932-8939.
[93] R. Levi, S. McNiven, S.A. Piletsky, S.-H. Cheong, K. Yano, I. Karube, Optical detection of chloramphenicol using molecularly imprinted polymers, Analytical Chemistry, 69 (1997) 2017-2021.
[94] A. Pizzariello, M. Stred'ansky, S. Stred'ansky, S. Miertuš, A solid binding matrix/molecularly imprinted polymer-based sensor system for the determination of clenbuterol in bovine liver using differential-pulse voltammetry, Sensors and Actuators B: Chemical, 76 (2001) 286-294.
[95] A. Rachkov, S. McNiven, A. El'skaya, K. Yano, I. Karube, Fluorescence detection of β-estradiol using a molecularly imprinted polymer, Analytica chimica acta, 405 (2000) 23-29.
[96] G.M. Birnbaumer, P.A. Lieberzeit, L. Richter, R. Schirhagl, M. Milnera, F.L. Dickert, A. Bailey, P. Ertl, Detection of viruses with molecularly imprinted polymers integrated on a microfluidic biochip using contact-less dielectric microsensors, Lab on a Chip, 9 (2009) 3549-3556.
[97] D. Kriz, K. Mosbach, Competitive amperometric morphine sensor based on an agarose immobilised molecularly imprinted polymer, Analytica chimica acta, 300 (1995) 71-75.

[98] Y. Tan, H. Peng, C. Liang, S. Yao, A new assay system for phenacetin using biomimic bulk acoustic wave sensor with a molecularly imprinted polymer coating, Sensors and Actuators B: Chemical, 73 (2001) 179-184.
[99] S. Drake, Cause, Experiment and Science: A galilean dialogue incorporating a new translation of galileo's bodies that stay a top water., (1981) 1564-1642.
[100] G. Galileo, Discorso intorno alle Cose che Stanno in su l'Acqua (Discourse on Floating Bodies), 1612.
[101] T. Young, III. An essay on the cohesion of fluids, Philosophical Transactions of the Royal Society of London, 95 (1805) 65-87.
[102] G. Lippmann, Relation entre les phénomènes électriques et capillaires, Annales de Chimie et de Physique, 5 (1975) 494-549.
[103] B. Berge, Électrocapillarité et mouillage de films isolants per l'eau, Comptes Rendus de l'Académie des Sciences Paris, Série II, 317 (1993) 6.
[104] H.C. Lee, S. Yun, S.H. Ko, K.H. Kang, An electrohydrodynamic flow in ac electrowetting, Biomicrofluidics, 3 (2009).
[105] S.H. Ko, H. Lee, K.H. Kang, Hydrodynamic flows in electrowetting, Langmuir, 24 (2007) 1094-1101.
[106] J.S. Yang, J.O. Kwon, J.B. Chae, M. Choi, S.K. Chung, Electrowetting-on-dielectric (EWOD) induced flow analysis, Journal of Micromechanics and Microengineering, 25 (2015) 087001.
[107] H.B. Eral, D. Mampallil Augustine, M.H.G. Duits, F. Mugele, Suppressing the coffee stain effect: how to control colloidal self-assembly in evaporating drops using electrowetting, Soft Matter, 7 (2011) 4954-4958.
[108] P. García-Sánchez, A. Ramos, F. Mugele, Electrothermally driven flows in ac electrowetting, Physical Review E, 81 (2010).
[109] F. Mugele, J.-C. Baret, Electrowetting: from basics to applications, Journal of Physics: Condensed Matter, (2005) 705-760.
[110] F. Mugele, J.-C. Baret, D. Steinhauser, Microfluidic mixing through electrowetting-induced droplet oscillations, Applied Physics Letters, 88 (2006).
[111] Y. Lu, A. Sur, C. Pascente, S.R. Annapragada, P. Ruchhoeft, D. Liu, Dynamics of droplet motion induced by Electrowetting, International Journal of Heat and Mass Transfer, 106 (2017) 920-931.
[112] O. Kudina, B. Eral, F. Mugele, e-MALDI: an electrowetting-enhanced drop drying method for MALDI mass spectrometry, Analytical chemistry, 88 (2016) 4669-4675.
[113] R.A. Hayes, B.J. Feenstra, Video-speed electronic paper based on electrowetting, Nature, 425 (2003) 2.
[114] Liquavista B.V., What is Electrowetting?/ Advantages, https://www.liquavista.com/technology.html, accessed: 25/06/2018
[115] S.C. Terry, J.H. Jerman, J.B. Angell, A gas chromatographic air analyzer fabricated on a silicon wafer, IEEE Transactions on Electron Devices, ED-26 (1979) 1880-1886.
[116] S. Gupta, K. Ramesh, S. Ahmed, V. Kakkar, Lab-on-chip technology: a review on design trends and future scope in biomedical applications, International Journal of Bio-Science and Bio-Technology, 8 (2016) 311-322.
[117] D. Mark, S. Haeberle, G. Roth, F. Von Stetten, R. Zengerle, Microfluidic lab-on-a-chip platforms: requirements, characteristics and applications., in: S. Kakaç, B. Kosoy, D. Li, A. Pramuanjaroenkij (Eds.) Proceedings of the NATO advanced study institute on microfluidics based microsystems, Springer (and IOS Press), Dordrecht, The Netherlands (and Amsterdam, The Netherlands), 2010.
[118] B. Berge, J. Peseux, Variable focal lens controlled by an external voltage: an application of electrowetting, The European Physical Journal E, 3 (2000) 159-163.

[119] H. Shirakawa, E.J. Louis, A.G. MacDiarmid, C.K. Chiang, A.J. Heegen, Synthesis of electrically conducting organic polymers: halogen derivatives of polyacetylene, (CH)x, Journal of the Chemical Society, Chemical Communications, (1977) 578-580.
[120] The Royal Swedish Academy of Sciences, The Nobel Prize in Chemistry, 2000: Conductive Polymers, in: B. Nordén, E. Krutmeijer (Eds.), 2000.
[121] A.G. Macdiarmid, L.S. Yang, W.S. Huang, B.D. Humphrey, Polyaniline: electrochemistry and application to rechargeable batteries, Synthetic Metals, 18 (1987) 393-398.
[122] C.O. Laoire, S. Mukerjee, K.M. Abraham, E.J. Plichta, M.A. Hendrickson, Influence of nonaqueous solvents on the electrochemistry of oxygen in the rechargeable lithium-air battery, Journal of Physical Chemistry C, 114 (2010) 9178-9186.
[123] H. Gao, L. Xue, S. Xin, J.B. Goodenough, A high-energy-density potassium battery with a polymer-gel electrolyte and a polyaniline cathode, Angewandte Chemie (2018).
[124] M. Armand, J.M. Tarascon, Building better batteries, Nature, 451 (2008) 652.
[125] T.E. Springer, T.A. Zawodzinski, S. Gottesfeld, Polymer electrolyte fuel cell model, Journal of Electrochemical Society, 138 (1991) 2334-2342.
[126] E. Perry Murray, T. Tsai, S.A. Barnett, A direct-methane fuel cell with a ceria-based anode, Nature, 400 (1999) 649.
[127] L. Nyholm, G. Nyström, A. Mihranyan, M. Strømme, Toward flexible polymer and paper-based energy storage devices, Advanced Materials, 23 (2011) 3751-3769.
[128] V.L. Pushparaj, M.M. Shaijumon, A. Kumar, S. Murugesan, L. Ci, R. Vajtai, R.J. Linhardt, O. Nalamasu, P.M. Ajayan, Toward flexible polymer and paper-based energy storage devices, Proceedings of the National Academy of Sciences of the United States of America, 104 (2007) 13574-13577.
[129] L. Bao, X. Li, Towards textile energy storage from cotton T-shirts, Advanced Materials, 24 (2012) 3246-3252.
[130] A.S. Aricò, P. Bruce, B. Scrosati, J.-M. Tarascon, W. van Schalkwijk, Nanostructured materials for advanced energy conversion and storage devices, Nature materials, 4 (2005) 366-377.
[131] R. Brooke, J. Edberg, D. Iandolo, M. Berggren, X. Crispin, I. Engquist, Controlling the electrochromic properties of conductive polymers using UV-light, Journal of Materials Chemistry C, (2018).
[132] H. Cheng, Y. Zhang, Method and device for fabricating flexible display device, BOE Technology Group Co Ltd United States, 2013.
[133] A. Tröls, H. Enser, B. Jakoby, Modeling and fabrication of low-cost electrowetting actuators for flexible microfluidic display applications, Sensors, (2016).
[134] H.H. Khaligh, K. Liew, Y. Han, N.M. Abukhdeir, I.A. Goldthorpe, Silver nanowire transparent electrodes for liquid crystal-based smart windows, Solar Energy Materials & Solar Cells, 132 (2015) 337-341.
[135] R. Baetens, B.P. Jelle, A. Gustavsen, Properties, requirements and possibilities of smart windows for dynamic daylight and solar energy control in buildings: a state-of-the-art review, Solar Energy Materials & Solar Cells, 94 (2010) 87-105.
[136] R.E. Wiley, Conductive coatings and foams for anti-static protection, energy absorption, and electromagnetic compatability, Archeson Ind Inc, United States, 1989.
[137] F. Jonas, J.T. Morrison, 3,4-Polyethylenedioxythiophene (PEDT): conductive coatings technical applications and properties, Synthetic Metals, 85 (1997) 1397-1398.
[138] J.L. Camalet, J.C. Lacroix, S. Aeiyach, P.C. Lacaze, Characterization of polyaniline films electrodeposited on mild steel in aqueous p-toluenesulfonic acid solution, Journal of Electroanalytical Chemistry, 445 (1998) 117-124.
[139] A. Talo, P. Passiniemi, O. Forsén, S. Ylăsaari, Polyaniline/epoxy coatings with good anti-corrosion properties, Synthetic Metals, 85 (1997) 1333-1334.

[140] S. Sathiyanarayanan, S. Muthukrishnan, G. Venkatachari, D.C. Trivedi, Corrosion protection of steel by polyaniline (PANI) pigmented paint coating, Progress in Organic Coatings, 53 (2005) 297-301.
[141] A.J. Dominis, G.M. Spinks, G.G. Wallace, Comparison of polyaniline primers prepared with different dopants for corrosion protection of steel, Progress in Organic Coatings, 48 (2003) 43-49.
[142] D.E. Tallman, G. Spinks, A. Dominis, G.G. Wallace, Electroactive conducting polymers for corrosion control. Part I general introduction and a review of non-ferrous metals, Journal of Solid State Electrochemistry, 6 (2002) 73-84.
[143] G.M. Spinks, A.J. Dominis, G.G. Wallace, D.E. Tallman, Electroactive conducting polymers for corrosion control. Part II Ferrous metals, Journal of Solid State Electrochemistry, 6 (2002) 85-100.
[144] S. Jin, C. Choi, Superhydrophobic and superoleophobic nanosurfaces, Google Patents, 2018.
[145] A.-I. Gopalan, S. Komathi, N. Muthuchamy, K.P. Lee, M.J. Whitcombe, D. Lakshmi, G. Sai-Anand, Functionalized conjugated polymers for sensing and molecular imprinting applications, Progress in Polymer Science, (2018).
[146] A.L. Beresford, A.R. Hillman, Electrochromic enhancement of latent fingerprints on stainless steel surfaces, Analytical chemistry, 82 (2009) 483-486.
[147] M. Šetka, J. Drbohlavová, J. Hubálek, Nanostructured polypyrrole-based ammonia and volatile organic compound sensors, Sensors, 17 (2017).
[148] G. Ćirić-Marjanović, Recent advances in polyaniline research: polymerization mechanisms, structural aspects, properties and applications, Synthetic Metals, 177 (2013) 1-47.
[149] F.F. Runge, Ueber einige Produkte der Steinkohlendestillation, Annalen der Physik und Chemie, 5 (1834) 65-78.
[150] P. Humpoliceka, V. Kasparkovaa, P. Sahaa, J. Stejskal, Biocompatibility of polyaniline, Synthetic Metals, 162 (2012) 722-727.
[151] B.A. Bolto, R. McNeill, D.E. Weiss, Electronic conduction in polymers: III. electronic properties of polypyrrole, Australian Journal of Chemistry, 16 (1963) 1090-1103.
[152] R. McNeill, R. Siudak, J.H. Wardlaw, D.E. Weiss, Electronic conduction in polymers: I. the chemical structure of polypyrrole., Australian Journal of Chemistry, 16 (1963) 1056-1075.
[153] B.A. Bolto, D.E. Weiss, Electronic conduction in polymers: II. the electrochemical reduction of polypyrrole at controlled potential, Australian Journal of Chemistry, 16 (1963) 1076-1089.
[154] A. Diaz, J.M. Vasquez Vallejo, A. Martinez Duran, [Pt]Polypyrrole: a new organic electrode material, IBM: Journal of Research and Development, 25 (1981) 42-50.
[155] N. Yi, M.R. Abidian, Chapter 10 Conducting polymers and their biomedical applications, in: L. Poole-Warren, P. Martens, R. Green (Eds.) Biosynthetic Polymers for Medical Applications, Woodhead Publishing Elsevier2016.
[156] R. Čabala, J. Škarda, K. Potje-Kamloth, Spectroscopic investigation of thermal treatment of doped polypyrrole, Physical Chemistry Chemical Physics, 2 (2000) 3283-3291.
[157] F. Jonas, L. Schrader, Conductive modifications of polymers with polypyrroles and polythiophenes, Synthetic Metals, 41-43 (1991) 831-836.
[158] G. Heywang, F. Jonas, Poly(alkylenedioxythiophene)s—new, very stable conducting polymers, Advanced Materials, 4 (1992) 116-118.
[159] I. Winter, C. Reese, J. Hormes, G. Heywang, F. Jonas, The thermal ageing of poly(3,4-ethylenedioxythiophene). An investigation by X-ray absorption and X-ray photoelectron spectroscopy, 194, (1995) 207-213.
[160] Bayer Ag, 1988.
[161] J.C. Gustafsson-Carlberg, O. Inganäs, M.R. Andersson, C. Booth, A. Azens, C.G. Granqvist, Tuning the bandgab for polymeric smart window and displays, Electrochemica Acta, 40 (1995) 2233-2235.

[162] O. Inganäs, C. Carlberg, T. Yohannes, Polymer electrolytes in optical devices, Electrochemica Acta, 43 (1998) 10-11.
[163] S.A. Sapp, G.A. Sotzing, J.L. Reddinger, J.R. Reynolds, Rapid switching solid state electrochromic devices based on complementary conducting polymer films, Advanced Materials, 8 (1996).
[164] H. Andriessen, Agfa-Gevaert, 2002
[165] A. Saito, EL SHEET, Seiko Precision.
[166] F. Jonas, A. Karbach, B. Muys, E. Van Thillo, R. Wehrmann, A. Elschner, R. Dujardin, Conductive coatings, Bayer Ag. , 1995.
[167] L.B. Groenendaal, F. Jonas, D. Freitag, H. Pielartzik, J.R. Reynolds, Poly(3,4-ethylenedioxythiophene) and its derivatives: past, present, and future, Advances Materials, 12 (2000) 481-494.
[168] L. Pigani, A. Heras, Á. Colina, R. Seeber, J. López-Palacios, Electropolymerisation of 3,4-ethylenedioxythiophene in aqueous solutions., Electrochemistry Communications, 6 (2004) 1192-1198.
[169] D. Bloor, B. Movaghar, Conductive polymers, IEE Proceedings, 130 (1983) 225-232.
[170] G. de Nascimento, M. de Souza, Chapter 8 Spectroscopy of nanostructured conducting polymers, in: E. Eftekhari (Ed.) Nanostructured conductive polymers, John Wiley & Sons, United Kingdom, 2010.
[171] J.L. Bredas, G.B. Street, Polarons, bipolarons, and solitons in conducting polymers, Accounts of Chemical Research, 18 (1985) 309-315.
[172] P.R. Somani, S. Radhakrishnan, Electrochromic materials and devices: present and future, Materials Chemistry and Physics, 77 (2002) 117-133.
[173] M. Rehahn, Der Weg zu einer neuen Materialklasse Elektrisch leitfähige Kunststoffe, Chemie in unserer Zeit, 37 (2003) 18-30.
[174] B. Milián-Medina, J. Gierschner, π-Conjugation, WIREs Computational Molecular Science, 2 (2011) 513-524.
[175] I.Y. Sapurina, M.A. Shishov, Chapter 9 Oxidative polymerization of aniline: molecular synthesis of polyaniline and the formation of supramolecular structures in: A. Da Sousa Gomes (Ed.) New polymers for special applications, IntechOpen2012.
[176] D. Bhattacharyya, R.M. Howden, D.C. Borrelli, K.K. Gleason, Vapor phase oxidative synthesis of conjugated polymersand applications, Journal of Polymer Science Part B: Polymer Physics, 50 (2012) 1329-1351.
[177] S. Sadki, P. Schottland, N. Brodie, G. Sabouraud, The mechanisms of pyrrole electropolymerization, Chemical Society Reviews, 29 (2000) 283-293.
[178] V. Noel, H. Randriamahazaka, C. Chevrot, Cyclic voltammetric studies of the relaxation processes during the oxidation of poly(3,4-ethylenedioxythiophene) in propylene carbonate solution, Journal of Electroanalytical Chemistry, 542 (2003) 33-38.
[179] P. Camurlu, Polypyrrole derivatives for electrochromic applications, RSC Advances, 4 (2014) 55832-55845.
[180] M.M. Gvozdenović, B.Z. Jugović, J.S. Stevanović, T.L. Trišović, B.N. Grgur, Chapter 4 Electrochemical polymerization of aniline, in: E. Schab-Balcerzak (Ed.) Electropolymerization, InTech, Croatia, 2011.
[181] N. Gospodinova, L. Terlemezyan, Conducting polymers prepared by oxidative polymerization: polyaniline, Progress in Polymer Science, 23 (1998) 1443-1484.
[182] E.T. Kang, K.G. Neoh, K.L. Tan, Polyaniline: a polymer with many interesting intrinsic redox states, Progress in Polymer Science, 23 (1998) 277-324.
[183] J. Stejskal, P. Kratochvil, A.D. Jenkins, The formation of polyaniline and the nature of its structures, Polymer, 2 (1996) 367-369.
[184] J.A. Halldorsson, Y. Wu, H.R. Brown, G.M. Spinks, G.G. Wallace, Surfactant-controlled shape change of organic droplets using polypyrrole, Thin Solid Films, 519 (2011) 6486-6491.

[185] Y.-T. Tsai, C.-H. Choi, N. Gao, E.-H. Yang, Tunable wetting mechanism of polypyrrole surfaces and low-voltage droplet manipulation via redox, Langmuir, 27 (2011) 4249-4256.
[186] L. Robinson, J. Isaksson, N.D. Robinson, M. Berggren, Electrochemical control of surface wettability of poly (3-alkylthiophenes), Surface Science, 600 (2006) L148-L152.
[187] J. Isaksson, C. Tengstedt, M. Fahlman, N. Robinson, M. Berggren, A solid-state organic electronic wettability switch, Advanced Materials, 16 (2004) 316-320.
[188] J.A. Halldorsson, S.J. Little, D. Diamond, G. Spinks, G. Wallace, Controlled transport of droplets using conducting polymers, Langmuir, 25 (2009) 11137-11141.
[189] M. Pyo, Surface roughness changes of poly (N-methylpyrrole)/poly (styrene sulfonate) with doping in perchlorate solutions of various cations, Journal of The Electrochemical Society, 152 (2005) E90-E93.
[190] A. Gelmi, M.K. Ljunggren, M. Rafat, E. Jager, Influence of conductive polymer doping on the viability of cardiac progenitor cells, Journal of Materials Chemistry B, 2 (2014) 3860-3867.
[191] T. Patois, B. Lakard, S. Monney, X. Roizard, P. Fievet, Characterization of the surface properties of polypyrrole films: Influence of electrodeposition parameters, Synthetic Metals, 161 (2011) 2498-2505.
[192] J. Chang, I.W. Hunter, Characterization and control of the wettability of conducting polymer thin films., Materials Research Society Symposium, 2009.
[193] T. Silk, Q. Hong, T. J., R.G. Compton, AFM studies of polypyrrole film surface morphology II. Roughness characterization by the fractal dimension analysis, Synthetic Metals, 93 (1998) 65-71.
[194] J. Tsukamoto, Recent advances in highly conductive polyacetylene, Advances in Physics 41 (1992) 509-546.
[195] A.I. Melato, M.H. Mendonça, L.M.J. Abrantes, Effect of the electropolymerisation conditions on the electrochemical, morphological and structural properties of PEDOTh films., Solid State Electrochem, 13 (2009) 417-426.
[196] F. Blanchard, B. Carré, F. Bonhomme, P. Biensan, H. Pagès, D. Lemordant, Study of poly(3,4-ethylenedioxythiophene) films prepared in propylene carbonate solutions containing different lithium salts., Journal of Electroanalytical Chemistry, 569 (2004) 203-210.
[197] J. Xia, N. Masaki, K. Jiang, S. Yanagida, The influence of doping ions on poly(3,4-ethylenedioxythiophene) as a counter electrode of a dye-sensitized solar cell, Journal of Materials Chemistry, 17 (2007) 2845.
[198] Y.-T. Kim, H. Yang, A.J. Bard, Electrochemical control of polyaniline morphology as studied by scanning tunneling microscopy, Journal of The Electrochemical Society, 138 (1991) 71-74.
[199] X. Ren, P.G. Pickup, Ion transport in poly pyrrole and a polypyrrole/polyanion composite, Journal of Physical Chemistry, 97 (1993) 5356-5362.
[200] M. Hato, Electrically Induced wettability change of polyaniline. Potential controlled tensiometric study, Chemistry Letters, (1988) 3.
[201] M.-H. Lee, In-situ measurement of surface tension during electrochemical doping of polypyrrole films, Molecular Crystals and Liquid Crystals Science and Technology. Section A. Molecular Crystals and Liquid Crystals, 316 (1998) 329-332.
[202] D. Mecerreyes, V. Alvaro, I. Cantero, M. Bengoetxea, P.A. Calvo, H. Grande, J. Rodriguez, J.A. Pomposo, Low surface energy conducting polypyrrole doped with a fluorinated counterion, Advanced Materials, 14 (2002) 749-752.
[203] L. Xu, W. Chen, A. Mulchandani, Y. Yan, Reversible conversion of conducting polymer films from superhydrophobic to superhydrophilic, Angewandte Chemie International Edition, 44 (2005) 6009-6012.
[204] A.F. Stalder, G. Kulik, D. Sage, L. Barbieri, P. Hoffmann, A snake-based approach to accurate determination of both contact points and contact angles, Colloids and surfaces A: Physicochemical and Engineering Aspects, 286 (2006) 92-103.

[205] A.F. Stalder, T. Melchior, M. Müller, D. Sage, T. Blu, M. Unser, Low-bond axisymmetric drop shape analysis for surface tension and contact angle measurements of sessile drops, Colloids and surfaces A: Physicochemical and Engineering Aspects, 364 (2010) 72-81.
[206] H.B. Eral, D.J.C.M. 't Mannetje, J.M. Oh, Contact angle hysteresis: a review of fundamentals and applications, Colloid and polymer science, 291 (2013) 247-260.
[207] W.B. Hardy, The Spreading of Fluids on Glass, Philosophical Magazine, 38 (1919).
[208] Q. Yuan, Y.-P. Zhao, Precursor Film in Dynamic Wetting, Electrowetting, and Electro-Elasto-Capillarity, Physical Review Letters, 104 (2010).
[209] A. Marmur, Soft contact: measurement and interpretation of contact angles, Soft Matter, 2 (2006) 12-17.
[210] D. Kim, N.M. Pugno, S. Ryu, Wetting theory for small droplets on textured solid surfaces, Scientific Reports, (2016).
[211] R.N. Wenzel, Resistance of solid surfaces to wetting by water, Industrial & Engineering Chemistry, 28 (1936) 988-994.
[212] A. Cassie, S. Baxter, Wettability of porous surfaces, Transactions of the Faraday society, 40 (1944) 546-551.
[213] G. Whyman, E. Bormashenko, T. Stein, The rigorous derivation of Young, Cassie-Baxter and Wenzel equation and the analysis of the contact angle hysteresis phenomenon, Chemical Physics Letters, 450 (2008) 355-359.
[214] G. McHale, Cassie and Wenzel: were they really so wrong?, Langmuir, 23 (2007) 8200-8205.
[215] M.V. Panchagnula, S. Vedantam, Comment on how Wenzel and Cassie were wrong by Gao and McCarthy, Langmuir, 23 (2007) 13242-13242.
[216] M. Nosonovsky, On the range of applicability of the Wenzel and Cassie equations, Langmuir, 23 (2007) 9919-9920.
[217] A. Marmur, E. Bittoun, When Wenzel and Cassie are right: reconciling local and global considerations, Langmuir, 25 (2009) 1277-1281.
[218] H.Y. Erbil, The debate on the dependence of apparent contact angles on drop contact area or three-phase contact line: A review, Surface Science Reports, 69 (2014) 325-365.
[219] L. Gao, T.J. McCarthy, How Wenzel and Cassie were wrong, Langmuir, 23 (2007) 3762-3765.
[220] T.B. Jones, J.D. Fowler, Y.S. Chang, C.-J. Kim, Frequency-Based Relationship of Electrowetting and Dielectrophoretic Liquid Microactuation, Langmuir, 19 (2003) 7646-7651.
[221] J. Sondag-Huethorst, L. Fokkink, Electrical double layers on thiol-modified polycrystalline gold electrodes, Journal of Electroanalytical Chemistry, 367 (1994) 49-57.
[222] F. Mugele, Fundamental challenges in electrowetting: from equilibrium shapes to contact angle saturation and drop dynamics Soft Matter, 5 (2009) 3377-3384.
[223] H.J.J. Verheijen, M.W.J. Prins, Reversible electrowetting and trapping of charge: model and experiments, Langmuir, 15 (1999) 6616-6620.
[224] M. Vallet, M. Vallade, B. Berge, Limiting phenomena for the spreading of water on polymer films by electrowetting, The European Physics Journal B, 11 (1999) 583-591.
[225] B. Shapiro, H. Moon, R.L. Garrell, C.-J.C. Kim, Equilibrium behavior of sessile drops under surface tension, applied external fields, and material variations, Journal of Applied Physics, 93 (2003) 5794-5811.
[226] G. Sauerbrey, Verwendung von Schwingquarzen zur Wägung dünner Schichten und zur Mikrowägung, Zeitschrift für Physik, 155 (1959) 206-222.
[227] Iontof, "Time-of-Flight Secondary Ion Mass Spectrometry", https://www.iontof.com/tof-sims-secondary-ion-mass-spectrometry.html, accessed: 6/5/2018
[228] National Mass Spectrometry Facility NMSF, Matrix-Assisted Laser Desorption/Ionisation, Mass Spectrometry Summer School 2017.

[229] C.-C. Wang, Y.-H. Lai, Y.-M. Ou, H.-T. Chang, Y.-S. Wang, Critical factors determining the quantification capability of matrix-assisted laser desorption/ionization– time-of-flight mass spectrometry, Phylosophical Transactions of the Royal Society A, 374 (2016).
[230] R. Knockenmuss, A quantitative model of ultraviolet matrix-assisted laser desorption/ionization, Journal of Mass Spectrometry, 37 (2002) 867-877.
[231] F.J. Hollor, D.A. Skoog, S.R. Crouch, Principles of instrumental analysis, 6th ed., Thomson Brooks/Cole, Belmont (USA), 2007.
[232] G. Haugstad, Atomic force microscopy: understanding basic modes and advanced applications, John Wiley & Sons2012.
[233] I. Zeta Instruments, Zeta-20 Zeta3D optical profiler, in: I. Zeta Instruments (Ed.), 2016.
[234] G. Verkerk, J.B. Broens, P.A.M. de Groot, W. Kranendonk, J.L. Sikkema, J.J. Westra, I.M. Wevers-Prijs, Binas, Wolters-Noordhoff B.V. , Groningen, The Netherlands, 1998.
[235] Perkin Elmer, Specifications Frontier FT Mid-IR and Far-IR System, in: P. Elmer (Ed.), 2010-2011.
[236] A. Marquart, SPR-pages, https://www.sprpages.nl/, accessed: 3/5/2018.
[237] BioNavis, Different configurations to achieve surface plasmon excitation by light, 2016.
[238] A. Otto, Excitation of Nonradiative Surface Plasma Waves in Silver by the Method of Frustrated Total Reflection Zeitschrift für Physik 216 (1968) 398-410.
[239] Instruments S.A., FluoroMax-2 with DataMax for Windows Hardware Operation Manual, 1995.

Potential driven changes in characteristics of conductive polymers 2

2.1. Introduction

Conductive polymers are known for their electronic properties, optical characteristics and flexibility, thus combining properties of both metals and polymers. [1] Therefore they are useful for a variety of applications; to transfer stimuli in a surface such as in smart windows [2, 3] and (electrowetting) displays [4-6] and as surface coating both anti-static [7, 8] and anti-corrosive [9-14].

In this chapter, another important surface characteristic was investigated, the hydrophobicity which is the property of repelling water. Being able to control the wettability is useful for the aerospace industry (ice-free aeroplane wings [15, 16]) and maritime industry (reduce friction drag of ships [17]) as well as for the formation of displays [4-6].

The hydrophobicity could be controlled by applying a potential across the liquid and/or underlying surface to obtain a so called electrowetting effect. In the conventional electrowetting set-up the amount of wetting was changed by applying a potential across the liquid and underlying surface (Figure 2.1A). In the second set-up a potential was applied on a part of the surface resulting in movement of the droplet and change of amount of wetting (Figure 2.1B). In this research, the whole surface was modified by the application of a potential as shown in Figure 2.1C.

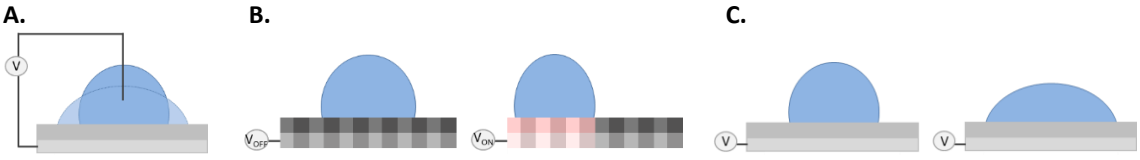

Figure 2.1 – Three ways of addressing electrowetting. The conventional electrowetting set-up: by applying a potential, the droplet spreads and retracts by removing the potential (**A**). Electrowetting of displays: the substrate is divided in areas which can be switched on and off independently (**B**; left: off, right: on). Electronic states of conductive polymers: change in electronic state of the conductive polymer film resulting in spreading/retraction of the droplet (**C**; left: electronic state 1, right: electronic state 2).

Here, the change in amount of wetting of conductive polymer films was determined to obtain more insight into potential driven interfacial energy changes. To get a complete overview of the impact of a potential on a surface, this research aimed to determine potential driven changes in characteristics of conductive polymer films focusing on the hydrophobicity, composition, morphology and topography. To justify sequential use of surface analysis and film formation techniques, the influence of wetting caused by a droplet (used for contact angle measurements) and by in solution film formation on the roughness measurements was determined. Next the influence of potential driven roughness changes on the contact angle was investigated. The objectives are summarised below and illustrated in Figure 2.2:

A. Determination of the influence of an applied potential on the hydrophobicity, composition, morphology and topography (roughness) of the conductive polymer film.
B. Estimation of the influence of wetting on the roughness measurements, focusing on wetting caused by a droplet and by in solution film formation.
C. Investigation of the influence of potential driven topographical (roughness) changes of the conductive polymer film on the contact angle measurements.

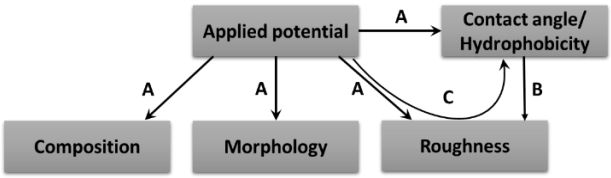

Figure 2.2 – Schematic overview of the investigated aspects, whereby the letters A-C correspond to the objectives A-C.

Three conductive polymers were used in this research: polyaniline, polypyrrole and poly(3,4-ethylenedioxythiophene) (PEDOT). Polyaniline was chosen as model polymer, because of its widely understood behaviour and their electronic state can be easily identified by colour. To determine the general validity of the findings, polypyrrole and PEDOT were analysed as well, they were chosen because of their use at room temperature and the relatively ease in forming a smooth and homogeneous PEDOT film. These polymers are also of use for a variety of applications, such as waterproof materials [18, 19], displays [4-6], smart textiles [20-22], fingerprint visualisation [23], anti-static coatings [7, 8] and anti-corrosion coatings [9-14].

2.2. Methods

Glass microscope slides were silanised and coated with gold to create a smooth and homogeneous metal surface, followed by the electropolymerisation of a conductive polymer film of polyaniline, polypyrrole or PEDOT on top. These polymer films were visually/microscopically inspected and the roughness and hydrophobicity of the polymer films were determined.

2.2.1. Silanisation and gold coating of glass microscope slides

Glass microscope slides were salinised in order to create a sulfur layer on the surface to which the gold can adhere as shown in Figure 2.3.

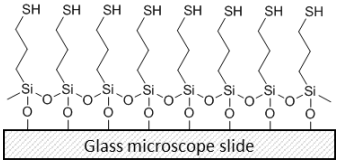

Figure 2.3 – Schematic illustration of silanisation of glass microscope slides.

Before silanisation, glass microscope slides were cleaned twice by sonicating in soapy water for 10 min, then rinsed with demi water followed by DI-water and finally dried. The slides were then rinsed with DI-water, sonicated in DI-water, dried, rinsed with IPA, dried, sonicated in IPA for 10 min and dried again. The cleaned glass slides were silanised by refluxing in 600 mL IPA, 18 mL 3-(mercaptopropyl)trimethoxysilane and 18 mL DI-water for 20 min. After cooling, the slides were rinsed with IPA, dried, sonicated in IPA for 10 min, dried, rinsed with IPA and dried again. The refluxing step and subsequent cleaning were repeated twice more. After the silanisation, the slides (ca. 34.84 cm^2) were immediately coated with gold using the EMS 300R T Sputter Coater (Electron Microscopy Sciences) for 200 s at 80 mA.

2.2.2. Electrodepositing of conductive polymers

The conductive polymers were electrodeposited using a conventional three-electrode electrochemical cell in which the gold coated surface functioned as a working electrode, an Ag/AgCl electrode as reference electrode and an IrO_2 coated Ti mesh electrode as counter electrode. Two different potentiostats were used; an Ivium potentiostat using

IVIUM software version 2.667 (Ivium) and an AUTOLAB potentiostat using GPES software version 4.9 (Eco Chemie).

The used monomer and electrolyte solutions as well as the potential window applied are discussed below. All prepaired monomer and monomer-free electrolyte solutions were stored in dark conditions at ca. 5 ^{o}C and at room temperature, respectively.

A polyaniline film was electrodeposited using cyclic voltammetry (potential window from -0.2 to 1.0 V) from a solution of 0.1 M aniline in an electrolyte solution of 0.1 M H_2SO_4. The used monomer-free electrolyte solution consisted of 0.1 M H_2SO_4.

A polypyrrole film was electrodeposited using cyclic voltammetry (potential window from -0.3 to 0.8 V) from a solution of 0.1 M pyrrole in an electrolyte solution of 0.1 M NH_4ClO_4 in water. The used monomer-free electrolyte solution consisted of 0.1 M NH_4ClO_4 in water.

A PEDOT film was electrodeposited using cyclic voltammetry (potential window from -0.4 to 1.2 V) from a solution of 0.1 M EDOT in an electrolyte solution of 0.1 M TBAP in acetonitrile. The used monomer-free electrolyte solution consisted of 0.1 M TBAP in acetonitrile.

Hereafter, the monomer plus electrolyte solution is referred to as monomer solution and the monomer-free electrolyte solution as electrolyte solution.

2.2.3. Contact angle measurements

The hydrophobicity of the deposited layers was determined by measuring the contact angle of droplets placed on the polymer films. Water, glycerol and chloroform droplets were used in this research as described below. The choice for these liquids was based on the density, solubility and polarity of the droplet and surrounding liquid, to ensure that the droplets stay on the surface (prevent floating and dissolving in surrounding liquid) and have a reasonable shape (not completely spread to allow changing contact angle). Droplets of approximately 5 µL were positioned on the films after which they spread till they reached a certain contact angle which corresponds to the hydrophobicity of the polymer film. The contact angles of the droplets were measured using the ThetaLite optical tensiometer (Biolin Scientific) in combination with OneAttension

software version 2.5, r5128 (Biolin Scientific) and/or using Image-J software versions 1.49e and 1.51g (National Institutes of Health, USA) in combination with drop analysis plugin LB-ADSA.

The contact angle measurements were performed both during cycling in monomer and electrolyte solution (in-situ measurements) and after removal from the solution (ex-situ measurements), as discussed below.

2.2.3.1. In-situ contact angle measurements

In the in-situ experiments, the hydrophobicity of the polymer films was determined while cycling in monomer or electrolyte solution. Droplets were positioned on the films (Figure 2.4) just after the oxidation or reduction peaks (Figure 2.5A) to measure the hydrophobicity of the film in oxidized or reduced state respectively. These in-situ experiments were performed using chloroform and glycerol droplets on polyaniline & polypyrrole and PEDOT films, respectively.

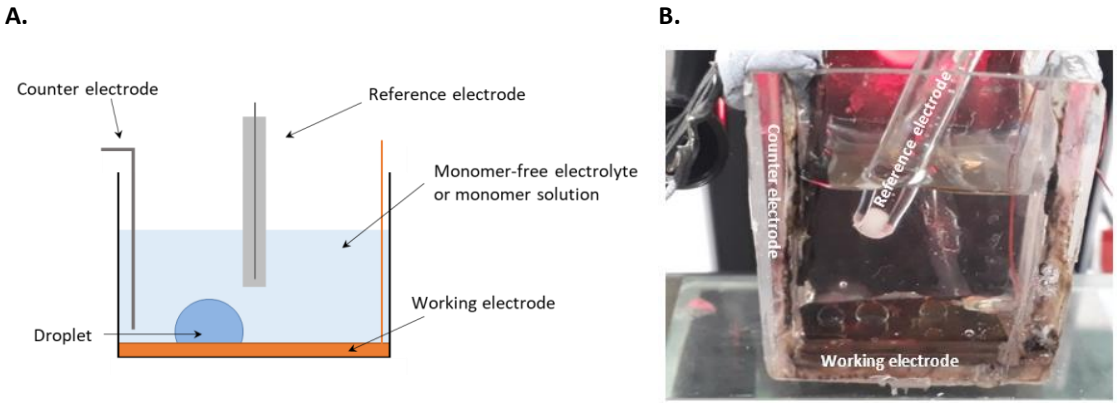

Figure 2.4 – Schematic illustration (**A**) and photo (**B**) of the in-situ contact angle measurement set-up. The three-electrode cell consists of an Ag/AgCl reference electrode, IrO_2 coated Ti mesh counter electrode and gold working electrode.

The droplet was left on the polymer film for a few cycles while new droplets were positioned on the film every half a cycle (Figure 2.5B). The change in hydrophobicity while a droplet is (partially) covering the surface was obtained together with an indication if the hydrophobicity was caused by a change in top-layer (covered by the droplet) or a lower layer.

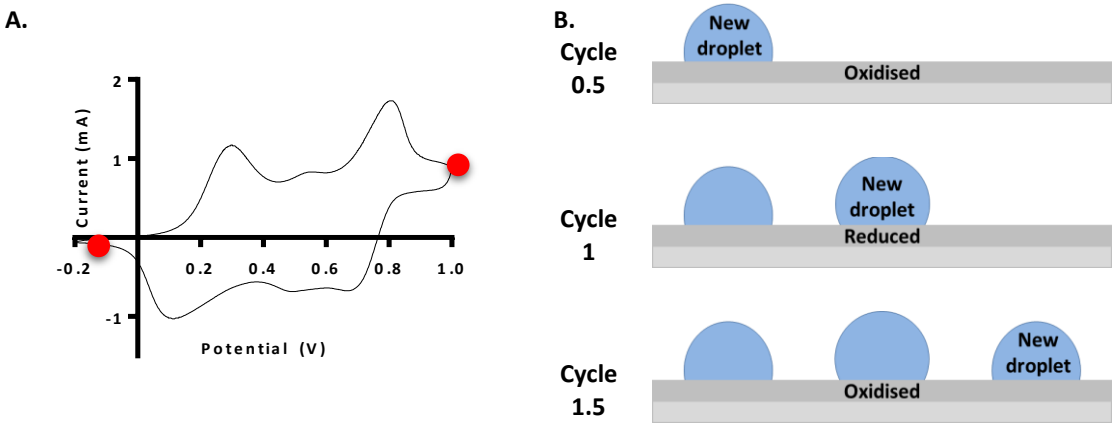

Figure 2.5 – Schematic illustration of the deposition of droplets every half a cycle, when fully reduced or oxidised as illustrated by the red dots in a cyclic voltammogram of polyaniline (**A**), while the droplet deposited in the former electronic state stays on the surface (**B**).

2.2.3.2. Ex-situ contact angle measurements

After the polymer film formation, the films were removed from the monomer or electrolyte solution and dried. In the experiments using polyaniline a drying procedure of 30 min in an oven at 60 °C and 5 min in THF was followed. Polypyrrole and PEDOT were dried in air for ca. 1 min. Subsequently, the hydrophobicity of the polymer film was determined by positioning a DI-water droplet on the polymer film while being surrounded by air as shown in Figure 2.6.

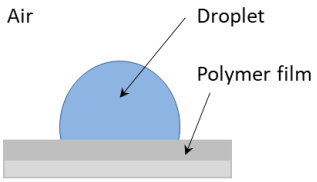

Figure 2.6 – Schematic illustration of ex-situ contact angle measurement set-up, showing the deposition of a droplet on the polymer film while being surrounded by air.

2.2.4. Roughness measurements

To retrieve information about the influence of the roughness of the polymer film on the droplets (used for contact angle measurements), the roughness of a profile (2D) and area (3D) was measured using the Zeta-20 True Colour Optical Profiler (Zeta Instruments), referred to as optical (3D) microscope hereafter. A variety of roughness representations exist. Here, R_a, S_a, the R-factor and f-value were chosen because of their wide use and provision of relevant information as discussed below.

2.2.4.1. R_a and S_a: arithmetical average of mean deviation

The R_a is the most commonly used representation of roughness and can be obtained by taking a line trace across the surface, which will be referred to as a cross-section in this thesis (Figure 2.7).

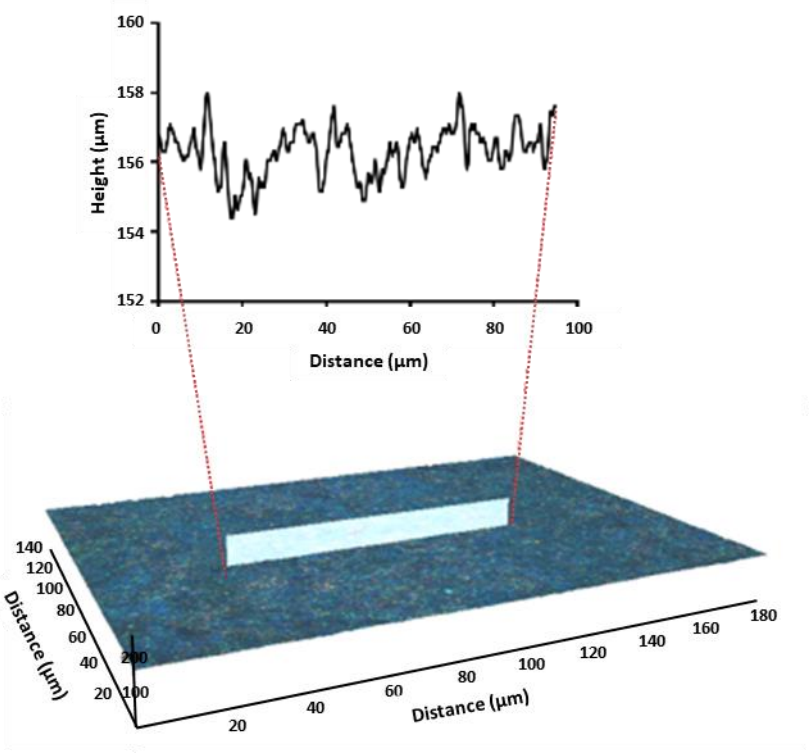

Figure 2.7 – Line trace across a polyaniline film used to determine the roughness.

Subsequently the R_a was calculated by taking the sum of the height deviation of each data point (r_i) of the cross-section resulting in the mean of the height deviations as shown in Equation 2.1; in which r_i is the height deviation of data point i and N is the number of data points. [24]

$$R_a = \frac{1}{N}\sum_{i=1}^{N} |r_i| \qquad \textbf{Equation 2.1}$$

The cross-sections were used to compare specific irregularities of the polymer film in different circumstances such as a polymer in reduced or oxidised state. To retrieve information about the complete polymer film instead of a single cross-section, S_a analysis was performed; S_a is an equivalent for R_a. R_a is measured over a cross-section and S_a over an area.

2.2.4.2. R-factor

The R-factor can be seen as a normalised surface roughness which corrects for the enlargement of the surface area due to irregularities by dividing the actual surface area by the projected surface area (Figure 2.8 and Equation 2.2).

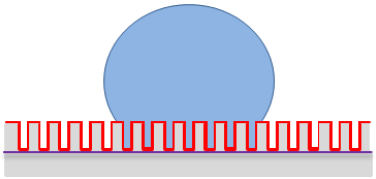

Figure 2.8 – Schematic illustration of the Wenzel model. The red line illustrates the actual surface area (also called topographical area) and the purple line the projected surface area, as used to determine the R-factor using Equation 2.2.

$$R\text{-}factor = \frac{actual\ area}{projected\ area} \qquad \textbf{Equation 2.2}$$

This R-factor is of particular interest because of its use in the Wenzel equation as shown in Chapter 1 (Section 1.5.2.1.). [25]

2.2.4.3. f-value

The f-value was used to define the roughness as used in the Cassie-Baxter model in which the f-value represents the ratio between the area in or between the grooves (formed by irregularities) and the total area. [26] For practical reasons, in this research this ratio was simplified to Equation 2.3.

$$f\text{-}value = \frac{actual\ area - projected\ area}{actual\ area} \qquad \textbf{Equation 2.3}$$

To summarise, four types of roughness measurements were performed. R_a to retrieve knowledge about a specific irregularity. S_a to obtain an overview of the roughness of the polymer film. The R-factor and f-value for the calculation of the possible influence of roughness on the contact angle using the Wenzel and Cassie-Baxter equation, respectively.

2.2.5. Chemicals and materials

In this study the chemicals and materials as outlined in Table 2.1 were used, all used as received. The in this research used deionized-water (DI-water) was obtained from the PURELAB Option water purification system of ELGA.

Table 2.1 – Chemicals and materials used in this research, including source and purity (when relevant).

Chemicals/ materials	**Source**
(3-Mercaptopropyl)trimethoxysilane (95%)	Sigma-Aldrich
3, 4-Ethylenedioxythiophene (97%)	Sigma Aldrich
Acetonitrile (HPLC grade)	Fisher Scientific
Ammonium perchlorate (>98%)	Fluka
Aniline (≥99.5%)	Sigma-Aldrich
Chloroform	Fisher
Glycerol	Fisher Scientific
Microscope glass slides	Fisher Scientific
Propan-2-ol	Fisher Scientific
Pyrrole (98%)	Sigma-Aldrich
Sulphuric acid (>95%)	Fisher Scientific
Tetrabutylammonium perchlorate (99%)	Acros Organics

2.3. Results

To get insight in the influence of an applied potential on the polymer film, the change in hydrophobicity, roughness, composition and morphology by applying a potential were investigated. First the electropolymerisation of the polymer films is discussed, whereby the film was as smooth as possible in order to prevent the droplet (used for contact angle measurements) from being influenced by irregularities. Subsequently, the characteristics of the polymer films and their potential driven changes are discussed.

2.3.1. Electrodepositing and characterization of conductive polymers

The polyaniline, polypyrrole and PEDOT films were electrochemically grown on gold coated microscopic slides using cyclic voltammetry as shown in Figure 2.9. The films were grown until a homogeneous covered film was obtained, as judged by eye. To minimise the variability between the experiments and type of films, the charge and obtained thickness were monitored. However, the calculated thicknesses based on the charge (Faraday's law; Chapter 1, Section 1.6.1.) were generally slightly smaller than the measured thicknesses. This could be explained by a few factors. First, only a small amount of the film was accessible by the charge. Second, the substrate could have been inhomogeneously covered by the polymer, such that the physical thickness was measured on a thick or thin part of the film while the thickness calculations were based on the average film layer. Although this effect should probably have been visible by eye/microscopic inspection. The third scenario is the buckling phenomenon, by buckling of the polymer film the calculated thicknesses would be smaller than the measured thickness. Additionally, the physical film thickness measurements were performed by scratching the film after which the height difference between the scratch (assumed to be the substrate) and the film was measured. This method could also lead to a discrepancy as the film close to the scratch could peel off/bend and the substrate could also have been scratched.

A.

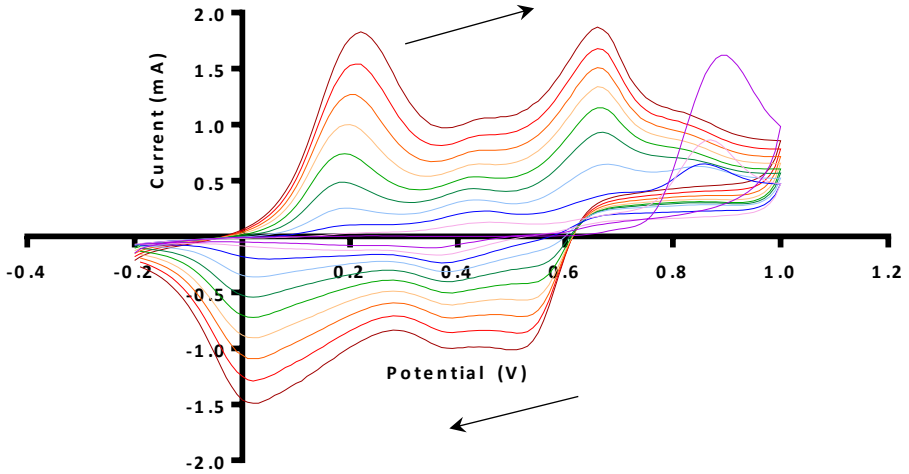

B.

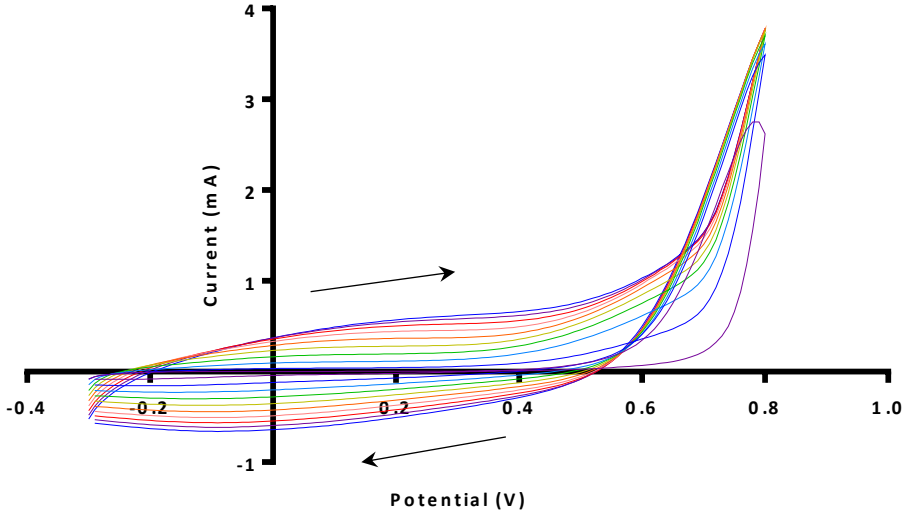

C.

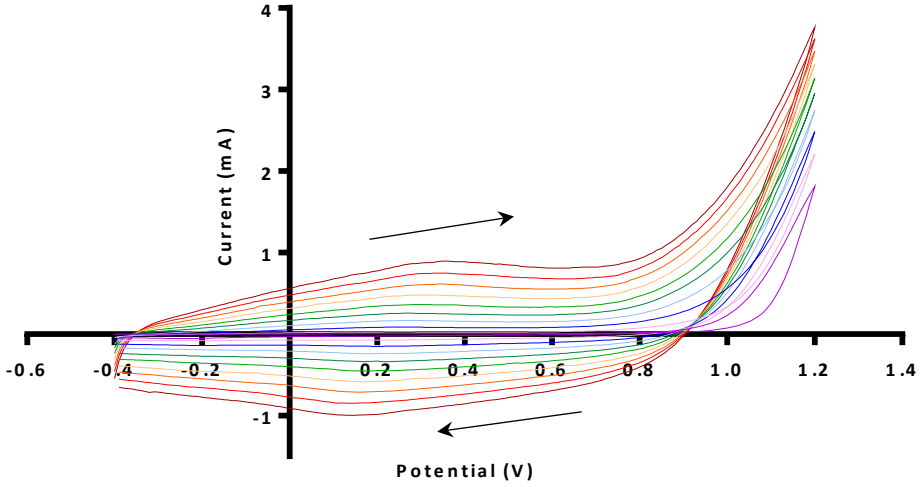

Figure 2.9 – Cyclic Voltammogram of a polyaniline (**A**), polypyrrole (**B**) and PEDOT (**C**) growth on a gold coated glass microscope slide.

The formation of the polymer film was, besides the colour change by oxidising/reducing the film as discussed in Section 2.3.2, also confirmed using FTIR (Figures 2.10-2.12). The pattern of peaks is consistent with that observed for an electrochemically grown polymer film in the literature [27-38] and could also be explained using general FTIR tables [39-43], although some discrepancies were observed, as briefly outlined in the Appendix (Section A.2).

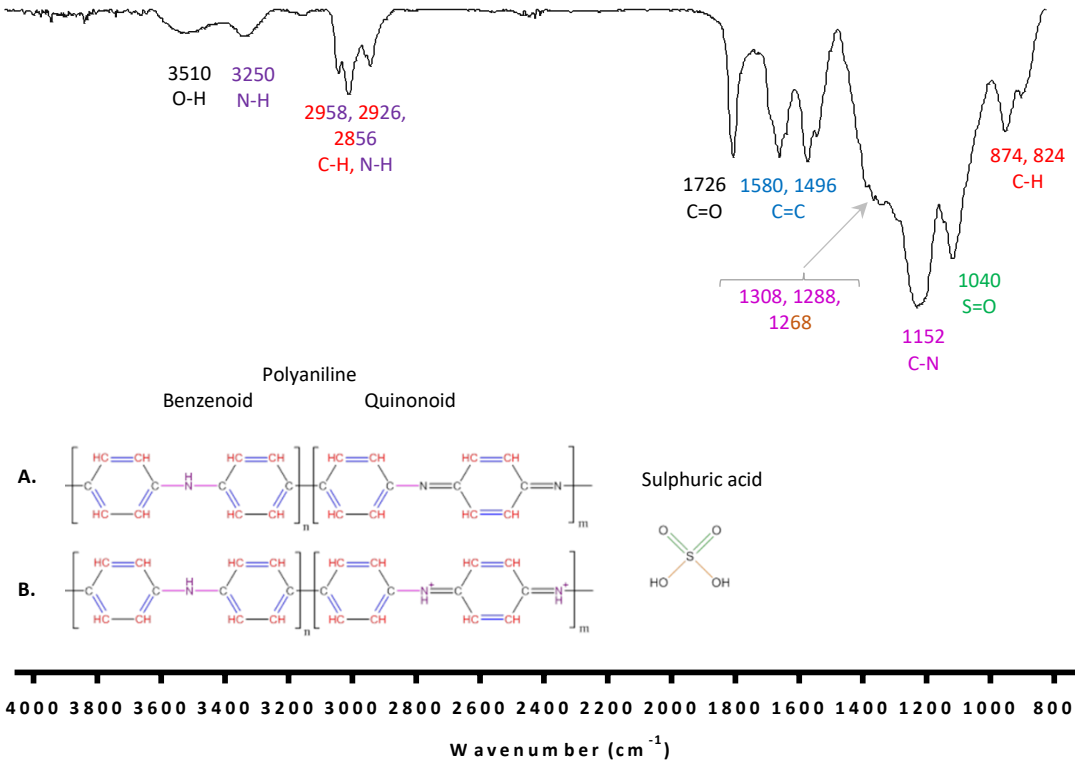

Figure 2.10 – FTIR spectrum of a polyaniline film (baseline corrected) with suggested peak annotations corresponding with the colours of the molecular structures of the polymer polyaniline and electrolyte sulphuric acid. The benzenoid configuration (left), quinonoid configuration (right), neutral form (**A**) and protonated form (**B**) of polyaniline are shown.

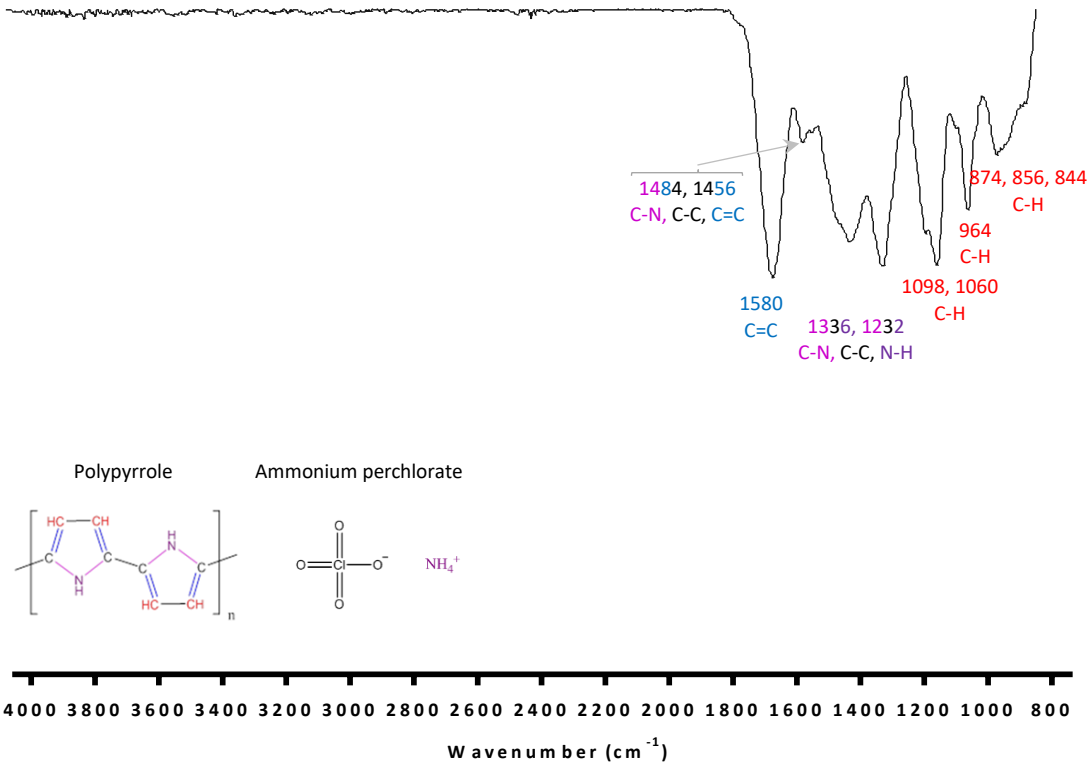

Figure 2.11 – FTIR spectrum of a polypyrrole film (baseline corrected) with suggested peak annotations corresponding with the colours of the molecular structures of polypyrrole and the electrolyte ammonium perchlorate.

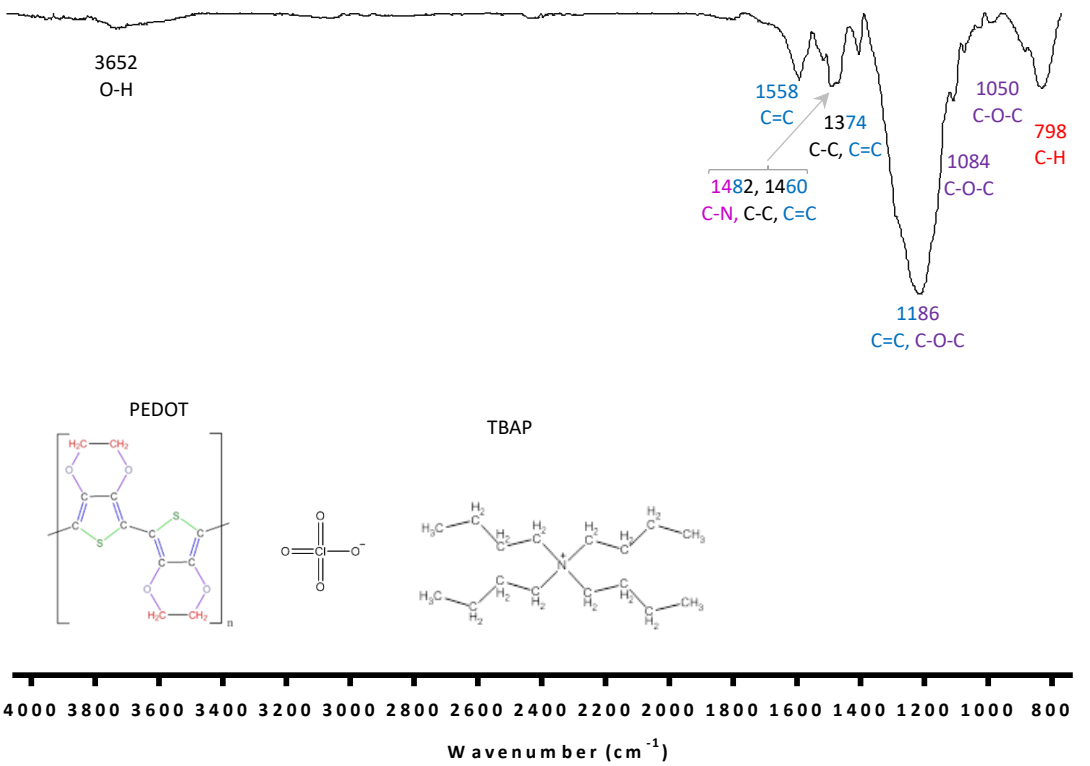

Figure 2.12 – FTIR spectrum of a PEDOT film (baseline corrected) with suggested peak annotations corresponding with the colours of the molecular structures of PEDOT and the electrolyte TBAP.

2.3.2. Morphological and compositional changes by oxidising or reducing of conductive polymer films

To determine the effect of an applied potential on the morphology and composition of the polymer films, the polymer films were oxidised (or reduced) in monomer and electrolyte solution after which they were removed from the solution and inspected using the optical (3D) microscope. As shown in Figure 2.13, the polymer films changed colour between reduced and oxidised state.

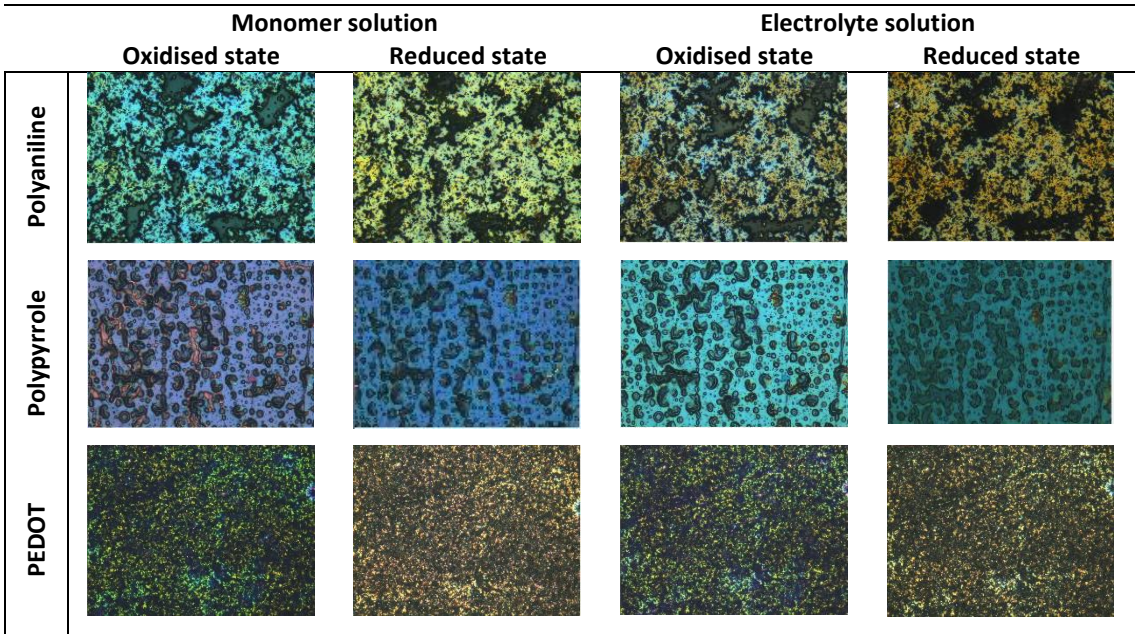

Figure 2.13 – Images of polyaniline, polypyrrole and PEDOT films after oxidising and reducing in monomer or electrolyte solution. Images were taken of an area of 190x143 µm using the optical (3D) microscope.

These colour changes (during redox switching) can be used as an indication for the formation of oxidised or reduced states. In addition, the slightly less prominently detectable colour change observed after cycling in electrolyte solution (in comparison to monomer solution) suggests that the composition of the already present polymer layer changed and that a fresh polymer layer (created by cycling in monomer solution) increased the colour changing effect but is not a requirement.

A more consistent colour switch was obtained for polyaniline (blue to green) and PEDOT (blue/green to orange) than for polypyrrole. The less-reversible and less consistent colour change is known for polypyrrole, possibly caused by colour fading over time and/or absence of a colour change using thick films (>1 µm). [44] Although some studies

showed reversibility whereby the colour generally changed from yellow in reduced state to blue/violet [45] or blue/black [46, 47] in oxidised state. The differences in electrolyte composition and slightly in monomer composition could possibly explain the variation in observed colours.

Although the measurements were taken in real colour, due to the nature of the optical (3D) microscope technique, reflection of light could have influenced the observed colour. In addition, variation in thickness within one polymer film could result in a multi-coloured image.

To conclude, changes in colour were observed by redox switching which suggests possible changes in composition. Besides that, no distinct morphological changes were observed.

2.3.3. Potential driven roughness changes of conductive polymer films

The roughness of a polymer film is of importance to obtain understanding about potential driven topographical changes of the polymer film as well as for the interpretation of the contact angle measurements used to determine the hydrophobicity of the polymer film. The latter, due to the possible influence of irregularities on the movement of the droplets used for contact angle measurements.

Before potential driven roughness changes of polymer films were determined, the possible influence of wetting, caused by the film formation and the contact angle measurements, on the roughness measurements was investigated.

2.3.3.1. Influence of wetting on the roughness

To determine the influence of wetting on the roughness measurements, the roughness of a polyaniline film was measured directly after electrodeposition and followed over time, including during the drying procedure (30 min in oven at 60 ^{o}C and 5 min in THF). As shown in Figure 2.14 no notable differences in roughness were obtained during the drying process.

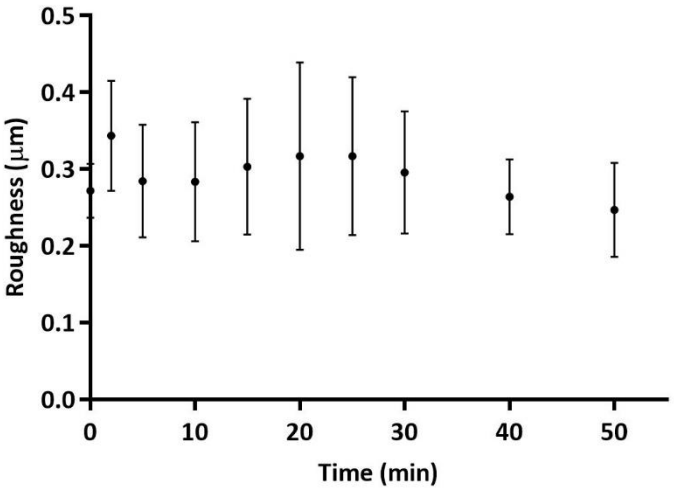

Figure 2.14 – Roughness of a polyaniline film directly after electropolymerisation and followed over time, after 30 min in the oven at 60 °C and 5 min in tetrahydrofuran (THF). Measurements were taken of an area of 190x143 µm using the optical (3D) microscope.

To determine the influence of wetting caused by a water droplet on the surface (used for contact angle measurements) on the roughness measurements, the roughness of a polyaniline film was measured before, during and after the deposition of a water droplet. As shown in the wetted right-top corner of Figure 2.15, wetting of the polymer film decreased the roughness slightly (0.88 to 0.85 µm). However, the variation in roughness values within one film (0.88 versus 0.98 µm; Figure 2.15A) and on the dry area of the surface (0.98, 0.92 and 0.88 µm) was larger than the change in roughness caused by wetting, suggesting the effect of wetting on the roughness was negligible.

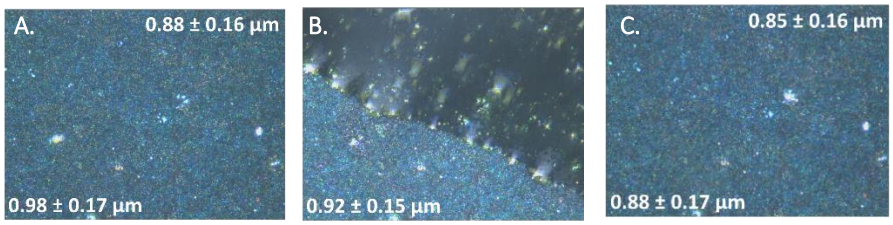

Figure 2.15 – Roughness of a polyaniline film before (**A**), during (**B**) and after (**C**) positioning a droplet on top. The S_a roughness values are positioned in the areas in which the roughness is measured. Images were taken of an area of 190x143 µm using the optical (3D) microscope.

To conclude, the influence of wetting both caused by a water droplet (used for contact angle measurements) and by in solution film formation on the roughness seems to be negligible. This suggest that the film formation or contact angle measurements could be followed by roughness measurements.

2.3.3.2. Influence of the electronic state of the polymer films on the roughness

The effect of an applied potential on the roughness of the polymer film was determined to obtain understanding about potential driven roughness changes as well as to determine the impact of potential driven roughness changes on the contact angle measurements used to determine potential driven hydrophobicity changes.

To determine the influence of an applied potential on the roughness of the polymer films, the polymer films were cycled in monomer or electrolyte solution and removed from solution when they were in oxidized or reduced state (as illustrated in Figure 2.5B) after which roughness measurements were performed. As shown in Figures 2.16-2.18, the roughness was generally higher in oxidized than in reduced state. Although the difference in roughness between both states was in some circumstances, such as the polypyrrole film in monomer solution (Figure 2.17A), rather small. Additionally, no consistent difference between the films cycled in monomer and electrolyte solution were obtained.

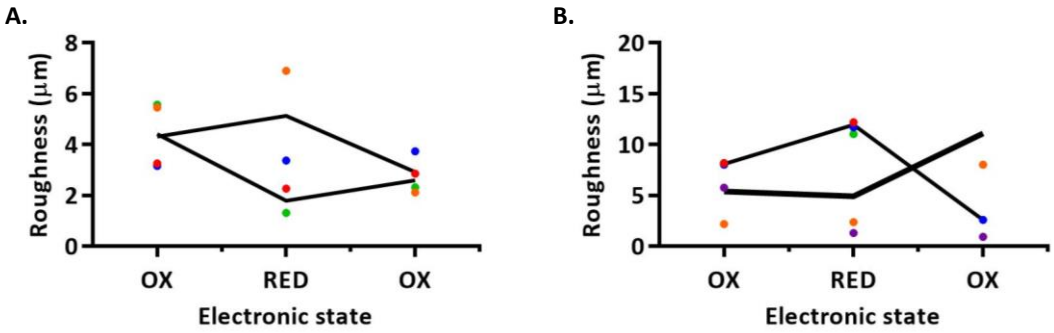

Figure 2.16 – Roughness of polyaniline oxidised and reduced films after cycling in monomer (**A**) or electrolyte (**B**) solution. The black lines are there to guide the eye, whereby the thickness of the line indicates the strength of the trend. Each colour per graph corresponds to another experiment.

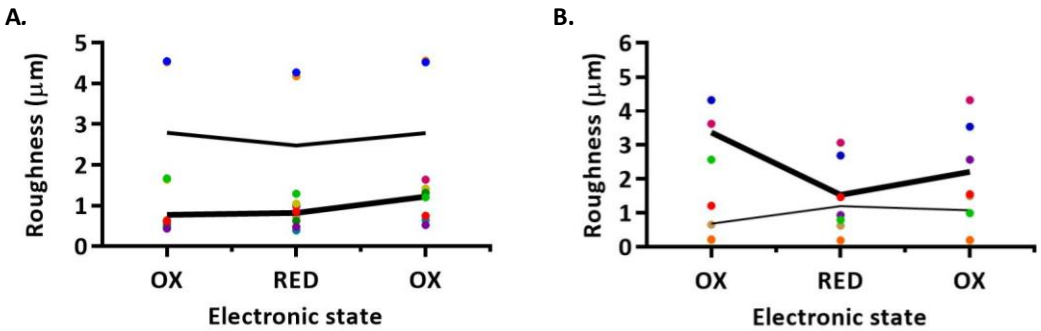

Figure 2.17 – Roughness of polypyrrole oxidised and reduced films after cycling in monomer (**A**) or electrolyte (**B**) solution. The black lines are there to guide the eye, whereby the thickness of the line indicates the strength of the trend. Each colour per graph corresponds to another experiment.

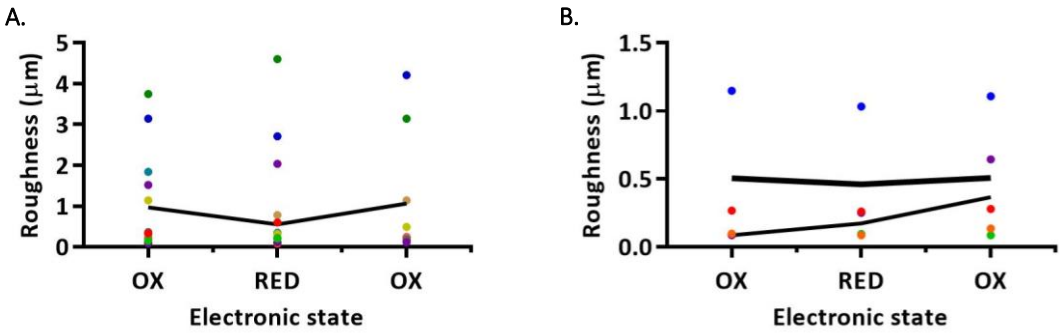

Figure 2.18 – Roughness of PEDOT oxidised and reduced films after cycling in monomer (**A**) or electrolyte (**B**) solution. The black lines are there to guide the eye, whereby the thickness of the line indicates the strength of the trend. Each colour per graph corresponds to another experiment.

The difference in roughness between the oxidized and reduced state was just above or similar to the standard deviation of the Zeta calibration reference sample. To minimize the amount of variation, where possible, the measurements of the oxidised and reduced polymer films were performed on the same location. In addition, despite the fact that the roughness values were close to the detection limit of the optical (3D) microscope (lower limit) and AFM (upper limit), test measurements using both techniques showed similarities in trends, therefore the trend is probably real and not an artifact.

The trend of increasing roughness by oxidising is in agreement with the study of Chang *et al.* [48] but differs from the research of Isaksson *et al.* [49] in which no difference in roughness between the reduced and oxidized state of a polyaniline film was observed. This could be caused by the different ways of film formation, applying a potential and/or electrolyte as outlined in Chapter 1 (Table 1.7).

To get a better understanding of the differences in roughness between the oxidized and reduced states, the location and development of the irregularities was followed over a few cycles by comparing cross-sections obtained using the optical (3D) microscope as shown in Figure 2.19. The roughness changed by the enlargement of grooves/hills or by filling of the spaces between the irregularities (smoothing of the surface). No clear differences in trends were observed between cycling in electrolyte and monomer solution. With respect to the interpretation of the cross-sections, it is important to keep in mind that small shifts (mainly horizontally) between the measurements could occur due to the nature of the analysis.

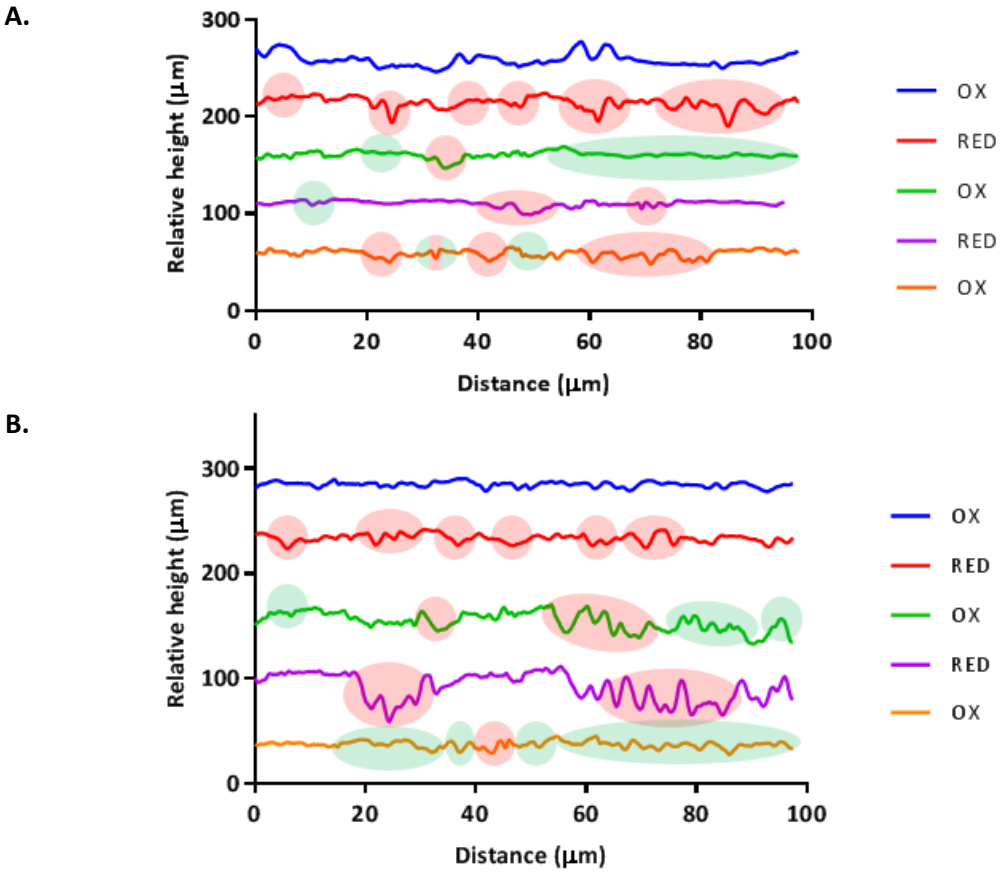

Figure 2.19 – Cross-sections of a polyaniline film in oxidised or reduced state over a few cycles, both measured after cycling in monomer (**A**) and electrolyte solution (**B**). The red and green coloured dots indicate a decrease and increase in height of the irregularities, respectively.

2.3.4. Potential driven hydrophobicity changes of conductive polymer films

To get insight in potential driven hydrophobicity changes of the polymer films, the hydrophobicity of a polymer film in reduced state was compared to the oxidised state. To determine the hydrophobicity, contact angle experiments were performed with varying droplet compositions (chloroform, glycerol and water). The choice of liquid was based on the density, solubility and polarity of the surrounding medium/solvent to ensure the droplet stayed on the surface (to prevent floating and dissolving in the surrounding liquid) and had a reasonable shape (not completely spread to allow changing contact angle). The effect of the droplet properties and surrounding medium on the spreading of the droplet is outlined in Figure 2.20 for neutral, hydrophobic and hydrophilic polymer films. Due to the use of non-aqueous droplets, the wettability is not directly related to the interaction with water. Therefore, the terms lyophobicity and lyophilicity were used in the experiments using non-aqueous droplets. Based on the

differences in polarity of the droplet compared to the surrounding medium, the terms were subsequently translated into the terms hydrophobicity and hydrophilicity for simplicity and comparison purposes, as outlined in Figure 2.20.

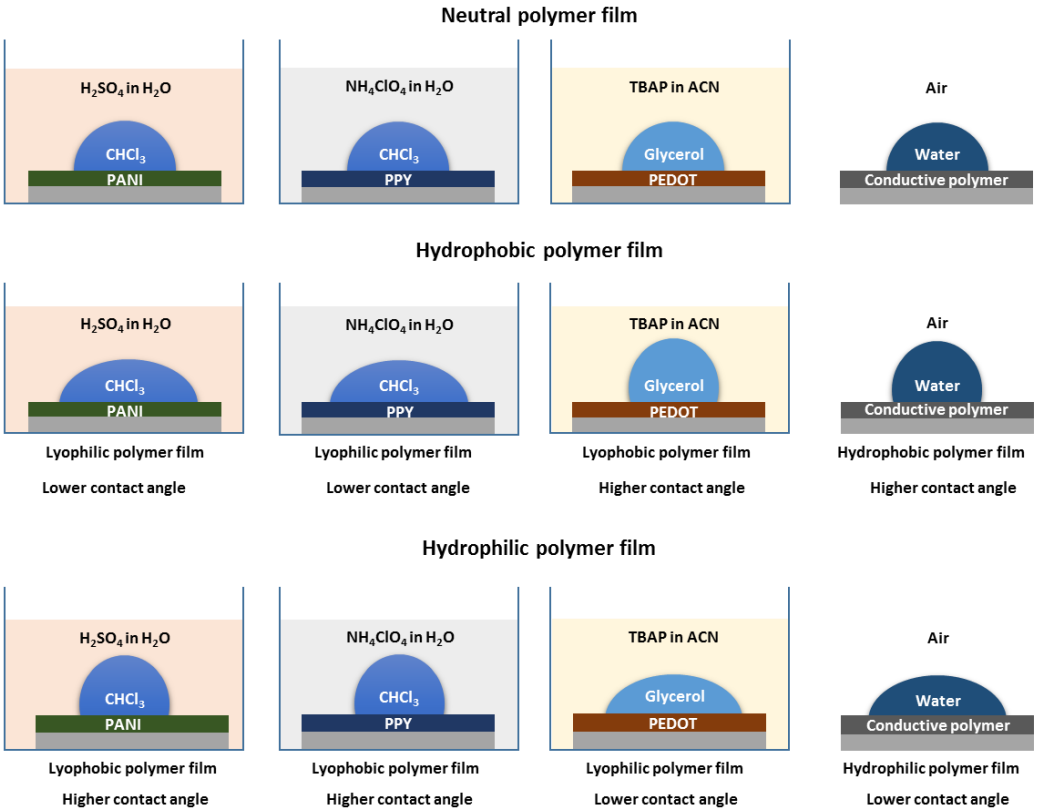

Figure 2.20 - Influence of the hydrophobicity of the polymer films on the amount of spreading of the droplet compared to a neutral polymer film. For the non-aqueous droplets the terms lyophobicity and lyophilicity were used and subsequently translated into the terms hydrophobicity and hydrophilicity based on the polarity of the droplet compared to the surrounding medium.

Two types of contact angle measurement experiments were performed, ex-situ and in-situ. In the ex-situ experiments, the polymer films were removed from solution after oxidising/reducing to determine the hydrophobicity and roughness sequentially under similar circumstances. By removal from the solution, the films could dry resulting in a lower water content and possibly different hydrophobicity. Therefore in-situ experiments were additionally performed by positioning droplets on the oxidised or reduced polymer films, while still being in the monomer or electrolyte solution.

2.3.4.1. In-situ contact angle measurements

To determine the hydrophobicity of the polymer films during electrodeposition, the contact angles of chloroform droplets on polyaniline and polypyrrole films and glycerol droplets on PEDOT films were measured.

In monomer solution the contact angle generally increased by oxidising the polyaniline and polypyrrole films (Figure 2.21A-D) and reducing the PEDOT films (Figure 2.21E, F) meaning the surface became more lyophobic. Translated to hydrophobicity, it means that the hydrophilicity of all three polymer films increased by oxidising and decreased by reducing the film. The less consistent and slightly contrary trend observed in electrolyte solution suggests that the formation of a new layer might be of influence.

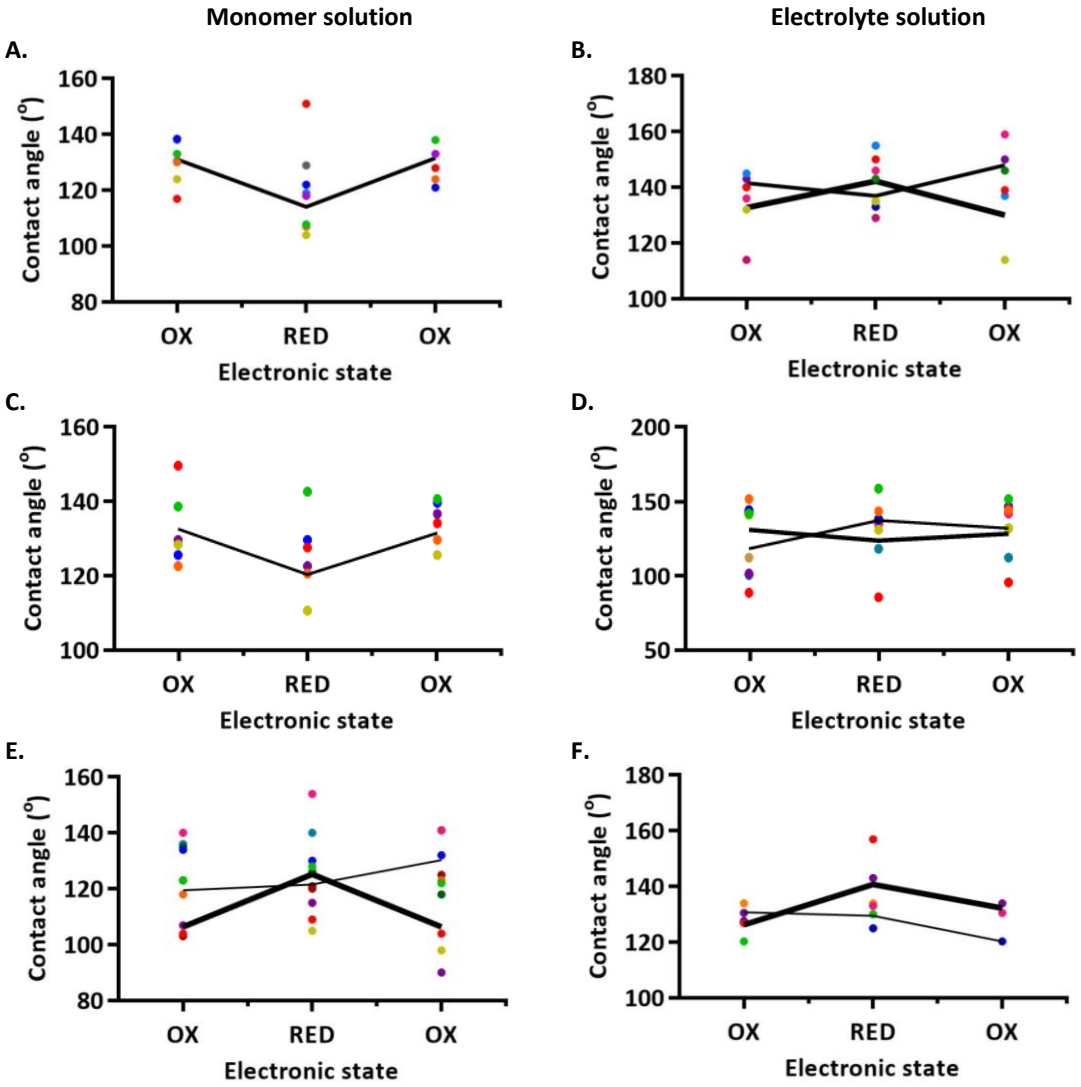

Figure 2.21 – Contact angles of droplets on polyaniline (**A, B**), polypyrrole (**C, D**) and PEDOT (**E, F**) oxidised and reduced films after cycling in monomer (**A, C, E**) or electrolyte (**B, D, F**) solution, measured in-situ. The black lines are there to guide the eye, whereby the thickness of the line indicates the strength of the trend. Each colour per graph corresponds to another experiment.

The higher hydrophilicity on the oxidised films compared to the reduced films was in agreement with the studies of Habib *et al*. [50] and Hato [51], partly supported by the study of Isaksson *et al.* [49] and opposite to the studies of Chang *et al.* [48] and Halldorsson *et al.* [52]. The differences between these studies with respect to the formation of the polymer film, the way of applying the potential and determining hydrophobicity (outlined in Chapter 1, Table 1.7) suggest that the hydrophobicity of a polymer film is probably sensitive to these aspects.

To investigate the difference in hydrophobicity more thoroughly, not only the hydrophobicity of polymer films in oxidised and reduced state were compared, but the droplets were also followed during the oxidation/reduction process. A droplet was positioned on the polymer film and left at the same position while cycling further. As reference, a new droplet was positioned on the polymer film every half a cycle, so when the polymer film was fully oxidised or reduced. In Figure 2.22 the droplets that were left on the polymer film during cycling are placed in the same column, so a droplet positioned on the oxidised polyaniline film has a contact angle of 135°, by reduction of the film the contact angle of this droplet decreased to 133°, while the contact angle of a newly positioned droplet was 102°. Overall, the contact angle of the droplet left on the polymer film appeared to change only slightly during oxidation/reduction of the film and remained closer to the initial contact angle (of this droplet in the former electronic state) than to the contact angle of the newly positioned droplet (in current electronic state) as shown in the examples of Figure 2.22.

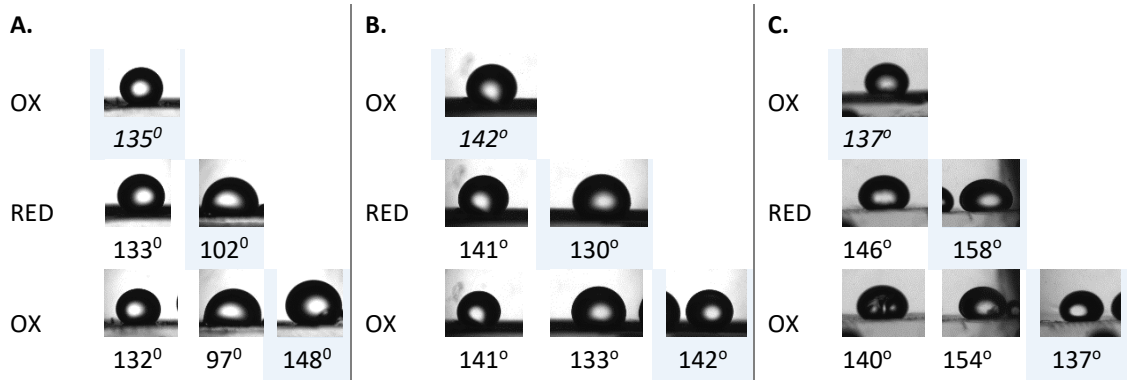

Figure 2.22 – Typical contact angles of droplets on polyaniline (**A**), polypyrrole (**B**) and PEDOT (**C**) oxidised and reduced films, measured in situ. Per film each column represents the same droplet which stays on the film during oxidising/reducing the film, newly positioned droplets have a blue background and still present droplets have a white background.

The limited amount of change in contact angle of the droplets that stay on the polymer film while cycling further indicates that when a droplet is covering the polymer film, the covered layer does not undergo a change in lyophobicity. This could possibly be caused by no/limited change in electronic state or it could be that the droplet is well adhered to the polymer film. An illustration of the lack of change of the polymer film in the area underneath the droplets by cycling further is shown in Figure 2.23. A chloroform droplet positioned on an oxidised film has a dark colour underneath, by reducing the film the colour underneath the droplet remained dark while the surrounding polymer film became yellow/green (Figure 2.23A, droplet left). Subsequently a new chloroform droplet was positioned on the oxidised film (Figure 2.23A, droplet right), after oxidising the film, the area underneath this droplet remained yellow/green (Figure 2.23B, droplet right) while the surrounding polymer film changed colour.

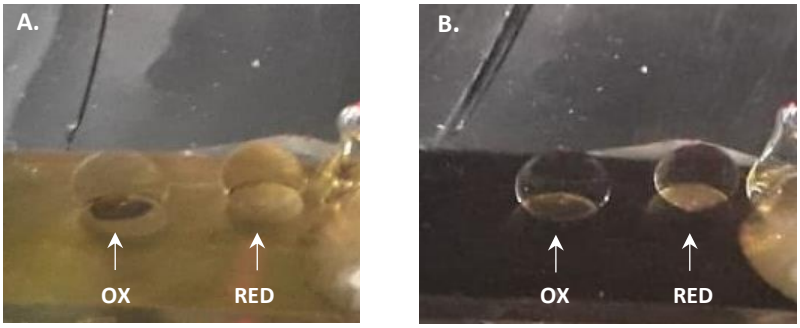

Figure 2.23 – Chloroform droplets on a polyaniline film in reduced (**A**) and oxidised (**B**) state, after cycling in monomer solution. The left and right droplets on both the reduced and oxidised film were positioned on the film when being in oxidised and reduced state, respectively.

2.3.4.2. Ex-situ contact angle measurements

To determine the hydrophobicity and roughness sequentially under similar circumstances, ex-situ contact angle measurements were performed. Similar to the in-situ experiments, the polymer films were oxidised and reduced both in monomer and electrolyte solution. After which the polymer films were removed from the solution to determine the roughness (Section 2.3.3.2) and hydrophobicity of the polymer films.

As shown in Figure 2.24 less obvious trends were observed in the ex-situ experiments compared to the in-situ experiments (in which the hydrophobicity generally increased by reduction). Be aware that here an increase in contact angle corresponds to a higher hydrophobicity. A slight increase in hydrophobicity by reduction was observed on the polyaniline films in Figure 2.24B while the PEDOT films in Figure 2.24E show no clear difference in contact angle between the oxidised and reduced film. Given the slightly clearer trends using the more thorough dried polyaniline films compared to the polypyrrole and PEDOT films, the lower consistency in the ex-situ measurements compared to the in-situ measurements could possibly be caused by the influence of the drying process on the hydrophobicity.

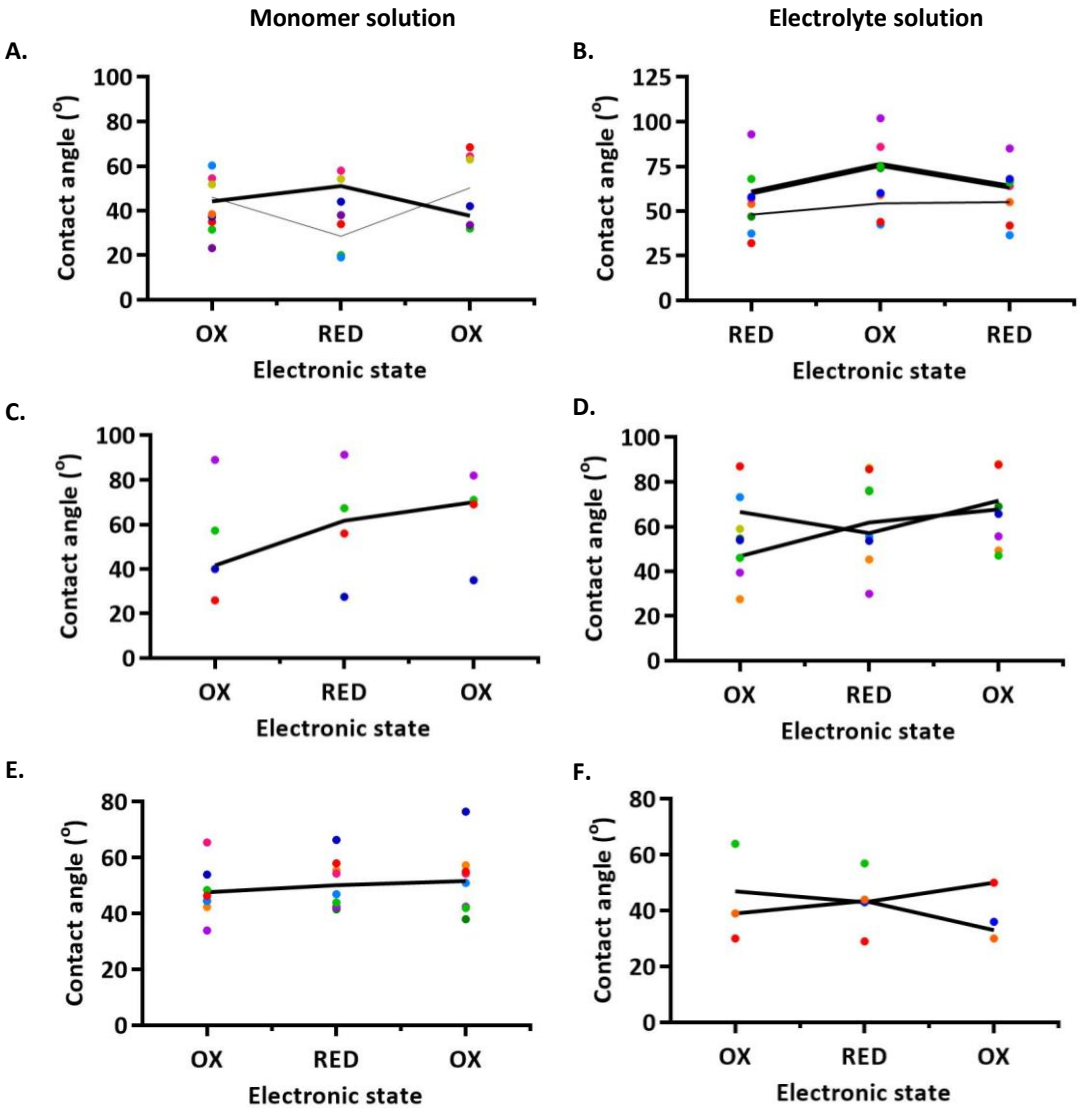

Figure 2.24 – Contact angles of water droplets on reduced and oxidised polyaniline (**A, B**), polypyrrole (**C, D**) and PEDOT (**E, F**) films after cycling in monomer (**A, C, E**) or electrolyte (**B, D, F**) solution, measured ex-situ. The black lines are there to guide the eye, whereby the thickness of the line indicates the strength of the trend. Each colour corresponds to another experiment.

2.3.5. Influence of roughness on the contact angle measurements

Irregularities of the polymer films could impact the movement of droplets (used for contact angle measurements) and thereby the determination of the hydrophobicity of the polymer films. To define the influence of roughness on the contact angle measurements, the measured contact angles were compared with calculated contact angles corresponding to an ideal smooth surface. The latter were calculated using the Wenzel and Cassie-Baxter models. The use of these models is justified because the droplet size (5 µL droplet typically covers an area of 0.5-3 mm^2) is more than 40 times larger than the roughness (typically <15 µm; Figures 2.16-2.18). [53, 54]

To determine what the contact angle would have been if the polymer film was ideally smooth, also known as Young's contact angle (θ_Y), Equations 2.4 and 2.5 of the Wenzel and Cassie-Baxter model were used, respectively. In which the measured contact angles, which were possibly subjected to roughness, were called the Wenzel and Cassie-Baxter contact angles (θ_w and θ_{CB} respectively), the R-factor is a surface area correction factor and f_{solid} is the area fraction of the solid material between the grooves. In this research f_{solid} is simplified to the ratio (actual area-projected area)/actual area as described in Section 2.2.4.3.

$$\cos\theta_Y = \cos\theta_W / R\text{-}factor \qquad \textbf{Equation 2.4}$$

$$cos\ \theta_Y = \frac{\cos\theta_{CB} + (1 - f_{solid})}{f_{solid}} \qquad \textbf{Equation 2.5}$$

As shown in Figure 2.25A, by oxidising the film (light blue to light red dots) both the roughness and the Wenzel contact angles increased (moved away from 90°) which is in agreement with the Wenzel theory, this suggests an influence of roughness on the contact angle. In addition, the measured Wenzel contact angles show a larger difference between the oxidised and reduced film than Young's contact angles as illustrated by the green and purple arrow in Figure 2.25A respectively. This implies that by removal of the influence of roughness the difference between the contact angles of both states decreases, suggesting that according to the Wenzel model the roughness has an influence on the contact angle. As there is still a difference present between the Young's contact angles on the oxidised and reduced film it is suggested that other factors such as charge might have an influence on the hydrophobicity as well.

Contrary to the Wenzel model, the application of the Cassie-Baxter model resulted in a larger difference between the contact angles on oxidised and reduced films on the ideal smooth surface compared to the rough measured surface (Figure 2.25B). This suggests that the difference in contact angles is less affected by the roughness than by other factors such as charge, which is contrary to the observations based on the Wenzel model.

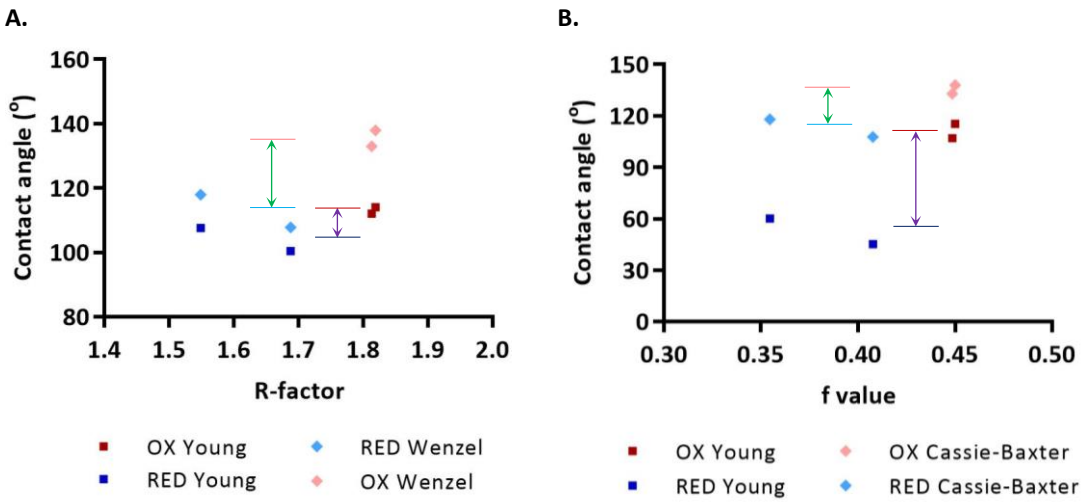

Figure 2.25 – Relation between roughness (R-factor, f-value) and contact angle on a polyaniline film, the latter was measured in-situ in monomer solution. The Wenzel (**A**) and Cassie-Baxter (**B**) contact angles correspond to the measured contact angles, the Young's contact angles to the calculated contact angles based on the Wenzel (**A**) and Cassie-Baxter (**B**) model. Purple and green arrow indicate the ox-red couple on a rough (Wenzel) and smooth (Young) film respectively. Both graphs were based on the same dataset.

As both Figure 2.25 A and B were based on the same dataset it can be concluded that in these measurements an increase in f-value (0.35 to 0.45) relates to an increase in R-factor (1.5 to 1.8) which corresponds to an increase in roughness while a f-value of 1 corresponds to an entirely smooth surface. This could be explained by the absence of a linear relation between f-value and roughness, perhaps the roughness increases by decreasing f-values from 1 to 0.5 and increasing f-values from 0 to 0.5. Additionally, the geography could be of importance for the interpretation of the f-values. It has to be noted that these speculations are based on a limited amount of data and therefore possibly not reliable.

In addition, limitations of the Wenzel equation were discussed using Figure 2.26. On the reduced polypyrrole film (light blue dots) the contact angle decreased (moved away from 90°) by increasing roughness which is in agreement with the Wenzel theory. This resulted in a constant Young's contact angle of 70° and thereby establishment of the hydrophobicity of the reduced film. On the other hand, the oxidised film showed a relatively constant contact angle by increasing roughness, resulting in a range of Young's contact angles and undefined influence of roughness on the contact angle measurements.

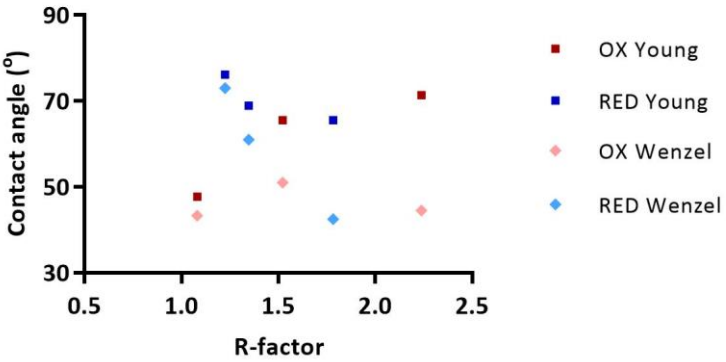

Figure 2.26 – Relation between roughness (R-factor) and contact angle on a polypyrrole film, measured ex-situ after cycling in monomer solution. The Wenzel contact angles correspond to the measured contact angles and the Young's contact angles to the calculated contact angles based on the Wenzel model.

To conclude, both models might give an indication about the influence of roughness on the contact angle but might not be appropriate for all films and/or several other unknown factors might influence the contact angle measurements. Another model, including other factors than roughness only would be of benefit.

2.4. Conclusion

This research aimed to obtain insight into potential driven interfacial energy changes, in which the effects of applying a potential onto a surface were investigated. To get a complete overview of the impact of a potential on a surface, potential driven changes in characteristics of conductive polymer films were determined, focussing on the hydrophobicity, composition, morphology and topography.

This study showed that the surface characteristics, hydrophobicity, composition and topography (roughness), could be tuned to a small or large extent (Obj. 1). Regarding the hydrophobicity of the polymer films, the in-situ contact angle measurements demonstrated that the polymer films were generally more hydrophilic in oxidised state than in reduced state as well as the roughness increased slightly by oxidising the polymer film. Although this was not observed under all circumstances and the ex-situ contact angle measurements showed less obvious trends compared to the in-situ measurements. Additionally, by applying a potential, the colour of the polymer film changed which was used as an indication that the electronic state of the polymer had changed and thereby its composition; the formation of a new polymer layer enlarged the colour changing effect but was no requirement. Besides this colour change no distinct morphological changes were observed during oxidation and reduction.

To justify sequential use of surface analysis and film formation techniques, the impact of the surface formation and analysis techniques on each other was investigated by determining the influence of wetting caused by a droplet (used for contact angle measurements) and by in solution film formation on the roughness measurements (Obj. 2). Wetting showed to have a negligible influence on the roughness measurements, therefore sequential contact angle and roughness measurements as well as film formation followed by roughness measurements could be performed.

In addition, the influence of potential driven topographical (roughness) changes of the polymer film on the contact angle measurements was investigated using several models (Obj. 3). This is of importance for the interpretation of contact angle measurements, used to determine the hydrophobicity, because they could be influenced by chemical/molecular factors such as polarity but also by physical/macroscopic factors

such as roughness of the polymer film. The simultaneous increase in roughness and change in contact angle (moved away from 90^{o}) by oxidising a polyaniline and polypyrrole film is in agreement with the Wenzel theory which describes that the hydrophobicity/hydrophilicity will be enlarged by increasing influence of roughness. This indicates that the roughness had an impact on the contact angle measurements. In addition, it was shown that the difference in contact angle between the oxidised and reduced films decreased notably by removal of the influence of the roughness, according to the Wenzel equation. This suggests that roughness is one of the main factors causing the difference in contact angle between the oxidised and reduced film. Given that there was still a difference in contact angle between the oxidised and reduced ideal smooth film, other factors apart from roughness may also have an influence on the contact angle. Contrary to this, the Cassie-Baxter model implied that the contact angles were less affected by the roughness than by other factors, such as possibly charge. This suggests that both models give an indication about the influence of roughness but might not be appropriate for all films/circumstances and another model might be of benefit. This was also implied by the undefined influence of roughness and undefined Young's contact angles in some datasets.

To conclude, the application of a potential can potentially be used to tune characteristics of a polymer film such as the composition and hydrophobicity and to a lesser extent roughness. The changes in contact angles (used to determine the hydrophobicity) could also be influenced by the roughness as well as other so far unknown factors.

2.5. References

[1] A.G. Macdiarmid, Nobel Prize 2000 Lecture "Synthetic metals": a novel role for organic polymers, Current Applied Physics I, (2001) 269-279.
[2] H.H. Khaligh, K. Liew, Y. Han, N.M. Abukhdeir, I.A. Goldthorpe, Silver nanowire transparent electrodes for liquid crystal-based smart windows, Solar Energy Materials & Solar Cells, 132 (2015) 337-341.
[3] R. Baetens, B.P. Jelle, A. Gustavsen, Properties, requirements and possibilities of smart windows for dynamic daylight and solar energy control in buildings: a state-of-the-art review, Solar Energy Materials & Solar Cells, 94 (2010) 87-105.
[4] R. Brooke, J. Edberg, D. Iandolo, M. Berggren, X. Crispin, I. Engquist, Controlling the electrochromic properties of conductive polymers using UV-light, Journal of Materials Chemistry C, (2018).
[5] H. Cheng, Y. Zhang, Method and device for fabricating flexible display device, BOE Technology Group Co Ltd United States, 2013.
[6] A. Tröls, H. Enser, B. Jakoby, Modeling and fabrication of low-cost electrowetting actuators for flexible microfluidic display applications, Sensors, (2016).
[7] R.E. Wiley, Conductive coatings and foams for anti-static protection, energy absorption, and electromagnetic compatability, Archeson Ind Inc, United States, 1989.
[8] F. Jonas, J.T. Morrison, 3,4-Polyethylenedioxythiophene (PEDT): conductive coatings technical applications and properties, Synthetic Metals, 85 (1997) 1397-1398.
[9] J.L. Camalet, J.C. Lacroix, S. Aeiyach, P.C. Lacaze, Characterization of polyaniline films electrodeposited on mild steel in aqueous p-toluenesulfonic acid solution, Journal of Electroanalytical Chemistry, 445 (1998) 117-124.
[10] A. Talo, P. Passiniemi, O. Forsén, S. Ylăsaari, Polyaniline/epoxy coatings with good anti-corrosion properties, Synthetic Metals, 85 (1997) 1333-1334.
[11] S. Sathiyanarayanan, S. Muthukrishnan, G. Venkatachari, D.C. Trivedi, Corrosion protection of steel by polyaniline (PANI) pigmented paint coating, Progress in Organic Coatings, 53 (2005) 297-301.
[12] A.J. Dominis, G.M. Spinks, G.G. Wallace, Comparison of polyaniline primers prepared with different dopants for corrosion protection of steel, Progress in Organic Coatings, 48 (2003) 43-49.
[13] D.E. Tallman, G. Spinks, A. Dominis, G.G. Wallace, Electroactive conducting polymers for corrosion control. Part I General Introduction and a review of non-ferrous metals, Journal of Solid State Electrochemistry, 6 (2002) 73-84.
[14] G.M. Spinks, A.J. Dominis, G.G. Wallace, D.E. Tallman, Electroactive conducting polymers for corrosion control. Part II Ferrous metals, Journal of Solid State Electrochemistry, 6 (2002) 85-100.
[15] Federal Aviation Administration, Chapter 15: Ice and Rain Protection, Aviation Maintenance Technician Handbook - Airframe Volume 12012.
[16] Shaping the future of aerospace, hydrophobic coating being developed to prevent ice build-up on aircraft, 2012.
[17] K. Fukuda, J. Tokunaga, T. Nobunaga, T. Nakatani, T. Iwasaki, Y. Kunitake, Frictional drag reduction with air lubricant over a super-waterrepellent surface, Journal of Marine Science and Technology, 5 (2000) 123-130.
[18] F. Yi, J. Wang, X. Wang, S. Niu, S. Li, Q. Liao, Y. Xu, Z. You, Y. Zhang, Z.L. Wang, Stretchable and waterproof self-charging power system for harvesting energy from diverse deformation and powering wearable electronics, ACS NANO, 10 (2016) 6519-6525.
[19] Z. Fu, Z. Wei, X. Lin, T. Huang, A. Yu, Polyaniline membranes as waterproof barriers for lithium air batteries, Electrochimica Acta, 78 (2012) 195-199.
[20] K. Cherenack, L. van Pieterson, Smart textiles: Challenges and opportunities, Journal of Applied Physics, 112 (2012).

[21] S. Coyle, Y. Wu, K.-T. Lau, D. De Rossi, G. Wallace, D. Diamond, Smart nanotextiles: a review of materials and applications, MRS Bulletin, 32 (2007).
[22] E. Devaux, V. Koncar, B. Kim, C. Campagne, C. Roux, M. Rochery, D. Saihi, Processing and characterization of conductive yarns by coating or bulk treatment for smart textile applications, Transactions of the Institute of Measurement and Control, 29 (2007) 355-376.
[23] A.L. Beresford, A.R. Hillman, Electrochromic enhancement of latent fingerprints on stainless steel surfaces, Analytical chemistry, 82 (2009) 483-486.
[24] I. Zeta Instruments, Zeta-200 Optical profiler Operational Manual, 2012.
[25] R.N. Wenzel, Resistance of solid surfaces to wetting by water, Industrial & Engineering Chemistry, 28 (1936) 988-994.
[26] A. Cassie, S. Baxter, Wettability of porous surfaces, Transactions of the Faraday society, 40 (1944) 546-551.
[27] Y. Furukawa, F. Ueda, Y. Hyodo, I. Harada, T. Nakajima, T. Kawagoe, Vibrational spectra and structure of polyaniline, Macromolecules 21 (1988) 1297-1305.
[28] Z. Ping, In situ FTIR-attenuated total reflection spectroscopic investigations on the base-acid transitions of polyaniline. Base-acid transition in the emeraldine form of polyaniline Journal of the Chemical Society, Faraday Transactions, 92 (1996) 3063-3067.
[29] M. Ahson Habib, S.P. Maheswari, Electrochromism of polyaniline: an in situ FTIR study, Journal of The Electrochemical Society, 136 (1989).
[30] E.T. Kang, K.G. Neoh, K.L. Tan, Polyaniline: a polymer with many interesting intrinsic redox states, Progress in Polymer Science, 23 (1998) 277-324.
[31] Eisazadeh, Studying the characteristics of polypyrrole and its composites, World Journal of Chemistry, 2 (2007) 67-74.
[32] I. Cucchi, A. Boschi, C. Arosio, F. Bertini, G. Freddi, M. Catellani, Bio-based conductive composites: preparation and properties of polypyrrole (PPy)-coated silk fabrics, Synthetic Metals, 159 (2007) 246-253.
[33] N.V. Blinova, J. Stejskal, M. Trchová, J. Prokeš, M. Omastová, Polyaniline and polypyrrole: a comperative study of the preparation, European Polymer Journal 43 (2007) 2331-2341.
[34] H. Kato, O. Nishikawa, T. Matsui, S. Honma, H. Kokado, Fourier transform infrared spectroscopy study of conductlng polymer polypyrrole: higher order structure of electrochemically syntheslzed fllm, Journal of Physical Chemistry, 95 (1991) 6014-6016.
[35] P.S. Rao, J. Anand, S. Palaniappan, Effect of sulphuric acid on the properties of polyaniline-HCl salt and its base, European Polymer Journal, 36 (2000) 915-921.
[36] H. Xu, J. Wu, C. Li, J. Zhang, J. Liu, Investigation of polyaniline films doped with Fe3+ as the electrode material for electrochemical supercapacitors, Electrochimica Acta, 165 (2015) 14-21.
[37] L. Li, Y. Huang, G. Yan, F. Liu, Z. Huang, Z. Ma, Poly(3,4-ethylenedioxythiophene) nanospheres synthesized in magnetic ionic liquid, Materials Letters, 63 (2009) 8-10.
[38] C. Kvarnström, H. Neugebauer, S. Blomquist, H.J. Ahonen, J. Kankare, A. Ivaska, In situ spectroelectrochemical characterization of poly(3,4-ethylenedioxythiophene), Electrochimica Acta, 44 (1999) 2739-2750.
[39] National Institute of Standards and Technology US, NIST Chemistry WebBook, NIST Standard Reference Database Number 69.
[40] Q. Du, R. Superfine, E. Freysz, Y.R. Shen, Vibrational spectroscopy of water at the vapor/water interface, Physical Review Letters, 70 (1993) 2313-2316.
[41] G. Verkerk, J.B. Broens, P.A.M. de Groot, W. Kranendonk, J.L. Sikkema, J.J. Westra, I.M. Wevers-Prijs, Binas, Wolters-Noordhoff B.V. , Groningen, The Netherlands, 1998.
[42] G. Socrates, Infrared and raman characteristic group frequencies, Third ed., John Wiley & Sons, LtD, Chinester, 2001.
[43] Perkin Elmer, Polymer identification using mid infrared spectroscopy, Application Note Infrared Spectroscopy, 2011.

[44] P.R. Somani, S. Radhakrishnan, Electrochromic materials and devices: present and future, Materials Chemistry and Physics, 77 (2002) 117-133.
[45] F. Garnier, G. Tourillon, Organic conducting polymers derived from substituted thiophenes as electrochromic material, Journal of Electroanalytical Chemistry, 148 (1983) 299-303.
[46] A. Diaz, J.M. Vasquez Vallejo, A. Martinez Duran, [Pt]Polypyrrole: a new organic electrode material, IBM: Journal of Research and Development, 25 (1981) 42-50.
[47] D. Curran, J. Grimshaw, S.D. Perera, Poly(pyrrole) as a support for electrocatalytic materials, Chemical Society Reviews, 20 (1991) 391-404.
[48] J. Chang, I.W. Hunter, Characterization and control of the wettability of conducting polymer thin films., Materials Research Society Symposium, 2009.
[49] J. Isaksson, C. Tengstedt, M. Fahlman, N. Robinson, M. Berggren, A solid-state organic electronic wettability switch, Advanced Materials, 16 (2004) 316-320.
[50] M.A. Habib, Electrogravimetric characterization of the electrochromic polyaniline film surface, Langmuir, 4 (1988) 1302-1304.
[51] M. Hato, Electrically induced wettability change of polyaniline. Potential controlled tensiometric study, Chemistry Letters, (1988) 3.
[52] J.A. Halldorsson, Y. Wu, H.R. Brown, G.M. Spinks, G.G. Wallace, Surfactant-controlled shape change of organic droplets using polypyrrole, Thin Solid Films, 519 (2011) 6486-6491.
[53] A. Marmur, Soft contact: measurement and interpretation of contact angles, Soft Matter, 2 (2006) 12-17.
[54] D. Kim, N.M. Pugno, S. Ryu, Wetting theory for small droplets on textured solid surfaces, Scientific Reports, (2016).

Flow formation in fingerprints using electrowetting 3

3.1. Introduction

Currently, latent fingermarks are visualised by powdering the fingerprint or by a reaction between the fingerprint visualisation reagents and components in the fingerprint residue such as amino acids and fatty acids. [1] This reaction could be problematic for aged fingerprints as molecules in aged fingerprints could be positioned closer to the fingerprint edges and the substrate, which could make it more difficult to react with the fingerprint residue and could lead to inhomogeneous visualisation of the fingerprint as illustrated in Figure 3.1. To address this limitation, the possibility to create a flow in a fingerprint ridge, resulting in more readily available target molecules (released from the surface) and homogeneously distributed fingerprint ridges, was investigated using the electrowetting process. Hereby it is of importance not to disturb the fingerprint pattern as that could make the fingerprint unusable for identification purposes.

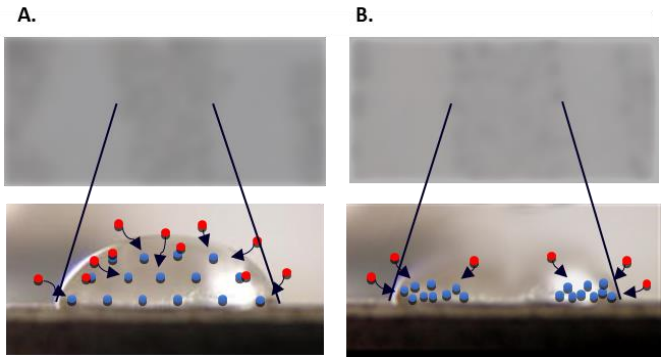

Figure 3.1 – Schematic illustration of a fresh (**A**) and aged (**B**) fingerprint. Top: Microscopic view of a fingerprint. Bottom: Droplet illustrating a cross-section of one single fingerprint ridge, the blue and red dots illustrate the molecules in a fingerprint ridge and visualisation reagents, respectively.

As discussed in Chapter 1, the principle of electrowetting is based on the application of a potential across a droplet and its underlying surface, resulting in spreading of the droplet and a change in the amount of wetting. By removal of the potential, the droplet will retract. In this study, the conventional electrowetting-on-a-dielectric technique was applied in which the substrate, working as electrode, is covered by a dielectric layer which functions as capacitor; this process is later referred to as electrowetting.

The main purpose of this research is the formation of a flow inside a droplet/simulated fingerprint, therefore the electrowetting effect was not only expressed in the conventional way by the change in contact angle (amount of spreading/retraction) but also by the amount of movement inside the droplet using the tracking of polymer microsphere particles added to the droplet. Research has demonstrated that there is formation of a hydrodynamic flow inside droplets induced by alternating current (AC) potential (rather than using direct current (DC) potential). This flow is believed to be caused by the oscillation of the droplet (continuous spreading and retracting of the droplet; generally in low frequency range) or by an electrothermal effect (generally in high frequency range). [2-5] Therefore, in this research an AC potential was applied across the droplets and underlying substrate. Additionally, the use of quartz crystal microbalance (QCM) was investigated as a potential method for detecting the electrowetting effect. This idea is based on the change in resonant frequency of a QCM crystal by changing surface coverage, a change in surface coverage could be caused by subjecting a droplet (positioned on a QCM crystal) to an external potential resulting in spreading/retraction of the droplet. This results in the investigation of the electrowetting effect from three perspectives; the conventional contact angle, the amount of coverage and the movement inside the droplet (Figure 3.2).

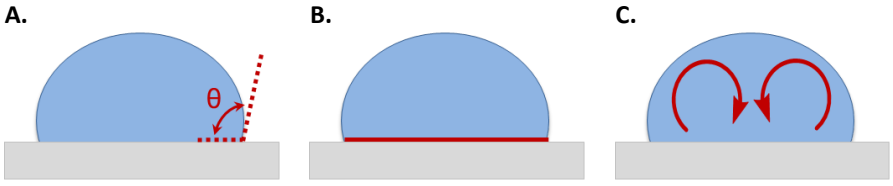

Figure 3.2 – Used methods to determine the electrowetting effect: contact angle measurements (**A**), the amount of coverage using QCM (**B**) and the movement of particles inside the droplet (**C**).

To define the possibilities and limitations of the electrowetting on fingerprints application, the effects of relevant fingerprint characteristics (both compositional and physical) such as viscosity (possible delaying/damping effect on the flow), salinity (possible effect on electric permittivity), height of the fingerprint, contact pinning and initial contact angle (both fingerprint-substrate interactions) were investigated. The objectives are summarised below:

- Determine if nano gravimetric methods (QCM) and the movements inside the droplet can deliver insights into electrowetting mechanisms.
- Estimate the influence of the evaporation process with respect to the influence of the potential on the droplet shape change during the electrowetting process.
- Investigating how the electrowetting process could be influenced by the characteristics of the dielectric layer and external factors such as potential and frequency.
- Understand how the electrowetting on fingerprints application could be affected by the composition and physical structure of the fingerprint as well as the consequences on the fingerprint pattern.

3.2. Methods

3.2.1. Coating formation on metal substrates

A dielectric layer was deposited on top of indium tin oxide (ITO) coated glass slides and Au QCM crystals, optionally followed by the deposition of a hydrophobic top-layer, as outlined below.

3.2.1.1. Cleaning procedure of ITO microscope glass slide

The ITO glass slides were first cleaned with acetone for 10 min, followed by 10 min in IPA and then washed with DI-water for 2 min, all in an ultrasonic bath. Subsequently the substrate was left in a 2 % (v/v) Hellmanex solution for 30 min at 65 ^{o}C and washed with water for 15 min, both in an ultrasonic bath.

3.2.1.2. Formation of SU-8 and Cytop coated substrates

On top of the ITO glass slides or Au QCM crystals, a dielectric layer of SU-8 was deposited, optionally followed by a hydrophobic layer of Cytop on top. SU-8 was spin coated at 2500-3000 rpm for 2 min and then baked at 90-95 ^{o}C for 3 min. To enable cross-linking, it was exposed to UV-light for 3 x 8 s as shown in Figure 3.3. Lastly, slides underwent spin-coating of Cytop, diluted 1:4 in its solvent (proprietary), at 2500-3000 rpm for 2 min and then baked for 3 min at 90-95 ^{o}C.

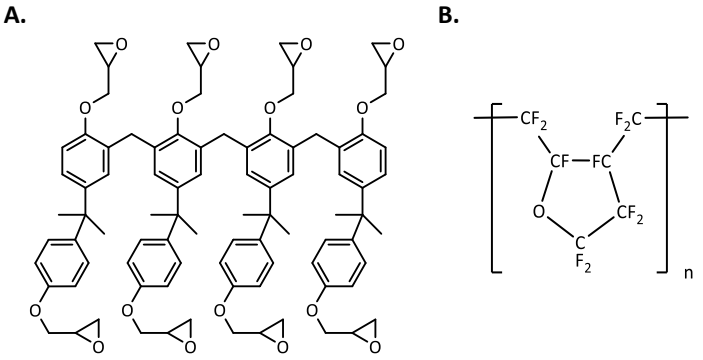

Figure 3.3 – Molecular structures of the epoxy based negative photoresist SU-8 (**A**) and the amorphous fluoropolymer Cytop (**B**).

3.2.2. Surface characterisation and analysis techniques

3.2.2.1. Microscopy

Fingerprints were recorded using the Zeta-20 True Colour Optical Profiler with Zeta3D software version 1.8.5 (Zeta Instruments).

3.2.2.2. Roughness measurements

Roughness measurements were performed using the Atomic Force Microscope (AFM; Digital Instruments, Veece Metrology Group) in tapping mode, operated using Nanoscope software version 6.12.

3.2.2.3. Thickness measurements

The thickness of the SU-8 layer (coated on ITO slides) was measured using the Contour GT Profilometer (Bruker).

3.2.2.4. Contact angle measurements

Contact angles were determined using the ThetaLite optical tensiometer (Biolin Scientific) in combination with OneAttension software version 2.5, r5128 (Biolin Scientific) and/or using Image-J 1.49e software in combination with the plugin drop analysis LB-ADSA.

3.2.2.5. QCM measurements

Quartz Crystal Microbalance (QCM) measurements were performed using the SEIKO EG&G QCM922A QCM Microbalance with IviumSoft version 2.667 (3) software (Ivium) and/or a fitting excel form to determine the electrowetting effect by means of change in droplet surface coverage.

Two types of QCM measurements were performed. One using a standard QCM set-up in which the working electrode (Figure 3.5, red) and ground electrode (Figure 3.5, black) were connected to the crystal to define the sensitivity of QCM towards a change in droplet surface coverage/mass-loading. Droplets of a range of volumes were compared as well as a hydrophobic (SU-8+Cytop) and hydrophilic (SU-8) coated QCM crystal. The

latter by comparing droplets with a similar volume (Figure 3.4A) and similar surface coverage (Figure 3.4B) on the hydrophobic and hydrophilic coated crystals. In addition, the influence of the droplet composition was explored by increase in glycerol content.

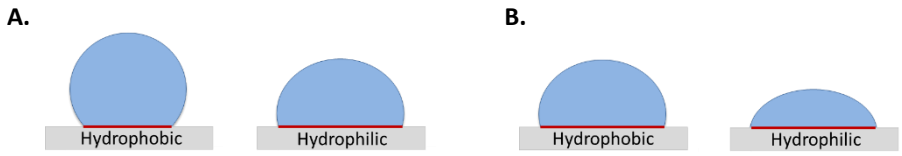

Figure 3.4 – Schematic illustration of droplets of a similar volume and different covered area (**A**) and droplets of a similar covered area and different volume (**B**) on a hydrophobic and hydrophilic surface.

In the second set-up an external potential was applied across a droplet and the underlying QCM crystal to determine the detectability of a difference in surface coverage caused by a difference in contact angle (spread versus retracted droplet). Here, the standard set-up was combined with the electrowetting set-up, whereby in addition to the working electrode (red) and ground electrode (black) of the standard QCM set-up an electrode was entering the droplet (yellow) and an electrode (blue) was connected to the ground electrode of the standard set-up (Figure 3.5).

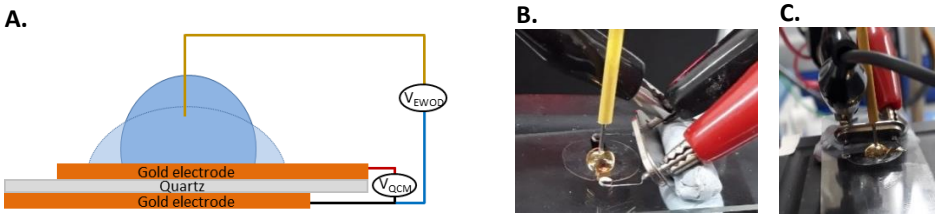

Figure 3.5 – QCM set-up extended with the electrowetting set-up; schematic illustration (**A**) and photos from two perspectives (**B** and **C**).

3.2.3. Particle tracking measurements

To follow the movement inside the droplets, particles (polymer microspheres, ca. 1 g/mL) were added to the droplet. Laser scattering of the particles was subsequently recorded by video. These particles were tracked using the video analysis software Tracker (Open Source Physics). It has to be noted that the movement of the particles was recorded and tracked in 2D while the actual movement of the particles was in 3D, therefore some back- and forward movement could have been missed.

3.2.4. AC high potential supplier

AC high potential was used to supply a range of potentials (0-250 V) and frequencies (0.5 Hz-10 kHz) using a high potential amplifier (TREK Model 2205) connected to a waveform generator. The experiments were performed using two set-ups with different but similar waveform generators, the BK Precision 4053 and the TENMA 72-3555.

3.2.5. Model fingerprint solution

In this study a model fingerprint solution was created to mimic a fingerprint. This composition was based on eccrine fingerprint compositions described in the literature and outlined in the Appendix (Tables A.1-A.3). Some studies were based on fingerprints and others on sweat as well as not all quantities were justified in the review articles, therefore overlap in data could be present. Due to the complexity of a fingerprint, only the most abundant molecules (>10 mM) and molecules of special interest such as amino acids were included in the model fingerprint solution. In addition, the high content of water in fingerprints resulted to the decision to include only the water-soluble protein albumin and no other proteins.

3.2.6. Chemicals and materials

In this study the chemicals as outlined in Table 3.1 were used, all used as received. The in this research used deionized-water (DI-water) was obtained from the PURELAB Option water purification system of ELGA.

Table 3.1 – Chemicals and materials used in this research, including source and purity (when relevant).

Chemical/ materials	Source
(3-Mercaptopropyl)trimethoxysilane (95%)	Sigma-Aldrich
L-Alanine (99%)	Aldrich
Albumin from bovine serum	Sigma
L-Aspartic acid (≥98%)	Sigma-Aldrich
Cytop	AGC Chemicals
L-Glutamic acid hydrochloride	Sigma
Glycerol	Fisher Scientific
Glycine (≥99%)	Sigma
Hellmanex	Hellma Analytics
L-Histidine (≥99%)	Sigma-Aldrich
Indium tin oxide coated glass slides	Delta Technologies

L-Isoleucine (99%)	Aldrich
Lactic acid (≥85%)	SAFC
L-Leucine (99%)	BDH biochemicals
L-Lysine (≥98%)	Sigma-Aldrich
Microscope glass slides	Fisher Scientific
L-Ornithine hydrochloride (99%)	Acros Organics
Polymer microsphere particles	Sigma-Aldrich
L-Phenylalanine (≥98%)	Sigma
Potassium chloride	Fisher Scientific
Propan-2-ol	Fisher Scientific
QCM crystals	Seiko
L-Serine (≥99%)	Sigma
Sodium chloride	Fisher Scientific
Sodium hydrogen carbonate	Fisher Scientific
SU-8	Microchem Corporation
L-Threonine (≥98%)	Sigma-Aldrich
L-Tyrosine (≥98%)	Sigma-Aldrich
L-Valine (≥98%)	Sigma-Aldrich
Urea	ChemCruz

3.3. Results

The possibility of creating an electrowetting effect in a fingerprint by applying a potential was explored by observing the electrowetting effect from three perspectives; contact angle, flow and surface coverage.

3.3.1. Use of QCM as alternative method to express the electrowetting effect

QCM was investigated as a potential method to detect the electrowetting effect by means of change in mass loading/surface coverage on the crystal. In the following sections the terms surface $_{CA}$coverage and $_{QCM}$coverage were used, which refer to the surface coverage of the droplet obtained using contact angle measurements and implied by QCM measurements, respectively. The used terms frequency and Q-factor change are defined by the change in frequency and Q-factor of the QCM crystal with a droplet on top with respect to the crystal without droplet ($\Delta F = |F_{air} - F_{droplet}|$).

3.3.1.1. Sensitivity of QCM measurements towards droplet surface coverage

To determine the sensitivity of QCM towards a change in droplet surface $_{CA}$coverage, water droplets of a range of volumes (as specified in Figure 3.6-3.10) were positioned on a QCM crystal. Figure 3.6 shows that with an increase of droplet volume, the frequency decreased. Also, admittance decreased and the peaks broadened with higher droplet volumes, due to energy losses.

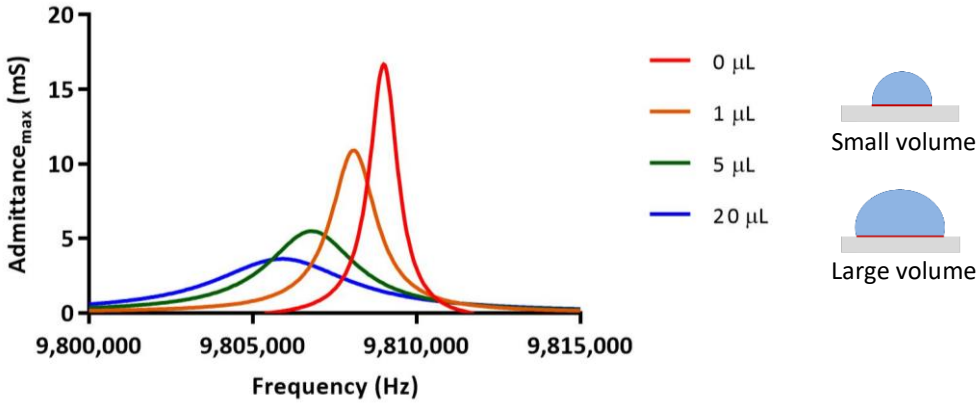

Figure 3.6 – QCM crystal resonance frequency and admittance as a function of deposited droplets of a range of volumes (0-20 µL) on a SU-8+Cytop coated QCM crystal. Including illustrations of the covered area (red line) of a small and large volume droplet.

This decrease in frequency with increasing volume indicates an increase in surface $_{QCM}$coverage/mass loading on the crystal [6] which is in line with the observed increase in surface $_{CA}$coverage of the droplet with volume (Figure 3.7). This suggests that QCM is able to detect the droplets and differentiate between different volumes.

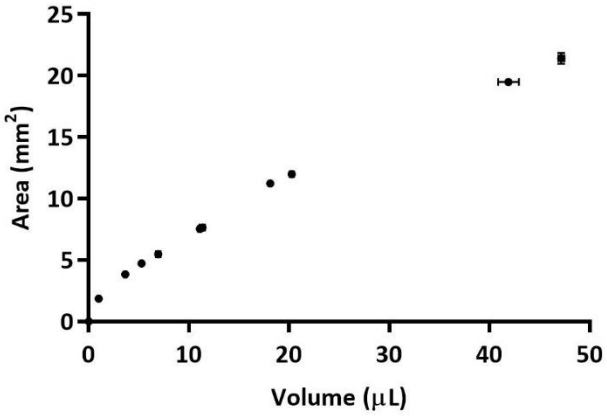

Figure 3.7 – Droplet area coverage on a SU-8+Cytop coated QCM crystal as a function of droplet volume. The covered area is based on the diameter of the droplet measured by the ThetaLite optical tensiometer.

To define whether the QCM is able to detect smaller differences in surface $_{CA}$coverage such as caused by a difference in contact angle, droplets of a range of volumes were deposited on both hydrophobic (SU-8+Cytop) and hydrophilic (SU-8) QCM crystals.

Droplets of equal volume deposited on both the hydrophobic (SU-8+Cytop) and hydrophilic (SU-8) coated crystals showed a smaller frequency change on the hydrophobic crystal (Figure 3.8).

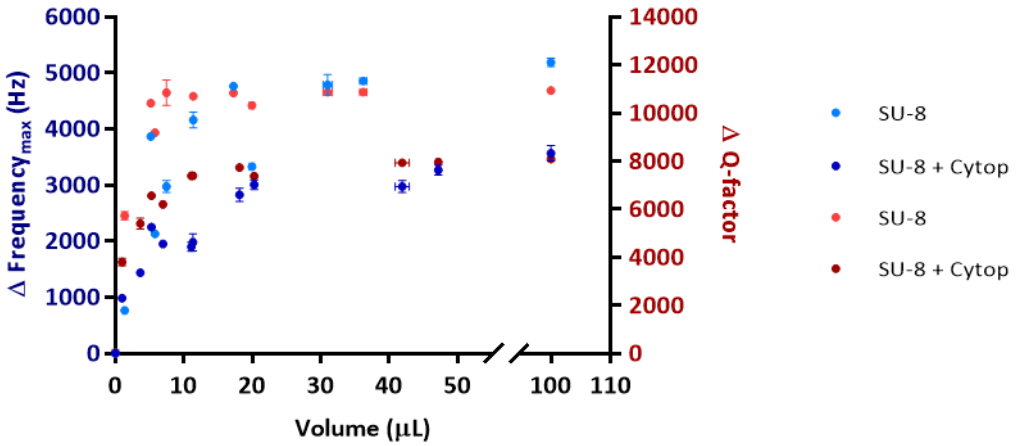

Figure 3.8 – QCM crystal resonance frequency change and Q-factor change as a function of volume of a water droplet deposited on the crystal. Droplets covering the complete QCM crystal plus the surrounding were set at 100 µL.

This indicates that on the hydrophobic (SU-8+Cytop) surface, the amount of surface $_{QCM}$coverage/mass loading on the crystal was lower compared to the hydrophilic surface (SU-8), possibly due to a higher contact angle, resulting in a smaller surface $_{CA}$coverage (Figure 3.4A). However, droplets with a similar surface $_{CA}$coverage on both the hydrophobic (SU-8+Cytop) and hydrophilic (SU-8) surface, created by depositing a larger droplet volume on the hydrophobic surface (Figure 3.4B), showed a smaller frequency change on the hydrophobic (SU-8+Cytop) surface compared to the hydrophilic (SU-8) surface (Figure 3.9).

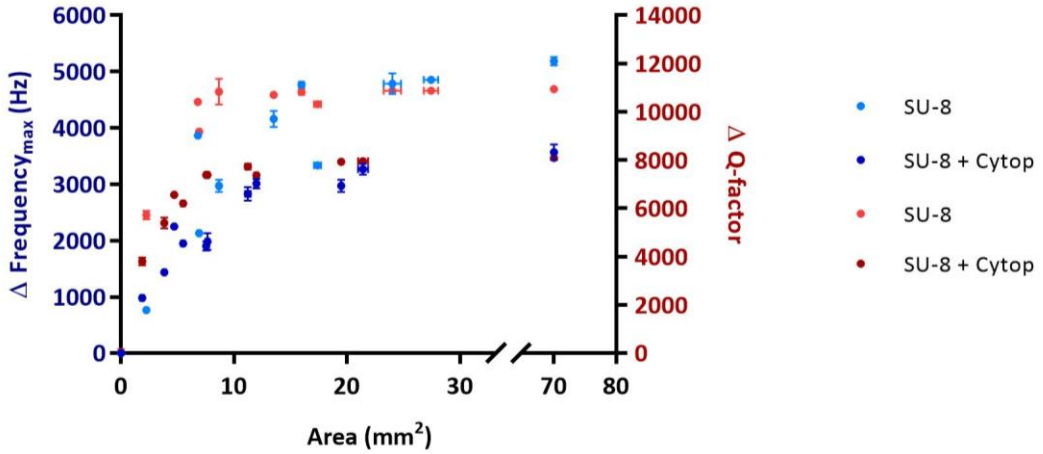

Figure 3.9 – QCM crystal resonance frequency change and Q-factor change as function of area coverage of a water droplet deposited on the crystal. Droplets covering the complete QCM crystal plus the surrounding were set at 70 mm^2.

The difference in frequency change of the two surfaces containing droplets with equal surface $_{CA}$coverage but different volumes is unlikely to be caused by the difference in height of the droplets due to the detection limit neither by a difference in surface $_{QCM}$coverage/mass loading. However, it could be caused by a difference in behaviour of the coated crystals such as the slip/no-slip phenomenon; at no slip the liquid has no velocity compared to the substrate, at slip it has. Possibly more slip was obtained on the hydrophobic surface (SU-8+Cytop) resulting in a smaller frequency change compared to the hydrophilic surface (SU-8). In addition, the change in Q-factor increased with volume/mass loading, this suggests an increase in energy loss. Also here a difference between the two surfaces (SU-8 vs. SU-8+Cytop) was observed, showing a smaller Q-factor change and thereby less energy loss on the hydrophobic (SU-8+Cytop) surface compared to the hydrophilic (SU-8) surface which is in agreement with the slip/no-slip

theory. The SU-8 and SU-8+Cytop coated crystals differ not only in hydrophobicity but also in coating thickness, due to the addition of the Cytop layer (ca. 20 nm) on top of the SU-8 layer to create the hydrophobic (SU-8+Cytop) crystal. This extra layer could increase the resistance.

The electrowetting effect is conventionally expressed by the contact angle, therefore the relationship between contact angle and both frequency and Q-factor was investigated. Figure 3.10 shows a smaller frequency and Q-factor change on the more hydrophobic (SU-8+Cytop) crystal compared to the hydrophilic (SU-8) crystal; this is similar to Figures 3.8 and 3.9 which are based on the same experiments. However, the variation in contact angles on the hydrophobic (SU-8+Cytop) surface did not follow the trend of increasing frequency and Q-factor change by decreasing contact angle.

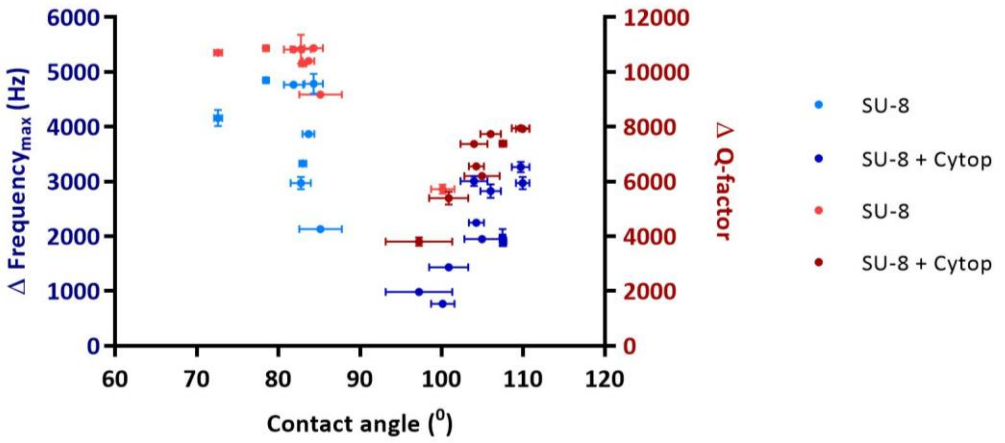

Figure 3.10 – QCM crystal resonance frequency change and Q-factor change as function of contact angle of the crystal deposited water droplets.

The increase in frequency change by increasing contact angle could possibly be caused by the here observed generally higher surface $_{CA}$coverage of the droplets with higher contact angles; an increase in contact angle could lead to a decrease in frequency change while an increase in surface $_{CA}$coverage could result in an increase in frequency change. Alternatively, it could be that a small difference in contact angle cannot be detected using QCM measurements and/or other unknown factors are of influence.

To conclude, QCM measurements demonstrated to be able to differentiate between different droplet volumes. However, the ability to detect a difference in contact angle could not be proven yet.

3.3.1.2. QCM to express the electrowetting process

To determine whether a difference in contact angle could be detected in an electrowetting setting, a droplet was spread and retracted by applying an external potential while the admittance/frequency was measured using QCM in parallel. To ascertain the sensitivity of QCM in such an environment, the ability to differentiate between the on-period and off-period and on-phase and off-phase were investigated. The terms on/off-period and on/off-phase are used to differentiate between the different periods/phases of the external applied AC potential as shown in Figure 3.11. The on-period starts by applying the potential manually and the off-period by removing the potential manually. The on/off-phase corresponds to the fractions of the frequency wave in which the potential was on/off.

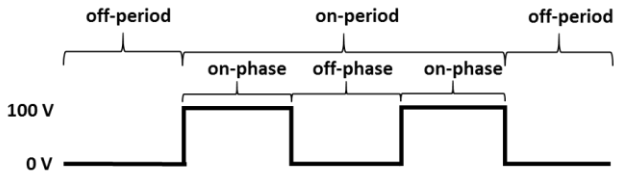

Figure 3.11 – Schematic illustration of used terminology of an applied AC potential. The on-period starts by applying the potential manually, the off-period by removing the potential manually. The on-/off phase corresponds to the on/off fractions within a frequency wave.

Admittance and frequency measurements averaged over a period of 15 s showed a lower frequency and admittance during the on-period compared to the off-period (Figure 3.12).

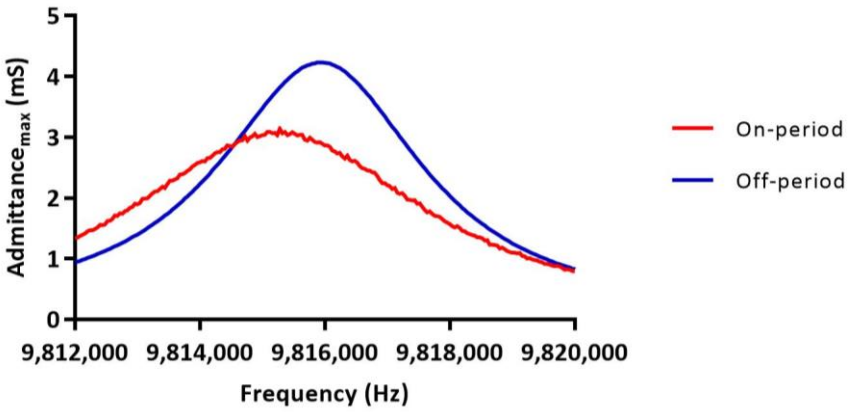

Figure 3.12 – QCM crystal resonance frequency and admittance as a function of an external AC potential of 200 V, 100 Hz applied between a water droplet and its underlying SU-8+Cytop coated QCM crystal. Measurements were averaged over a period of 15 s.

The lower frequency during the on-period compared to the off-period suggests an increase in mass loading/surface $_{QCM}$coverage caused by the spreading droplet by applying a potential. This is in line with an increase in energy loss, implied by the decrease in admittance, possibly caused by an increase in resistance with liquid coverage due to spreading of the droplet during the on-period. Additionally, the curve of the on-period is more irregular compared to the off-curve, which could be due to the presence of 'on-off-on-off' phases in the on-period of an AC potential (Figure 3.11).

As shown in Figure 3.13, during a sequence of on/off periods, the frequency and Q-factor first decreased slightly, then increased, after which the pattern/consistency vanished.

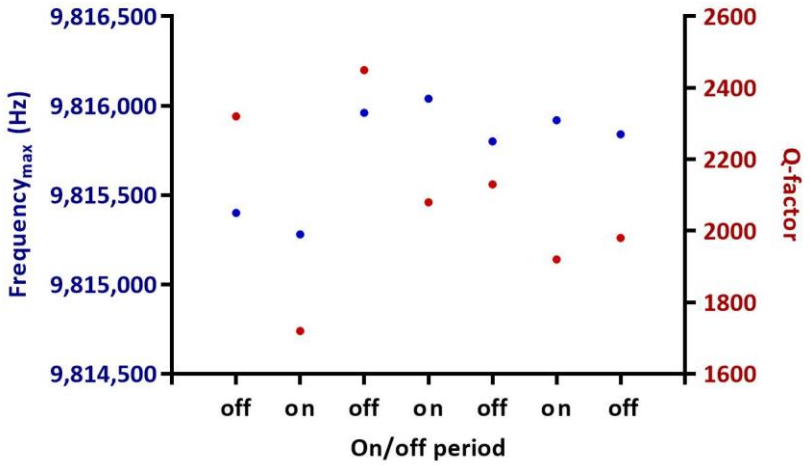

Figure 3.13 – QCM crystal resonance frequency (blue) and Q-factor (red) as a function of an external AC potential of 200 V, 100 Hz applied between a water droplet and underlying SU-8+Cytop coated QCM crystal.

The decrease and subsequent increase in frequency by application and removal of the potential in the first cycle corresponds to an increase and decrease of mass loading, as also shown previously (Figure 3.12). Afterwards the pattern in frequency change vanished, this suggests that the QCM did not detect a considerable difference in mass loading between the on-period and off-period anymore. However, the increase in energy loss, expressed using the Q-factor, at the on-period compared to the off-period, could indicate that spreading of the droplet, resulting in a higher liquid coverage and thereby increase in resistance, was still detected.

The mass-sensitivity of QCM crystals decreases towards the edges as illustrated by the Gaussian curve in Figure 3.14. [6] Possibly an increase in surface coverage caused by spreading of the droplet (red area) falls within the low mass-sensitive range and therefore, while present was not detectable.

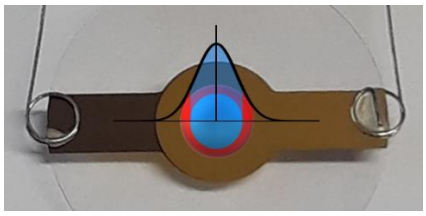

Figure 3.14 – Schematic illustration of a QCM crystal with a droplet on top. Blue area illustrates the droplet in retracted state (no potential applied) and the red plus blue area illustrates the droplet in spread state (potential applied). Including the mass sensitivity Gaussian distribution.

To conclude, differences in frequency and admittance between the on-period and off-period were observed, however sometimes to a limited extent. To determine whether QCM is capable of differentiating the on-phase and off-phase, continuous QCM measurements were performed while applying an external AC potential. Simultaneously the contact angle was also measured.

As shown in Figure 3.15 the application of an external potential of 150V, 500 mHz (square waveform) results in a decrease in frequency and contact angle by applying the potential at t=0 s, followed by an increase in frequency and contact angle half a frequency cycle later (t=~1 s, off-phase).

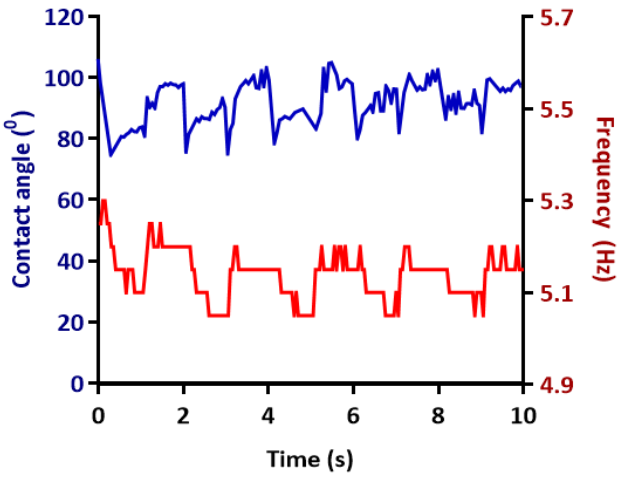

Figure 3.15 – Change in contact angle (blue) and QCM resonance frequency (red) by applying 150V, 500 mHz across a water droplet and the underlying SU-8+Cytop coated QCM crystal.

The decrease and increase in contact angle/frequency both indicating spreading and retraction of the droplet respectively, this suggests that QCM has potential to detect an electrowetting effect. However, it is not as simple as that as other data showed opposing changes in frequency pattern (mirror image). It has to be noted that the droplet has the tendency to move to the outer sides of the QCM crystal, but was hindered in that movement by the contact with the top-electrode. This could influence the measurements as the mass sensitivity decreases towards the edges of the crystal (Figure 3.14). In addition, using lower potentials (<100 V), little to no electrowetting effect was observed while by using higher potential (≥ 150 V) electrolysis and breakdown occurred very rapidly.

The QCM crystal was also covered completely by a water droplet, to exclude the influence of other factors than surface coverage on the frequency change. By applying an external AC potential, no change in surface coverage could be detected by the QCM as the droplet contact line was located outside/on the edge of the QCM crystal. This resulted in the detection of some irregular frequency changes which could feasibly be attributed to noise (Figure 3.16).

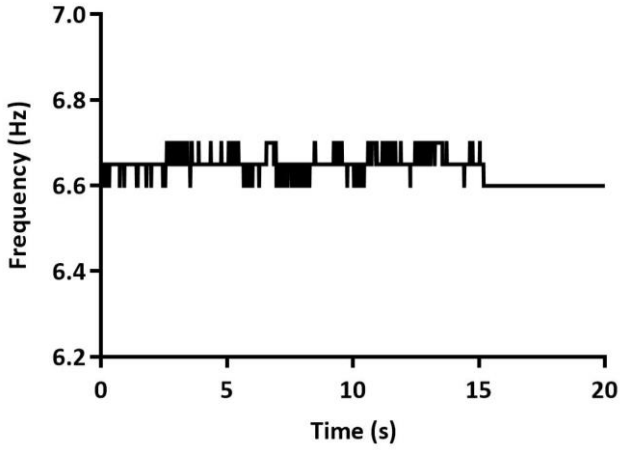

Figure 3.16 – Continuous QCM measurements illustrating the change of QCM resonance frequency by applying a potential of 150 V, 500 mHz across a water droplet and underlying SU-8+Cytop coated QCM crystal.

In a study of Lin *et al.* [7] a frequency change was observed by applying a potential across a Teflon coated QCM crystal (upper electrode) and water droplet, immersing the entire crystal and surrounded by oil. This was probably caused by the presence of an oil film

under the droplet which thickness changed by applying a potential, resulting in a change in viscosity and therefore frequency.

3.3.1.3. Influence of droplet composition on the QCM measurements.

To explore the influence of the droplet composition on the QCM measurements, droplets of a range of glycerol volumes (0-50%) were deposited on a QCM crystal. Glycerol was chosen because of the possible influence of the viscosity on the QCM measurements and the probable increase in viscosity of fingerprints over time, therefore relevant for fingerprint applications.

The admittance curve shows a decrease in admittance and to a certain extent decrease in frequency by increase in glycerol content (Figure 3.17).

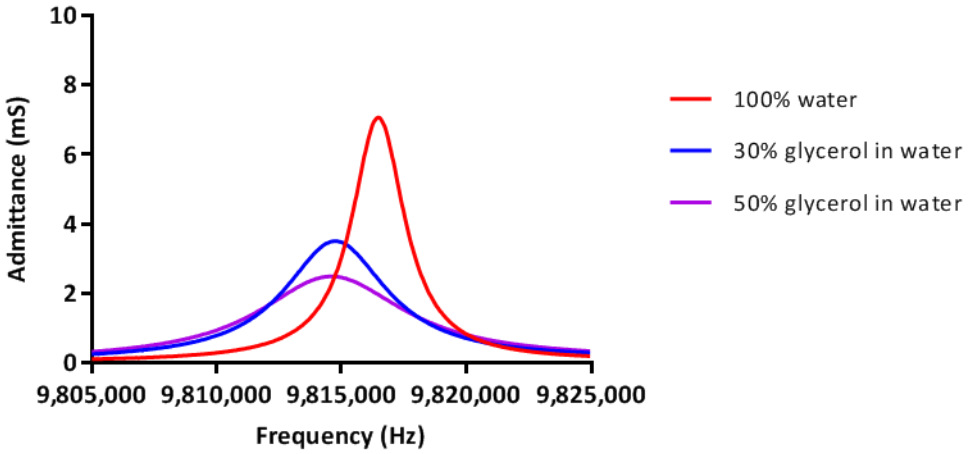

Figure 3.17 – Admittance as a function of QCM resonance frequency of a SU-8+Cytop coated QCM crystal with a water (red), 30% glycerol in water (blue) and 50% glycerol in water (purple) droplet on top.

The decrease in frequency by increasing glycerol content could be attributed to an increase in surface $_{QCM}$coverage due to a lower contact angle of glycerol than water. Although the difference in frequency between the 30% glycerol and 50% is minimal, if not insignificant, which could indicate an influence of the viscosity (and therefore glycerol content) on the frequency change. An increase in viscosity could result in a decrease in frequency, however because of the assumed proportional relation of the frequency with the square root of the viscosity, the influence of viscosity on the frequency change decreases with increasing viscosity (Table 3.2). [8]

Table 3.2 – Viscosity (at 20 °C) of water and glycerol mixtures. NA=not applicable.

	100% Water	30% Glycerol	50% glycerol	References
Viscosity (cP)	1.00	3.00	8.37	[9]
$\sqrt{\textbf{viscosity}}$	1	1.73	2.89	NA

The increase in viscosity by increasing glycerol content could also have contributed to the decrease in admittance.

To conclude, QCM was capable of differentiating different droplet volumes as well as droplets in actuated state (applied potential) from rest state (no potential) to a certain extent. Therefore QCM may have potential to be used as an alternative method for the detection of the electrowetting effect, although more research is needed before application due to uncertainty about the influence of certain factors (such as hydrophobicity), inexplicable observations and the necessity to optimise the dielectric layer to prevent breakdown.

3.3.2. Use of particle tracking as alternative method to express the electrowetting effect

To study the formation of a flow inside a droplet/simulated fingerprint induced by electrowetting, particles were added to the droplet and tracked using the video analysis software Tracker.

The observed particle movements by applying an AC potential can be categorised as shown in Figure 3.18. To get a better understanding of the behaviour of the droplet, not only the movements were observed but also the velocity of the particles was measured.

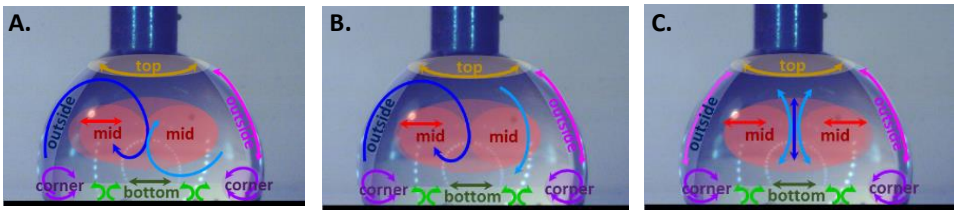

Figure 3.18 – Three types of commonly observed movements; movement of the left and right side in the same or contrary direction in standard sized droplet (**A**), movement in droplets of a smaller diameter (**B**) and a non-continuous flow (**C**).

3.3.2.1. Frequency

To cover the whole spectrum of frequencies, the influence of 10 frequencies (0.5 Hz, 10 Hz, 50 Hz, 100 Hz, 200 Hz, 500 Hz, 750 Hz, 1 kHz, 5 kHz and 10 kHz) on the movement of the particles was investigated. Based on the observed type and amount of movements the frequencies can be divided in the following 5 groups as outlined in Table 3.3.

Table 3.3 – Overview of the types of movements by applying the reported frequencies, including the time that the particles kept moving after removal of the potential.

Frequency	Type of movement	Time after movement
0.5 Hz	Particle movement in line with the clearly visible spreading and retraction of the droplet.	-
10 and 50 Hz	On real time speed, a 'vigorous movement' (Figure 3.19) was obtained which made the particle tracking challenging.	~1 s
100 and 200 Hz	Spreading and retracting of the droplet is less vigorous and appear to be more organised than using 10 and 50 Hz, resulting in better trackable particle movement.	~2-3 s
500 and 750 Hz	Trackable particle movement	~≤1.5 s
1, 5 and 10 kHz	Trackable particle movement.	<1 s

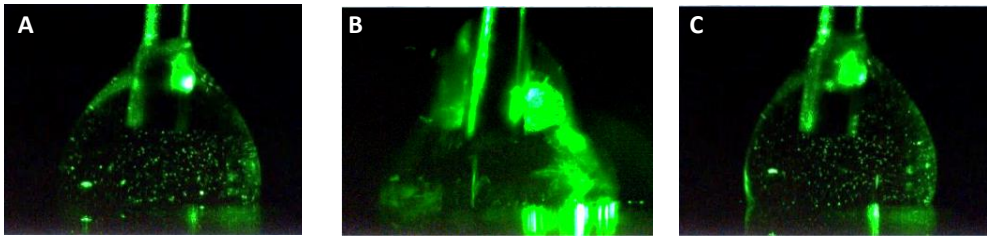

Figure 3.19 – Laser scattering of the particles added to a water droplet, before (**A**), during (**B**) and after (**C**) applying 200V, 50 Hz.

Despite the fact that the particles were not trackable at all frequencies, the time of movement after removing the potential suggests that the highest particle velocity was observed by applying 100-200 Hz.

3.3.2.2. Potential

To determine the influence of potential on the velocity of the particles in the droplet, four potentials were applied; 100, 150, 200 and 250 V.

In general, by increasing potential the velocity of the particles inside the droplet increased, although within the droplet differences between regions were present (Figure 3.20). As the movement of the particles was not restricted to one region, some overlap could have been present.

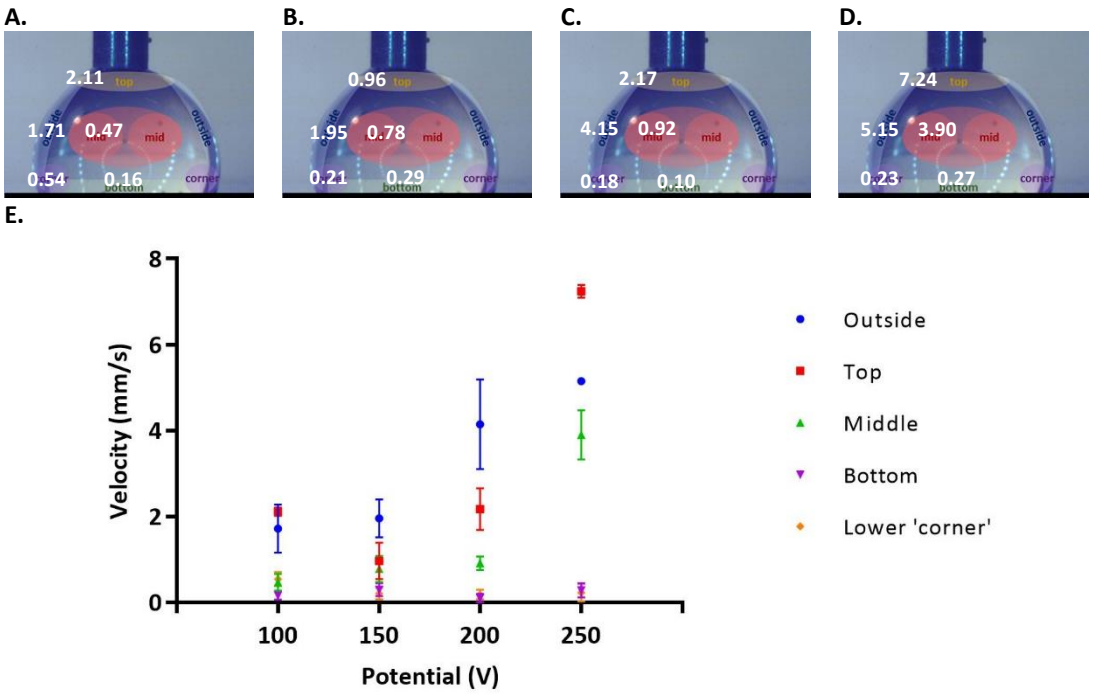

Figure 3.20 – Velocity of particles (mm/s) inside a water droplet, by applying 100 V (**A**), 150 V (**B**), 200 V (**C**), 250 V (**D**) and 500Hz across the droplet and its underlying SU-8+Cytop coated substrate. Alternative representation in the form of a graph (**E**).

The lower particle velocity at the bottom of the droplet could be a limitation for the applicability of electrowetting on fingerprints, as the molecules which are difficult to reach by fingerprint visualisation reagents are probably mainly positioned in these regions.

To conclude, the movements inside the droplet could be of value for getting more insight in the electrowetting process. As the contact angle gives information about the behaviour of the outside of the droplet and the flow measurements about the inside of the droplet, both techniques could best be used to complement each other.

3.3.3. Determination of the influence of the dielectric layer, potential and frequency on the electrowetting process

In this research electrowetting was obtained using a dielectric layer on top of the substrate/bottom electrode, functioning as capacitor. To determine the optimal conditions for obtaining electrowetting, characteristics of the dielectric layer such as hydrophobicity, thickness, dielectric strength and dielectric constant as well as external factors such as potential and frequency will be discussed.

The influence of the dielectric layer on the potential driven change in contact angle can be described by the Young-Lippmann equation (3.1).

$$\cos\theta = \cos\theta_Y + \frac{\varepsilon_d \cdot \varepsilon_0}{2 \cdot \sigma_{LV} \cdot d} \cdot V^2 = \cos\theta_Y + \frac{C}{\sigma_{LV}} \cdot V^2 \qquad \textbf{Equation 3.1}$$

Equation 3.1 shows that the contact angle (θ) obtained by applying a potential (V) is influenced by the surface tension at the liquid-vapour interface (σ_{LV}), the capacitance (C) of the dielectric layer and the Young's or initial contact angle (θ_Y). The capacitance depends on the thickness of the dielectric layer (d) and the dielectric constant of the dielectric (ε_d) and in vacuum (ε_0).

The influence of the hydrophobicity of the surface, defined by the initial contact angle, on the contact angle change was investigated using two types of experiments. First, the initial contact angle was adjusted by holding the retraction of the droplet during a previous applied potential resulting in a lower initial contact angle. This resulted in a decrease in magnitude of contact angle change with initial contact angle (Figure 3.21A). Secondly, the initial contact angle was increased by coating a hydrophobic Cytop layer on top of the SU-8 dielectric layer. As shown in Figure 3.21B, by applying a potential (at ca. 0.3 s) the contact angle decreased and then increased half a frequency cycle later (at ca. 1.3 s). Similar to the previous type of experiment, the contact angle change increased with initial contact angle which is in agreement with several studies [10, 11].

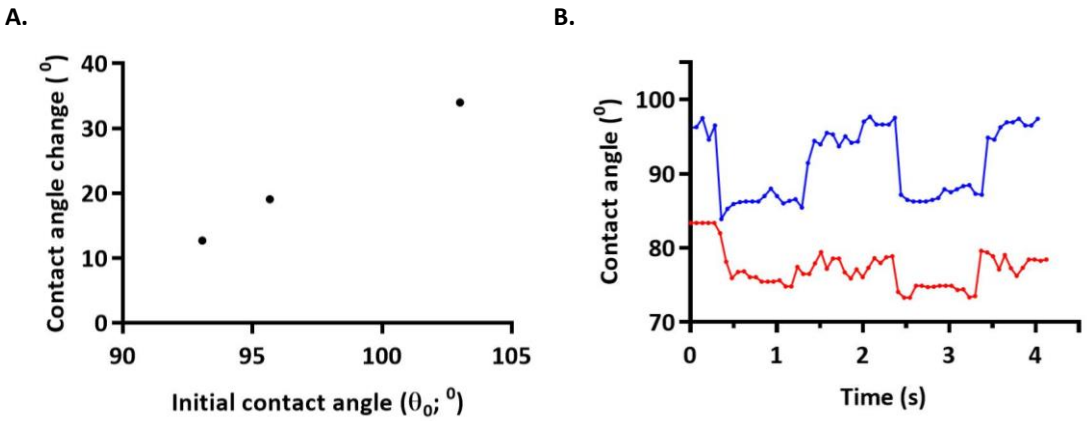

Figure 3.21 – Contact angle change as function of initial contact angle by applying 150V, 500 mHz. Using an adjusted initial contact angle on a surface of SU-8+Cytop (**A**) and by comparing a droplet on a hydrophobic surface SU-8+Cytop (blue, **B**) with a hydrophilic SU-8 surface (red, **B**).

By coating a hydrophobic Cytop layer on top of the SU-8 dielectric, not only the initial contact angle was adjusted but the addition of an extra layer with a different dielectric constant (3.2 for SU-8 and 2.05 for Cytop [12]) could also have affected the capacitance (Equation 3.1). However, calculations using typical thicknesses of 4 µm and 20 nm for SU-8 and Cytop respectively, show that the difference in capacitance between SU-8 and SU-8+Cytop is less than 1% and therefore probably negligible (Equations 3.2 and 3.3).

$$C_{SU-8} = \frac{\varepsilon_{d,SU-8} \cdot \varepsilon_0}{d_{SU-8}} = \frac{3.2 \cdot 8.85 \cdot 10^{-12}}{4 \cdot 10^{-6}} = 7.08 \cdot 10^{-6}\ F \qquad \textbf{Equation 3.2}$$

$$C_{SU-8+Cytop} = \frac{C_{SU-8} \cdot C_{Cytop}}{C_{SU-8} + C_{Cytop}} = \frac{\frac{\varepsilon_{SU-8} \cdot \varepsilon_0}{d_{SU-8}} \cdot \frac{\varepsilon_{Cytop} \cdot \varepsilon_0}{d_{Cytop}}}{\frac{\varepsilon_{SU-8} \cdot \varepsilon_0}{d_{SU-8}} + \frac{\varepsilon_{Cytop} \cdot \varepsilon_0}{d_{Cytop}}} \qquad \textbf{Equation 3.3}$$

$$= \frac{\frac{3.2 \cdot 8.85 \cdot 10^{-12}}{4 \cdot 10^{-6}} \cdot \frac{2.05 \cdot 8.85 \cdot 10^{-12}}{2 \cdot 10^{-8}}}{\frac{3.2 \cdot 8.85 \cdot 10^{-12}}{4 \cdot 10^{-6}} + \frac{2.05 \cdot 8.85 \cdot 10^{-12}}{2 \cdot 10^{-8}}} = 7.03 \cdot 10^{-6}\ F$$

Due to the higher initial contact angle and thereby larger contact angle change by coating the hydrophobic Cytop layer on top of the SU-8 dielectric layer, the further experiments were all performed using a dielectric layer of SU-8 with a top-layer of Cytop.

The influence of the potential on the magnitude of contact angle change was investigated by applying a range of potentials (50-250 V) between a water droplet and the underlying SU-8+Cytop coated substrate. This demonstrates an increase in contact angle change with potential (Figure 3.22).

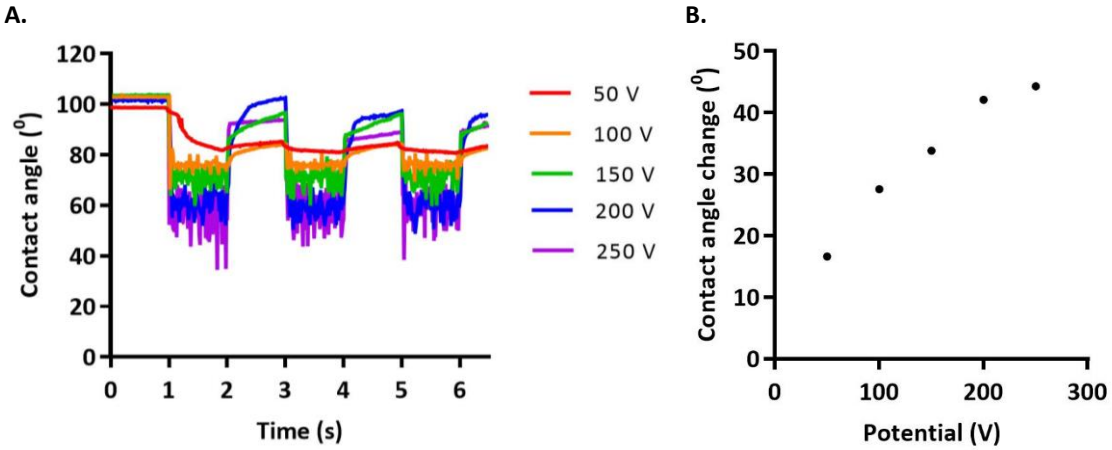

Figure 3.22 – Influence of the potential on the contact angle change by applying a range of potentials (50-250 V; 500 mHz) across a water droplet and underlying SU-8+Cytop coated substrate. Represented in two formats, contact angle over time (**A**) and contact angle change as function of potential (**B**).

Although this trend of increasing contact angle change with initial contact angle is in agreement with the Young-Lippmann equation, the experimentally determined contact angles were smaller than the theoretical equivalents (ca. 91, 75 and 30^{o} using 50, 100 and 150 V respectively). This is probably caused by imperfections of the surface and other experimental factors. Additionally, due to the widely known contact angle saturation phenomenon, the contact angle is less/barely affected by high potentials. [13-17] The use of potentials >250 V resulted sometimes in dielectric breakdown, despite the theoretical SU-8 breakdown potential of 460 V. This difference could be caused by coating imperfections. A higher potential limit could be obtained by increasing the thickness of the dielectric layer, however a higher potential is then also required to obtain an electrowetting effect. Therefore, 200 V was chosen as optimum potential to obtain the most electrowetting effect.

As shown in Figure 3.22A the droplet does not always retract back to its initial contact angle after half a frequency cycle (as at ca. 2 s). This can be caused by several factors such as charge trapping in the dielectric layer, pinning of the liquid to the surface or contact line friction. Ions could be trapped in the dielectric layer when the electrostatic

force between the ions and the charged substrate is larger than the liquid-ion interaction, resulting in a decrease in electric field at the surface-liquid interface and therefore reduced electrowetting effect. [18] The droplet, or more precisely its contact line is more difficult to move when it is strongly pinned (adhered) to the surface or experiences high friction. [19] The amount of retraction could also be limited by the time available to retract. To demonstrate this theory, a droplet which retracted only partially was subjected to a potential in which the off-phase was proportionally enlarged/reduced. This resulted in a slight increase in amount of retraction by increasing retraction time (Figure 3.23B). By removing the potential manually (t=30 s), thereby giving the droplet infinite time to retract, the droplet retracted slowly to its initial contact angle (Figure 3.23A). This implies that the time available to retract limited the amount of retraction. However, the amount or maximum wetting (lowest contact angle) by applying a potential was not influenced.

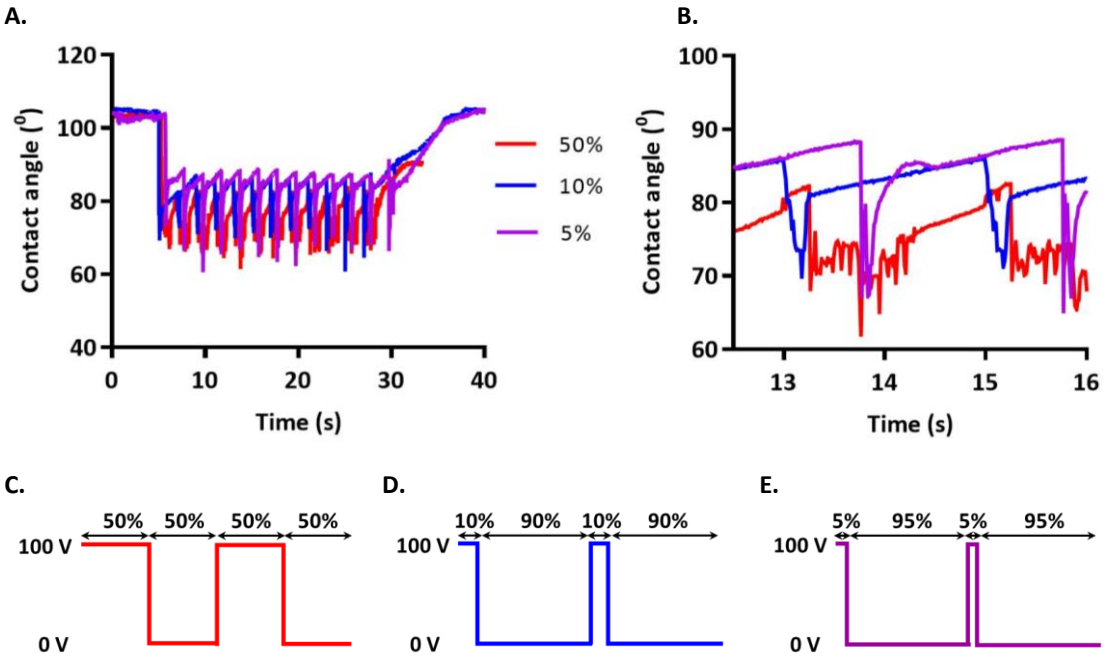

Figure 3.23 – Contact angle change over time by applying 100V, 500 mHz across a water droplet and its underlying SU-8+Cytop coated substrate with varying on/off phase timescales (**A** is overview, **B** is zoomed in); 50/50% (red; **C**), 10/90% (blue; **D**) and 5/95% (purple; **E**).

The applied potential is not only defined by its magnitude, but is also dependent on frequency. The behaviour of a droplet by subjecting to an AC potential was studied by applying a range of frequencies (200 mHz-10 kHz). To define the response of the droplet to an applied frequency, the movements of the droplet were counted (Figures 3.24-3.26). As shown in Figure 3.24, in the low frequency range (<50 Hz) the contact angle decreased, meaning spreading of the droplet, by applying the potential (t=1 s) and retracted after half a frequency cycle. This pattern repeated to the end of the measurements demonstrating that the movement of the droplet corresponds to the applied potential and the droplet is able to follow the frequency.

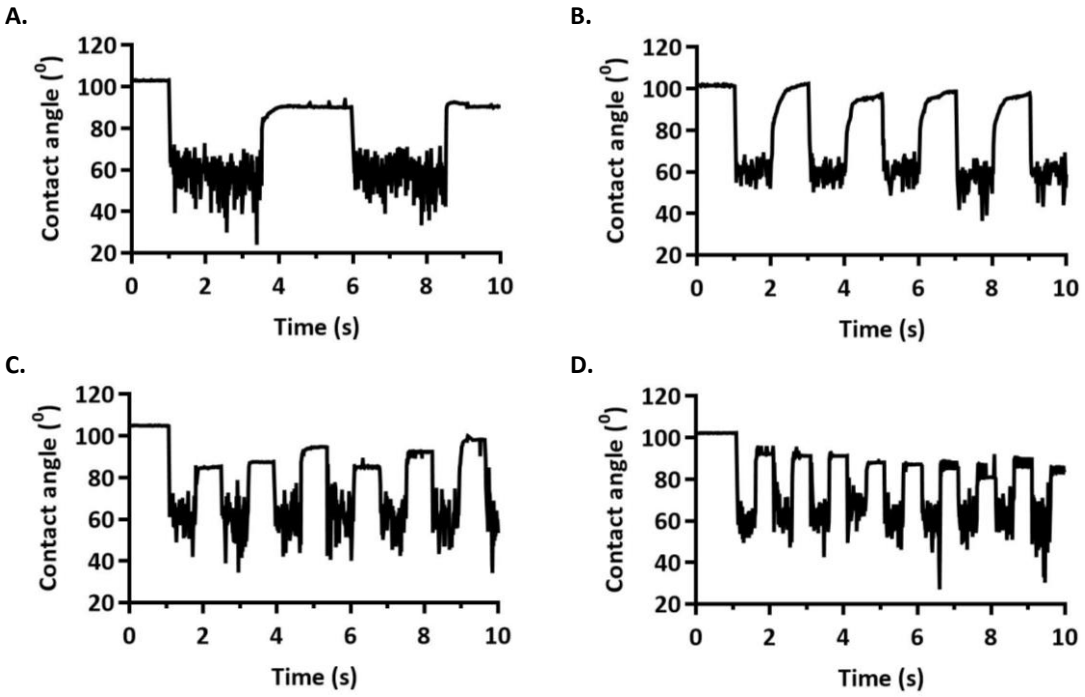

Figure 3.24 – Change in contact angle by applying 200V and a range of frequencies (200 mHz–1 Hz) across a water droplet and its underlying SU-8+Cytop coated substrate. For 200 mHz 0.20 cycle/s were observed (**A**), for 500 mHz 0.50 cycle/s (**B**), for 700 mHz 0.70 cycle/s (**C**) and for 1 Hz 1.00 cycle/s (**D**). Measurements were obtained using 87 FPS.

At higher frequencies (≥50 Hz), the detected movements of the droplet, expressed using the number of cycles per second, were lower than the applied frequency (Figure 3.25 and 3.26).

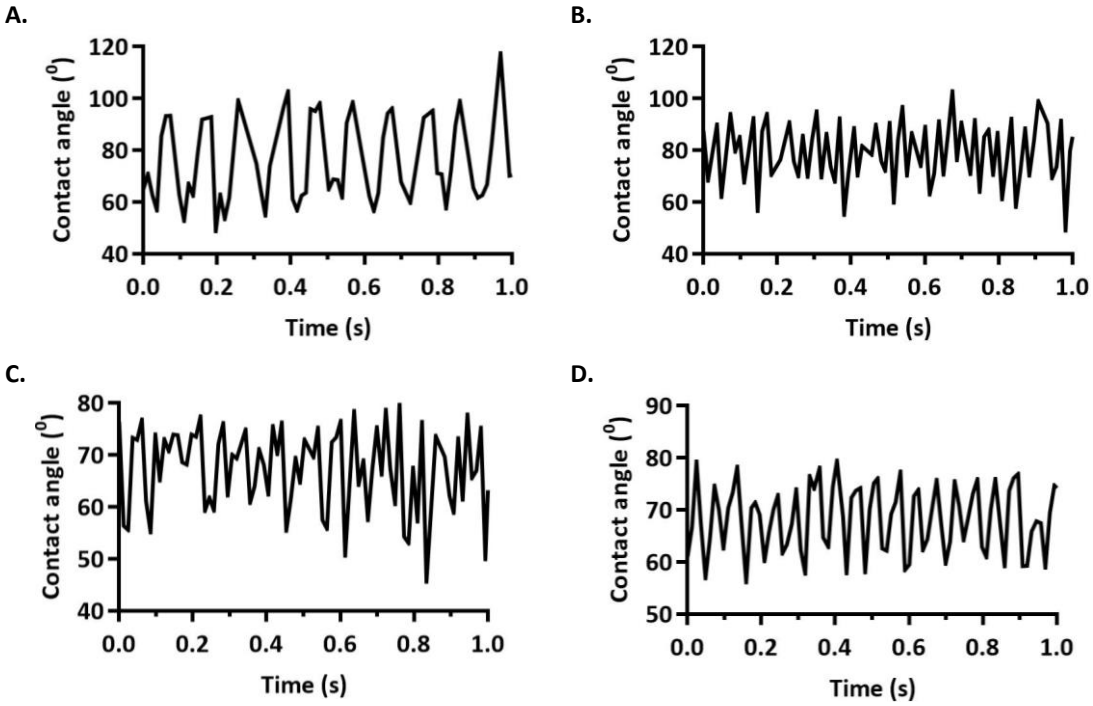

Figure 3.25 – Change in contact angle by applying 200V and a range of frequencies (10 Hz-100 Hz) across a water droplet and its underlying SU-8+Cytop coated substrate. For 10 Hz ~10 cycles/s were observed (**A**), 30 Hz ~29 cycles/s (**B**), 50 Hz ~23 cycles/s (**C**), 100 Hz ~20 cycles/s (**D**). Measurements were obtained using 87 FPS.

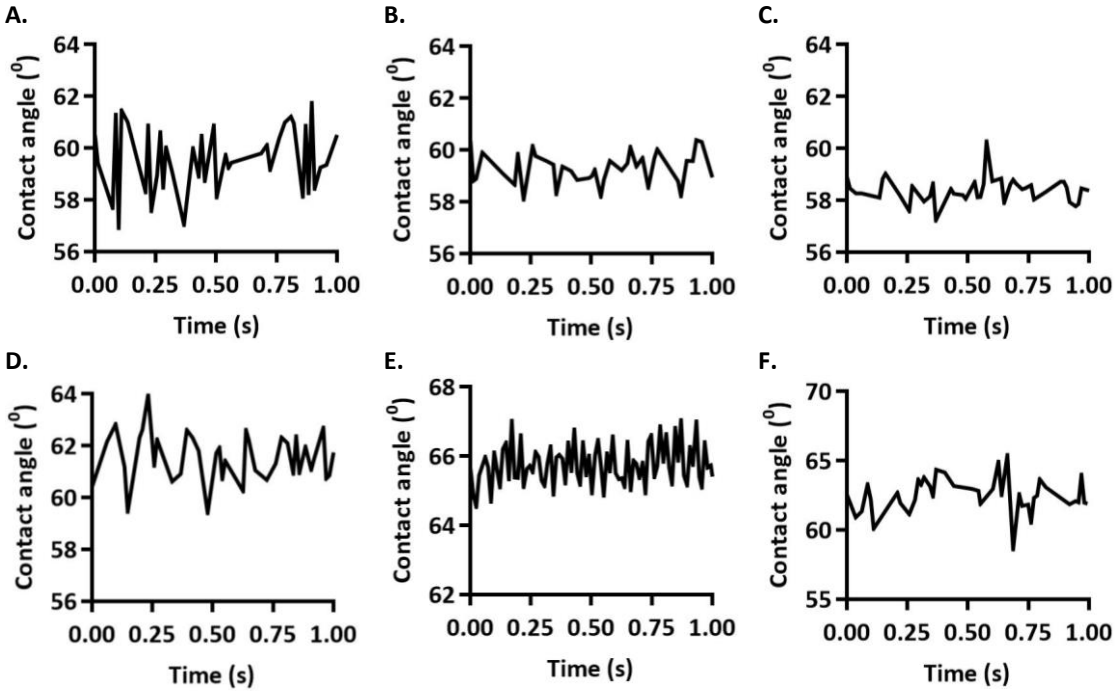

Figure 3.26 – Change in contact angle by applying 200V and a range of frequencies across a water droplet and its underlying SU-8+Cytop coated substrate; 200 Hz (**A**), 750 Hz (**B**), 1 kHz (**C**), 5 kHz (**D**), 6 kHz (**E**) and 10 kHz (**F**). Measurements obtained using 87 FPS showed an undefined number of cycles/s.

In addition, by increasing frequency the amount of retraction generally decreased while the actuated contact angle (contact angle obtained by applying a potential) was similar, as illustrated in Figure 3.27 in which an AC potential was applied from ca. 0.5 s.

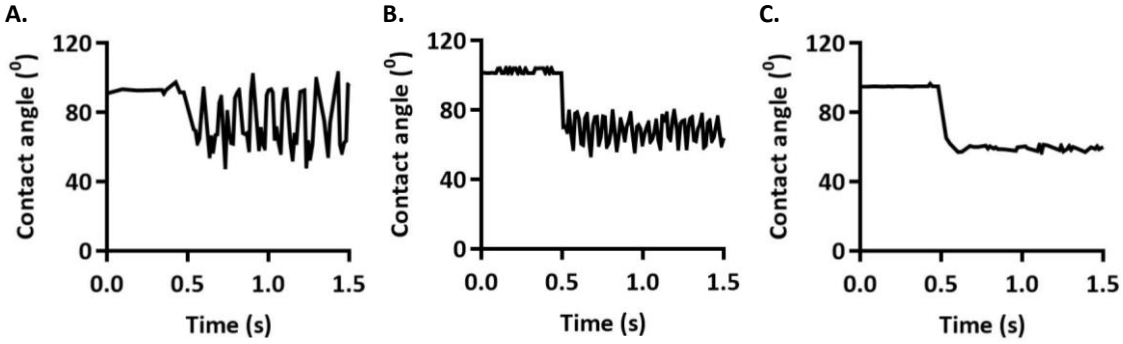

Figure 3.27 – Change in contact angle by applying 200V and a range of frequencies across a water droplet and its underlying SU-8+Cytop coated substrate; 10 Hz (**A**), 100 Hz (**B**), 200 Hz (**C)**. Measurements obtained using 87 FPS.

The fact that the number of the observed cycles/s of the droplets subjected to high frequencies (>50Hz) does not correspond to the frequency could be caused by the number of frames per second (FPS) the data was recorded with. With the used 87 FPS only a fraction of the movement of droplets subjected to frequencies >87 Hz could be detected. However, even using frequencies lower than 87 Hz the detected movement does not always correspond to the applied frequency (Figure 3.25B). The not-detected fraction of the movement is also not in proportion to the number of frames per second. These observations together with the generally decrease in retraction by increasing frequency indicates that other aspects, such as the lack of thermodynamic response of the droplet, could be of influence in the high frequency range. Similar results were obtained in the study of Lu *et al.* [20], in which the droplets responded up to a frequency of 33 Hz and the visible movement almost completely disappeared at 200 Hz.

To conclude, the Cytop top-layer proved to be an advantage above the use of a dielectric layer of SU-8 only, due to the higher initial contact angle and therefore larger electrowetting effect. The amount of contact angle change increased with potential, however due to dielectric breakdown above 250 V, 200 V was chosen as optimum potential. The frequency showed to have an influence on the behaviour of the droplet, although different frequencies resulted in a similar actuated contact angle, this suggests that the whole range of frequencies can be used to obtain an electrowetting effect.

3.3.4. Evaporation phenomena of the droplet

The electrowetting experiments were performed in air, therefore the shape change of the droplet was possibly not only caused by the applied potential but also by evaporation. To determine the actual influence of the potential on the droplets during the electrowetting process, the evaporation process and their influence on the droplet shape was investigated.

3.3.4.1. Evaporation process

To describe the evaporation process, the diameter, height and contact angle were measured while evaporating the droplet on a smooth (Figure 3.28A) and rough (Figure 3.28B) surface.

As illustrated in Figure 3.28 the evaporation process can be divided into four stages, which are in line with the literature [21] and described as follows. In stage 1 the droplet diameter remained constant while the height and contact angle decreased slightly. The contact line of the droplet was still pinned (adhered) to the surface. In stage 2 the contact angle and height decreased more rapidly than during the 1st stage, although the 1st and 2nd phase can also be submerged. The diameter remained constant, so the contact line was still pinned to the surface. In stage 3 the height and diameter of the droplet decreased simultaneously on smooth surfaces (droplet was no longer pinned to the surface) resulting in a constant contact angle. Upon rough surfaces the diameter and height did not decrease simultaneously. The change in contact angle up until the unpinning stage can be defined by contact angle hysteresis; the advancing contact angle at the beginning of the process which decreases until the receding contact angle just before unpinning. [22] In stage 4 the contact angle, diameter and height decreased to zero resulting in a completely evaporated droplet on smooth surfaces. On rough surfaces a more stepwise motion was observed, the constant diameter at the beginning of this stage indicates that the contact line of the droplet was again pinned to the surface and moved stepwise during the whole evaporation process. This stepwise motion could be caused by stopping of the movement of the droplet contact line due to irregularities. The time scale of each stage could depend on several factors such as the volume and composition of the liquid and could therefore vary.

A.

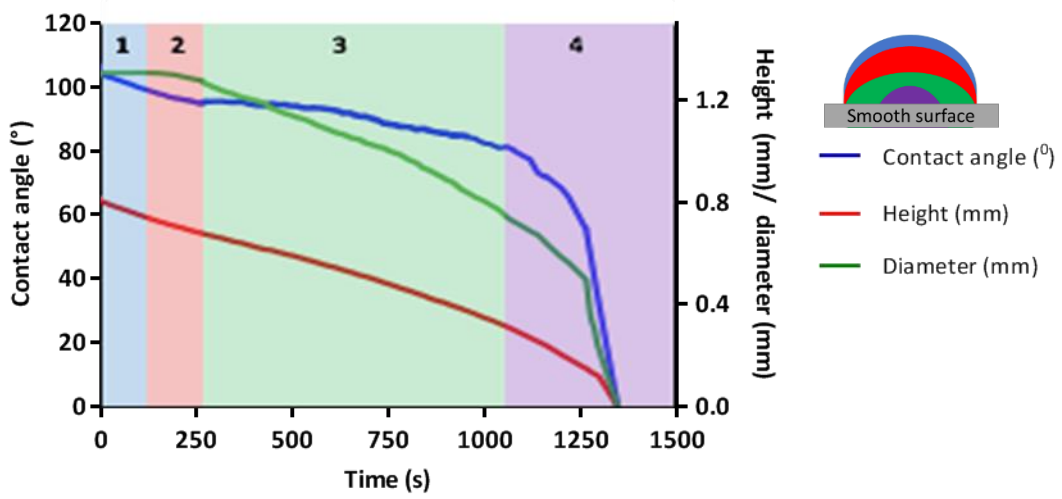

B.

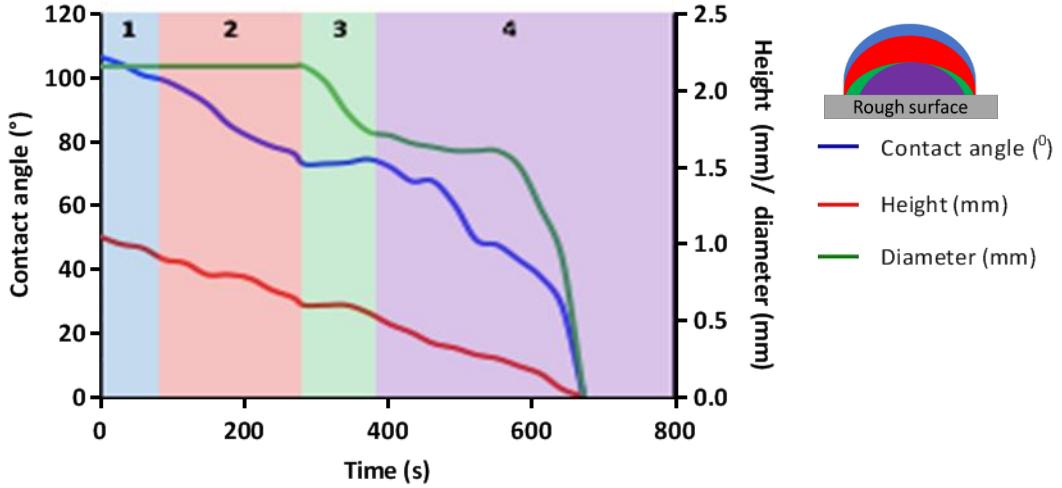

Figure 3.28 – Four stages of the evaporation process of a droplet (1 µL, 10 mM NaCl) positioned on a smooth (Cytop, $R_a \approx$ 2 nm; **A**) and rough (polystyrene, $R_a \approx$ 30 nm; **B**) surface. Including a droplet image with colours corresponding to the four stages in the graphs.

When the contact line of the droplet remains pinned to the surface during the whole evaporation process, a so called “coffee stain” effect will be formed by an outwards flow of the liquid inside the droplet induced by the pinned contact line and relatively higher evaporation flux at the periphery of the droplet. This ring shaped stain develops only when the contact angle of the liquid with the surface is more than zero, the contact line is pinned to the surface and the liquid evaporates. [23]

One of the main influences on the evaporation of droplets is the ambient temperature, therefore the effect of ambient temperature (17-22 ^{o}C) on the amount of evaporation was investigated. As illustrated in Figure 3.29 the rate of contact angle change of small droplets (ca. 1 µL) increased with temperature. A less apparent influence of the ambient temperature on the contact angle change rate was observed for larger droplets (ca. 25 µL). Probably due to a larger surface/volume ratio of small droplets (compared to large droplets), the evaporation is more affected by a temperature increase.

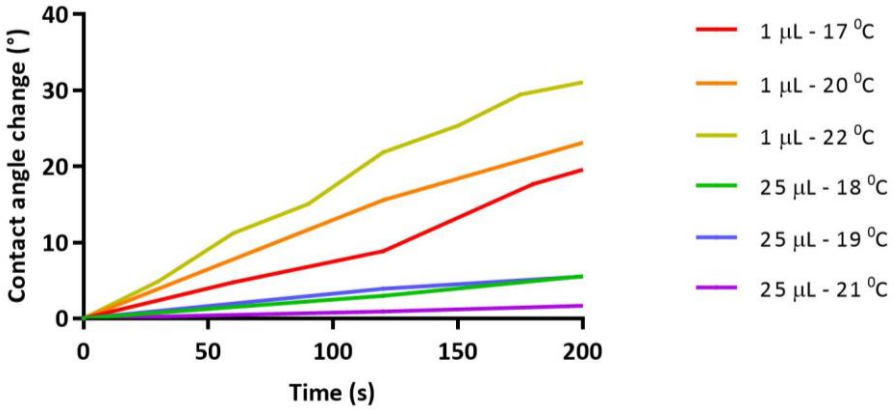

Figure 3.29 – Change in contact angle of a 10 mM NaCl droplet (1 and 25 µL) over time using a range of ambient temperatures (17-22 ^{o}C).

3.3.4.2. Comparison of shape change during the evaporation and electrowetting process

To exclude the influence of evaporation on the shape change of the droplet observed during the electrowetting process, the changes in droplet shape during evaporation were compared with the droplet shape changes during the electrowetting process. Since the main aim of this study is to create an electrowetting effect in fingerprints, the shape changes of droplets with compositions relevant to a fingerprint were recorded during evaporation; DI-water, glycerol (viscosity), 50 mM NaCl (salinity) and the model fingerprint solution. This resulted in a considerably larger droplet shape change during the electrowetting process than during evaporation only, even after 2 minutes of evaporation while the electrowetting process is typically on the order of a second (Table 3.4).

Table 3.4 – Droplet shape change during 2 min of evaporation and by applying a potential (200 V, 500 mHz) across a 5 µL DI water droplet and its underlying SU-8+Cytop coated substrate. The droplet shape change is defined by the change in horizontal, diagonal and vertical size as well as using the contact angle as illustrated in Figure 3.30.

		Horizontal (%)	Diagonal (%)	Vertical (%)	Contact angle (%)
Electrowetting	**DI-water**	12.10	8.00	11.76	16.35
Evaporation	**DI-water**	3.11	1.06	5.94	4.40
	Glycerol	0.83	0.50	1.05	1.12
	50 mM NaCl	0.39	0.82	3.23	2.04
	Model fingerprint solution	5.62	3.20	6.05	5.69

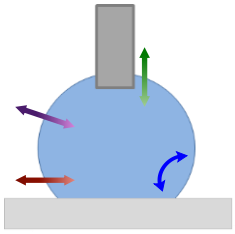

Figure 3.30 – Droplet illustrating the type of measurements to determine the droplet shape change: horizontal (red), diagonal (purple), vertical (green) and contact angle (blue).

The relatively large droplet shape change during the electrowetting process compared to the evaporation process suggests that the applied potential has an influence on the contact angle change. Although by vigorous movements of the droplet, a higher evaporation rate could be expected.

3.3.5. Influence of the fingerprint composition on the electrowetting on fingerprints application

To define the possibilities and limitations of the electrowetting on fingerprints application, the effects of the following fingerprint characteristics (compositional and physical) on the electrowetting process were investigated; salinity, viscosity, thickness of the fingerprint ridge, contact pinning and initial contact angle. Finally, the electrowetting on fingerprints application was studied using a mimicked fingerprint.

3.3.5.1. Influence of salinity on the electrowetting effect

The influence of salts on the electrowetting process was investigated due to their presence in a fingerprint and a decrease in electric permittivity is expected by increasing salt concentration which could affect the electrowetting process.

Droplets of a range of NaCl concentrations (0-50 mM) were subjected to a potential while the change in contact angle and movement of particles (added to the droplet) inside the droplet were measured. Figure 3.31 shows that the contact angle change slightly decreased by increasing NaCl concentration. The particle velocity decreased also by increasing NaCl concentration. On a side note, in the experiments using 50 mM NaCl, electrolysis occurred very rapidly, therefore these measurements might be less reliable.

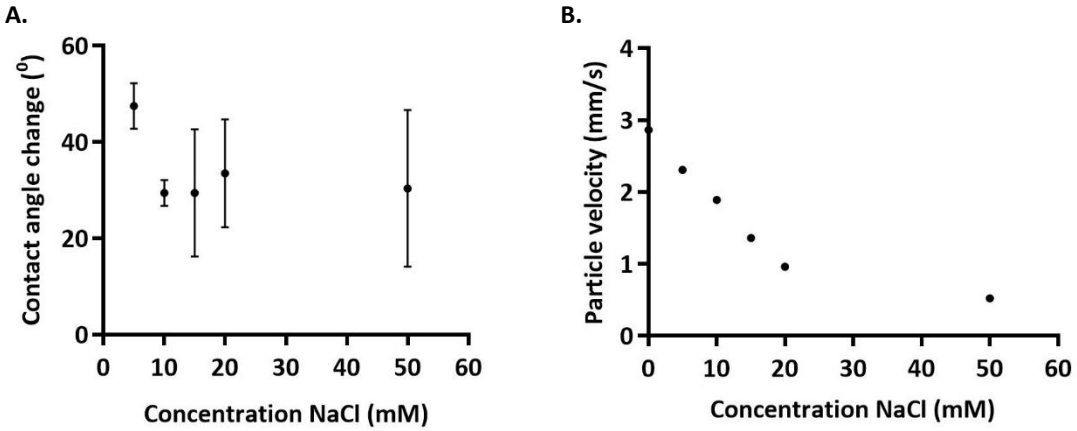

Figure 3.31 – Influence of salinity on the contact angle change by applying 200V, 500 mHz (**A**) and particle velocity by applying 200 V, 100 Hz (**B**) across a water droplet and its underlying SU-8+Cytop coated substrate.

The decrease in electrowetting effect by increasing salt concentration could be caused by the decrease in electric permittivity. An internal electric field generated by the salt ions could inhibit the external applied electric field, thereby suppressing the electrowetting effect. [24] The increase in salt concentration could also increase the surface tension, thereby decreasing the contact angle. A higher salt content could possibly also suppress the droplet contact line instability. [25] Contrary, Peykev *et al.* [26] suggested an independence of the electrowetting effect on the salt concentration as according to them the electrowetting effect is mainly caused by the polarisation of the dielectric layer rather than by a rearrangement of the double layer only.

To conclude, it was demonstrated that it is possible to obtain an electrowetting effect using low salt concentrations. However, a typical fingerprint salt concentration (ca. 45-88 mM NaCl and 15 mM KCl; Appendix, Table A.1) could be challenging because of the decreasing amount of movement by increasing salt concentration and the rapidly occurring of electrolysis and dielectric breakdown at high salt concentrations.

3.3.5.2. Influence of viscosity on the electrowetting effect

During ageing of fingerprints, the water content could decrease resulting in an increase in viscosity. To investigate whether this increase in viscosity is a limitation for the application of electrowetting on fingerprints, droplets of a range of glycerol/water content (0-90% glycerol in water) were subjected to a potential. By increasing glycerol content, not only the viscosity increases but also the dielectric constant. However, the difference in dielectric constant of water and glycerol is 700x smaller than the difference in viscosity, this suggests that the influence of the dielectric constant is probably considerably smaller than the viscosity (Table 3.5).

Table 3.5 – Viscosity and dielectric constant (at 20°C) of water and glycerol.

	Water	**Glycerol**	**References**
Viscosity (cP)	1.00	1414	[9]
Dielectric constant	80.36	41.14	[27, 28]

By increasing glycerol content and therefore viscosity, the movements of the particles inside the droplet slowed down and the contact angle change remained constant (Figure 3.32). This decrease in movement inside the droplet by increasing viscosity is in agreement with the literature [29] and may be a problem for the formation of a flow in more viscous aged fingerprints.

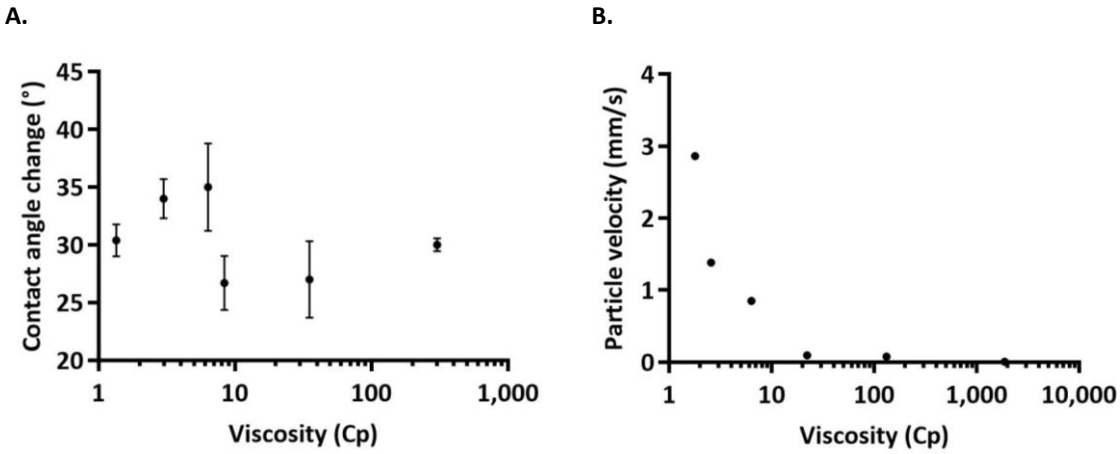

Figure 3.32 – Change in contact angle (**A**) and particle velocity (**B**) as function of viscosity by applying a potential of 200 V, 100 Hz across a water droplet and underlying SU-8+Cytop coated substrate.

3.3.5.3. Influence of a model fingerprint solution on the electrowetting effect

The fingerprint composition might raise limitations for the application of electrowetting on fingerprints, therefore not only the influence of salinity and viscosity were investigated but also the possibility of creating an electrowetting effect using a droplet of a model fingerprint solution. This mixture of fingerprint molecules, as outlined in the Appendix (Section A.1), could raise other limitations or possibilities.

A droplet of model fingerprint solution was positioned on a SU-8+Cytop coated substrate after which the droplet spread by applying a potential. However, by removing the potential manually and even after waiting for 30 s, the droplet retracted only slightly (Figure 3.33). The droplet is probably too much pinned to the surface and does not have enough force to return to its initial position.

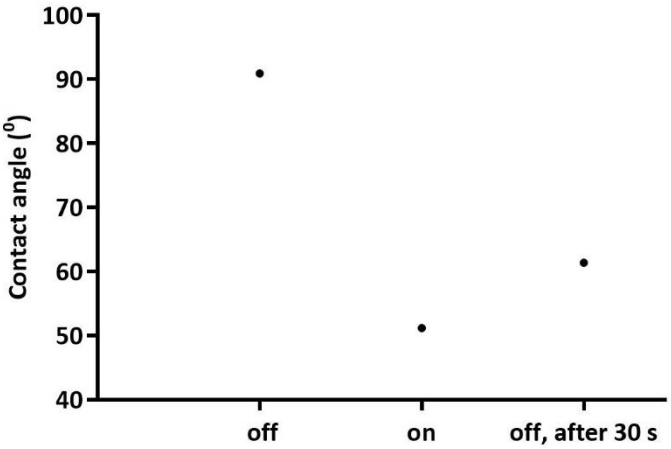

Figure 3.33 – Change in contact angle by applying 200 V, 500 mHz across a droplet of model fingerprint solution and the underlying SU-8+Cytop coated substrate.

To conclude, an increase in movement was obtained by decreasing salinity (both contact angle and particle movement) and viscosity (only particle movement). This might induce challenges to create a flow in a fingerprint, due to the high salt concentration in fingerprints (compared to the used concentration range) and the increasing viscosity by ageing of the fingerprint. Given that the droplet of model fingerprint solution almost did not retract upon removal of the potential, other unknown factors might also be of importance.

3.3.6. Influence of the physical structure of the fingerprint on the electrowetting on fingerprints application

Aside from the influence of the composition of the fingerprint solution, the physical characteristics of the fingerprint and interactions between the fingerprint and the surface could limit or ease the electrowetting process.

3.3.6.1. Influence of physical fingerprint characteristic on the electrowetting process

Initial contact angle

Despite the relatively high contact angle of the model fingerprint solution (90^{o}; Figure 3.33), literature mentioned contact angles of actual fingerprints on a variety of substrates of smaller than 30^{o}. [30] This low contact angle might be a problem for the application as less electrowetting effect was observed for lower initial contact angles (Figure 3.21). A possible solution could be the addition of a water droplet on top of the fingerprint or humidification of the fingerprint as discussed below.

Contact pinning

In contrast to a droplet, fingerprints have a wobbly contact line (edges of the fingerprint ridges; Figure 3.34), this indicates that fingerprint ridges are pinned to the surface at several positions.

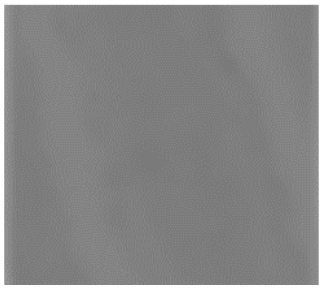

Figure 3.34 – Fingerprint recorded using the optical (3D) microscope (Zeta Instruments).

To obtain an electrowetting effect, the positions at which a liquid is pinned to the surface needs to be overcome to spread and retract the complete liquid. To investigate the pinning effect, a liquid pinned to the surface was simulated by the formation of a droplet of which one part was more pinned to the surface than the other part. This was

created by positioning a droplet on a hydrophobic surface (SU-8+Cytop) close to a hydrophilic surface (SU-8), after applying a potential (200V, 500 mHz) the droplet moved to the hydrophilic part but was hindered in its movement due to the presence of the top-electrode. This resulted in a droplet located partly on the hydrophobic and partly on the hydrophilic surface (Figure 3.35).

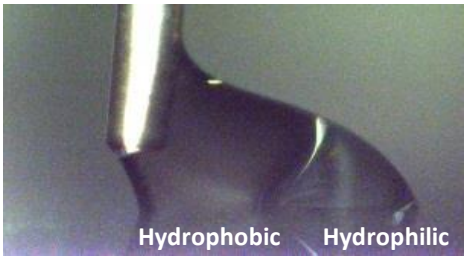

Figure 3.35 – Illustration of an irregular droplet, created by positioning partly on a hydrophobic surface (SU-8+Cytop) and partly on a hydrophilic surface (SU-8).

As shown in Figure 3.36, by applying a potential across a regular and irregular shaped droplet and the underlying substrate, the contact angle change of the regular shaped droplet was larger than the irregular shaped droplet (A/B versus C/D). The movement of the particles seemed also to be influenced by the droplet shape as shown by the fluorescent lines in the irregular shaped droplet (Figure 3.36D). It should be noted that the location of the needle could also be of influence.

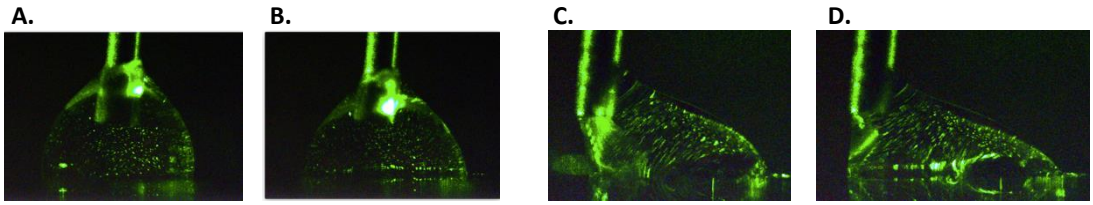

Figure 3.36– Illustrating the contact angle change and visualised movement inside a regular (**A, B**) and irregular shaped (**C, D**) droplet before (**A, C**) and by applying a potential of 200 V, 500 mHz across a water droplet and the underlying surface (**B, D**).

Thickness of the fingerprint ridge

The variation in height of the fingerprint residue might also be an issue for the applicability of electrowetting on fingerprints, as differences in height make it difficult to reach every part of the fingerprint in the same way which could result in the formation of more contact angle change/flow in certain parts. This problem can possibly be solved by the addition of a small amount of water to the fingerprint in the form of a

droplet or using humidification. Optical inspection showed that the addition of a water droplet did not lead to a considerable difference in shape and could therefore be considered as an option to enlarge the volume (Figure 3.37A/B). In contrast, immersion in salt water led to a destructive effect on the shape of the fingerprint (Figure 3.37C/D).

Figure 3.37 – Change in fingerprint shape before (**A**) and after immersing in DI water (**B**) and before (**C**) and after immersing in 0.8 M NaCl solution (**D**). Recorded using the optical (3D) microscope (Zeta Instruments).

To explore more thoroughly the possibility of adding water to a fingerprint to compensate for differences in height and a low initial contact angle, a fingerprint was mimicked by drying a droplet of model fingerprint solution on the SU-8+Cytop surface. Subsequently, a water droplet was placed on top of this stain and a potential of 200 V, 500 Hz was applied across the droplet and the underlying SU-8+Cytop coated substrate. This resulted in spreading of the droplet and very limited retraction by removal of the potential. This illustrates that the electrowetting of fingerprints application remains challenging.

3.3.6.2. Fingerprint pattern alteration during the electrowetting process

Besides the challenges that the physical structure of the fingerprint entails to obtain electrowetting, the consequences of the application of the electrowetting process on fingerprints must also be taken into account. By applying a potential across a fingerprint and the underlying substrate, the contact angle will change, resulting in a slight movement of the contact line. With respect to fingerprints, it is of importance not to alter the fingerprint pattern by this movement to avoid making a fingerprint unusable for identification purposes. Therefore, the amount of movement of the contact line was determined, whereby the scenario in which fingerprint ridges touch each other is taken as the worst-case scenario as ridge detail could then be lost. As shown in Figure 3.38, the distance between the ridges is ca. 1/3 of the width of a fingerprint ridge. To prevent the ridges from touching each other, the maximum allowed movement of the ridges is

then 16.6% of the width of the ridge. Experiments using a droplet with a diameter of ca. 5 mm showed a movement of 0.18–0.33 mm which is 3.3-7.4% of the droplet diameter. According to the literature a droplet with a diameter of 2 mm resulted in a movement of 0.05-0.10 mm which is 2.5-5.0% of the droplet diameter. [31] Given that the movement is smaller than the allowed 16.6% it is suggested that the chance that the fingerprint ridges would touch each other (and possibly merge together) under the used circumstances is negligible. Although, some minor changes of the fingerprint patterns could potentially occur.

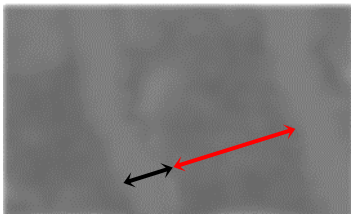

Figure 3.38 – Fingerprint recorded using the optical (3D) microscope (Zeta Instruments). Red arrow (~136 µm) indicating the fingerprint ridge width, black arrow (~54 µm) the fingerprint furrow width.

In addition, a possible change in contact line is likely to be irrelevant for the electrowetting on fingerprints application when a droplet of water is positioned on top of the fingerprint.

3.4. Conclusion

To improve the detection of fingerprints, the possibility of creating a flow in an (aged) fingerprint using electrowetting was explored. This could enhance the ability of fingerprint molecules to react with visualisation reagents and to create more homogenously distributed fingerprint ridges. The electrowetting effect was not only expressed in the conventional way by contact angle measurements but also by the amount of movement inside the droplet using particle tracking and by the change in surface coverage using QCM (Obj. 1). It was shown that QCM may have scope for detecting an electrowetting effect, although more research is required before application. Optimisation of the dielectric layer to prevent dielectric breakdown and obtaining a better understanding of the influence of certain factors (such as hydrophobicity) and inexplicable data are recommended. In addition, electrowetting induced movements inside the droplets were observed by the tracking of particles added to the droplets.

The droplets used in this study were not only subjected to a potential, but also to evaporation as the experiments were performed in air (Obj. 2). It was demonstrated that the evaporation had a negligible effect on the droplet shape change compared to the potential, but by vigorous movements of the droplet a higher evaporation rate could be expected.

The impact of the dielectric layer characteristics, potential and frequency on the electrowetting process were investigated to define the optimum conditions of this electrowetting application (Obj. 3). The most (trackable) movement inside the droplets was obtained using a frequency of 100/200 Hz and a high potential. The actuated contact angle appeared to be independent on frequency and increased with potential. 200 V was chosen as optimum, considering the strength of the dielectric layer. The addition of a hydrophobic top-layer increased the amount of electrowetting effect and was therefore used for further experiments in this research.

To determine the impact of the composition and physical structure of the fingerprint on the electrowetting of fingerprints application, the effect of the following fingerprint characteristics on the electrowetting process were investigated; viscosity, salinity,

height of the fingerprint, contact pinning and initial contact angle (Obj. 4). The amount of movement inside the droplet decreased by increasing viscosity and salinity as well as high salinity resulted rapidly in electrolysis, which might be inconvenient for the formation of a flow in (aged) fingerprints. Additional challenges might be present, suggested by the incomplete retraction of model fingerprint solution droplets after being subjected by a potential. The amount of contact pinning, low initial contact angle and uneven height distribution of a fingerprint could possibly also make this electrowetting of fingerprints application challenging. The structure and composition of the fingerprint does not only impact the electrowetting process, but the electrowetting process could also have an impact on the fingerprint (Obj. 4). Movements of the contact line could be a drawback of e.g. high potentials as the physical structure of the fingerprint could be affected when a potential is applied directly across the fingerprint and the underlying substrate, although it is unlikely that fingerprint ridges would merge and thereby alter the pattern. By applying a potential across a droplet positioned on top of a fingerprint and the underlying substrate, movement of the contact line of the droplet is likely to be irrelevant.

In summary, electrowetting could be used to create a flow in a droplet, however for application of electrowetting on fingerprints several challenges still needs to be overcome.

3.5. References

[1] H.C. Lee, R.E. Gaensslen, Advances in fingerprint technolgy, 2nd ed., CRC Press2001.
[2] H.C. Lee, S. Yun, S.H. Ko, K.H. Kang, An electrohydrodynamic flow in ac electrowetting, Biomicrofluidics, 3 (2009).
[3] L. Chen, E. Bonaccurso, Electrowetting - From statics to dynamics, Advances in Colloid and Interface Science, 210 (2014) 2-12.
[4] P. García-Sánchez, A. Ramos, F. Mugele, Electrothermally driven flows in ac electrowetting, Physical Review E, 81 (2010).
[5] D. Mampallil, D. van den Ende, F. Mugele, Controlling flow patterns in oscillating sessile drops by breaking azimuthal symmetry, Applied Physics Letters, 99 (2011).
[6] G. Sauerbrey, Verwendung von Schwingquarzen zur Wägung dünner Schichten und zur Mikrowägung, Zeitschrift für Physik, 155 (1959) 206-222.
[7] J.-W. Lin, D.-S. Wang, S.-K. Fan, Adjustment and measurement of contact angle with electrowetting on a quartz-crystal microbalance, Inventions, 3 (2018) 46.
[8] S. Bruckenstein, M. Shay, Experimental aspects of use of the quartz crystal microbalance in solution, Electrochimica Acta, 30 (1985) 1295-1300.
[9] University of Reading, Calculate density and viscosity of glycerol/water mixtures, http://www.met.reading.ac.uk/~sws04cdw/viscosity_calc.html, accessed: 26/4/2018.
[10] H. You, A.J. Steckl, Electrowetting on non-fluorinated hydrophobic surfaces, Journal of the SID, 21 (2014) 411-416.
[11] D.P. Papageorgiou, E.P. Koumoulos, C.A. Charitidis, A.G. Boudouvis, A.G. Papathanasiou, Evaluating the robustness of top coatings comprising plasma-deposited fluorocarbons in electrowetting systems, Journal of Adhesion Science and Technology,, 26 (2012) 12-17.
[12] Microchem, SU-8 3000 Permanent Photoresist.
[13] A. Quinn, R. Sedev, J. Ralston, Contact angle saturation in electrowetting, Journal of Physical Chemistry B, 109 (2005) 6268-6275.
[14] F. Mugele, J.-C. Baret, Electrowetting: from basics to applications, Journal of Physics: Condensed Matter, (2005) 705-760.
[15] F. Mugele, Fundamental challenges in electrowetting: from equilibrium shapes to contact angle saturation and drop dynamics Soft Matter, 5 (2009) 3377-3384.
[16] D. Klarman, D. Andelman, M. Urbakh, A model of electrowetting, reversed electrowetting, and contact angle saturation, Langmuir, 27 (2011) 6031-6041.
[17] A.G. Papathanasiou, A.T. Papaioannou, A.G. Boudouvis, Illuminating the connection between contact angle saturation and dielectric breakdown in electrowetting through leakage current measurements, Jounal of applied physics, 103 (2008).
[18] H.J.J. Verheijen, M.W.J. Prins, Reversible electrowetting and trapping of charge: model and experiments, Langmuir, 15 (1999) 6616-6620.
[19] H. Li, M. Paneru, R. Sedev, J. Ralston, Dynamic electrowetting and dewetting of ionic liquids at a hydrophobic solid–liquid interface, Langmuir, 29 (2013) 2631-2639.
[20] Y. Lu, A. Sur, C. Pascente, S.R. Annapragada, P. Ruchhoeft, D. Liu, Dynamics of droplet motion induced by Electrowetting, International Journal of Heat and Mass Transfer, 106 (2017) 920-931.
[21] C. Bourges-Monnier, M.E.R. Shanahan, Influence of evaporation on contact angle, Langmuir, 11 (1995) 2820-2829.
[22] M. Nagy, J. Škvarla, Determination of contact angle hysteresis of water microdroplets evaporating on hydrolyzed PET foils, Acta Montanistica Slovaca, 18 (2013) 125-128.
[23] R.D. Deegan, O. Bakajin, T.F. Dupont, G. Huber, S.R. Nagel, T.A. Witten, Capillary flow as the cause of ring stains from dried liquid drops, Nature, (1997) 827-829.
[24] N.P. Gavish, K., Dependence of the dielectric constant of electrolyte solutions on ionic concentrations - a microfield approach, Physical Review E, 94 (2016).

[25] M. Vallet, M. Vallade, B. Berge, Limiting phenomena for the spreading of water on polymer films by electrowetting, The European Physics Journal B, 11 (1999) 583-591.
[26] V. Peykov, A. Quinn, J. Ralston, Electrowetting: a model for contact-angle saturation, Colloid and Polymer Science, 278 (2000) 789-793.
[27] J. Wyman Jr, Measurements of the dielectric constants of conducting media, Physical Review, 35 (1930) 623-634.
[28] G. Akerlof, Dielectric constants of some organic solvent-water mixtures at various temperatures, Journal of the American Chemical Society, 54 (1932) 4125-4139.
[29] F. Mugele, J.-C. Baret, D. Steinhauser, Microfluidic mixing through electrowetting-induced droplet oscillations, Applied Physics Letters, 88 (2006).
[30] B. Scruton, B.W. Robins, B.H. Blott, The deposition of fingerprint films, Journal of Physics D Applied Physics, 8 (1975) 714-723.
[31] F. Lapierre, M. Jonsson-Niedziolka, Y. Coffinier, R. Boukherroub, V. Thomy, Droplet transport by electrowetting: lets get rough!, Microfluidics and Nanofluidics, (2013).

Detection of fingerprints using MIPs 4

4.1. Introduction

At present, fingerprint techniques and/or research are used for two purposes, identification (visualisation) and retrieving intelligence information. Here, intelligence information is defined as knowledge about the fingerprint donor's behavior such as smoking [1], diet [2, 3], cosmetics [4, 5], drug use [6, 7] and explosive residue [8] and/or characteristics such as gender [9, 10], age [11, 12] and blood group [13]. In this chapter, molecularly imprinted polymers (MIPs) were explored to address both purposes (visualisation and retrieving of intelligence information) simultaneously.

Currently, most widely used fingerprint techniques and/or research uses visualisation reagents (such as ninhydrin [14], indanedione [15, 16], physical developer and cyanoacrylate), mass spectrometry [17-19], nanoparticles and/or antibodies [20]. [21] Each of these techniques/methodologies have their advantages and disadvantages as outlined in Table 4.1. For the purpose of visualisation, the mentioned visualisation reagents are shown to be the established methodology for casework because of their relative ease of use and good visualisation properties. The nanoparticles are being investigated as a technique for visualisation purposes and in combination with antibodies to detect molecules of interest to retrieve intelligence information. [1] Fluorescent antibodies on its own could also be used to address both the visualisation/identification and retrieving intelligence information purpose. However, an alternative for this technique is desired because of the limited storage capabilities [22] and the requirement to use test animals, [23] resulting in an expensive production.

MIPs have shown in the last years to possess good recognition characteristics and have been seen as the synthetic equivalent of biological recognition molecules such as antibodies. Therefore, MIPs could possibly act as an alternative for antibodies with the aim of detecting fingerprints. The optical (fluorescence) and recognition characteristics

of fluorescent MIPs makes MIPs not only a good candidate for visualising fingerprints, but also to retrieve intelligence information. As fluorescent MIPs could recognise and bind specifically to their target molecule, a fluorescent fingerprint could be obtained when the target molecule is present in the fingerprint, gaining information about the presence of specific molecules in the fingerprint and visualising the fingerprint simultaneously.

Till now, intelligence information is mainly retrieved using mass spectrometry, which has demonstrated to be able to detect molecules in a fingerprint with high specificity, however it requires specialist knowledge to obtain the results. MIPs can perhaps function as a preliminary technique or in case of high enough specificity as an alternative for mass spectrometry.

Table 4.1 – Characteristics of currently used/investigated fingerprint techniques. NA=not applicable. *No requirement of specific (instrumental) knowledge. *[2]Nanoparticles/quantum dots can be used in combination with antibodies to retrieve intelligence information.

	Visualisation reagents	Mass spectrometry	Nanoparticles/ quantum dots	Antibodies	MIPs
High stability	✓	NA	✓	X	✓
Relatively cheap	✓	X	X /✓	X	✓
Easy applicable*	✓	X	✓	✓	✓
Visualisation	✓	X	✓	✓	✓
Intelligence information	X	✓	X*[2]	✓	✓

A possible drawback of using MIPs for the detection of fingerprints is the choice of synthesis solvent. As MIPs are synthesised in the presence of their target molecule, also called template, both the MIPs and the target molecule (here the protein albumin) are dissolved in the same solvent, which can be an organic solvent or water. Because of the destructive effect of organic solvents on the target molecule albumin (a protein), water was chosen as solvent for this application. However, this could cause a challenge as in this application MIPs have to move from the aqueous phase, in which they are synthesised, into fingerprints, which are relatively hydrophobic, to bind to the target molecule present in the fingerprint. Therefore, the influence of the hydrophobicity of

fingerprints and MIPs on this application was investigated by adjusting the MIPs composition, the hydrophobicity of the MIPs was modified by varying the ratio tBAm/acrylamide monomers, and the fingerprint composition. The latter was addressed by the formation of model fingerprint solutions with a low and high content of hydrophobic molecules which were subsequently positioned in the form of a stamp or droplet on a substrate; hereafter referred to as simulated fingerprints. Another possible limiting factor for this application may be the influence of the fingerprint matrix. As mentioned earlier, the presence of hydrophobic molecules such as fatty acids, wax esters and triglycerides in the fingerprint could decrease the permeability of MIPs in the fingerprint. In addition, the presence of molecules different to albumin, such as other proteins, in the fingerprint could result in false positives when these molecules also bind to the MIPs. Therefore, the specificity of the MIPs was determined by measuring the affinity of the MIPs towards their target molecule albumin and other relevant molecules.

To summarise, in this research MIPs were explored for the purpose of fingerprint visualisation and specific component detection (retrieving intelligence information) whereby the following objectives were investigated:

- Determination of the most appropriate type of MIPs as well as retrieving compositional information about the MIPs.
- Understand the influence of the fingerprint composition/matrix on the behaviour of the MIPs (including false positives).
- Determination of the influence of the substrate on the detection of fingerprints using MIPs.
- Estimation of the visualisation quality of the fingerprints visualised using MIPs.
- Investigation of the scope and limitations of the detection of fingerprints using MIPs, by analytical techniques.

4.2. Methods

The MIPs technique is based on the molecularly recognition characteristics of polymers towards a target molecule, whereby monomers were polymerised around a target molecule, followed by extraction of the target molecule. Resulting in a polymer (MIP) with a cavity/series of recognition sites which suits the target molecule. In this section, first the choice of target molecule, MIPs synthesis solvent and substrate of the fingerprint are discussed followed by the synthesis of these MIPs, set-up of the fingerprint application and analyses.

In this research albumin was used as target molecule and trypsin as control molecule, because of their high abundancy and assumed absence in fingerprints, respectively. [24] Bovine serum albumin (BSA) and human serum albumin (HSA) have similar sequential and structural properties, [25] therefore they could both be used interchangeably, but in this research BSA was chosen over HSA for logistic reasons. As the MIP technique is based on molecular recognition, a small change in sequence and/or structure of the target molecule might affect the affinity with the MIPs. Therefore, the affinity between BSA imprinted MIPs (MIPs synthesised for the target molecule BSA) and both HSA and BSA was measured.

The MIPs can be synthesised in organic solvents or water. In this research water was chosen as solvent because of the destructive effect of organic solvents on proteins such as albumin, which could affect the recognition capabilities of the MIPs towards albumin. However, the use of aqueous soluble MIPs brings an extra challenge. As fingerprints are relatively hydrophobic and become more so with time, the permeability of aqueous MIPs in a relative hydrophobic fingerprint environment might be a limiting factor for this application and was therefore investigated.

The fingerprints were deposited on a variety of substrates, glass, plastics and stainless steel, to obtain a good understanding on which type of substrates fingerprints could be detected using MIPs. Porous surfaces were not taken into consideration because of the complexity regarding the absorption of the MIP solution on the substrate and the difficulty to perform the washing step (Section 4.2.3).

4.2.1. Synthesis of the MIPs

The production of the fluorescent MIPs was performed via solid-phase synthesis, based on the protocol of Canfarotta *et al.* [26]. The procedure used in this research consists of the following 5 parts as schematically represented in Figure 4.1 and discussed in more detail in the next section (mentioned amounts correspond to two batches).

1. Solid-phase preparation: glass beads were salinised in order to introduce primary amines to the surface of the glass beads.
2. Immobilisation of the target molecule: the target molecule (here the proteins albumin or trypsin) was bound via glutaraldehyde to the glass beads.
3. Synthesis of the polymer around the target molecule.
4. Collection of the MIPs: separation of high affinity-MIPs from low-affinity MIPs, unreacted monomers and the target molecule (connected to the glass beads) using solid-phase extraction cartridges.
5. Removal of residual fluorescent monomers: fluorescent monomers which were not implemented in the polymer were removed using gel or centrifuge filtration.

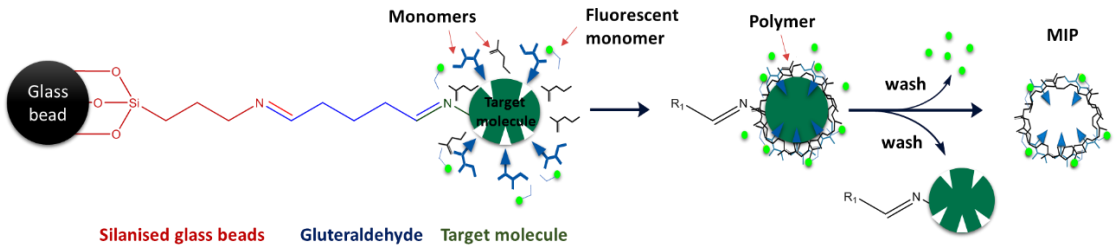

Figure 4.1 - Schematic overview of the synthesis of the MIPs and separation from the glass beads and unbound fluorescent molecules. R_1 is the glass beads and glutaraldehyde rest-chain.

Step 1: Activation and silanisation of glass beads

Glass beads were hydroxylated/activated by boiling in 4M sodium hydroxide for 15 min. (Figure 4.2). Thoroughly rinsed with deionised water and placed in a solution of 50/50 sulphuric acid/water for 30 min. Subsequently washed with water and phosphate buffered saline (PBS) to restore the pH to 6-8. Afterwards the glass beads were rinsed with acetone and dried under vacuum for 15 min and in the oven at 150 °C for 30 min.

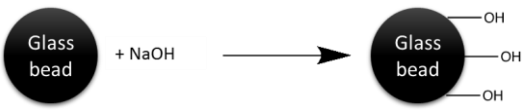

Figure 4.2 – Hydroxylation of the glass beads

After cooling, the activated glass beads were silanised by immersing in anhydrous toluene containing 2% v/v (3-aminopropyl)triethoxy-silane (0.4 mL/gram glass beads), while purging under nitrogen. The solution was left overnight at 70 ^{o}C to react (Figure 4.3). Afterwards, the silanised glass beads were rinsed with methanol and acetone, and dried under vacuum for 15 min and in the oven at 150 ^{o}C for 30 min.

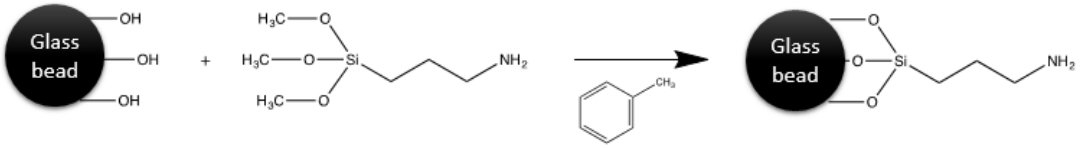

Figure 4.3 – Silanisation of the hydroxylated glass beads.

The stability and presence of silane was confirmed by two tests. 1 mL of acetonitrile and a spatula tip of dansyl chloride was added to a spatula tip of silanised glass beads and incubated in the dark for 1 hour. Subsequently the acetonitrile was removed and the glass beads were placed under a UV lamp to observe green fluorescence when silane was present. In the second test, a spatula tip of glass beads was added to 1 mL of 65 ^{o}C water, following by removal of the water (repeated twice) then 1 mL cold water was added and removed again. After these warm and cold-water treatments, the first test was repeated to confirm the presence of silane.

Step 2: Immobilisation of the target molecule

Silanised glass beads were incubated in a solution of glutaraldehyde (5%) in PBS solution (pH 7.4) while slightly stirring for 1 hour. The mechanism of the reaction between glutaraldehyde and the primary amines on the silanised beads is described in Figure 4.4.

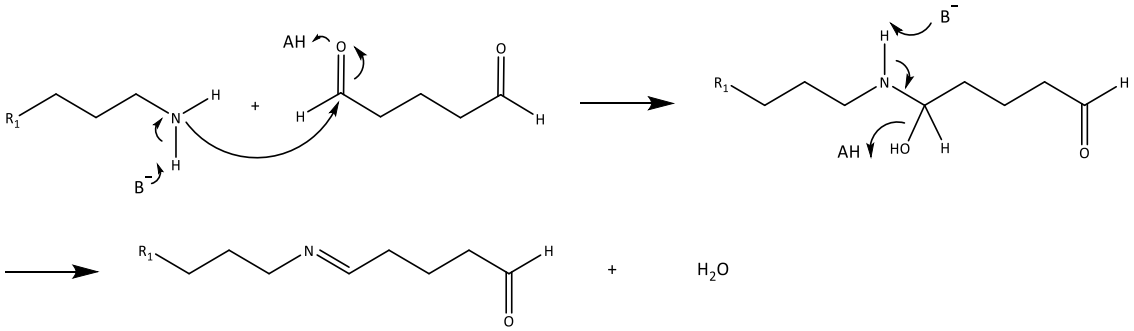

Figure 4.4 – Reaction mechanism for the binding of glutaraldehyde to the glass beads (R_1=silanised glass beads binding side, AH=acid, B=base).

Subsequently the solution was washed with water using a vacuum filter to remove the residual glutaraldehyde and rinsed with PBS to secure a pH of 7.4. In the meantime, the target molecule (here the proteins BSA or trypsin) was dissolved in PBS (1 mg/mL) and added to the glass beads. This solution was stirred for 1 hour and left overnight to react (Figure 4.5). To remove unbound proteins, the solution was washed with water.

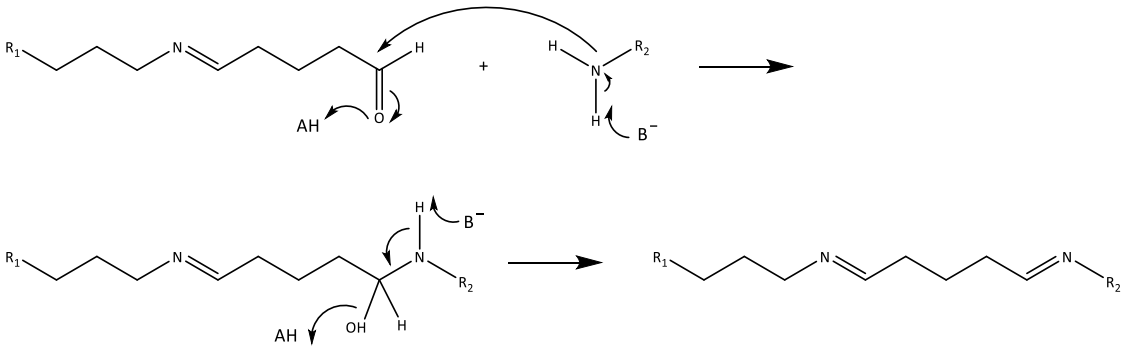

Figure 4.5 – Reaction mechanism for coupling the template molecule to the glass beads. R_1=silanised glass beads binding side, R_2= template, AH=acid and B=base.

To confirm the presence of proteins in the solution (bound to the glutaraldehyde), a bicinchoninic acid protein test was performed, showing a colour change from green to purple when proteins were present. In this test, cupper is reduced (Cu^{2+} to Cu^{+}) in an alkaline medium using the amino groups of the protein (step 1 of Figure 4.6). After which a purple complex was formed by chelation of bicinchoninic acid (step 2 of Figure 4.6). [27] Subsequently the solution was left under vacuum/nitrogen (inert environment); later referred to as the protein solution.

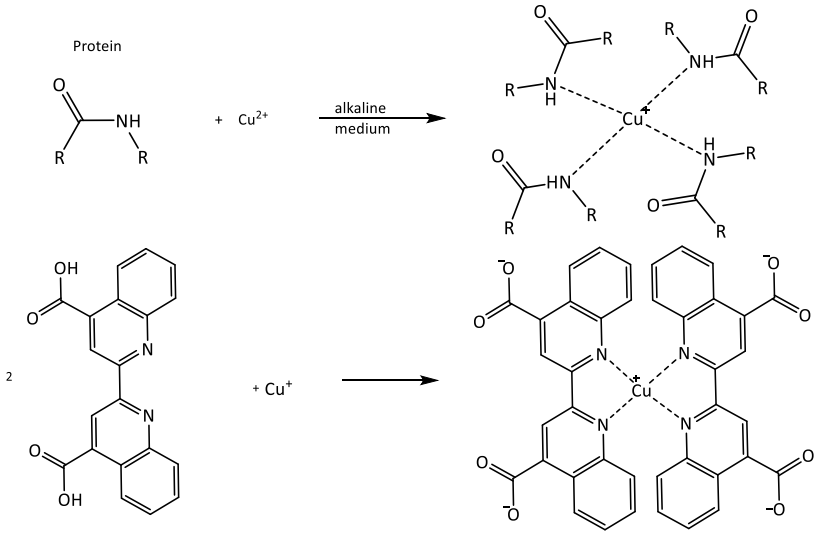

Figure 4.6 – Bicinchoninic acid protein test reaction equation. Step 1 (top): reduction of Cu^{2+} to Cu^{+} using a protein. Step 2 (bottom): the formation of a purple bicinchoninic acid – Cu^{+} complex.

Step 3: Synthesis of the fluorescent polymer shell

After immobilising the target molecule (here the proteins albumin or trypsin) to the glass beads, the monomers were polymerised around the target molecule.

Two type of polymers, nano and linear MIPs, were synthesised to investigate the ease of permeability of MIPs in fingerprints by varying the size/shape and possibly hydrophobicity of the MIPs, hereafter referred to as $_{N}$MIPs and $_{L}$MIPs, respectively. The $_{L}$MIPs and $_{N}$MIPs were formed using the monomer mixtures as outlined in Table 4.2. To create $_{L}$MIPs of a range of hydrophobicities, the ratio of acrylamide and tBAm was varied while the total molar amount acrylamide plus tBAm was kept constant. The acrylamide/tBAm ratios of MIP solutions 1 to 5 were respectively, 12/5 (outlined MIP mixture), 10/7, 5/12, 3/14, 2/15. To form $_{N}$MIPs, acrylamide, tBAm and APMA were not included because of their relatively negligible influence in comparison to NIPAm and BIS.

Table 4.2 – Composition to form linear MIPs (left) and nano MIPs (right)

Linear MIPs	
Fluoresceinylacrylamide	1.3 mg
Acrylic acid	2.2 µL
Acrylamide	30.0 mg
tBAm	22.3 mg
APMA	5.5 mg
DI-water	100 ml

Nano MIPs	
Fluoresceinylacrylamide	1.3 mg
Acrylic acid	2.2 µL
NIPAm	39.0 mg
BIS (cross-linker)	3.0 mg
DI-water	100 ml

The monomer solution was sonicated for approximately 2 min and placed under nitrogen. The initiator ammonium persulphate and the catalyst sodium bisulfite were dissolved in DI-water and added together with the monomer solution to the protein solution under nitrogen conditions. This mixture was left overnight in the dark. The mechanism of the free-radical polymerisation is described in Figure 4.7.

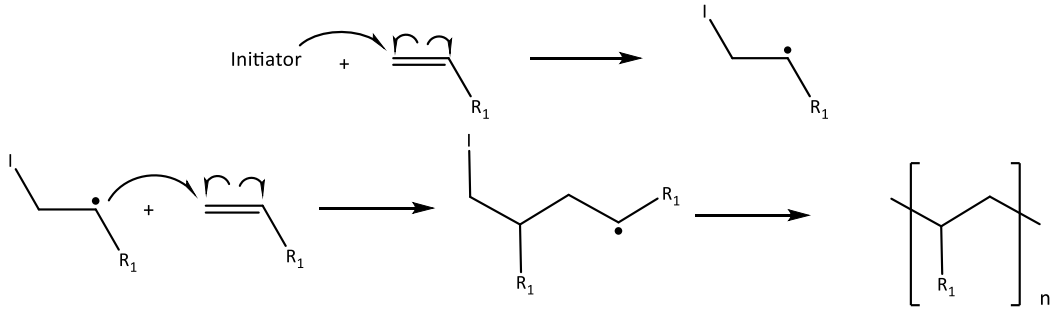

Figure 4.7 – Free-radical polymerisation mechanism, first formation of a radical monomer using an initiator after which the polymerisation continues. R_1= monomer rest-group.

Step 4: Collection of the MIPs

The glass beads and polymer mixture formed at the end of step 3 were transferred to a SPE cartridge, after which by addition of water at room temperature residual unreacted monomers and MIPs with a low affinity to the target molecule were eluted by means of vacuum. Afterwards the high-affinity MIPs were eluted by addition of heated (65 ^{o}C) water.

Step 5: Removing of unreacted fluorescent monomers

After the synthesis of the MIPs, residual unreacted fluoresceinylacrylamide was removed to ensure that the fluorescence of the MIP solution only originates from fluorescent MIPs and not from unreacted fluoresceinylacrylamide. Due to a difference in size of the $_{N}$MIPs and $_{L}$MIPs, both MIPs require another procedure as discussed below. After the removal of the unreacted fluoresceinylacrylamide, the MIP solution was stored in the fridge to prevent bacteria growth and in the dark to prevent photo bleaching.

Gel filtration was used to remove the residual unreacted fluoresceinylacrylamide from the fluorescent $_{L}$MIPs. This technique is a size separation based method, the largest molecules will go quickest through the gel followed by the smaller ones which stay longer in the pores. The $_{L}$MIPs of step 4 were added to a SPE cartridge filled with Toyopearl HW-50S (500-80.000 MW) gel. After the $_{L}$MIPs have entered the gel, a solution of 50/50 acetonitrile/water was added to elute the solution within a practical elution time and to provide a good separation. Subsequently, the eluted solution was collected in fractions. Afterwards the gel was washed with 50/50 acetonitrile/water solution to ensure that the complete MIP solution was removed from the gel. This process was repeated until the required volume of MIP solution was collected. To determine which fractions were fluorescent, the fluorescence of the fractions was measured using the FluoroMax-2 spectrofluorometer (Horiba Scientific).

Centrifugal filtration was used to remove the residual unreacted fluoresceinylacrylamide from the fluorescent $_{N}$MIPs solution. In this research the SIGMA 3-16P centrifuge (SIGMA) and 30 kDa MWCO filter were used, as the MIPs were

expected to be larger than 30 kDa and the unreacted fluoresceinylacrylamide smaller. The unreacted fluoresceinylacrylamide will go through the filter (filtrate) and the fluorescent MIPs remain above the membrane. The $_N$MIP solution of step 4 was centrifuged at 3000 RPM for 10 min, the filtrate was removed and water was added to the MIP solution. To keep the MIPs concentration equal, a similar amount of water was added to the solution as removed via the filtrate. This process was repeated till fluorescence was no longer observed in the filtrate, suggesting all unreacted fluoresceinylacrylamide was removed from the MIP solution.

4.2.2. Analysis of the MIPs

4.2.2.1. Surface plasmon resonance (SPR) measurements

The affinity between the MIPs and the molecules of interest (target and control molecules) was measured using two SPR instruments, the BIAcore 3000 SPR system with BIAEvaluation fitting software (GE Healthcare) and the SPR Navi 220A (BioNavis).

First the SPR chips were conditioned in mercaptoundecanoic acid to create a carboxylic end group at the surface, followed by coupling of the MIP or protein via a NH_2-group using EDC/NHS as shown in Figures 4.8 and 4.9.

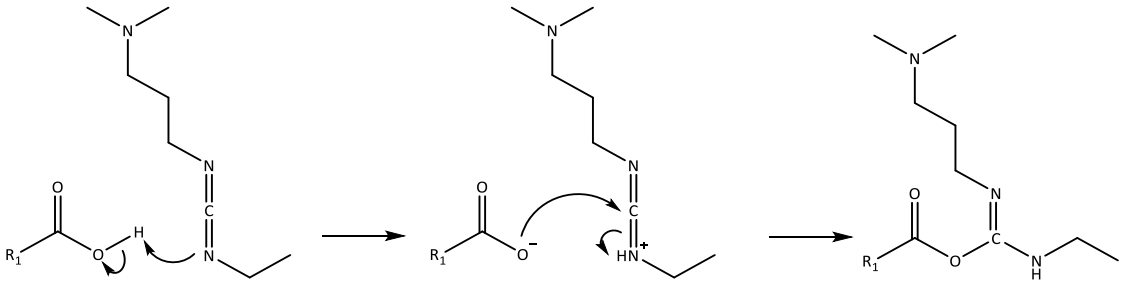

Figure 4.8 – N-(3-dimethylaminopropyl)-N-ethylcarbodiimide (EDC) coupling to the SPR chip (R_1).

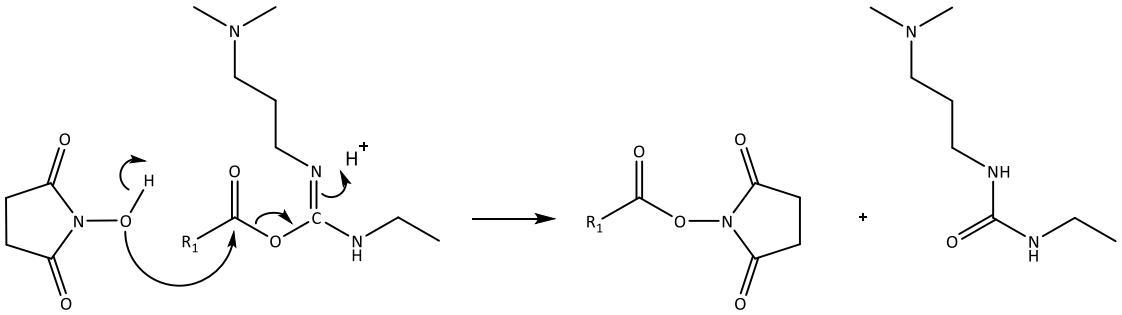

Figure 4.9 – N-hydroxysuccinimide (NHS) coupling to the SPR chip (as prepared in Figure 4.8). In which R_1 is SPR chip.

Subsequently the MIPs or target molecules were immobilised to the SPR chip (Figure 4.10).

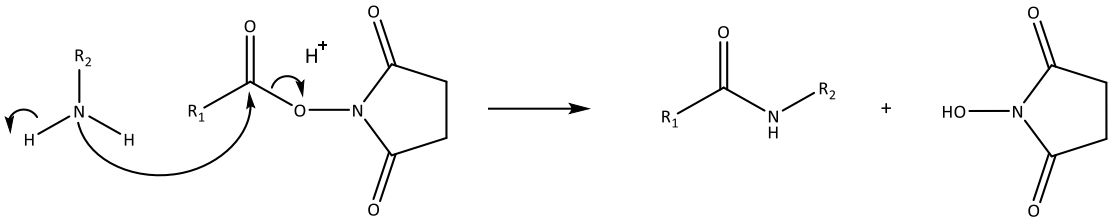

Figure 4.10 - Coupling of the target molecule or MIP to the SPR chip (as prepared in Figure 4.9). In which R_1 is gold SPR chip and R_2 is the target molecule or MIP to be coupled to the SPR chip.

Both the EDC/NHS coupling and the coupling of the MIPs or target molecules to the SPR chip were performed inside the SPR instrument.

Depending on the type of measurements, MIPs or target molecules were immobilised on the SPR chip after which the complementary molecules (target molecules when MIPs were immobilised, MIPs when target molecules were immobilised) were injected during the analysis. In addition, analysis performed to determine the dissociation constant required the injection of at least 5 concentrations of MIPs (when target molecules were immobilised) or target molecules (when MIPs were immobilised).

In this research the target molecules HSA, BSA, trypsin and streptavidin were dissolved in PBS solution and the MIPs in DI-water or acetate buffer. Buffer exchange of the keratin solution was performed by replacing urea with PBS using centrifuge filtration.

4.2.2.2. Matrix-assisted laser desorption/ionisation - Time of Flight - Mass Spectrometry (MALDI-ToF-MS)

MALDI-ToF-MS analysis were performed using the Voyager-DE STR with Voyager software (Applied Biosystems) to study the composition of the $_L$MIPs. This soft ionisation technique was chosen because of the possibility to retrieve knowledge about the order and thereby ratio of the monomers in the polymer. Developing a method to retrieve knowledge about the order of the monomers would be useful for the development of MIPs which are targeting peptides with an amino acid sequence of interest.

These analyses were performed using an accelerating voltage of 25 kV, 71.4% grid voltage, delay time of 200 ns and laser intensity of 2012. Spectra were obtained in

reflective mode and based on a sum of spectra of in total 50 shots. The samples were prepared as follows; the MIPs solutions were dried, dissolved in THF and mixed with a matrix of 0.2M 2,5-dihydroxybenzoic acid. Subsequently the sample was spotted on the MALDI plate.

4.2.2.3. Time of Flight - Secondary Ion Mass Spectrometry (ToF-SIMS)

ToF-SIMS measurements were performed on the ToF-SIMS 5 (IONTOF GmbH) to investigate the molecular composition of a fingerprint visualised using MIPs. Measurements were performed using a 25 keV Bi_3^+ primary ion beam, in positive ion mode and by applying the flood gun. Fingerprint imaging measurements were performed by scanning several patches of 500x500 µm each. The spectra were internally calibrated using a mass list, containing at least 5 of the following ions CH_3^+, Na^+, $C_2H_3^+$, Si^+, $C_2H_5^+$, K^+, $C_3H_3^+$, $C_3H_5^+$, $C_3H_7^+$, $C_3H_8^+$, $C_4H_5^+$, $C_4H_7^+$, $C_4H_9^+$, $C_5H_7^+$, $C_6H_7^+$, $C_7H_7^+$ and $C_5H_{10}^+$.

4.2.3. Application of MIPs on fingerprints

In this study fluorescent MIPs targeting BSA and trypsin were synthesised to detect BSA and trypsin in a fingerprint and thereby visualising the fingerprint.

The substrates used to deposit fingerprints on were cleaned by sonicating in acetone for 10 min. Hands were washed with water and soap. Both were dried and fingerprints were deposited on the cleaned substrates after 30 min. Subsequently, the fingerprints were spiked with a protein solution to start the experiments with a known concentration; a third of the fingerprints were immersed in aqueous BSA solution (10 µM), a third in aqueous trypsin solution (10 µM) and a third was kept natural. The fingerprints were left overnight to give the proteins the time to enter the fingerprint. Subsequently, the fingerprints were washed with water to remove proteins which did not enter the fingerprint. After immersing in MIP solution for 72h, whereby drying out of the fingerprint was prevented by adding MIP solution, the fingerprints were washed with water to remove unbound MIPs. The effect of the washing procedure on the application was based on the amount of removed fluorescence in and around the fingerprint as well as the amount of removed target molecule. The latter was investigated by tracking of BSA and trypsin (labelled with fluorescein for visibility

purposes) throughout the complete procedure of spiking the fingerprint with protein, washing, immersing in MIP solution and washing. As both the BSA/trypsin and the MIPs were labelled with fluorescein, and therefore indistinguishable, in this tracking experiment the MIP solution was replaced by DI-water. BSA and trypsin were labeled with fluorescein by adding 50 µL fluorescein in anhydrous dimethyl sulfoxide (1 mg/ml) very slowly to 1 mL of a BSA or trypsin in 0.1M sodium carbonate buffer solution (2 mg/ml), while continuously stirring the solution. To incubate, the solution was left in the dark at 2-8 ^{o}C for 8 hours. Unbound fluorescein was removed from the solution using gel filtration whereby PBS functioned as elution/washing solvent, resulting in a solution containing fluorescent albumin/trypsin only. Subsequently the fingerprints were spiked with fluorescent albumin/trypsin, washed, immersed in DI-water (as replacement of the MIPs) and washed again, resulting in a loss of ca. 32% of albumin and ca. 60% of trypsin.

During the washing procedures the fingerprints could also be removed, resulting in a decrease in maximum percentage of detectable fingerprints. The presence of the fingerprints was confirmed visually by eye and using optical light microscopy in the form of the Zeta-20 3D Optical Microscope (Zeta Instruments). To compensate for the loss of fingerprints during washing, the percentages of fluorescent fingerprints were normalised which was performed as follows. If 14% of the deposited fingerprints were fluorescent and 50% of the fingerprints were removed during washing, based on the percentage by eye or light microscope visible fingerprints, the normalised percentage of fluorescent fingerprints would be 28% (14*100/50).

The fluorescent labelled BSA/trypsin (used in the tracking experiments) as well as the fluorescent fingerprints obtained by treatment of fluorescent MIPs (in the standard experiments) were observed using an excitation wavelength of 445 nm, created using the 8x4 Crime-Lite, along a 515 nm long-pass viewing filter; both part of the DCS 5 Fingerprint Imaging Workstation (Foster & Freeman). These optimal viewing settings were determined by comparing the fluorescence intensities of multiple combinations of excitation wavelengths and viewing filters. As shown in Figure 4.11, the highest fluorescence intensity was obtained using an excitation wavelength of 495 nm. However, due to restrictions of the light sources to a range of long-pass viewing filters, only a fraction of the maximum fluorescence intensity could be observed. As illustrated

by the orange (λ_{ex}=445 nm, λ_{filter}≥495 nm) and yellow (λ_{ex}=475 nm, λ_{filter}≥550 nm) marked area in Figure 4.11, an excitation wavelength of 445 nm results in a higher total amount of fluorescence compared to 475 nm and was therefore chosen.

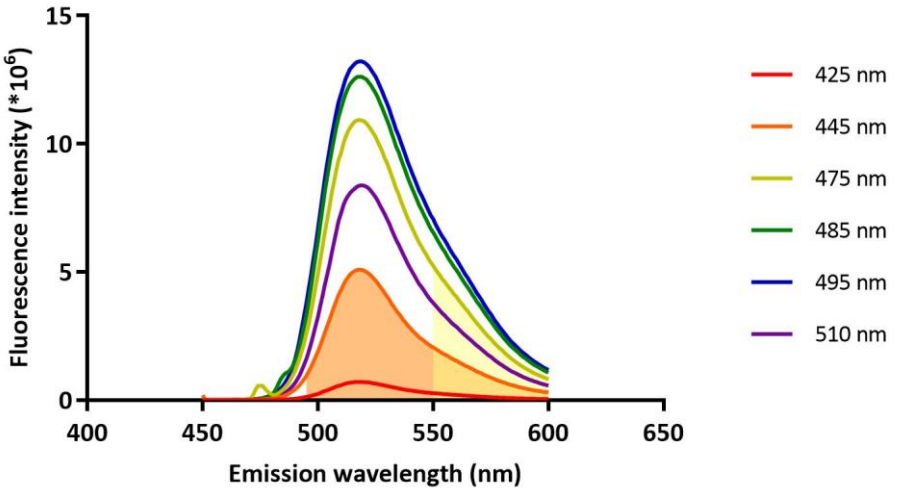

Figure 4.11 – Fluorescent intensity of a BSA imprinted linear MIPs solution, obtained over a range of emission wavelengths (450-600 nm) and using a range of excitation wavelengths (425 till 510 nm). Filled area is marking the lowest long-pass viewing filter wavelength.

As shown in Table 4.3 an excitation wavelength of 445 nm showed the highest fluorescence intensity using a long-pass viewing filter of 495 or 515 nm.

Table 4.3 – Droplets of fluoresceinylacrylamide recorded using a series of long-pass viewing filters (455-570 nm) and two excitation wavelengths (445 and 475 nm).

Filter / λ_{ex}	no	455 nm	495 nm	515 nm	530 nm	550 nm	570 nm
445 nm							
475 nm							

After recording the fingerprints visualised using MIPs, every fingerprint was given a score, from 0 to 100% to determine the performance of that MIP. As shown in Table 4.4 the rating depends on the number of fingerprint ridges visualised using MIPs and the consistency of these, but also the clearness (amount of background staining) was taken into account. Alternative fingerprint grading systems are the Bandey/CAST scale and UNIL scale, however not used in this research.

Table 4.4 – Fingerprint scoring system.

Score	Description
0%	No fluorescence visible.
3.1%	Some fluorescence, no fluorescent fingerprint characteristics visible.
6.3%	Some fluorescence, some fluorescent fingerprint characteristics visible.
16%	A few fluorescent fingerprint ridges visible; <33% of the fingerprint.
33%	Some fluorescent fingerprint ridges visible; ~33% of the fingerprint.
50%	Fluorescent fingerprint ridges visible; 33-75% of the fingerprint and/or dotted ridges.
75%	Most of the fluorescent fingerprint visible; >75% and/or dotted ridges.
100%	Fluorescent fingerprint visible.

4.2.4. Overview of performed experiments

As briefly mentioned above, in this research fingerprints spiked with BSA, trypsin and natural fingerprints were exposed to BSA and trypsin imprinted MIPs, hereafter referred to as $_{BSA}$fingerprints, $_{TR}$fingerprints, $_{NAT}$fingerprints, $_{BSA}$MIPs and $_{TR}$MIPs, respectively. These 6 experiments, as outlined in Table 4.5, could result in the following information.

Table 4.5 – Overview of the 6 experiments performed by adding albumin imprinted MIPs and trypsin imprinted MIPs to natural, albumin and trypsin spiked fingerprints, illustrating the expected results.

	BSA-spiked fingerprint	Natural fingerprint	Trypsin-spiked fingerprint
BSA imprinted MIPs			
Trypsin imprinted MIPs			

The possibility to detect fingerprints using MIPs could be confirmed by exposure of $_{BSA}$fingerprints and $_{TR}$fingerprints to $_{BSA}$MIPs and $_{TR}$MIPs respectively, expected to result in a fluorescent fingerprint. Depending on the sensitivity of the MIPs in this application and actual presence of albumin in $_{NAT}$fingerprints, the $_{NAT}$fingerprints and $_{TR}$fingerprints could likewise become fluorescent by exposure to $_{BSA}$MIPs. Information about the specificity of the MIPs in this application could be obtained by exposure of $_{BSA}$fingerprints and $_{TR}$fingerprints to $_{TR}$MIPs and $_{BSA}$MIPs respectively. In case of high specificity, the MIPs only bind to their target molecule thus it is not expected that both fingerprints become fluorescent. However, the $_{TR}$fingerprints could become fluorescent by exposure to $_{BSA}$MIPs in case of high enough sensitivity to detect possible naturally present amounts of albumin in the fingerprint. The exposure of $_{BSA}$fingerprints and $_{NAT}$fingerprints to $_{TR}$MIPs could function as control experiment, as it is assumed that trypsin is not present in a natural fingerprint.

4.2.5. Model fingerprint solution

In this study a model fingerprint solution was created to mimic a fingerprint. This composition was based on fingerprint compositions described in the literature and outlined in the Appendix (Section A.1). Some studies were based on fingerprints and others on sweat as well as not all quantities were justified in the review articles, therefore overlap in data could be present. Due to the complexity of a fingerprint, only the most abundant molecules (>10 mM) and molecules of special interest such as amino acids were included in the model fingerprint solution. In addition, the high content of water in fingerprints resulted to the decision to include only the water-soluble protein albumin and no other proteins.

Two types of model fingerprint solutions were created, one containing sebaceous fingerprint molecules and one containing eccrine plus ca. 1% sebaceous fingerprint molecules to simulate aqueous/standard fingerprints and hydrophobic/viscous fingerprints, respectively. The sebum content of ca. 1% of the total fingerprint content was based on the solubility of the sebaceous mixture in water. This mixture contained fatty acids, wax esters and triglycerides. Due to the limited quantitative literature about wax esters and triglycerides, the high abundancy of C14, C16 and C18 fatty acids chains in a fingerprint was held as guideline for the selection of wax esters and triglycerides. [28]

4.2.6. Chemicals and materials

In this study the chemicals and materials as outlined in Table 4.6 were used, all used as received. The in this research used deionized-water (DI-water) was obtained from the PURELAB Option water purification system of ELGA.

Table 4.6 – Chemicals and materials used in this research, including source and purity (when relevant).

Chemicals/ materials	Source
N-(3-Aminopropyl)methacrylamide hydrochloride (>98%)	Polysciences
N-(3-Dimethylaminopropyl)-N-ethylcarbodiimide hydrochloride	Alfa-Aesar
2,5-Dihydroxybenzoic acid	Lancaster
(3-Aminopropyl)triethoxysilane (95%)	Sigma-Aldrich
Acetate buffer	GE healthcare

Acetone	Tennants
Acetonitrile (HPLC grade)	Fisher Scientific
Acrylamide (97%)	Aldrich
Acrylic acid	Sigma-Aldrich
L-Alanine (99%)	Aldrich
Albumin from bovine serum	Sigma
Albumin from human serum	Sigma-Aldrich
Amicon Ultra-15 Centrifugal Filter Unit with Ultracel-30 membrane	Merck Millipore
Ammonium persulphate (APS, 98-99.99%)	Aldrich, Alfa Aesar, Fluka
L-Aspartic acid (≥98%)	Sigma-Aldrich
BCA Protein Assay Kit	Thermo Scientific
Cetyl Palmitate	Sigma-Aldrich
Cholesterol	Lancaster
Dansyl chloride (≥99%)	Sigma-Aldrich
Dimethyl sulfoxide (anhydrous)	Sigma-Aldrich
Ethanol	VWR
Fluorescein	Sigma-Aldrich
Fluoresceinylacrylamide	Prepared and characterised by the Biotechnology group, Chemistry Department, University of Leicester
Glass beads	Blagden
L-Glutamic acid hydrochloride	Sigma
Glutaraldehyde	Fluka
Glycerol tristearate	BDH biochemicals
Glyceryl trioleate (≥99%)	Sigma-Aldrich
Glycine (≥99%)	Sigma
L-Histidine (≥99%)	Sigma-Aldrich
N-Hydroxysuccinimide	Merck
L-Isoleucine (99%)	Aldrich
N-Isopropylacrylamide (≥99%)	Sigma-Aldrich
Keratin from human epidermis	Sigma-Aldrich
Lactic acid (≥85%)	SAFC
L-Leucine (99%)	BDH biochemicals
L-Lysine (≥98%)	Sigma-Aldrich
Mercaptoundecanoic acid	Sigma-Aldrich
Methanol (≥99.9%)	Sigma-Aldrich
N,N-Methylenebisacrylamide (99%)	Sigma-Aldrich
Microscope glass slides	Fisher Scientific
Myristic acid (99-100%)	Sigma
Myristic acid methyl ester (≥99%)	Sigma-Aldrich
Oleic acid (≥99%)	Sigma-Aldrich
L-Ornithine hydrochloride (99%)	Acros Organics
Palmitic acid (99%)	Aldrich
Palmitoleic Acid	Cambridge Bioscience
L-Phenylalanine (≥98%)	Sigma

Phosphate buffered saline	Life technologies
Potassium chloride	Fisher Scientific
L-Serine (≥99%)	Sigma
Sodium bicarbonate	Fisher Scientific
Sodium bisulfate	Sigma-Aldrich
Sodium chloride	Fisher Scientific
Sodium hydrogen carbonate	Fisher Scientific
Sodium hydroxide	Fisher Scientific
SPE cartridges	Sigma-Aldrich
SPR chips	GE Healthcare
Squalene (99%)	Acros Organics
Stearic acid (≥98.5%)	Sigma-Aldrich
Streptavidin	Sigma-Aldrich
Sulphuric acid (>95%)	Fisher Scientific
N-tert-Butylacrylamide (97%)	Sigma-Aldrich
Tetrahydrofuran	Fisher Scientific
L-Threonine (≥98%)	Sigma-Aldrich
Toluene	Fisher Scientific
Toyopearl HW-50S (500-80.000MWE)	Sigma-Aldrich
Trifluoroacetic acid (HPLC grade)	Fisher
Trypsin from bovine pancreas	Sigma
L-Tyrosine (≥98%)	Sigma-Aldrich
L-Valine (≥98%)	Sigma-Aldrich
Urea	ChemCruz

4.3. Results

A few aspects which could affect the detection of fingerprints using MIPs were investigated; type of MIPs, fingerprint composition/matrix and substrate. To define the performance of the fluorescent MIPs, the visualisation quality of the fingerprint as well as the yield, specificity and sensitivity were considered. The yield was described by the percentage with target molecule spiked fluorescent fingerprints, specificity by the percentage false positives versus yield and sensitivity by the influence of the concentration of the target molecule on the yield (spiked fingerprint versus natural fingerprint). Possible limitations and further possibilities of this application were explored using analytical techniques.

4.3.1. Structure of the MIPs

The detection of fingerprints using MIPs might be influenced by the size and shape of the MIPs as well as by the affinity of the MIPs with their target molecule. Therefore the performance of the cross-linked and spherical $_{N}$MIPs was compared with the not-crosslinked and smaller $_{L}$MIPs. [29]

4.3.1.1. Nano MIPs

The possibility to detect albumin or trypsin present in a fingerprint using $_{N}$MIPs was investigated by exposure of $_{BSA}$fingerprints, $_{TR}$fingerprints and $_{NAT}$fingerprints to $_{TR\text{-}N}$MIPs and $_{BSA\text{-}N}$MIPs. This resulted in fluorescent fingerprints using each type of fingerprint and MIP (red dots in Figure 4.12). Using $_{BSA\text{-}N}$MIPs the addition of the target molecule to the fingerprint ($_{NAT/TR}$fingerprint versus $_{BSA}$fingerprint) did not result in considerably more fluorescent fingerprints (13%/10% versus 14%) while using $_{TR\text{-}N}$MIPs more fluorescent fingerprints were obtained using $_{TR}$fingerprints compared to $_{NAT/BSA}$fingerprints (12% versus 7%/6%) as shown in Figure 4.12 (red dots). The latter was enlarged after normalisation (green dots in Figure 4.12B) in which was compensated for the loss of fingerprints during the washing procedure.

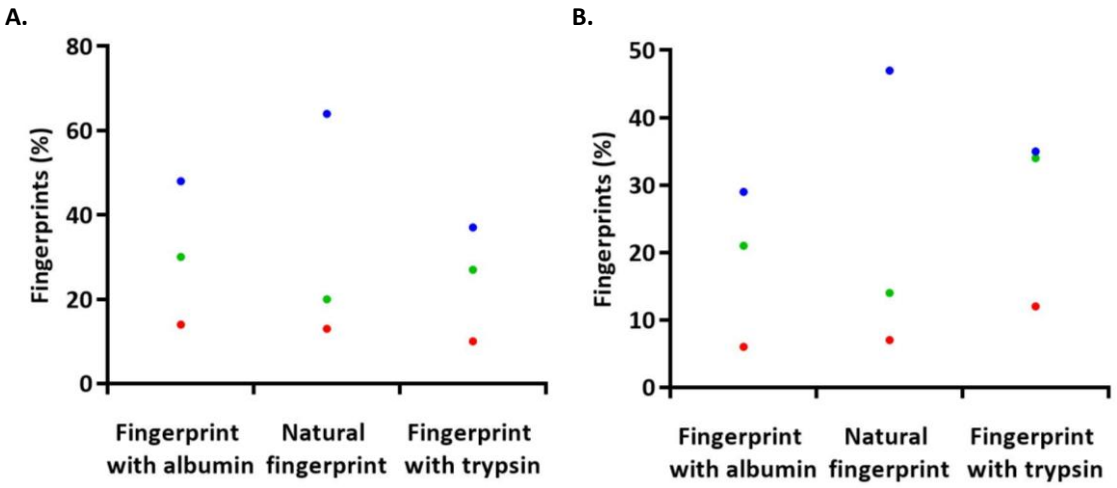

Figure 4.12 – Percentages visualised fingerprints using albumin imprinted nano MIPs (**A**) and trypsin imprinted nano MIPs (**B**). Blue dots illustrate the percentage of fingerprints visible by eye/light microscope, red dots the percentage of fluorescent fingerprints and green dots the normalised percentage of fluorescent fingerprints.

The increase in percentage of fluorescent fingerprints by addition of the target molecule to the fingerprints suggests that the $_{TR\text{-}N}$MIPs behaved specifically in this application. The $_{BSA\text{-}N}$MIPs on the other hand did not show a considerable higher percentage of fluorescent fingerprints using $_{BSA}$fingerprints compared to $_{TR}$fingerprints, this suggests that $_{BSA\text{-}N}$MIPs did not behave specifically or the concentration albumin naturally present in a fingerprint was above the saturation limit of $_{BSA\text{-}N}$MIPs. The latter would result in the detection of the same maximum concentration albumin in $_{BSA}$fingerprints and $_{NAT}$fingerprints, although this is probably not very likely. A higher specificity of $_{TR\text{-}N}$MIPs compared to $_{BSA\text{-}N}$MIPs could possibly be caused by a difference in affinity or size; the smaller molecular weight of trypsin compared to albumin (27 kDa and 66 kDa, respectively) could perhaps result in smaller MIPs which might be more mobile in the fingerprint. The higher percentage of removed $_{BSA/TR}$fingerprints during the washing procedure compared to $_{NAT}$fingerprints could suggest an alteration of the fingerprint by immersing the fingerprint in albumin/trypsin solution. This enhanced perhaps the permeability of MIPs in the fingerprint resulting in a higher percentage of fluorescent $_{BSA/TR}$fingerprints compared to $_{NAT}$fingerprints in case of non-specific binding of the $_{BSA\text{-}N}$MIPs towards trypsin and albumin. In case of specific binding of the $_{BSA\text{-}N}$MIPs, the similar percentages of fluorescent $_{BSA}$fingerprints and $_{TR}$fingerprints could be caused by the presence of a concentration albumin naturally present in a fingerprint which was above the saturation limit of the $_{BSA\text{-}N}$MIPs.

4.3.1.2. Linear MIPs

The size of the MIPs might be of influence on the detection of fingerprints using MIPs, more precisely on the ease of entering the fingerprint, mobility in the fingerprint, ease to get washed away and the influence of steric effects when binding the target molecule. Therefore, the applicability of the generally smaller $_{L}$MIPs than $_{N}$MIPs was investigated.

Using $_{BSA\text{-}L}$MIPs (red dots in Figure 4.13A) a higher percentage of fluorescent $_{BSA}$fingerprints was obtained compared to $_{NAT}$fingerprints and $_{TR}$fingerprints (37% versus 8%/13%), showing an increase in percentage by addition of albumin. After normalisation (to compensate for the loss of fingerprints during the washing process) a similar trend was observed (green dots in Figure 4.13A). The use of $_{TR\text{-}L}$MIPs resulted also in a higher percentage of fluorescent fingerprints using the target molecule-spiked fingerprints (trypsin) compared to the $_{NAT/BSA}$fingerprints (34% versus 18%/19%; green dots in Figure 4.13B).

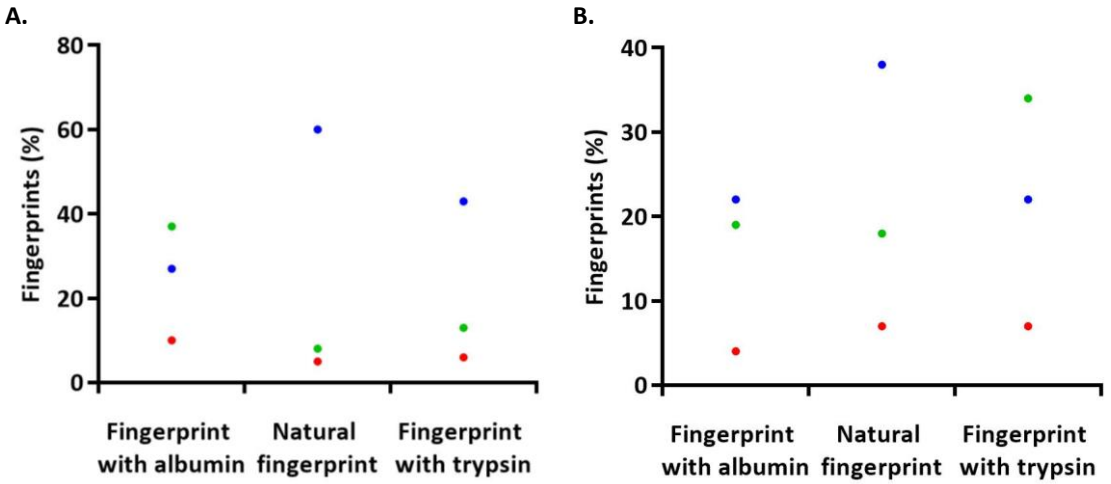

Figure 4.13 – Percentages visualised fingerprints using albumin imprinted linear MIPs (**A**) and trypsin imprinted linear MIPs (**B**). Blue dots illustrate the percentage of fingerprints visible by eye/light microscope, red dots the percentage of fluorescent fingerprints and green dots the normalised percentage of fluorescent fingerprints.

The increase in percentage of fluorescent fingerprints by spiking the fingerprint with the target molecule compared to another protein suggests that both the $_{TR\text{-}L}$MIPs and $_{BSA\text{-}L}$MIPs behaved specifically. Given the higher percentage of fluorescent $_{BSA}$fingerprints compared to $_{TR/NAT}$fingerprints (containing only naturally present albumin), the

behaviour of the $_{BSA\text{-}L}$MIPs could also be concentration dependent. Although due to uncertainty about the sensitivity of the MIPs and the presence of albumin in natural fingerprint, this is speculative.

Additionally, as for the experiments using $_{N}$MIPs, the spiked fingerprints treated with $_{L}$MIPs were washed away more readily than the $_{NAT}$fingerprints, indicated by the lower number of present (by eye/ light microscope visible) spiked fingerprints (blue dots in Figure 4.13). This had a considerable effect on the interpretation of the performance of $_{TR\text{-}L}$MIPs, only after normalisation the percentage of fluorescent $_{TR}$fingerprints was higher than the percentage of fluorescent $_{NAT}$fingerprints and $_{BSA}$fingerprints (green dots in Figure 4.13B).

4.3.1.3. Comparison of nano and linear MIPs

Regarding both $_{TR\text{-}N}$MIPs and $_{TR\text{-}L}$MIPs, an increase in yield was obtained by spiking the fingerprint with the target molecule trypsin compared to albumin, this suggests that both types of MIPs behaved specifically. Regarding the $_{BSA}$MIPs, the $_{BSA\text{-}L}$MIPs behaved more specifically than the $_{BSA\text{-}N}$MIPs based on the increase in yield by spiking the fingerprint with the target molecule albumin compared to trypsin. A lower specificity of $_{N}$MIPs compared to $_{L}$MIPS could possibly be caused by a lower affinity with the target molecule and/or lower mobility in the fingerprint of the $_{N}$MIPs compared to the $_{L}$MIPS. The concentration of albumin naturally present in a fingerprint could also have an influence on these interpretations. A concentration of albumin naturally present in a fingerprint which is above the saturation limit of the $_{BSA\text{-}N}$MIPs could lead to a negligible increase in yield by addition of albumin to the fingerprint. The concentration of albumin could also have affected the performance of the $_{BSA\text{-}L}$MIPs, suggested by the higher percentage fluorescent $_{BSA}$fingerprints compared to the fingerprints containing naturally present albumin only. Although due to uncertainty about the sensitivity of the MIPs and the presence of albumin in natural fingerprint, this is speculative and questionable. In addition, during the washing process more spiked fingerprints were removed than natural fingerprints, using $_{BSA\text{-}N}$MIPs that resulted in a higher percentage of fluorescent spiked fingerprints compared to $_{NAT}$fingerprints which could suggests that immersing the fingerprints in protein solution perhaps enhances the permeability of the $_{BSA\text{-}N}$MIPs

in the fingerprint in case of non-specific binding of the $_{BSA\text{-}N}$MIPs towards trypsin and albumin.

Due to the possible higher specificity and concentration dependency of the $_{L}$MIPs compared to $_{N}$MIPs, $_{L}$MIPs were used in the rest of this research.

4.3.2. Analysis of the composition of the MIPs using MALDI-ToF-MS

To gain a better understanding of the composition of the MIPs, MALDI-ToF-MS measurements were performed. This soft ionisation technique was chosen because of the possibility to retrieve knowledge about the order and thereby ratio of the monomers in the $_{BSA\text{-}L}$MIPs.

As shown in Figure 4.14 a polymer of ca. 2000 m/z was detected using MALDI-ToF-MS which is of the same order as mentioned in the literature. [29] The order of the monomers in MIPs was tentatively determined by comparing the mass distances between the peaks with the molecular weight of the monomers (Figure 4.14). However, due to the complexity the possible order of monomers was not completely unambiguous. Some neighbouring peaks have similar intensities, for instance m/z 1129-1201 and m/z 1795-1867, which could be caused by a range of factors such as difference in origin or ionisation strength. Some peaks can be obtained by a variety of fragmentation patterns, for instance m/z 1399 can possibly be obtained by losing acrylamide from m/z 1470 or tBAm from m/z 1526. Another example is peak m/z 1470 which can fragment to m/z 1328 by losing APMA or to m/z 1399 by losing acrylamide. A special notion should also be given to peak m/z 1795 which could be the end peak of this chain, a fragment of m/z 1867 by losing acrylic acid or a fragment of m/z 1994 by losing a cluster of acrylic acid and tBAm. The latter could be caused by in-source fragmentation. The loss of a cluster of tBAm and acrylamide could also have happened from m/z 1129 to m/z 931, although unlikely at this position. By taking these remarks into account, some possible orders of monomers were obtained as shown in Figure 4.15.

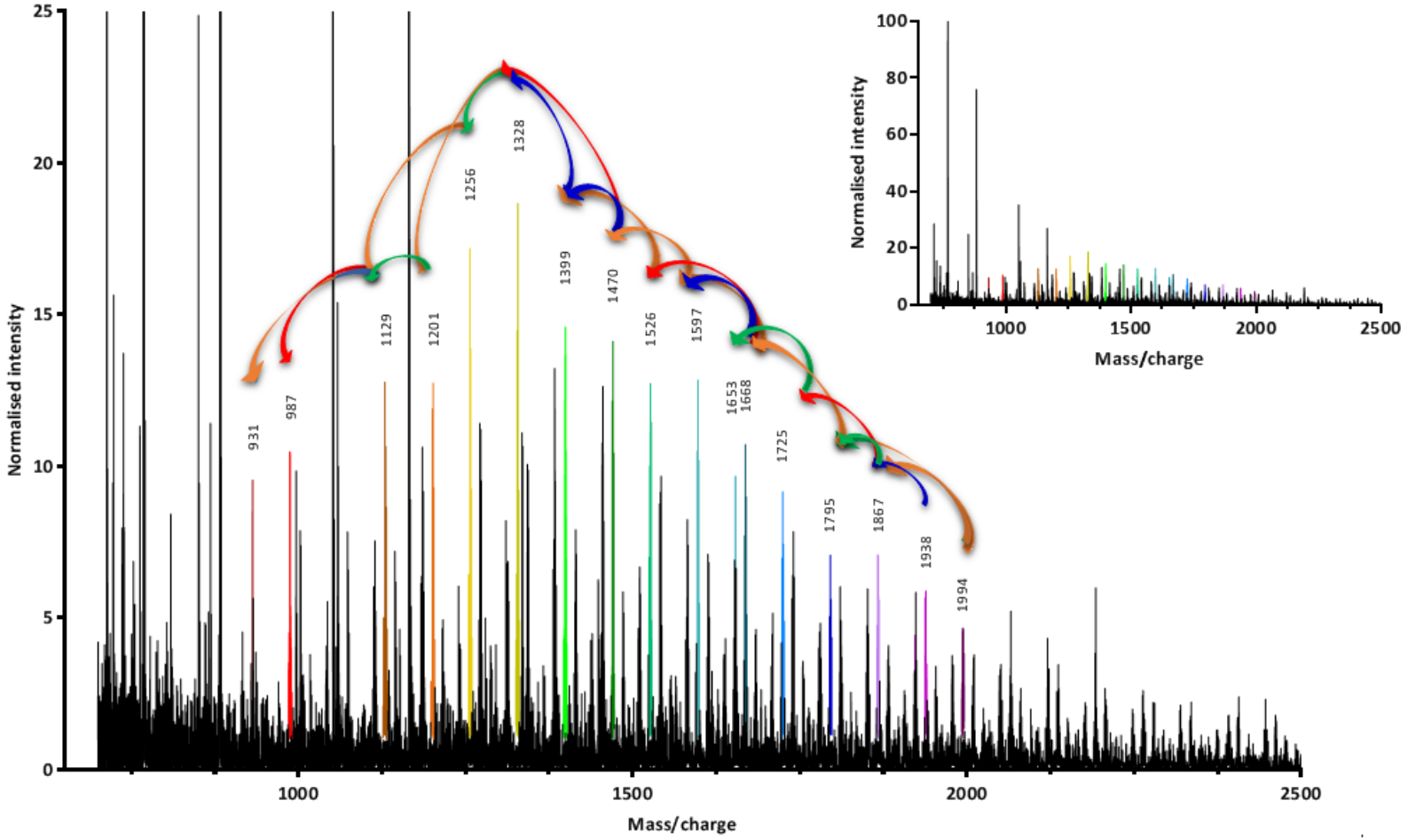

Figure 4.14 – MALDI-MS spectra of albumin imprinted linear MIPs. The arrows indicate the proposed monomers based on mass difference between the peaks, red arrows APMA (Δm/z 142), orange arrows tBAm (Δm/z 127), green arrows acrylic acid (Δm/z 72), blue arrows acrylamide (Δm/z 71). Inset: zoom out of the main mass spectra.

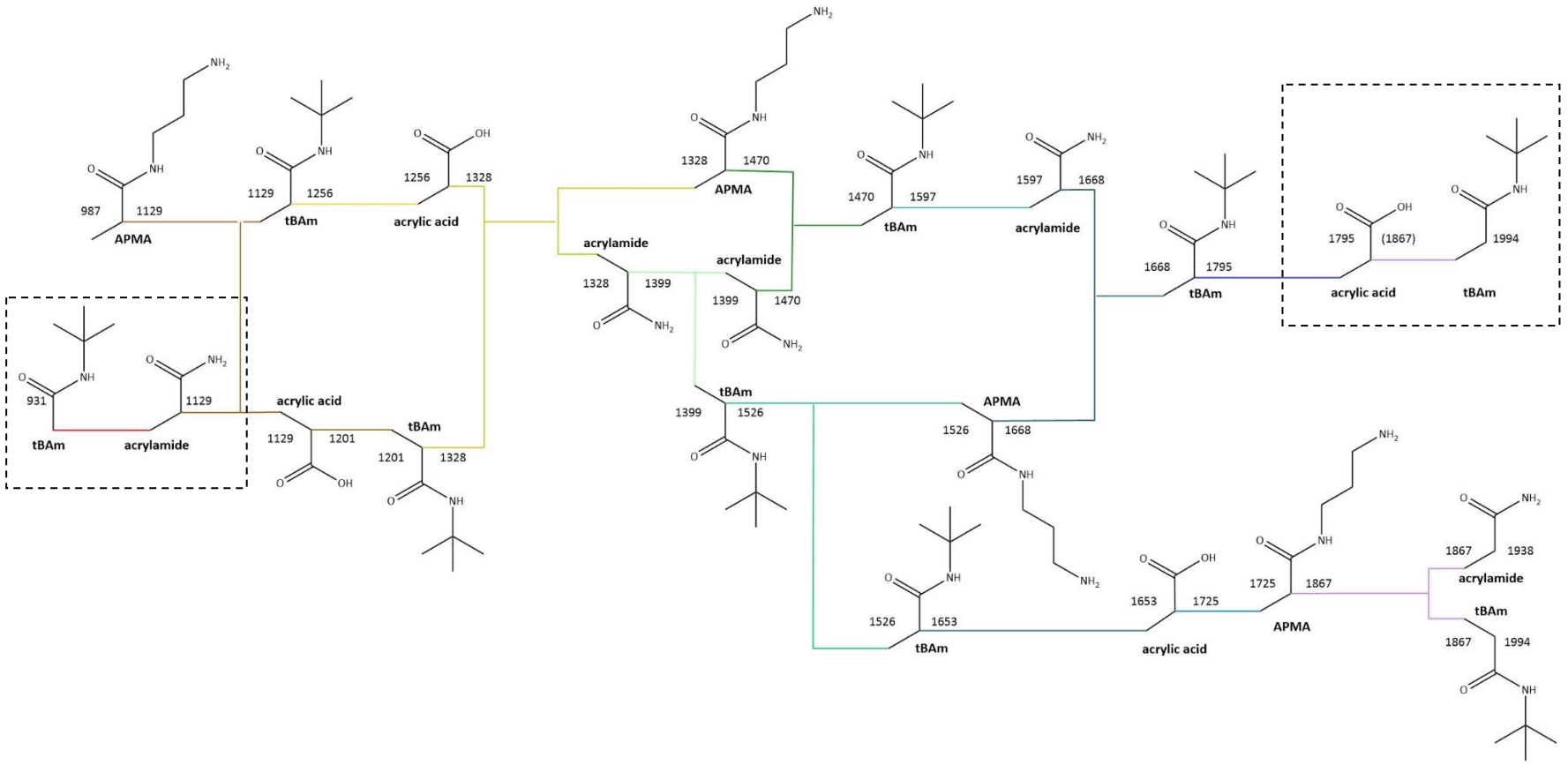

Figure 4.15 – Order of monomers tentatively determined based on the MALDI-MS spectra of Figure 4.14. The colours of the connecting lines correspond to the colours of the peaks of the mass spectra. The numbers are the mass to charge ratios of the beginning/end of a proposed monomer or cluster, the latter is indicated by a square.

To conclude, MALDI-ToF-MS was able to tentatively determine an order of monomers. However, there are also drawbacks to this method. Due to similar mass differences of the monomers, such as APMA (142 g/mol) equals an acrylamide dimer (2x71 g/mol), and the complexity of the spectra an unambiguous order of monomers was not obtained. Additionally, this method does not eliminate the option of having a MIPs solution with multiple different structures/monomer orders. Another drawback of this method is the experimental challenge of ionising the MIPs, this is possibly caused by low volatility and not fully optimised sample preparation. Overall, these analyses demonstrate that MALDI-ToF-MS is a promising method for retrieving information about the composition of the MIPs.

4.3.3. Affinity of linear MIPs to target and other relevant molecules

To get a better understanding of the specificity of the $_{BSA\text{-}L}$MIPs, the affinity of these MIPs towards the target molecule albumin, the control molecule trypsin and other molecules of interest as listed in Table 4.7 was measured using SPR.

The analysed molecules were selected based on their similarity with albumin regarding molecular weight and isoelectric point, as both properties could be of influence on the interactions of the target molecule with the MIPs. In addition, their relevance was taken into account, such as keratin and HSA are both present in the fingerprint and therefore of extra interest.

Table 4.7 – Molecular weight and isoelectric point of the molecules used for SPR analysis.

Molecule	Molecular weight (kDa)	Isoelectric point (pI)	References
BSA	66.43	4.9	[30]
HSA	66.43	4.7	[31]
Trypsin	23.3	10.1-10.5	[32]
Streptavidin	60	5.5	[33]
Keratin	40-65	6.5-8.5	[34, 35]

4.3.3.1. Affinity of albumin imprinted linear MIPs towards albumin and trypsin

To determine the affinity and selectivity of the $_{BSA\text{-}L}$MIPs, their affinity with BSA and the control trypsin was measured. $_{BSA\text{-}L}$MIPs were immobilised on the SPR chip after which a range of concentrations of BSA and trypsin (0.59, 2.35, 9.38, 37.50 and 150 nM) were passed over the chip.

As shown in Figure 4.16, $_{BSA\text{-}L}$MIPs were found to bind in higher amounts to BSA than to trypsin, this suggests that the affinity of the $_{BSA\text{-}L}$MIPs with BSA was higher than with trypsin. The fact that trypsin barely bound to the $_{BSA\text{-}L}$MIPs, only slight binding was observed at high concentration, makes this protein a good negative control for the $_{BSA\text{-}L}$MIPs. Additionally, the affinity of the $_{BSA\text{-}L}$MIPs with BSA was expressed using the dissociation constant of 0.2 nM.

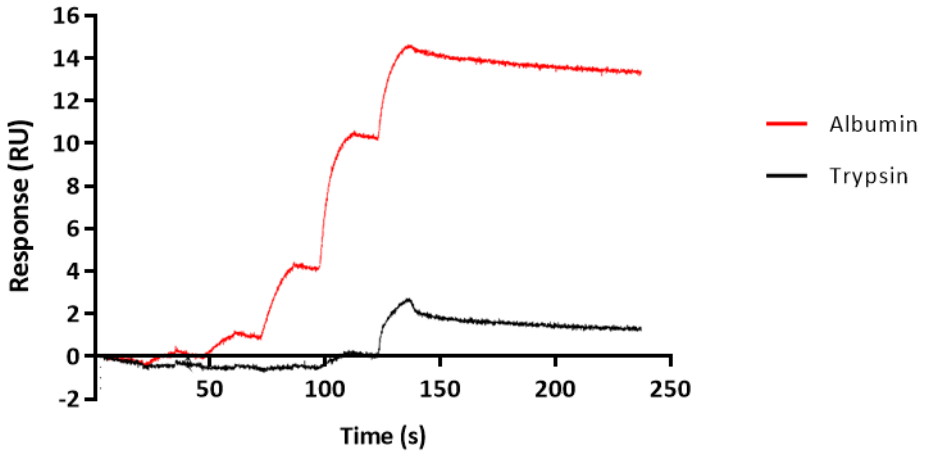

Figure 4.16 – Fitted sensorgram illustrating the amount of binding of albumin imprinted linear MIPs (in acetate solution) towards albumin (red) and trypsin (black). $K_{D,\ albumin\text{-}trypsin}$ = 0.2 nM. Measurements of a range of trypsin and albumin concentrations (0.59, 2.35, 9.38, 37.50 and 150 nM) were performed using the SPR Navi 220A (BioNavis).

4.3.3.2. Affinity of albumin imprinted linear MIPs towards albumin and streptavidin

To determine the specificity of the $_{BSA\text{-}L}$MIPs towards similar molecules, with respect to molecular weight and isoelectric point, the affinity of the $_{BSA\text{-}L}$MIPs towards BSA was compared to streptavidin. Hereby BSA and streptavidin were immobilised on the SPR chip after which a range of concentrations of the MIP solution (dilutions in water: 1, 1/3, 1/9, 1/27, 1/81, 1/243) were injected over the chip.

As shown in Figure 4.17, by increasing MIP concentration, more streptavidin and albumin was found to bind to the MIPs. After reaching saturation at ca. 4000 s (6th injection), unbound MIPs were washed away. This resulted in a higher response (response at t=0 s minus response at t>4000 s) and thereby more binding between $_{BSA\text{-}L}$MIPs and BSA compared to streptavidin.

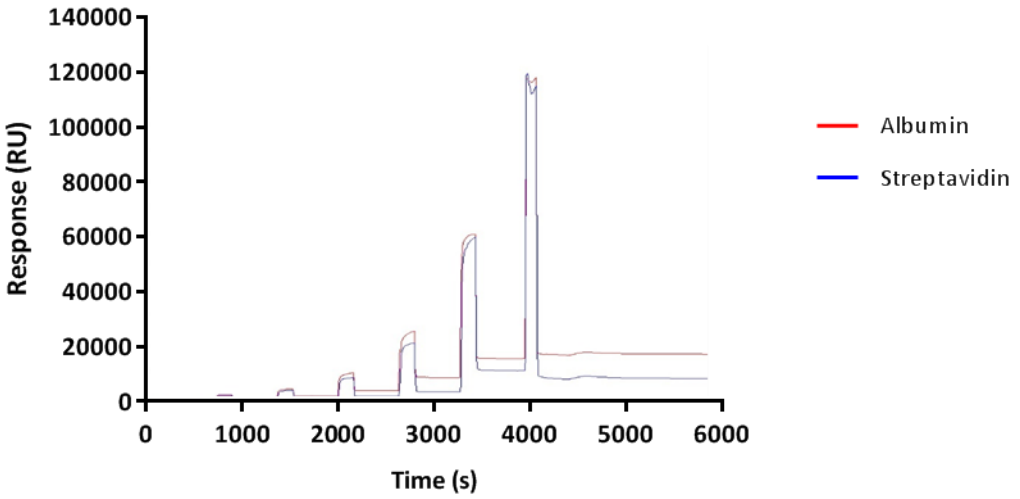

Figure 4.17 - Sensorgram illustrating the amount of binding of albumin imprinted linear MIPs (in water) with albumin (red) and streptavidin (blue). Measurements of a range of MIP concentrations (dilutions in water: 1, 1/3, 1/9, 1/27, 1/81, 1/243) were performed using the BIACore 3000 SPR system (GE Healthcare).

4.3.3.3. Affinity of albumin imprinted linear MIPs towards BSA, HSA and keratin

In this research the $_{BSA\text{-}L}$MIPs were imprinted with BSA and the fingerprints were spiked with BSA, while HSA is naturally present in the fingerprint. To determine whether $_{BSA\text{-}L}$MIPs would also bind to the HSA naturally present in fingerprints, the affinity between $_{BSA\text{-}L}$MIPs and HSA was measured. In addition, to determine whether the $_{BSA\text{-}L}$MIPs would bind to other molecules present in the fingerprint, resulting in false positives, the affinity between the $_{BSA\text{-}L}$MIPs and keratin was measured. Keratin is, after albumin, one of the most abundant proteins in a fingerprint and therefore chosen.

The affinity of $_{BSA\text{-}L}$MIPs towards BSA compared to HSA and keratin was measured by immobilising BSA, HSA and keratin on the SPR chip after which $_{BSA\text{-}L}$MIPs were injected over the chip.

As shown in Figure 4.18, both BSA and HSA bind to the $_{BSA\text{-}L}$MIPs, therefore both are suitable for the end-application. In addition, minor binding between keratin and the $_{BSA\text{-}L}$MIPs was observed which was directly broken during washing as the response drops down completely at ca. 200 s (Figure 4.18). As keratin showed only minor to no binding with $_{BSA\text{-}L}$MIPs and less binding than $_{BSA\text{-}L}$MIPs with albumin, it is assumed that other molecules, especially proteins, present in the fingerprint would probably not lead to false positives.

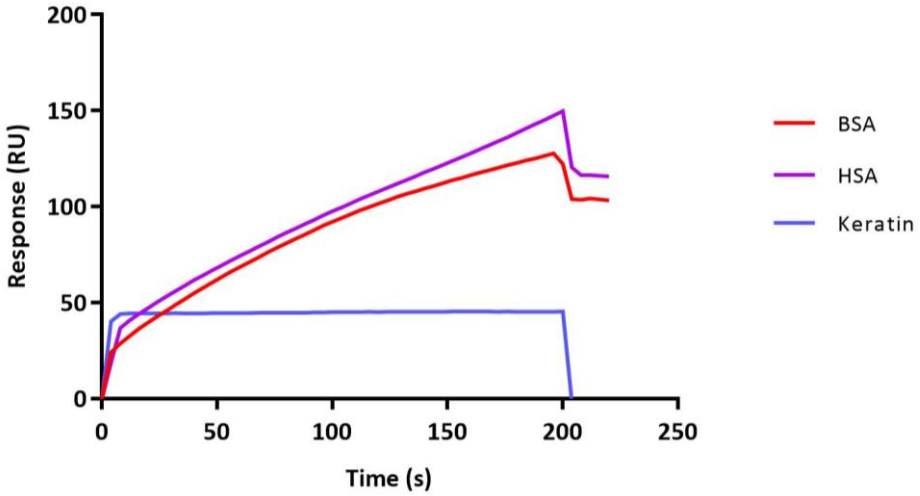

Figure 4.18 – Sensorgram illustrating the affinity of BSA imprinted linear MIPs (in water) towards BSA, HSA and keratin. Measurements performed using the BIACore 3000 SPR system (GE Healthcare).

4.3.3.4. Affinity of albumin towards albumin imprinted linear MIPs and trypsin imprinted linear MIPs

Besides the above discussed affinities of the $_{BSA\text{-}L}$MIPs towards a variety of molecules (Figures 4.16-4.18), the affinity of $_{TR\text{-}L}$MIPs with BSA was compared to the affinity of $_{BSA\text{-}L}$MIPs with BSA. This type of specificity could be of use when a series of MIPs are simultaneously applied on one fingerprint, such as by the detection of several drugs in a fingerprint using a series of coloured MIPs whereby each colour corresponds to another drug.

In these SPR measurements, $_{BSA\text{-}L}$MIPs and $_{TR\text{-}L}$MIPs were immobilised to the SPR chips after which a range of concentrations (0.01, 0.1, 0.5, 1 and 10 nM) of BSA were injected over the chip.

As shown in Figure 4.19, BSA was found to bind as well to $_{BSA\text{-}L}$MIPs as to $_{TR\text{-}L}$MIPs, suggested by the similar K_D values. However, by comparing the response of the SPR measurement (y-axis) it is shown that there was 4-5 times more binding between BSA and $_{BSA\text{-}L}$MIPs than between BSA and $_{TR\text{-}L}$MIPs. This could be explained by efficient non-specific binding of BSA to the $_{TR\text{-}L}$MIPs, as proteins tend to stick easily to surfaces, and specific binding between BSA and $_{BSA\text{-}L}$MIPs.

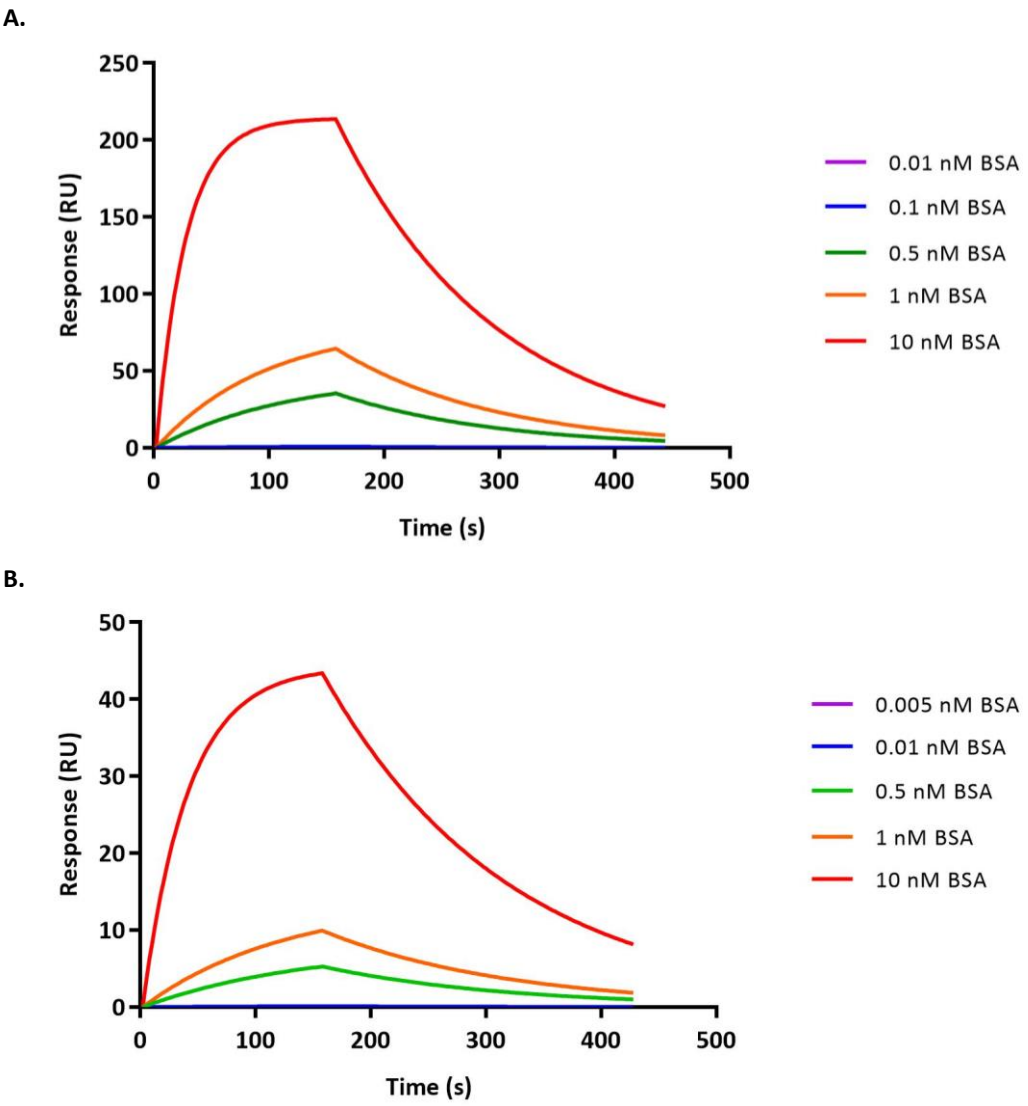

Figure 4.19 – Fitted sensorgram illustrating the affinity of a variety of concentrations albumin towards albumin imprinted MIPs (**A**; K_D=2.27 nM) and trypsin imprinted MIPs (**B**; K_D=3.23 nM), both in water. Measurements were performed using the BIACore 3000 SPR system (GE Healthcare).

4.3.3.5. Conclusion affinity experiments

To increase understanding of the specificity of $_{BSA\text{-}L}$MIPs, the affinity of $_{BSA\text{-}L}$MIPs towards the target molecule BSA and other relevant (fingerprint) molecules was measured. Given that $_{BSA\text{-}L}$MIPs were found to bind both to BSA and HSA, no distinction was made between these molecules. $_{BSA\text{-}L}$MIPs were found to bind more specifically to its target molecule BSA than to trypsin, streptavidin and keratin. Given that the $_{BSA\text{-}L}$MIPs displayed no/negligible binding to one of the most abundant proteins in a fingerprint after albumin, keratin, it is probably unlikely that false positives will be obtained by binding of the $_{BSA\text{-}L}$MIPs to other fingerprint molecules. Additionally, the higher specificity of BSA towards $_{BSA\text{-}L}$MIPs than towards $_{TR\text{-}L}$MIPs provides potential for the simultaneous detection of multiple molecules in one fingerprint using a series of MIPs.

4.3.4. Behaviour of fluorescence in the fingerprint

Fluorescent fingerprints were obtained after treatment with fluorescent MIPs, to ensure the fluorescence was caused by fluorescent MIPs only, other possible origins of fluorescence in the fingerprints were discussed. Natural fingerprints were inspected with the DCS 5 (same settings as used for the visualised fingerprints) and did not show any fluorescence despite the presence of the fluorescent amino acids phenylalanine, tyrosine and tryptophan. The fluorescence intensity of albumin detected by a spectrofluorometer was also negligible compared to $_{BSA\text{-}L}$MIPs (Figure 4.20). The fluorescence intensity even decreased slightly by addition of albumin to the MIPs which could be caused by a decrease in clarity of the solution.

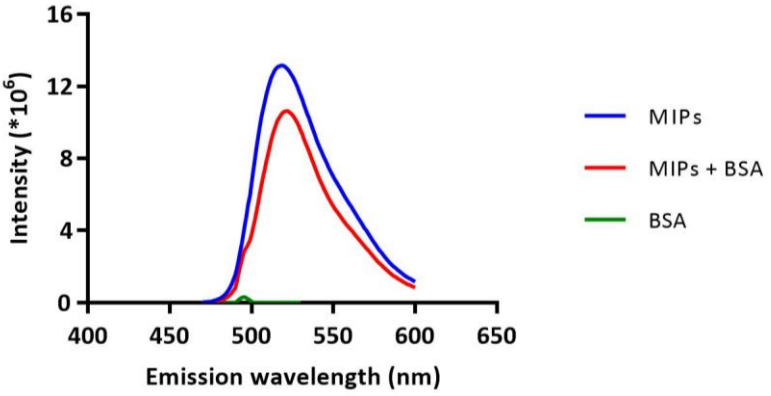

Figure 4.20 – Fluorescence intensity of BSA imprinted linear MIPs solution, BSA solution and BSA plus BSA imprinted MIPs solution. Measurements were performed using an excitation wavelength of 495 nm and a range of emission wavelengths (400-650 nm).

To conclude, the relatively low intensity of fluorescence of albumin compared to $_{BSA\text{-}L}$MIPs and absence of detectable fluorescence in a natural fingerprint suggests that the fluorescence in the visualised fingerprints were rather caused by the fluorescent MIPs than by fluorescent groups naturally present in the fingerprint or by spiked albumin.

4.3.5. ToF-SIMS analysis of fingerprints visualised with MIPs

The presence of MIPs in/on the visualised fingerprint was not only optically confirmed but also investigated analytically. Visualised fingerprints were analysed using ToF-SIMS to understand why some areas in a fingerprint were less well visualised. This could aid in determining the possible uses and limitations of this application.

As illustrated in Figure 4.21, the peaks in the ToF-SIMS spectrum of a fingerprint visualised with $_{BSA\text{-}L}$MIPs can tentatively be assigned to endogenous fingerprint (amino acids, fatty acids and salts) and MIPs fragment ions. This suggests that both endogenous fingerprint and MIP fragments could be present in the fluorescent fingerprint. However, some of the fragments/masses were assigned to multiple groups, such as m/z 57 could possibly be $C_4H_9^+$ which could be assigned to amino acids, fatty acids and MIPs. This could have an influence on the interpretation of the spectrum and the confirmation of the presence of the MIPs and endogenous fingerprint molecules in the visualised fingerprint.

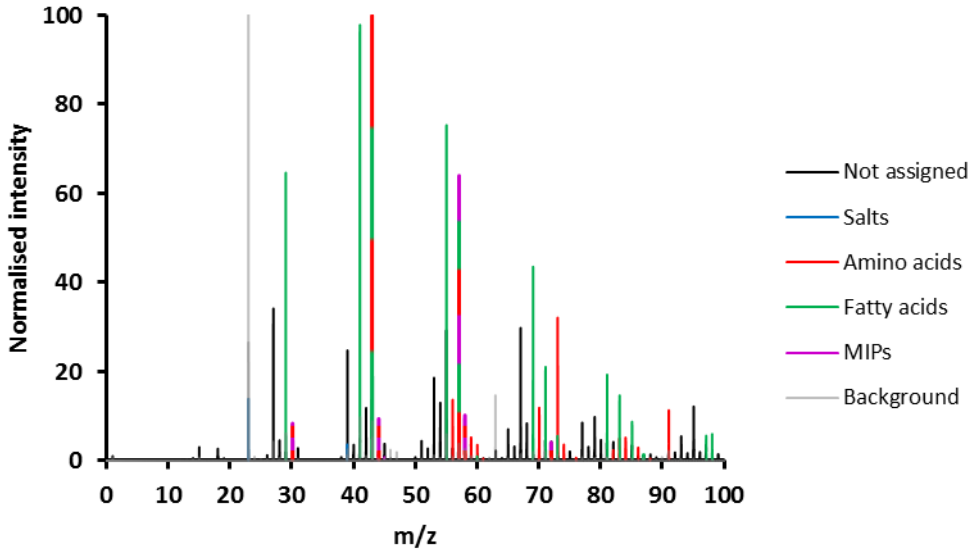

Figure 4.21 - ToF-SIMS spectrum of a visualised fluorescent fingerprint. The peaks were tentatively assigned to the fingerprint compounds (salts, amino acids, fatty acids) and the MIPs visualisation reagent.

Next to the tentatively assigned peaks, several other masses were detected. As ToF-SIMS is sensitive to the detection of plasticisers which could originate from vials, pipette tips or tape and other substrate contamination, a determination of the origin of these peaks is very speculative. To minimize the influence of the background, control measurements of the glass microscope slide were acquired as shown by the grey spectrum in Figure 4.21. It has to be noted that variation in intensities were observed between measurements, possibly resulting in (slightly) different spectrum.

The presence of MIPs and endogenous fingerprint molecules in the visualised fingerprint was also investigated using the imaging capabilities of the ToF-SIMS technique. Fragments assigned to amino acids, fatty acids and MIPs were grouped (Appendix, Section A.3) and a SIMS image was made of each group. Visibility of fingerprint ridges and composition differences of well and poorly visualised areas were investigated.

The well visualised fingerprint area showed a clear fingerprint ridge/furrow pattern in the ToF-SIMS images whereby the fingerprint ridges, recognisable by the pores, showed on average a higher intensity of the selected masses (Figure 4.22).

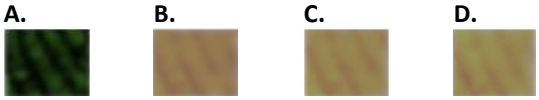

Figure 4.22 – Mass-selected ToF-SIMS images of a well visualised fingerprint area (**A**). The ToF-SIMS images were based on groups of fragments which were tentatively assigned to MIPs (**B**), amino acids (**C**) and fatty acids (**D**). The colour scales of the ToF-SIMS were individually adjusted to obtain optimal contrast, a high and low intensity was indicated by the yellow and red colour respectively.

In the poorly visualised area a less distinct fingerprint ridge/furrow pattern was observed in the ToF-SIMS images compared to the well visualised fingerprint area (Figure 4.23 versus Figure 4.22).

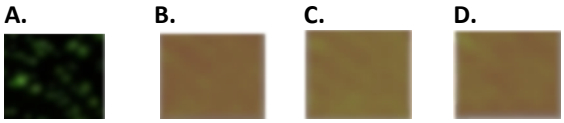

Figure 4.23 – Mass-selected ToF-SIMS images of a poorly visualised fingerprint area (**A**). The ToF-SIMS images were based on group of fragments which are tentatively assigned to MIPs (**B**), amino acids (**C**) and fatty acids (**D**). The colour scales of the ToF-SIMS were individually adjusted to obtain optimal contrast, a high and low intensity was indicated by the yellow and red colour respectively.

A less distinct pattern in the ToF-SIMS images could indicate a smaller difference in intensity of the selected masses between the ridges and furrows. This could suggest that masses tentatively assigned to amino acids, fatty acids and MIPs had a lower intensity, were absent or smudged in that area. Unfortunately, the cause of the poorly visualised area could not be discovered by mass-selected ToF-SIMS images. It must be kept in mind that the intensity is not always related to the concentration of the ions as it depends on several experimental factors, such as the difference in behaviour of the fingerprint residue and the glass substrate regarding the formation of secondary ions and thereby intensity; also called the matrix effect.

In some parts of the non-fluorescent fingerprint area, fingerprint ridges were observed in the ToF-SIMS images, both by selecting ions tentatively assigned to the MIPs and endogenous fingerprint molecules (Figure 4.23). This could have been caused by an incorrect assignment of the peaks due to an overlap in proposed MIP and endogenous fingerprint fragments as well as by possible contamination, resulting in a non-representative image. Alternatively, the fluorescence of the MIPs could have been bleached away, the MIPs in this region did not contain fluorescent groups and/or MIPs in this region were buried in the fingerprint and therefore not detectable by the camera. However, due to the nature of the ToF-SIMS technique, only the top-layer was analysed which makes it unlikely that fluorescent MIPs were not recorded by the camera (DCS 5) but were detected using ToF-SIMS.

To conclude, ToF-SIMS demonstrated the ability to image fingerprints with enough resolution to observe fingerprint ridges and even pores. However, no unambiguous explanation has been found to why certain areas in the fingerprint were less well visualised with the MIPs than other areas, perhaps due to the complexity of the used fingerprint matrix and lack of specificity of the fragments which made the interpretations speculative.

4.3.6. Hydrophobicity range of linear MIPs

As (aged) fingerprints are relatively hydrophobic, increasing the hydrophobicity of the aqueous MIPs could make it easier for the MIPs to enter the fingerprint and increase

the percentage of fluorescent fingerprints. The hydrophobicity of the $_{BSA\text{-}L}$MIPs was modified by varying the ratio of the monomers tBAm and acrylamide, after which the effect of the hydrophobicity of the $_{BSA\text{-}L}$MIPs on the performance of the $_{BSA\text{-}L}$MIPs was investigated.

Hereby must be taken into account that by increasing the ratio tBAm/acrylamide the affinity of the $_{L}$MIPs towards the target molecule albumin could be affected. As illustrated in Figure 4.24, the tert-butyl group of tBAm probably does not increase the strength of the interactions but can lead to steric effects, thus reducing the strength of the bonds. Resulting in possibly a higher affinity of the protein albumin with acrylamide than to tBAm.

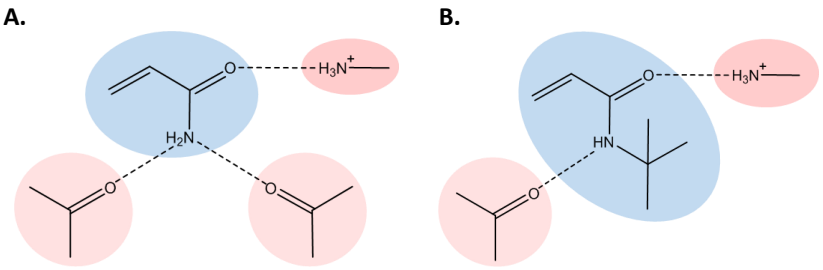

Figure 4.24 – Affinity of albumin with acrylamide (**A**) and tBAm (**B**) in which the red clouds illustrate functional groups of albumin, darker colour suggests stronger binding.

Besides the possible decrease in affinity of the $_{BSA\text{-}L}$MIPs towards albumin, the ease of entering the fingerprint increases probably also by increasing tBAm/acrylamide ratio due to the increase in hydrophobicity. Due to these opposing interests, an optimum of these factors, ease of the MIPs to enter the fingerprint without getting washed away while retaining enough affinity with the target molecule, has to be sought. In this section, the possible influence of these aspects was discussed by comparing fingerprints visualised using a range of $_{BSA\text{-}L}$MIPs synthesised with varying ratios acrylamide/tBAm.

Although a clear trend is lacking, Figure 4.25 illustrates that the highest percentage of fluorescent fingerprints was obtained using MIP solution number 3 which could indicate that both the ease of entering the fingerprint and the affinity of the MIPs with the target molecule were of influence on the performance of the $_{BSA\text{-}L}$MIPs.

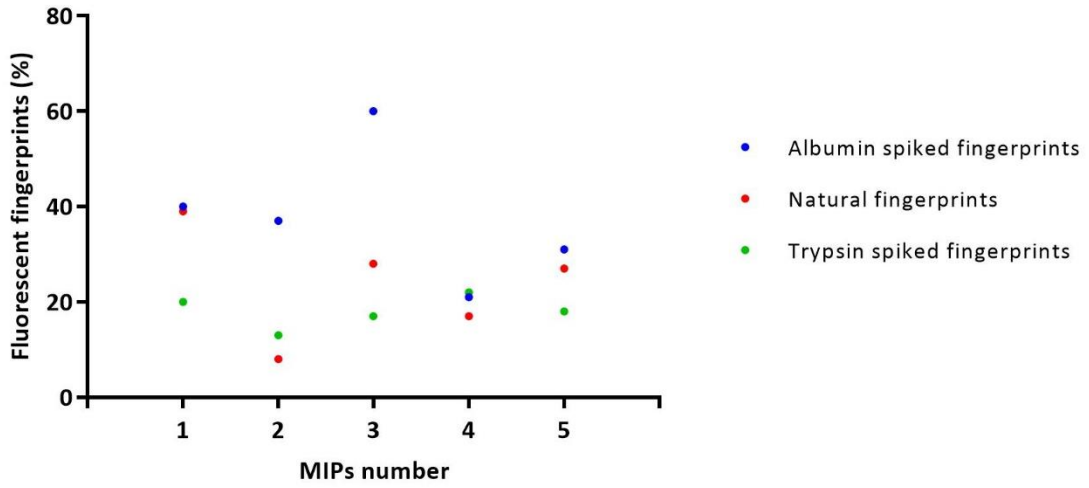

Figure 4.25 – The percentage of fluorescent fingerprints (normalised) obtained by exposure of natural, BSA-spiked and trypsin-spiked fingerprints to albumin imprinted linear MIPs. A range of MIP compositions were used, in which MIP nr.1 is the most hydrophilic and MIP nr. 6 is the most hydrophobic (lowest and highest tBAm/acrylamide ratio, respectively).

Although both the ease of entering the fingerprint and the affinity of the MIPs are probably interwoven into each other, the following explanations can possibly be made. By increasing the hydrophobicity of the $_{L}$MIPs, it became possibly easier for the $_{BSA\text{-}L}$MIPs to enter the fingerprint and less easily to get washed away, resulting in a higher percentage of fluorescent fingerprints in general ($_{BSA}$fingerprints, $_{NAT}$fingerprints and $_{TR}$fingerprints). By decreasing the hydrophobicity of the $_{L}$MIPs, the recognition capacities of the $_{L}$MIPs towards the target molecule possibly increases, resulting in a higher percentage of specific binding and thereby percentage of fluorescent $_{BSA}$fingerprints. It has to be noted that the concentration of albumin naturally present in a fingerprint could also be of influence on the interpretation of these results. A concentration of albumin naturally present in the fingerprint which is above the saturation limit of the $_{L}$MIPs could lead to an indistinguishability of the $_{BSA}$fingerprints and the fingerprints containing naturally present albumin only.

4.3.7. Influence of the substrate on the detection of fingerprints

To determine whether the detection of albumin in fingerprints using MIPs is limited to glass substrates or could also be performed on other substrates, deposited fingerprints on plastic substrates (polystyrene (PS), polyvinylchloride (PVC) and polyethyleneftalate (PET)) and stainless steel were detected using $_{BSA\text{-}L}$MIPs. Important factors, such as the

properties of the substrate (hydrophobicity and adsorption to albumin) and substrate-fingerprint interaction (causing a change in fingerprint structure), which might have an influence on the performance of the $_{L}$MIPs are outlined in Table 4.8.

Table 4.8 – Properties of the tested substrates; glass, stainless steel, polystyrene (PS), polyvinylchloride (PVC) and polyethyleneftalate (PET). *Hydrophobicity determinations were performed by contact angle measurements of a water droplet placed on the substrate. NR=not reported. N/A=not applicable.

	Glass	Stainless steel	PS	PVC	PET	Ref.
Contact angle (^{0})*	50	85	93	78	66	N/A
Adsorption of albumin	Possibly/Yes	Possibly/Yes	Yes	Yes	Yes	[36-39]
Change in fingerprint structure	No	NR	Yes	Yes	Yes	[40]

4.3.7.1. Plastics

In this study, the possibility to detect fingerprints deposited on different plastics (PS, PVC and PET) using $_{BSA\text{-}L}$MIPs was investigated.

Spiking the fingerprints deposited on PET with albumin increased the percentage of fluorescent fingerprints (green dots in Figure 4.26). Contrary to this, the addition of albumin (or trypsin) to fingerprints deposited on PS and PVC did not result in a higher percentage of fluorescent fingerprints.

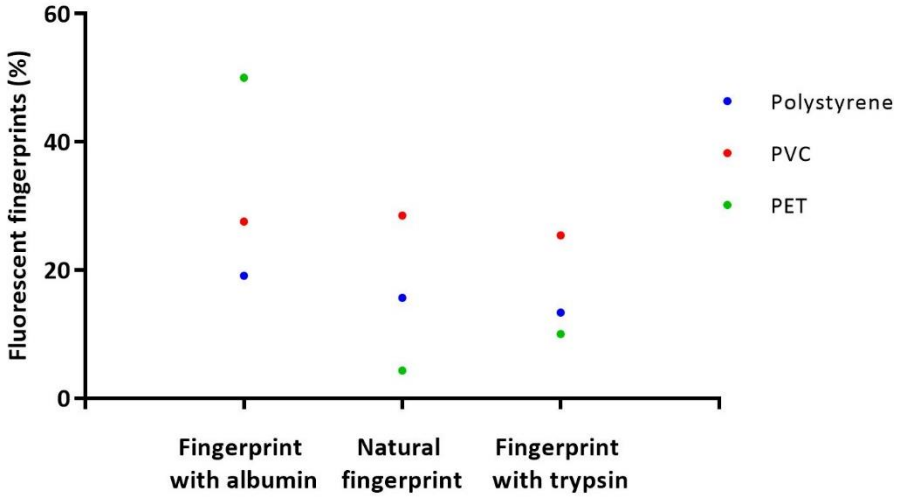

Figure 4.26 – The percentage of fluorescent fingerprints (normalised) obtained by BSA imprinted linear MIPs treatment of BSA-spiked, natural and trypsin-spiked fingerprints deposited on polystyrene (PS), polyvinylchloride (PVC) and polyethyleneftalate (PET) substrates.

Regarding PET, the increased percentage of fluorescent fingerprints by spiking with albumin could be explained by specific binding of the $_{BSA\text{-}L}$MIPs whereas for PS and PVC

non-specific binding could be attributed to no change. Alternative explanations could be that the concentration albumin naturally present in a fingerprint was above the saturation limit of $_{BSA\text{-}L}$MIPs and/or the total amount of albumin spiked on the fingerprints was not detected. Fingerprints deposited on PET substrates resulted in a higher percentage of fluorescent fingerprints than using PS or PVC substrates. These differences in percentages could possibly be explained by the differences in hydrophobicity of the PET, PVC and PS substrates (Table 4.8). It is known that the tertiary structure of albumin could change upon adsorption to plastics. [41] Difference in adsorption strength and associated structure change are possible for the different plastics because of the different hydrophobicity characteristics of the plastics. However, there is discrepancy about the exact influence of hydrophobicity on the adsorption; adsorption on polystyrene and barely on hydrophilic substrates such as glass has been observed [42] as well as adsorption on hydrophilic substrates [43]. An increase in adsorption of albumin with hydrophobicity could lead to an increase in change in tertiary structure which could explain limited recognition capabilities of the MIPs using PS and PVC substrates.

The detection of fingerprints using MIPs could possibly also be influenced by the structure and/or morphology of the fingerprint residue. This is suggested by the change in structure and morphology of fingerprints deposited on plastics over time, while fingerprints deposited on glass remain relatively stable. [40] These changes could possibly alter the location and reachability of the target molecules by the MIPs. In addition, the 'history' of the substrate such as contamination by previous substances could also be of influence on the deposition of the fingerprints and thereby on the detection of fingerprints using MIPs.

4.3.7.2. Stainless steel

Similar to the experiments performed on glass and plastic substrates, fingerprints deposited on stainless steel substrates were detected using $_{BSA\text{-}L}$MIPs. After which the obtained percentage of fluorescent fingerprints were normalised to compensate for the loss of fingerprints during the washing procedure. The percentage of fingerprints completely/partly removed during the washing process were determined by eye or light

microscope. However, because of the high amount of irregularities on the stainless steel substrates, the fingerprints were difficult to recognize. This resulted in a low percentage of present/observed fingerprints and after normalisation in an unrealistic high percentage of fluorescent fingerprints (blue dots in Figure 4.27). The percentages of fluorescent fingerprints before normalisation showed that spiking the fingerprints with the target molecule albumin did not increase the percentage of fluorescent fingerprints (Figure 4.27). This suggests that the $_{BSA\text{-}L}$MIPs behaved non-specifically and/or the concentration albumin naturally present in a fingerprint was above the saturation limit of $_{BSA\text{-}L}$MIPs.

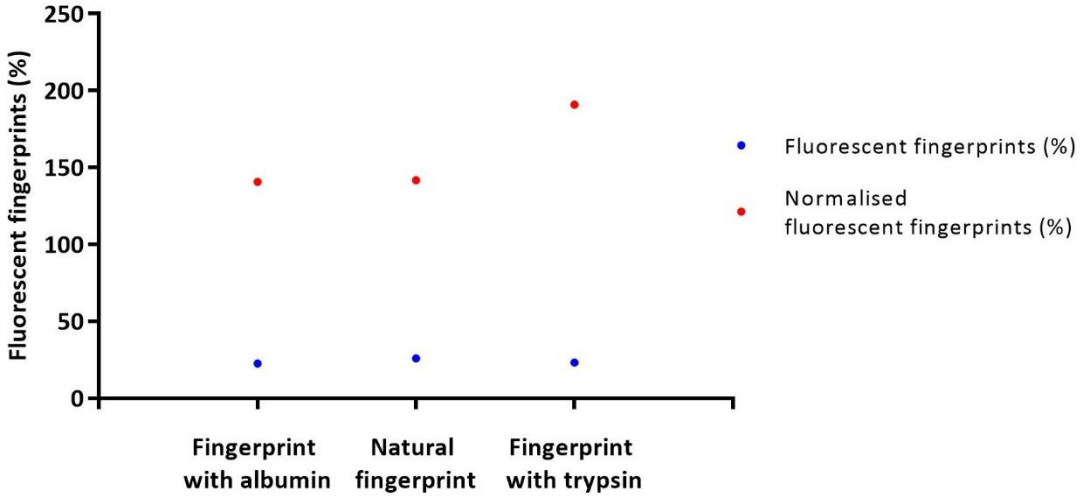

Figure 4.27 – The percentage of fluorescent fingerprints obtained by BSA imprinted linear MIPs treatment of BSA-spiked, natural and trypsin-spiked fingerprints deposited on stainless steel. The percentage of fluorescent fingerprints were shown before and after normalisation.

Similar to the plastic substrates, adsorption of albumin to the stainless steel substrates could be of influence on the detection of albumin in the fingerprint using MIPs. [37, 44] This could possibly result in a decrease in detected amount of albumin and thereby lower percentage of fluorescent fingerprints. The 'history' of the substrate such as 'contamination by previous substances could also be of influence on the deposition of the fingerprints and thereby on the detection of fingerprints using MIPs. This is implied by the difficulties to observe the fingerprints by eye or light microscope due to the presence of irregularities on the substrate which might also have influenced the deposition of the fingerprint and interaction between the fingerprint and the substrate.

To conclude, fingerprints deposited on plastic or stainless steel could be detected using $_{BSA\text{-}L}$MIPs, although it is questionable whether the $_{BSA\text{-}L}$MIPs behaved specifically. In addition, both the interactions of the substrate with the target molecule albumin and with the fingerprint could be of influence on the performance of the $_{BSA\text{-}L}$MIPs. Here, the structure of the protein, type of substrate and 'history' of the substrate could be of importance.

4.3.8. Influence of the fingerprint composition on the detection of fingerprints

The influence of the fingerprint composition on the detection of albumin in a fingerprint using $_{BSA\text{-}L}$MIPs was explored in a controlled manner by simulating fingerprints. Fingerprints were simulated by depositing ca. 5µL of a model fingerprint solution on a microscope glass slide in the form of a stamp or droplet. Subsequently they were treated with $_{BSA\text{-}L}$MIPs. Similar to the experiments using fingerprints, natural, albumin containing and trypsin containing simulated fingerprints were created. Due to the absence of albumin in the 'natural' simulated fingerprints as well as in the simulated fingerprints containing trypsin, both could function as negative control.

The model fingerprint solutions were formed of eccrine and/or sebaceous molecules (Appendix, Section A.1) to cover a range of fingerprint types. One model fingerprint solution contained eccrine plus 1% sebaceous fingerprint molecules to simulate aqueous fingerprints. The other model fingerprint solution contained only sebaceous fingerprint molecules to simulate hydrophobic/viscous fingerprints. Hereafter referred to as eccrine/sebaceous and sebaceous, respectively. Due to the viscosity of the sebaceous model fingerprint solution, this solution was only deposited on the microscope glass slides in the form of a stamp.

As shown in Table 4.9, in general a lower percentage of fluorescent stamps/droplets were obtained using the sebaceous solution than using the eccrine/sebaceous solution. This could be caused by a decrease in ease of the $_{BSA\text{-}L}$MIPs to enter the stamp/droplet by increasing hydrophobicity/viscosity, resulting in a decrease in percentage of fluorescent stamps/droplets. The decrease in percentage of fluorescent stamps (albumin and trypsin containing ones) by increasing drying/immersion time could

perhaps be caused by an increase in hydrophobicity/viscosity during drying and thereby a decrease in ease of the $_{BSA\text{-}L}$MIPs to enter the stamp. Although a contrary effect was observed in the experiments using the 'natural' stamps and albumin/trypsin containing droplets.

In addition, the percentage of fluorescent stamps/droplets was not consistently higher using the albumin containing stamps/droplets compared to the natural and trypsin containing stamps/droplets. This indicates that the $_{BSA\text{-}L}$MIPs behaved non-specifically. However, in the experiments using fingerprints (Figure 4.13A) specific binding of these $_{BSA\text{-}L}$MIPs was observed. This suggests that the performance of the $_{BSA\text{-}L}$MIPs was possibly influenced by the environment.

Table 4.9 – Percentage of fluorescent stamps/droplets obtained by exposure of albumin containing stamps/droplets, natural stamps/droplets and trypsin containing stamps/droplets to albumin imprinted linear MIPs. The stamps/droplets contained eccrine plus 1% sebaceous molecules (model fingerprint solution 1) or sebaceous molecules only (model fingerprint solution 2). *Drying/immersion time is the time between the positioning of the stamp/droplet and the first washing step.

	Stamps/droplets containing albumin		**'Natural' stamps/droplets**		**Stamps/droplets containing trypsin**	
Drying/immersion time	1h	24h	1h	24h	1h	24h
Model fingerprint solution 1	1.74% (droplet) 6.25% (stamp)	6.77% (droplet) 2.09% (stamp)	13.77% (droplet) 1.46% (stamp)	2.94% (droplet) 9.70% (stamp)	1.88% (droplet) 5.19% (stamp)	5.27% (droplet) 1.25% (stamp)
Model fingerprint solution 2	4.30%	2.73%	3.00%	0.63%	3.80%	6.92%

Exposure of stamps/droplets and fingerprints to $_{BSA\text{-}L}$MIPs resulted in a lower percentage of fluorescence in the stamps/droplets (Table 4.9) compared to the fingerprints (Figure 4.13A). This could possibly be caused by differences in thickness between the stamps, droplets and fingerprints. The thicker droplets and stamps compared to the fingerprints could have resulted in difficulties to detect albumin or fluorescent MIPs present in the lower part of the stamps/droplets resulting in a lower percentage of detected fluorescent stamps/droplets.

Additionally, the amount of albumin removed during the washing procedure could perhaps have an impact on the performance of the $_{BSA\text{-}L}$MIPs. For that reason albumin

was tracked in the stamp/droplet during the washing procedure. To be able to follow albumin, albumin was labelled with fluorescein.

This resulted in a higher percentage of fluorescent albumin in the sebaceous stamps than in the eccrine/sebaceous stamps/droplet (Table 4.10). Additionally, by increasing the drying/immersion time the percentage of fluorescent albumin increased or in other words the percentage during washing removed fluorescent albumin decreased. This could be caused by an increase in adherence to the hydrophobic sebaceous stamps and/or decrease in ease to get washed away in the sebaceous stamps compared to the eccrine/sebaceous stamps. Contrary to this theory, fingerprints are assumed to be less hydrophobic and viscous than the sebaceous stamps while a lower percentage of albumin was removed during washing in the fingerprints than in the stamps (32% versus 38-50%). This makes it likely that other aspects are also of influence on the performance of the $_{BSA\text{-}L}$MIPs such as the amount of fingerprint residue, physical shape of the fingerprint ridges/stamp and the accuracy of the albumin detection. In addition, the fluorescence intensity could also vary per solution/composition due to the dependency on a wide variety of factors such as solvent polarity, pH, oxygen solubility, viscosity [45] and refractive index. [46]

Table 4.10 – Percentage of fluorescent albumin present in the model fingerprint solutions 1 (eccrine plus 1% sebaceous molecules) and 2 (sebaceous molecules) after the washing steps. *Drying/immersion time is the time between the positioning of the stamp/droplet and the first washing step.

Drying/immersion time	Model fingerprint solution 1	Model fingerprint solution 2
1h	2.26% (droplet) 0.83% (stamp)	50%
24h	30% (droplet) 12% (stamp)	62%

To conclude, the experiments using the model fingerprint solutions demonstrated that the hydrophobicity, viscosity, amount of fingerprint residue and physical shape of the fingerprint ridges/stamp might have an influence on the performance of the MIPs.

4.3.9. Development quality of the fingerprint

As discussed earlier, this research aimed to address both the identification (visualisation) and retrieving intelligence information (specific component detection) purpose simultaneously. The specific component detection was discussed in the previous sections by the detection of the target molecule albumin present in a fingerprint using MIPs, expressed by the percentage of fluorescent fingerprints. To define the quality of the visualisation process, the visualised fingerprints were inspected in the presence of fingerprint ridges, fingerprint patterns and their consistency following the scoring guidelines of Table 4.4 as well as the presence of fingerprint ridge characteristics. To use fingerprints for identification purposes, fingerprint characteristics must be visible as discussed in Chapter 1 (Section 1.1.2.). As shown in Figure 4.28, primary level details such as whorls, secondary level characteristics such as ridge endings or bifurcations and even tertiary detail level such as pores were visible in the with MIPs visualised fingerprint which makes this technique promising for identification purposes

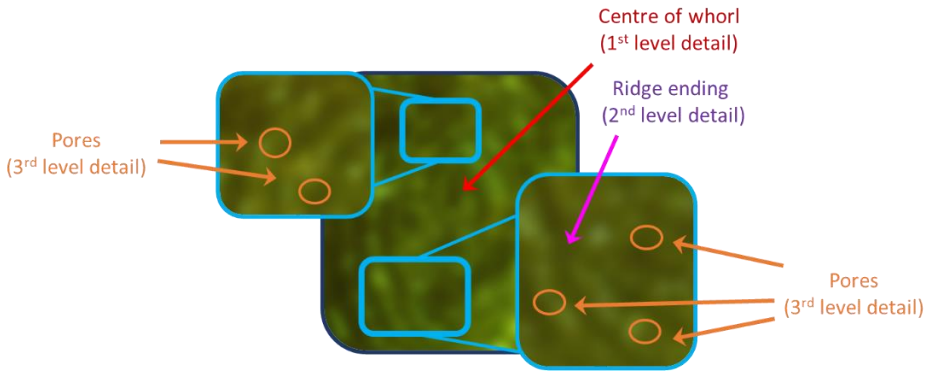

Figure 4.28 – Fingerprint visualised using fluorescent albumin imprinted linear MIPs, showing primary, secondary and tertiary level detail, obtained using excitation wavelength of 445 nm and long-pass viewing filter of 495 nm.

4.4. Conclusion

The aim of this research was to develop a novel fingerprint detection method using MIPs. Fluorescent MIPs were investigated to visualise fingerprints and to detect specific molecules in fingerprints because of their potential to recognise and bind to particular molecules. Here the protein albumin was chosen as target molecule in fingerprints.

A variety of MIPs were synthesised, of which the relatively hydrophobic linear MIPs appeared to be the most successful; defined by the yield (percentage of fluorescent fingerprints) and specificity (Obj. 1). This could be caused by a difference in shape and size of MIPs, $_{L}$MIPs may have entered the fingerprint more easily and remained more mobile in the fingerprint than the $_{N}$MIPs. These aspects as well as the recognition capacities of the $_{L}$MIPs could also be influenced by the hydrophobicity of the $_{L}$MIPs. In addition, the affinity of the linear MIPs and nano MIPs with their target molecule could have been of influence. Compositional information was obtained using MALDI-MS which demonstrated potential to determine the order of monomers in the MIPs chain, although some improvements are required to obtain an unambiguous monomer pattern. This knowledge could be of importance for the development of new MIPs, for instance imprinted towards a peptide with an amino acid sequence of interest.

The influence of the fingerprint composition/matrix on the behaviour of the MIPs was investigated using model fingerprint solutions and by determining potential causes of false positives (Obj. 2). The lower percentage of fluorescence obtained using sebaceous model fingerprint solution stamps compared to its eccrine (including 1% sebaceous) equivalent and to actual fingerprints suggest that the viscosity, hydrophobicity, amount of fingerprint residue and/or physical structure of the fingerprints could influence the performance of the $_{L}$MIPs. To define potential causes of false positives, the affinity of the MIPs with the target molecule compared to other relevant molecules and the presence of fluorescent molecules other than fluorescent MIPs were determined. SPR measurements showed that $_{BSA\text{-}L}$MIPs had a high affinity with their target molecule albumin and considerably lower affinity with other similar molecules. One of the most abundant proteins in the fingerprint (after albumin), keratin, displayed no/negligible binding to the $_{BSA\text{-}L}$MIPs, this suggests that it is probably unlikely that false positives will

be obtained by binding of the $_{BSA\text{-}L}$MIPs with other fingerprint molecules. Additionally, fluorescence was not detected in natural fingerprints or in the target compound albumin, this excludes another possible source of false positives.

The influence of the substrate on the detection of fingerprints using MIPs was determined using a variety of substrates; glass, polystyrene, PET, PVC and stainless steel (Obj. 3). Fingerprints were detected on each of the substrates, but it is questionable whether the substrate used has an influence on the ability of the $_{L}$MIPs to bind to specific target molecules. The performances of the $_{L}$MIPs could possibly be influenced both by interactions of the substrate with the target molecule albumin and with the fingerprint in which the structure of the protein, type of substrate and 'history' of the substrate could be of importance.

The MIPs appeared to have good visualisation properties, due to the observation of tertiary level detail this technique is promising for identification purposes (Obj. 4).

The scope and limitation of this application were investigated using analytical techniques (Obj. 5). ToF-SIMS was used to gain understanding why some areas in a fingerprint were less well visualised using MIPs. ToF-SIMS demonstrated the ability to image fingerprints with enough resolution to observe fingerprint ridges and even pores. In addition, the peaks present in a mass spectrum of a visualised fingerprint could tentatively be assigned to both fingerprint molecules (amino acids, fatty acids, salts) and MIPs. However, mass-selected ToF-SIMS images did not give unambiguous evidence why certain areas in the fingerprint were better visualised with the MIPs than other areas, perhaps due to the complexity of the used fingerprint matrix and lack of specificity of the fragments which makes the interpretation speculative. SPR measurements showed that there is potential to detect multiple molecules in one fingerprint using a series of MIPs which bind each to one type of molecule.

In conclusion, MIPs appear to be able to detect fingerprints by specific binding with albumin, although several aspects such as ease of entering the fingerprints, mobility in the fingerprint and substrate influence could vary per circumstances and need to be considered.

4.5. References

[1] R. Leggett, E.E. Lee-Smith, S.M. Jickells, D.A. Russell, "Intelligent" fingerprinting: simultaneous identification of drug metabolites and individuals by using antibody-functionalized nanoparticles, Angewandte Chemie International Edition, 46 (2007) 4100-4103.
[2] K. Kuwayama, K. Tsujikawa, H. Miyaguchi, K. T., Y.T. Iwata, H. Inoue, Time-course measurements of caffeine and its metabolites extracted from fingertips after coffee intake: a preliminary study for the detection of drugs from fingerprints, Analytical and Bioanalytical Chemistry, 405 (2013) 3945-3952.
[3] S. Lambrechts, A. van Dam, J. de Vos, A. van Weert, T. Sijen, M. Aalders, On the autofluorescence of fingermarks, Forensic science international, 222 (2012) 89-93.
[4] B. Hartzell-Baguley, R.E. Hipp, N.R. Morgan, S.L. Morgan, Chemical composition of latent fingerprints by gas chromatography-mass spectrometry, Journal of Chemical Education, 84 (2007) 689-691.
[5] C. Ricci, S.G. Kazarian, Collection and detection of latent fingermarks contaminated with cosmetics on nonporous and porous surfaces, Surface and Interface Analysis, 42 (2010) 386-392.
[6] P. Hazarika, S.M. Jickells, K. Wolff, D.A. Russell, Imaging of latent fingerprints through the detection of drugs and metabolites., Angewandte Chemie (International Edition in English), 47 (2008) 10167-10170.
[7] M.J. Bailey, R. Bradshaw, S. Francese, T.L. Salter, c. Costa, M. Ismail, R.P. Webb, I. Bosman, K. Wolff, M. de Puit, Rapid detection of cocaine, benzoylecgonine and methylecgonine in fingerprints using surface mass spectrometry Analyst, 140 (2015) 6254-6259.
[8] M. Abdelhamid, F. Fortes, M. Harith, J. Laserna, Analysis of explosive residues in human fingerprints using optical catapulting–laser-induced breakdown spectroscopy, Journal of Analytical Atomic Spectrometry, 26 (2011) 1445-1450.
[9] L.S. Ferguson, F. Wulfert, R. Wolstenholme, J.M. Fonville, M.R. Clench, V.A. Carolan, S. Francese, Direct detection of peptides and small proteins in fingermarks and determination of sex by MALDI mass spectrometry profiling, Analyst, 137 (2012) 4686-4692.
[10] V.C. Nayak, P. Rastogi, T. Kanchan, K. Yoganarasimha, G.P. Kumar, R.G. Menezes, Sex differences from fingerprint ridge density in Chinese and Malaysian population, Forensic science international, 197 (2010) 67-69.
[11] P. Ramasastry, D.T. Downing, P.E. Pochi, J.S. Strauss, Chemical composition of human skin surface lipids from birth to puberty, Journal of Investigative Dermatology, 54 (1970) 139-144.
[12] M. Nazzaro-Porro, S. Passi, L. Boniforti, F. Belsito, Effects of aging on fatty acids in skin surface lipids, Journal of Investigative Dermatology, 73 (1979).
[13] I. Ishiyama, M. Orui, K. Ogawa, T. Kimura, The determination of isoantigenic activity from latent fingerprints: mixed cell agglutination reaction in forensic serology, Journal of Forensic Science, 22 (1977) 365-375.
[14] S. Oden, B. von Hofsten, Detection of fingerprints by the ninhydrin reaction., Nature, 173 (1954) 449.
[15] S.P. Kaspar, D.J. Minnillo, A.M. Rockhold, Validation IND (1,2 - idanedione), Forensic Science Communications, 4 (2002).
[16] R. Ramotowski, A.A. Cantu, M.M. Joullie, O. Petrovskaia, 1,2-Indanediones: a preliminary evaluation of a new class of amino acid visualizing compounds., Fingerprint Whorld, 23 (1997) 131.
[17] S.J. Hinder, J.F. Watts, SIMS fingerprint analysis on organic substrates, Surface and Interface Analysis, 42 (2009) 826-829.
[18] M.J. Bailey, N.J. Bright, R.S. Croxton, S. Francese, L.S. Ferguson, S. Hinder, S. Jickells, T.B. Jones, B.N. Jones, S.G. Kazarian, J.J. Ojeda, R.P. Webb, R. Wolstenholme, S. Bleay, Chemical characterization of latent fingerprints by matrix-assisted laser desorption ionization, time-of-

flight secondary ion mass spectrometry, mega electron volt secondary mass spectrometry, gas chromatography/mass spectrometry, x-ray photoelectron spectroscopy, and attenuated total reflection fourier transform infrared spectroscopic imaging: an intercomparison, American Chemical Society, 84 (2012) 8514-8523.
[19] R. Wolstenholme, R. Bradshaw, M.R. Clench, S. Francese, Study of latent fingerprints by matrix-assisted laser desorption/ionisation mass spectrometry imaging of endogenous lipids., Rapid communications in mass spectrometry, 23 (2009) 3031-3039.
[20] A. van Dam, M.C.G. Aalders, K. van de Braak, H.J.J. Hardy, T.G. van Leeuwen, S.A.G. Lambrechts, Simultaneous labeling of multiple components in a single fingermark, Forensic Science International, 232 (2013) 173-179.
[21] R.S. Ramotowski, Chapter 3: Composition of latent fingerprint residue, Advances in fingerprint technology, CRC Press LLC2001.
[22] D. Lowe, K. Dudgeon, R. Rouet, P. Schofield, L. Jermutus, D. Christ, Aggregation, stability, and formulation of human antibody therapeutics., Advanced Protein Chemistry and Structural Biology, 84 (2011) 41-61.
[23] S. Dubel, O. Stoevestandt, M.J. Taussig, M. Hust, Generating recombinant antibodies to the complete human proteome, Trends in Biotechnology, 28 (2010) 333-339.
[24] A.D. Reinholtz, Albumin development method to visualize friction ridge detail on porous surfaces, Journal of Forensic Identification, 58 (2008) 524-539.
[25] J. Steinhardt, J. Krijn, J.G. Leidy, Differences between bovine and human serum albumins: binding isotherms, optical rotatory dispersion, viscosity, hydrogen ion titration, and fluorescence effects, Biochemistry, 10 (1971) 11.
[26] F. Canfarotta, A. Poma, A. Guerreiro, S. Piletsky, Solid-phase synthesis of molecularly imprinted nanoparticles, Nature protocols, 11 (2016) 443-455.
[27] Chemistry of Protein Assays, Thermo Fisher Scientific, https://www.thermofisher.com/uk/en/home/life-science/protein-biology/protein-biology-learning-center/protein-biology-resource-library/pierce-protein-methods/chemistry-protein-assays.html, accessed: 12/2/2018
[28] A. Girod, R. Ramotowski, C. Weyermann, Composition of fingermark residue: a qualitative and quantitative review, Forensic Science International, 223 (2012) 10-24.
[29] A. Motib, A. Guerreiro, F. Al-Bayati, E. Piletska, I. Manzoor, S. Shafeeq, A. Kadam, O. Kuipers, L. Hiller, T. Cowen, S. Piletsky, P.W. Andrew, H. Yesilkaya, Modulation of quorum sensing inaGram-positive pathogen by linear molecularly imprinted polymers with anti-infective properties, Anti-infective Agents, 129 (2017) 16782-16785.
[30] Albumin from bovine serum, https://www.sigmaaldrich.com/content/dam/sigma-aldrich/docs/Sigma/Product_Information_Sheet/b8667pis.pdf.
[31] Sigma-Aldrich, Human Albumin, https://www.sigmaaldrich.com/life-science/metabolomics/enzyme-explorer/enzyme-reagents/human-albumin.
[32] Sigma-Aldrich, Trypsin, https://www.sigmaaldrich.com/technical-documents/articles/biology/trypsin
[33] Sigma-Aldrich, Product Information Streptavidin from Streptomyces acidinii, https://www.sigmaaldrich.com/content/dam/sigmaaldrich/docs/Sigma/Product_Information_Sheet/1/s4762pis.pdf
[34] E. Fuchs, H. Green, The expression of keratin gener in epidermis and cultured epidermal cells, Cell, 15 (1978) 887-897.
[35] H.H. Bragulla, D.G. Homberger, Structure and functions of keratin proteins in simple, stratified, keratinized and cornified epithelia, Journal of Anatomy, 214 (2009) 516-559.
[36] K. Nakanishi, T. Sakiyama, K. Imamura, On the adsorption of proteins on solid surfaces, a common but very complicated phenomenon, Journal of bioscience and bioengineering, 91 (2001) 233-244.
[37] S. Fukuzaki, H. Urano, K. Nagata, Adsorption of protein onto stainless-steel surfaces, Journal of Fermentation and Bioengineering, 80 (1995) 6-11.

[38] H.B. Bull, Adsorption of bovine serum albumin on glass, Biochimica et biophysica acta, 19 (1956) 464-471.
[39] M.R. Duncan, J.M. Lee, M.P. Warchol, Influence of surfactants upon protein/peptide adsorption to glass and polypropylene, International journal of pharmaceutics, 120 (1995) 179-188.
[40] S. Moret, X. Spindler, C. Lennard, C. Roux, Microscopic examination of fingermark residues: Opportunities for fundamental studies, Forensic Science International, (2015) 28-37.
[41] J.R. Smith, M.T. Cicerone, C.W. Meuse, Tertiary structure changes in albumin upon surface adsorption observed via fourier transform infrared spectroscopy, Langmuir, 25 (2009) 4571-4578.
[42] G. Sagvolden, I. Giaever, J. Feder, Characteristic protein adhesion forces on glass and polystyrene substrated by atomic force microscopy, Lanmuir, 14 (1998) 5984-5987.
[43] W. Norde, J.P. Favier, Structure of adsorbed and desorbed proteins, Colloids and surfaces, 64 (1992) 87-93.
[44] T. Sakiyama, J. Tomura, K. Imamura, K. Nakanishi, Adsorption characteristics of bovine serum albumin and its peptide fragments on a stainless steel surface, Colloids and Surfaces B: Biointerfaces, 33 (2004) 77-84.
[45] J. Widengren, R. Rigler, Mechanisms of photobleaching investigated by fluorescence correlation spectroscopy, Bioimaging, 4 (1996) 149-157.
[46] C. Jones, K. Suhling, Refractive index sensing using fluorescence lifetime imaging (FLIM), Journal of Physics: Conference Series, IOP Publishing, 2006, pp. 223.

Conclusions and future work 5

5.1. Conclusions

Most fingerprints found at a crime scene are not yet visible to the naked eye and require a visualisation process before they can be used for identification, which makes the fingerprint visualisation process of high importance. [1] This research aimed to improve the detection of fingerprints by two approaches; enhance currently used techniques by creating a flow in a fingerprint using electrowetting (5.1.1) and developing a novel detection method using molecularly imprinted polymers (MIPs) (5.1.2).

5.1.1. Enhancement of currently used fingerprint visualisation techniques by creating a flow in a fingerprint using electrowetting

The first aim of this research was to improve the detection of fingerprints by the formation of a flow in a fingerprint induced by applying a potential across a droplet/simulated fingerprint and its underlying substrate, also known as the electrowetting process. This could lead to enhancement of the reachability of fingerprint molecules, which is advantageous for visualisation reagents to increase reaction and homogeneously distribution within fingerprint ridges, resulting is more and homogenously visualised fingerprints.

To obtain insight into potential driven interfacial energy changes, the effects of applying a potential onto a surface were determined in **Chapter 2.** The surface characteristics of conductive polymers were investigated, demonstrating that the following characteristics could be tuned to a small or large extent; hydrophobicity, topography (roughness) and composition (Obj. 1). The oxidation and reduction of the polymer films resulted in colour and compositional changes, however no distinct potential driven morphological changes were observed. The polymer films were generally more

hydrophilic in oxidised state than in reduced state. The roughness increased slightly by oxidising the film. However, these trends were not observed under all circumstances.

To justify sequential use of surface analysis and film formation techniques, the impact of surface analysis and film formation techniques on each other was investigated by determining the influence of wetting caused by a droplet (used for contact angle measurements) and by in solution film formation on the roughness measurements (Obj. 2). Wetting of the polymer film caused by a droplet or by in solution film formation appeared to have no influence on the roughness measurements, therefore sequential contact angle and roughness measurements as well as the roughness measurements directly after the polymer film formation could be performed.

In addition, the influence of potential driven topographical (roughness) changes of the polymer film on the contact angle measurements was investigated using several models (Obj. 3). This is of importance for the interpretation of contact angle measurements, used to determine the hydrophobicity, because they could be influenced by chemical/molecular factors such as polarity but also by physical/macroscopic factors such as roughness of the polymer film. The exact influence of roughness compared to other factors, such as charge, on the contact angle differed with each model. The Wenzel model, suggesting a movement of the droplet into the grooves of the surface, [2] showed a relatively large influence of the roughness compared to other factors on the contact angle change. While the Cassie-Baxter model, suggesting the presence of surrounding air/liquid trapped into the grooves, [3] illustrated a contrary trend. Neither of the models were applicable for all films, suggesting that a model including more factors would be best to describe the influences on the contact angle.

In conclusion, by applying a potential across a droplet and the underlying surface, several characteristics such as hydrophobicity, composition and topography (roughness) could be tuned to a large or small extent, whereby factors such as charge and roughness could be of influence.

Chapter 3 focussed on the formation of a flow in a fingerprint induced by electrowetting. To provide insight into electrowetting mechanisms, the electrowetting

effect was not only expressed in the conventional way by the change in contact angle but also by nano gravimetric methods (quartz crystal microbalance; QCM) and movements inside the droplet (Obj. 1). It was demonstrated that QCM may have potential to detect an electrowetting effect, although more research is needed before application. Optimisation of the dielectric layer to prevent breakdown and obtaining a better understanding of the influence of certain factors (such as hydrophobicity) and inexplicable observations are recommended. The movements inside the droplets were followed by the tracking of particles added to the droplet, showing a movement induced by electrowetting.

The droplets used in this study were not only subjected to a potential, but also to evaporation as the measurements were performed in air (Obj. 2). It was shown that the influence of evaporation on the shape change of droplets was negligible compared to the potential, although vigorous movements of the droplets could enhance the evaporation.

The optimum conditions and limitations of this electrowetting application were determined by investigating the impact of the dielectric layer, potential and frequency (Obj. 3) as well as the composition and physical structure of the fingerprint (Obj. 4) on the electrowetting process. Regarding the impact of the dielectric layer and external factors (potential and frequency) on the electrowetting process, the most (trackable) movement in a droplet was observed using a frequency of 100/200 Hz and a high potential. The actuated contact angle appeared to be independent on frequency and increased with potential. Due to the dielectric strength of the surface, 200 V was chosen as optimum. The addition of a hydrophobic top-layer increased the amount of electrowetting effect and was therefore used for further experiments in this research. To determine the impact of the composition and physical structure of the fingerprint on the electrowetting of fingerprints application, the effects of the following fingerprint characteristics (both compositional and physical) were investigated; viscosity, salinity, height of the fingerprint, contact pinning and initial contact angle (Obj. 4). The amount of movement inside the droplet decreased by increasing viscosity and salinity as well as electrolysis occurred using droplets with high salinity, which might be inconvenient for the formation of a flow in (aged) fingerprints. Other challenges might be present,

suggested by the experiments using a model fingerprint solution, in which the subjection of a model fingerprint solution droplet to an AC potential did not result in complete retraction of the droplet. Additionally, the amount of contact pinning, low initial contact angle and uneven height distribution of a fingerprint could make this electrowetting of fingerprints application challenging. The structure and composition of the fingerprint does not only impact the electrowetting process, but the electrowetting process could also have an impact on the fingerprint (Obj. 4). Movements of the contact line could possibly affect the physical structure of the fingerprint when a potential is applied directly across the fingerprint and the underlying substrate, although a significant change is unlikely. Additionally, by applying a potential across a droplet positioned on top of a fingerprint and the underlying substrate, a movement in contact line of the droplet is likely to be irrelevant.

To conclude, it was shown that it is possible to create a flow in a droplet, however for the formation of a flow in a fingerprint induced by electrowetting several challenges must be overcome.

5.1.2. Detection of fingerprints using MIPs

The second aim of this research was to develop a novel fingerprint detection method using MIPs. Fluorescent MIPs were explored to visualise fingerprints and to detect specific molecules in fingerprints because of their potential to recognise and bind to particular molecules. Here the protein albumin was chosen as target molecule in fingerprints.

A variety of MIPs were synthesised, of which the linear relatively hydrophobic MIPs appeared to be the most successful for this application; defined by the yield and specificity (Obj. 1). The shape, size and hydrophobicity of the MIPs seem to be of influence on the performance of the MIPs in this application; linear MIPs may have entered the fingerprint more easily and remained more mobile within the fingerprint than the nano MIPs. A decrease in hydrophobicity of the linear MIPs may have resulted in an increase in recognition capacities but also in a decreased accessibility of the linear MIPs to the fingerprint. Additionally, the affinity of the linear MIPs and nano MIPs with their target molecule could have been of influence. Compositional information was

obtained using Matrix Assisted Laser Desorption/Ionisation Time of Flight Mass Spectrometry (MALDI-ToF-MS) which demonstrated potential to determine the order of monomers in the MIPs chain, although some improvements are required to obtain an unambiguous monomer pattern. This knowledge could be of importance for the development of new MIPs, for instance imprinted towards a peptide with an amino acid sequence of interest.

In addition, the influence of the fingerprint composition/matrix on the behaviour of the MIPs was investigated using model fingerprint solutions and by determining potential causes of false positives (Obj. 2). The lower percentage of fluorescence obtained using sebaceous model fingerprint solution stamps compared to its eccrine (including 1% sebaceous) equivalent and to actual fingerprints suggest that the viscosity, hydrophobicity, amount of fingerprint residue and/or physical structure of the fingerprints might have an influence on the performance of the $_{L}$MIPs. The impact of the fingerprint composition/matrix leading to false positives was investigated by the presence of fluorescent molecules other than fluorescent MIPs and the affinity of the MIPs with the target molecule compared to other relevant molecules. This is of special interest for the use of MIPs for specific component detection. Surface plasmon resonance analysis showed that albumin imprinted linear MIPs have a higher affinity with their target molecule albumin than to other similar relevant molecules. One of the most abundant proteins in the fingerprint (after albumin), keratin, showed no to minor binding to the albumin imprinted linear MIPs which suggests a low ratio of false positives. Additionally, fluorescence was not detected in a natural fingerprint or in the target molecule, excluding the influence of fluorescent groups which are naturally present in fingerprints (such as the amino acids phenylalanine, tyrosine and tryptophan) on the percentage of fluorescent fingerprints.

The influence of the substrate on the detection of fingerprints using MIPs was determined using a variety of substrates; glass, polystyrene, PET, PVC and stainless steel (Obj. 3). Fingerprints deposited on glass, plastic and stainless steel were detected using MIPs, but it is unclear whether the substrate has an influence on the ability of the linear MIPs to bind to specific target molecules. Substrate-albumin and substrate-fingerprint

interactions could affect the detection of fingerprints using MIPs, in which the structure of the protein, type of substrate and 'history' of the substrate could be of importance.

In addition, the MIPs appeared to have good visualisation properties, even tertiary level detail was observed which makes the use of MIPs promising for identification purposes (Obj 4).

The scope and limitations of the detection of fingerprints using MIPs were investigated using analytical techniques (Obj. 5). Visualised fingerprints were analysed using the mass spectrometry imaging technique Time of Flight Secondary Ion Mass Spectrometry (ToF-SIMS) to gain understanding why some areas in a fingerprint were less well visualised using MIPs. ToF-SIMS demonstrated ability to image fingerprints with enough resolution to observe the fingerprint pattern and even pores. ToF-SIMS was also able to detect fragments which could tentatively be assigned to fingerprint molecules (amino acids, fatty acids and salts) and MIPs in a visualised fingerprint. However, mass-selected ToF-SIMS images did not give unambiguous evidence why certain areas in a fingerprint were less visualised using MIPs, perhaps due to the complexity of the matrix (fingerprint and polymers on glass) and lack of specificity of the fragments which made the interpretations speculative. Additionally, using affinity measurements it was shown that there is potential to detect multiple molecules in one fingerprint using a series of MIPs which bind each to one type of molecule.

In conclusion, MIPs appeared to be able to detect fingerprints by specific binding with albumin, although several aspects such as ease of entering the fingerprints, ease of being washed away and substrate influences could vary with circumstances and need to be kept in mind.

5.2. Future work

5.2.1. Enhancement of currently used fingerprint visualisation techniques by creating a flow in a fingerprint using electrowetting

To increase the understanding of the behaviour of potential driven characteristics of polymer films in addition to current literature and the research findings presented in this thesis, the influence of physical and chemical influences on the characteristics of the polymer films need to be studied. More knowledge about the development of these characteristics throughout the entire redox process is desired. Therefore, analysing characteristics of the polymer films such as hydrophobicity and roughness at several stages during the redox reaction is recommended.

In addition, in-situ roughness measurements are recommended to exclude the effect of drying on the polymer films and to measure the roughness continuously throughout the electrochemical reaction. Preliminary tests using the optical (3D) microscope showed potential for in-situ measurements although an improved set-up is necessary to address several challenges such as having the surface continuously in focus while being immersed in solution and determining the right positions of the electrodes.

Additionally, it is recommended to explore the characteristics of a range of materials such as conductive polymers of each group (Chapter 1) or materials conventionally used to obtain electrowetting-on-a-dielectric.

For the formation of movement in a fingerprint induced by electrowetting, more research focussing on the flow formation and possible relation between flow formation and contact angle change is desired. Additionally, change in the electrowetting set-ups such as a plate as top-electrode instead of a wire or the use of individually addressable electrodes which make the top-electrode no longer required (Chapter 2, Figure 2.1) could possibly open opportunities for the formation of a flow in a fingerprint using electrowetting.

To obtain a more thorough understanding of the application of QCM for expressing the electrowetting effect, the dielectric layer needs to be optimised to prevent dielectric breakdown. In addition, investigating the influences of an external applied potential,

droplet composition and hydrophobicity of the surface on the QCM measurements are desired.

5.2.2. Detection of fingerprints using MIPs

To get a better understanding of the possibilities of the detection of fingerprints using MIPs, the sensitivity in terms of concentration needs to be determined. To make the detection of fingerprints using MIPs more suitable for practise, a shorter MIPs immersion time and applicability on porous substrates are desired. In addition, a comparison with currently used fingerprint visualisation techniques should be performed to evaluate the performance of the MIPs for the detection of fingerprints.

An increase in knowledge of the MIPs composition, possibly using MALDI in combination with MS/MS, would be of use for the development of MIPs which are targeting peptides with an amino acid sequence of interest. Additionally, the detection of more forensically or medically relevant molecules would make this application more suitable for practise. For instance, the detection of a drug in a fingerprint or tracking of the amount of medication present in a patient by detection of the medication in the patients' fingerprint. In some promising studies (eccrine) sweat has already been analysed for diagnostic purposes. [4, 5]

5.3. References

[1] R.S. Croxton, M.G. Baron, D. Butler, T. Kent, V.G. Sears, Variation in amino acid and lipid composition of latent fingerprints, Forensic Science International, 199 (2010) 93-102.
[2] R.N. Wenzel, Resistance of solid surfaces to wetting by water, Industrial & Engineering Chemistry, 28 (1936) 988-994.
[3] A. Cassie, S. Baxter, Wettability of porous surfaces, Transactions of the Faraday society, 40 (1944) 546-551.
[4] M.M. Raiszadeh, M.M. Ross, P.S. Russo, M.A. Schaepper, W. Zhou, J. Deng, D. Ng, A. Dickson, C. Dickson, M. Strom, Proteomic analysis of eccrine sweat: implications for the discovery of schizophrenia biomarker proteins, Journal of proteome research, 11 (2012) 2127-2139.
[5] A. Mena-Bravo, M.L. De Castro, Sweat: a sample with limited present applications and promising future in metabolomics, Journal of pharmaceutical and biomedical analysis, 90 (2014) 139-147.

Appendix

A.1. Fingerprint composition

The composition of a fingerprint, based on the literature is outlined in Tables A.1-A.7, including the references mentioned in the review articles as well as the model fingerprint solution which has been used to mimic a fingerprint.

Table A.1 – Overview of molecules present in a fingerprint as well as the molecules included in the model fingerprint solution. X= quantity not specified. NR=not reported. *=Molecular concentration based on average ion concentrations.

Compound	Model fingerprint solution	Girod *et al. [1]*	Ramotowski *[2]*	Bayford *[3]*
Water	98.95%	99%	98%	99.7-99.0%
NaCl *	45.4 – 88.8 mM	54.0 mM (Na) [2, 4] 1-15 µg (Cl) [2, 5-7]	46 mEq (Cl) [8] 34-266 mEq/L (Na) 60 mEq/L (Na) [8] 140 mEq/L (Na) [9]	39 mEq/L (Cl)
KCl *	15.8 mM	1-15 µg (Cl) [2, 5-7] 0.2-5 µg or 39.9 µM (K) [2]	46 mEq (Cl) [8] 5-59 mEq/L (K) [8] 4.9-8.3 mEq/L (K) [10] 8.8 mEq/L (K) [11]	39 mEq/L (Cl) ([K] > [Na])
$NaHCO_3$ *	9.6 mM	54.0 mM (Na) [2, 4]	15-20 mM (HCO_3)	NR
Urea	0.88 g/L	0.4-1.8 µg [12-16]	10-15 mM [17]	30-2000 mg/L
Uric acid	NR	150 µM [2, 18]	NR	X
Lactic acid	154 mM	9-10 µg or 154 mM [2, 12, 13, 18, 19]	NR	NR
Ammonia	NR	0.2-0.3 µg or 5.13 mM [2, 3]	0.5- 8 mM [20]	12-400 mg/L
Pyruvate	NR	NR	0.2-1.6 mM [21]	NR
Proteins	0.2 g/L	384 µg [22, 23]	15-25 mg/dL	NR
Glucose	NR	NR	0.2-0.5 mg/dL [21]	< 7.5 mg/L
Glycogen	NR	NR	NR	~7.5-30 mg/L
Lactate	NR	NR	30-40 mM [17]	NR
Pyruvate	NR	NR	NR	NR
Amino acids	1.45 mg/L	0.2-1 µg [12, 13, 15, 16, 24-29]	0.3-2.59 mg/L [3]	0.3-2.59 mg/L
Sterols	NR	NR	0.01-0.12 µg/mL	NR
Phenol	NR	0.06-0.25 µg [2]	NR	NR
Calcium	NR	0.03-0.3 µg or 5.49 mM [2, 4]	3.4 mEq/L	NR
Sulphide	NR	0.02-0.2 µg [2]	NR	NR
Magnesium	NR	1.67 mM [3]	1.2 mEq/L	NR
Choline	NR	X [2, 16]	NR	NR
Sulphate	NR	NR	7-190 mg/L [30]	NR
Phosphate	NR	NR	10-17 mg/L [30]	NR

Fluoride	NR	NR	0.2-1.18 mg/L [30]	NR
Bromide	NR	NR	0.2-0.5 mg/L [30]	NR
Iodide	NR	NR	5-12 µL [30]	NR
Iron	NR	NR	1-70 mg/L [30]	NR
Vitamins	NR	X [2]	NR	NR
Creatinine	NR	X [16]	X [31]	NR
Zinc, copper, cobalt, lead, manganese, molybdenum, sulphur, tin and mercury	NR	NR	X [3, 17, 32]	NR

Table A.2 – Overview of amino acids present in a fingerprint (outlined per percent ratio) as well as the amino acids included in the model fingerprint solution. NR=not reported

Amino acids	**Model fingerprint solution (%)**	**Hadorn *et al.* *[33]***	**Hamilton *[34]***	**Oró and Skewes *[35]***
Serine	100	100	100	100
Glycine	60	54	67	59
Ornithine	39	45	32	44-45
Alanine	30	35	27	28
Aspartic acid	19	11	22	23
Threonine	15	9	17	19
Histidine	15	13	17	15
Valine	10	10	12	9
Glutamic acid	9	12	8	6
Lysine	8	5	10	NR
Leucine	9	7	10	10
Isoleucine	7	6	8	8
Phenylalanine	6	5	7	5
Tyrosine	5	3	6	7

Table A.3 – Overview of proteins present in a fingerprint as well as the proteins included in the model fingerprint solution. X= quantity not specified. NR=not reported

Proteins	**Model fingerprint solution (%)**	**Drapel *et al.* *[23]***	**Reinholtz *et al.* *[22]* (%)**	**Ramotowski*[2]***	**Other studies**
Albumin	100	X	60	X [36]	X [37-39]
Keratin 1	NR	X	NR	NR	NR
Keratin 10	NR	X	NR	NR	NR
Cathepsin-D	NR	X	NR	NR	NR
Dermcidin	NR	X	NR	NR	NR
Zn-α2-glycoprotein	NR	NR	NR	X [36]	X [40, 41]
Lysozyme	NR	NR	NR	X [36]	X[38]
α1-acid glycoprotein orosomucoid	NR	NR	NR	X [36]	X[38]
γ-globulins	NR	NR	NR	X [37]	X [37]
α- and β-lipoproteins	NR	NR	NR	X [37]	X [37]
Glycoproteins	NR	NR	NR	X [37]	X [37]

Transferrin	NR	NR	NR	NR	X [37, 38]
IgA, IgG, IgD, IgE	NR	NR	NR	NR	X[38, 42, 43]

Table A.4 – Overview of sebum molecules present in a fingerprint as well as the molecules included in the model fingerprint solution. *= wax esters and diglycerides. **= triglycerides, monoglycerides and cholesterol esters.

Sebum compounds	Model fingerprint solution (%)	Girod *et al. [1]*	Ramotowski *[2]*
Cholesterol	2.95	3.8% or 1032 ng [12-14, 25, 28, 44-51]	2.1%
Squalene	14.18	14.6% or 28-5311 ng [12-15, 19, 25, 26, 29, 44-50, 52-55]	14.34%
Fatty esters	30.56	37.6% [12-15, 24-26, 28, 29, 44-52, 54, 56]	24.68%, 0.01-0.1 µg/mL
Wax esters	24.42	25%* [12, 13, 15, 19, 25, 44, 47-50, 52, 53]	24.85%
(Tri)glycerides	27.90	21%** [12, 15, 19, 25, 57]	36.12%

Table A.5 – Overview of triglycerides included in the model fingerprint solution.

Triglycerides			Model fingerprint solution (%)
Triolein	$C_{57}H_{104}O_6$	C18:1/ C18:1/C18:1	50
Tristearin	$C_{57}H_{110}O_6$	C18:0/ C18:0/C18:0	50

Table A.6 – Overview of fatty acids present in a fingerprint as well as the fatty acids included in the model fingerprint solution. X=quantity not specified. NR=not reported.

Fatty acid		Model fingerprint solution (%)	Girod *et al.*[1] (ng/fingermark)
Octanoic acid	C8:0	NR	X [24]
Nonanoic acid	C9:0	NR	X[14, 29, 48, 52]
Decanoic acid	C10:0	NR	X [24]
Dodecanoic acid	C12:0	NR	X [12-14, 24, 26, 29, 48, 49, 52]
Tridecanoic acid	C13:0	NR	X[12, 48, 52]
Myristic acid	C14:0	10.81	16-712 [12-14, 24, 26, 29, 45, 49, 52, 56-59]
Myristoleic acid	C14:1	NR	10-428 [48, 52]
Pentadecanoic acid	C15:0	NR	23-720 [12, 13, 24, 26, 48, 52, 56, 59]
Pentadecenoic acid	C15:1	NR	X [48]
Hexadecanoic acid/ Palmitic acid	C16:0	25.43	75-1637 [12-14, 24, 26, 29, 44-49, 52, 56, 57, 59]
Cis-9-hexadecanoic acid/ palmitoleic acid	C16:1	35.86	0-4326 [12, 14, 29, 45, 48, 49, 51, 52, 56, 59]
Margarin acid	C17:0	NR	6-316 [13, 52]
Heptadecenoic acid	C17:1	NR	8-450 [52]
Octadecanoic acid/ Stearic acid	C18:0	13.76	22-904 [12-14, 24, 26, 29, 45, 46, 48, 49, 51, 52, 56, 57, 59]
Oleic acid	C18:1	14.15	32-1675 [12-14, 26, 29, 44-46, 48, 49, 51, 52, 56, 59]
Linoleic acid	C18:2	NR	33-277 [24, 52]
Nanodecanoic acid	C19:0	NR	X [13, 24, 26, 51]

Eicosanoic acid	C20:0	NR	9-43 [13, 46, 52]
Heneicosanoic acid	C21:0	NR	X [13, 52]
Docosanoic acid	C22:0	NR	X [13, 46, 52]
Tricosanoic acid	C23:0	NR	X[13, 52]
Tetracosanoic acid	C24:0	NR	18-69 [13, 24, 46, 52]

Table A.7 – Overview of wax esters present in a fingerprint as well as the wax esters included in the model fingerprint solution. X=quantity not specified. NR=not reported.

Wax ester		**Model fingerprint solution (%)**	**Girod *et al.* [1]**
Dodecyl pentadecanoate	C12:0/ C15:0	NR	X [13]
Dodecyl palmitoleate	C12:0/ C16:0	NR	X [13, 48]
Tridecyl palmitoleate	C13:0/ C16:1	NR	X [13]
Myristyl myristoleate	C14:0/ C14:1	NR	X [48]
Myristyl myristate	C14:0/ C14:0	50	X [48]
Myristyl pentadecanoate	C14:0/ C15:0	NR	X [48]
Myristyl palmitoleate	C14:0/ C16:1	NR	X [13, 48]
Palmityl myristoleate	C16:0/ C14:1	NR	X [48]
Myristyl palmitate	C14:0/ C16:0	NR	X [48]
Palmityl pendecenoate	C16:0/ C15:1	NR	X [48]
Myristyl heptadecenoate	C14:0/ C17:1	NR	X [48]
Heptadecyl myristoleate	C17:0/ C14:1	NR	X [48]
Pentadecyl palmitoleate	C15:0/ C16:1	NR	X [13, 48]
Palmityl pentadecenoate	C16:0/ C15:1	NR	X [48]
Palmityl palmitoleate	C16:0/ C16:1	NR	X [13, 48, 49, 52]
Stearyl myristate	C18:0/ C14:0	NR	X [48]
Palmityl palmitate	C16:0/ C16:0	50	X [48]
Heptadecyl palmitoleate	C17:0/ C16:1	NR	X [48]
Stearyl palmitoleate	C18:0/ C18:1	NR	X [48, 49, 52]
Stearyl palmitate	C18:0/ C18:0	NR	X [48, 49, 52]
Eicosyl pentadecanoate	C20:0/ C15:0	NR	X [48]
Eicosyl palmitoleate	C20:0/ C16:1	NR	X [48, 49, 52]

A.2. FTIR spectra descriptions

Table A.8 – Description of the wavenumbers of polyaniline FTIR spectrum (Figure 2.10)

Wavenumber (cm^{-1})	Description
3510	The broadness of this peak indicates an O-H band originating from H_2O. [60, 61]
3250	N-H stretching. [62-64]
2958, 2926, 2858	• C-H bonds:[62] C-H bonds are normally present in the range of 3525-2700 cm^{-1}, whereby stronger/shorter bonds enclose the higher range. [62] Due to the presence of benzene or cyclohexane rings in polyaniline, the bonds are relatively short resulting in peaks in the higher/middle wavenumber region. The range 3100-3000 cm^{-1} is typical for benzene, this could be decreased slightly by the presence of 1,4-cyclohexane rings. A shift to lower wavenumbers could also be caused by polymer conductivity and/or the presence of small amounts of electrolyte. [65] • N-H bonds [63, 66]: The peaks around ~2900 cm^{-1} could also be assigned to N-H stretching and bending vibrations of polyaniline in reduced state. [66] • Contamination caused by the use of plastic and glass laboratory ware. [67, 68]
1726	Could be assigned to a C=O bond, originating from contamination. [62]
1582, 1496	C=C bonds, these can be used to differentiate the two possible configurations quinonoid (1582 cm^{-1}) and benzenoid (1496 cm^{-1}) from each other. [63, 64]
Bands ~1300	C-N bonds, potential to be used to identify the ratio of quinonoid and benzenoid monomers as investigated by Kang *et al.* [69]. 1268 cm^{-1}: besides a C-N bond, this peak could also correspond to a S-O bond, originating from sulphuric acid.
1152	C-N bonds, which are one of the specific polyaniline bonds. [64]
1040	S=O bond, originating from sulphuric acid.
874 and 824	C-H bonds from the benzene or 1,4-disubstituted rings. [64]

Table A.9 – Description of the wavenumbers of polypyrrole FTIR spectrum (Figure 2.11)

Wavenumber (cm^{-1})	Description
1580, 1456	Ring stretching vibrations. [70, 71]
1484	Can be assigned to ring-stretching [65] or a shifted C-N stretching vibration band. [72] Similar to the research of Kato et al. [65], the peak intensity of the C-C bond vibrations (1484-1456 cm^{-1}) is around half of the C-H (1098-1060 cm^{-1}).
1336, 1232	C-N bonds, [62, 73] N-H bonds or C-C bonds. [74]
1098, 1060	C-H bonds
964, 874-844	C-H bonds. [62, 65]

Table A.10 – Description of the wavenumbers of PEDOT FTIR spectrum (Figure 2.12)

Wavenumber (cm^{-1})	Description
3652	The broadness of this peak indicates an O-H band originating from H_2O. [60, 61]
1558	Could originate from C=C, although a second C=C band would then be expected. [62]
1482, 1460	Assigned to ring-stretching [75] or a C-N stretching vibration band. [72]
1374	Could originate from ring-vibrations; C-C (quinoidal part) and C=C. [76]
1186, 1084, 1050	Corresponds to C-O-C bonds, this bond is present in PEDOT and not in PPY and PANI and could therefore be used for differentiation. [77] However, 1186 cm^{-1} could also origin from a C=C bond. [78]
798	Could be assigned to C-H bond vibrations. [62, 65]

A.3. Fragmentation of the fingerprint molecules and monomers

An overview of the amino acid and hydrophobic molecules (fatty acids, wax esters and triglycerides) present in fingerprints as well as the monomers including their expected fragments is shown in Figures A.1-A.3 and Table A.11. [60, 79-87]

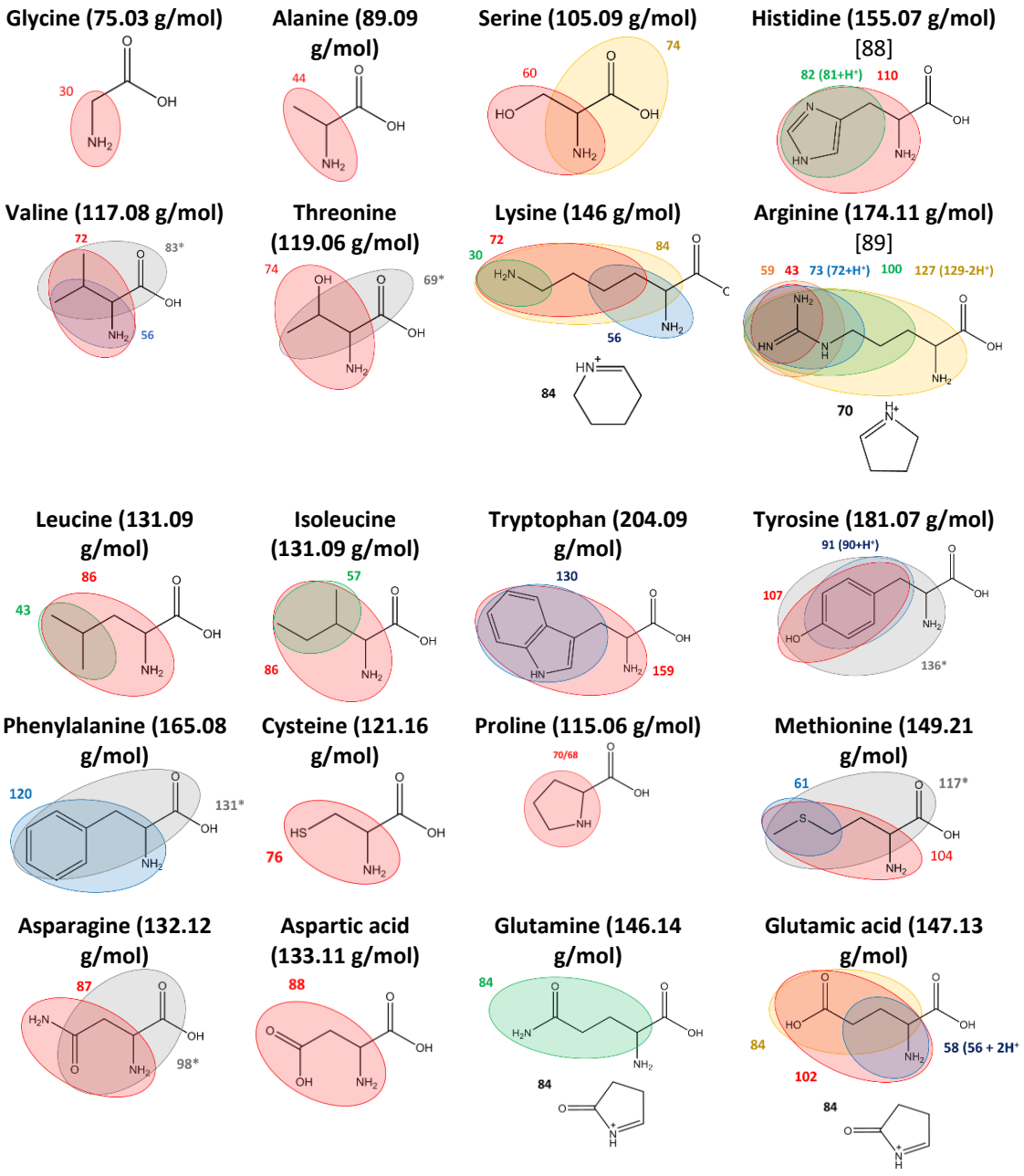

Figure A.1– Overview of amino acids including their fragments and corresponding molecular weight and m/z. *Fragments which are likely only to be obtained in peptide/protein form.

Squalene (410.72 g/mol) [90]

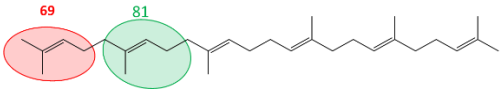

Cholesterol (386.65 g/mol) l[91]

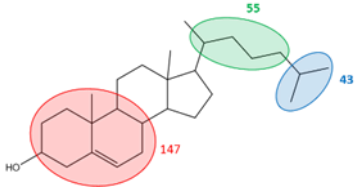

Docosane (310.60 g/mol)

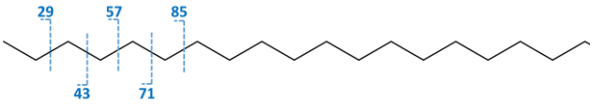

Myristic acid (228.37 g/mol)

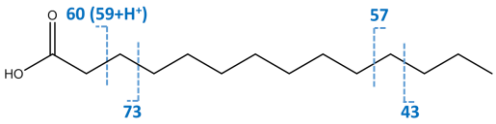

Dodecanoid acid (200.32 g/mol)

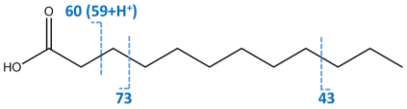

Palmitoleic acid (254.41 g/mol)

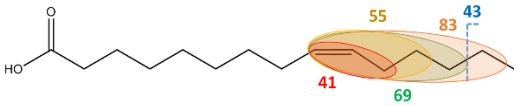

Stearic acid (284.48 g/mol)

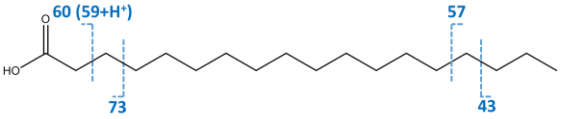

Myristic acid methyl ester (242.40 g/mol)

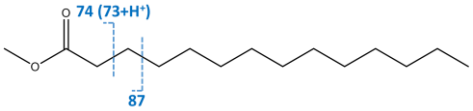

Nonanoic acid (158.24 g/mol)

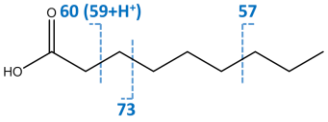

Palmitic acid (256.4 g/mol)

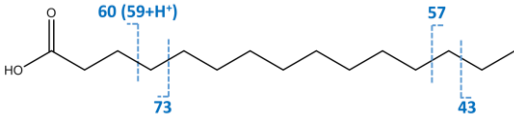

Cetyl Palmitate (480.86 g/mol)

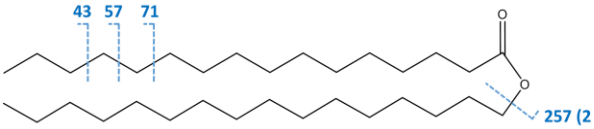

Oleic acid (282.47 g/mol)

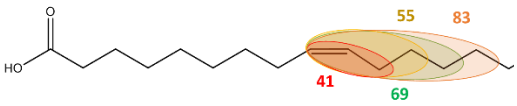

Glyceryl trioleate (885.45 g/mol)

Glycerol tristearate (891.48 g/mol)

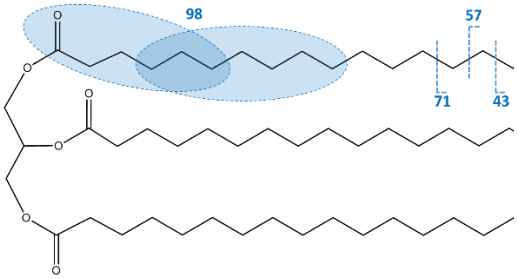

Figure A.2 – Overview of fatty acids, wax esters and triglycerides including their fragments and corresponding molecular weight and m/z

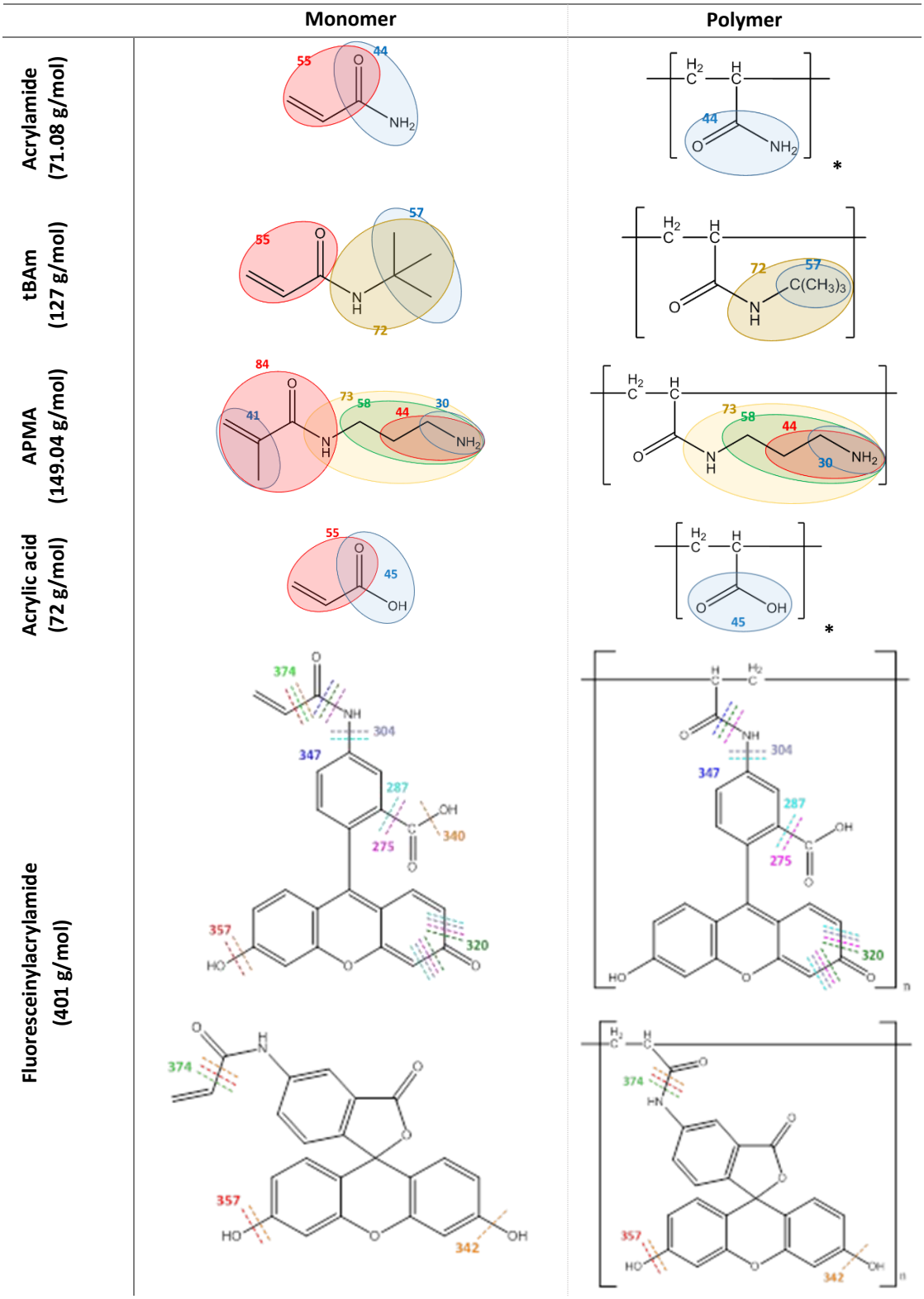

Figure A.3 – Overview of the fragmentation of the monomers and expected fragments of the polymerized monomers acrylamide, tBAm, APMA, acrylic acid and fluoresceinylacrylamide, including the corresponding molecular weights and m/z. *Although these fragments were observed for polyacrylamide in the literature, it is not very likely to occur, based on the spectra of alkaneamides and carboxylic acids [82].

Table A.11 – Fragments of salts, amino acids, fatty acids and MIPs till a mass of 100 g/mol. Colours indicate overlap between groups; blue is overlap between amino acids, fatty acids and MIPs, orange is overlap between amino acids and MIPs and green is overlap between amino acids and fatty acids. Bold & underlined: most abundant fragments for that molecule. *=Not always identifiable *[2]=Fragments which are likely to be obtained only in peptide/protein form.

Salts	Amino acids (MW)	Fatty acids (MW)	Linear MIPs (MW)
Na^+ (22.9898)	CH_4N^+ (30.0344; **<u>Gly</u>**, Lys)	$C_2H_5^+$ (29.0391)	CH_4N^+ (30.0344)
K^+ (38.9637)	$C_3H_7^+$ (43.0548, Leu)	$C_3H_5^+$ (41.0391)	CH_2NO^+ (44.0136)
	$CH_3N_2^+$ (43.0296, Arg)*	$C_3H_7^+$ (43.0548)	$C_2H_6N^+$ (44.0500)
	$C_2H_6N^+$ (44.0500; **<u>Ala</u>**)	$C_4H_7^+$ (55.0548)	CHO_2^+ (44.9977)
	$C_3H_6N^+$ (56.0500, Val, **<u>Lys</u>**)	$C_4H_9^+$ (57.0704)	$C_4H_9^+$ (57.0704)
	$C_4H_9^+$ (57.0704, ILeu)	$C_2H_4O_2^+$ (60.0211)	$C_3H_8N^+$ (58.0657)
	$C_3H_8N^+$ (58.0657, Glu)	$C_5H_9^+$ (69.0704)	$C_4H_{10}N^+$ (72.0813)*
	$CN_3H_5^+$ (59.0483, Arg)	$C_5H_{11}^+$ (71.0861)*	$C_3H_9N_2^+$ (73.0766)*
	$C_2H_6NO^+$ (60.0450; **<u>Ser</u>**)	$C_3H_5O_2^+$ (73.0290)*	
	$C_2H_5S^+$ (61.0112, **<u>Met</u>**)	$C_3H_6O_2^+$ (74.0367)*	
	$C_4H_6N^+$ (68.0500, Pro) *	$C_6H_9^+$ (81.0704)	
	$C_4H_5O^+$(69.0340, Thr)*[2]	$C_6H_{11}^+$ (83.0861)	
	$C_3H_4NO^+$ (70.0293, Asp)*	$C_6H_{13}^+$ (85.1017)	
	$C_4H_8N^+$ (70.0656, Arg, **<u>Pro</u>**) *	$C_4H_7O_2^+$ (87.0446)	
	$C_4H_{10}N^+$ (72.0813; **<u>Val</u>**, Lys)*	$C_7H_{13}^+$ (97.1017)	
	$C_2H_7N_3^+$ (73.0640, Arg)	$C_6H_{10}O^+$ (98.0732)	
	$C_2H_4NO_2^+$ (74.0242 Ser)*	$C_7H_{14}^+$(98.1096)*	
	$C_3H_8NO^+$ (74.0606; **<u>Thr</u>**)		
	$C_2H_6NS^+$ (76.0221, **<u>Cys</u>**)*		
	$C_4H_6N_2^+$ (82.0531, **<u>His</u>**)		
	$C_5H_7O^+$ (83.0500, Val)*[2]		
	$C_4H_6NO^+$ (84.0450, **<u>Glu</u>**)		
	$C_5H_{10}N^+$ (84.0813, **<u>Lys</u>**)		
	$C_5H_{12}N^+$ (86.0970, **<u>Leu</u>**)		
	$C_3H_7N_2O^+$ (87.0558, **<u>Asp</u>**)*		
	$C_3H_6NO_2^+$ (88.0399, **<u>Asp</u>**)		
	$C_7H_7^+$ (91.0548, Tyr)		
	$C_4H_4NO_2^+$ (98.0242, Asp)*		

A.4. References

[1] A. Girod, R. Ramotowski, C. Weyermann, Composition of fingermark residue: a qualitative and quantitative review, Forensic Science International, 223 (2012) 10-24.

[2] R.S. Ramotowski, Chapter 3: Composition of latent fingerprint residue, Advances in fingerprint technology, CRC Press LLC2001.

[3] F. Bayford, Sweat, Fingerprint Whorld, 1 (1976) 42-43.

[4] J. Terasawa, K. Mitsuya, A. Ishii, T. Tsuda, Quantitative determination of K^+ , NH_4^+ , Na^+ , Ca^{2+} and Mg^{2+} cations in secreted human sweat by capillary zone electrophoresis, Bunseki Kagaku – Japan Society for Analytical Chemistry, 50 (2001) 813-817.

[5] F. Cuthbertson, The chemistry of fingerprints, United Kingdom Atomic Energy Authority, Atomic Weapons Research Establishment (AWRE), 1969.

[6] E. Angst, Procédé pour la détermination de l'âge d'empreintes dactyloscopique sur le papier, Rev. Int. Criminol. Police Techn., 16 (1962) 134-146.

[7] F. Cuthbertson, J.R. Morris, The chemistry of fingerprints, SCD, Memorandum, United Kingdom Atomic Energy Authority, Atomic Weapons Research Establishment (AWRE), 1972.

[8] E. Seutter, N. Goedhart-De Groot, H.M. Sutorius, E.J.M. Urselmann, The quantitative analysis of some constituents of crude sweat, Dermatologica, 141 (1970) 226-233.

[9] K. Sato, R.L. Dobson, Regional and individual variations in the function of the human eccrine sweat gland, Journal of Investigative Dermatology, 54 (1970) 443-449.

[10] K. Sato, C. Feibleman, R.L. Dobson, The electrolyte composition of pharmacologically and thermally stimulated sweat: a comparative study, Journal of Investigative Dermatology, 55 (1970) 433-438.

[11] T. Verde, R.J. Shephard, P. Corey, R. Moore, Sweat composition in exercise and in heat, Journal of Applied Physiology: Respiratory, Environmental and Exercise Physiology, 53 (1982) 1540-1545.

[12] F. Wehrli, Réactivité du révélateur physique et composition des sécrétions d'empreintes digitales, Institut de Police Scientifique, Lausanne University, 1998.

[13] N. Rosset, Aspects divers de la composition des traces digitales - Une revue, Institut de Police Scientifique, Lausanne University, 2000.

[14] B. Hartzell-Baguley, R.E. Hipp, N.R. Morgan, S.L. Morgan, Chemical composition of latent fingerprints by gas chromatography-mass spectrometry, Journal of Chemical Education, 84 (2007) 689-691.

[15] C. Ricci, P. Phiriyavityopas, N. Curum, K.L.A. Chan, S. Jickells, S.G. Kazarian, Chemical imaging of latent fingerprint residues, Applied Spectroscopy, 61 (2007) 514-522.

[16] R.M. Connatser, S.M. Prokes, O.J. Glembocki, R.L. Schuler, C.W. Gardner, S.A. Lewis, L.A. Lewis, Toward surface-enhanced Raman imaging of latent fingerprints, Journal of Forensic Sciences, 55 (2010) 1462-1470.

[17] K. Sato, The physiology, pharmacology, and biochemistry of the eccrine sweat gland, Reviews of Physiology, Biochemistry and Pharmacology, 79 (1979) 52-131.

[18] S. Sugase, T. Tsuda, Determination of lactic acid, uric acid, xanthine and tyrosine in human sweat by HPLC, and the concentration variation of lactic acid in it after the intake of wine, Bunseki Kagaku 51 (2002) 429-435.

[19] D.K. Williams, C.J. Brown, J. Bruker, Characterization of children's latent fingerprint residues by infrared microspectroscopy: Forensic implications, Forensic Science International, 206 (2011) 161-165.

[20] S.W. Brusilow, E.H. Gordes, Ammonia secretion in sweat, Amer. J. Physiol, 214 (1967) 513-517.

[21] L. Förström, M.E. Goldyne, R.K. Winkelmann, IgE in human eccrine sweat, Journal of Investigative Dermatology, 64 (1975) 156-157.

[22] A.D. Reinholtz, Albumin development method to visualize friction ridge detail on porous surfaces, Journal of Forensic Identification, 58 (2008) 524-539.

[23] V. Drapel, A. Becue, C. Champod, P. Margot, Identification of promising antigenic components in latent fingermark residues, Forensic Science International, 184 (2008) 47-53.
[24] R.S. Croxton, M.G. Baron, D. Butler, T. Kent, V.G. Sears, Development of a GC-MS method for the simultaneous analysis of latent fingerprint components, Journal of Forensic Science, 51 (2006) 1329-1333.
[25] S. Bramble, Separation of latent fingermark residue by thin-layer chromatography, Journal of Forensic Sciences, 40 (1995) 969-975.
[26] R.S. Croxton, M.G. Baron, D. Butler, T. Kent, V.G. Sears, Variation in amino acid and lipid composition of latent fingerprints, Forensic Science International, 199 (2010) 93-102.
[27] A. Richmond-Aylor, S. Bell, P. Callery, K. Morris, Thermal degradation analysis of amino acids in fingerprint residue by pyrolysis GC-MS to develop new latent fingerprint developing reagents, Journal of Forensic Sciences, 52 (2007) 380-382.
[28] A.A. Frick, D. Berryman, S.W. Lewis, Mass spectral imaging: a powerful new tool for the study of latent fingermark chemistry, Identification Canada 34 (2011).
[29] A.Y. Lim, Z. Mab, J. Ma, F. Rowell, Separation of fingerprint constituents using magnetic silica nanoparticles and direct on-particle SALDI-TOF-mass spectrometry, , Journal of Chromatography B, 879 (2011) 2244-2250.
[30] H.H. Mitchell, T.S. Hamilton, The dermal excretion under controlled environmental conditions of nitrogen and minerals in human subjects, with particular reference to calcium and iron. , The Journal of Biological Chemistry, 178 (1949) 345-361.
[31] W.C. Lobitz, H.L. Mason, Chemistry of palmar sweat. VII. Discussion of studies on chloride, urea, glucose, uric acid, ammonia nitrogen, and creatinine. , Archives of Dermatology and Syphilology, 57 (1948).
[32] R.D. Olsen, The chemical composition of palmar sweat, Fing. Ident. Mag., 53(10), 4, 1972., 53 (1972).
[33] B. Hadorn, F. Hanimann, P. Anders, H.-C. Curtius, R. Halverson, Free amino-acids in human sweat from different parts of the body, Nature, 215 (1967) 416-417.
[34] P.B. Hamilton, Amino-acids on hands, Nature, 205 (1965) 284-285.
[35] J. Oro, H.B. Skewes, Free amino-acids on human fingers: the question of contamination in microanalysis, Nature, 207 (1965) 1042-1045.
[36] N. Nakayashiki, Sweat protein components tested by SDS-polyacrylamide gel electrophoresis followed by immunoblotting, The Tohoku Journal of Experimental Medicine, 161 (1990) 25-31.
[37] M. Uyttendaele, M. De Groote, V. Blaton, H. Peeters, Analysis of the proteins in sweat and urine by agarose-gel isotachophoresis, Journal of Chromatography, 132 (1977) 261-266.
[38] C.O. Page, J.S. Remington, Immunologic studies in normal human sweat, Journal of Laboratory and Clinical Medicine, 69 (1967) 634-650.
[39] S. Yanagawa, H. Yokozeki, K. Sato, Origin of periodic acid-Schiff-reactive glycoprotein in human eccrine sweat, Journal of Applied Physiology, 60 (1986) 1615-1622.
[40] J.R. Poortmans, K. Schmid, The level of Zn-a2-glycoprotein in normal human body fluids and kidney extract, Journal of Laboratory and Clinical Medicine, 71 (1968) 807-811.
[41] N. Nakayashiki, S. Katsura, Four variants of human plasma Zn-a2- glycoprotein (ZAG) in the Japanese population. , Human Genetics, 82 (1989) 293-295.
[42] Y. Ishiguro, K. Kato, Y. Ito, Sensitive solid phase enzyme immunoassay for human IgA, secretory IgA, and secretory component., Clinica Chimica Acta, 116 (1981) 237-243.
[43] T. Okada, H. Konishi, M. Ito, H. Nagura, J. Asai, Identification of secretory immunoglobulin A in human sweat and sweat glands., Journal of Investigative Dermatology, 90 (1988) 648-651.
[44] A. Jacquat, Evolution des substances grasses des empreintes digitales au cours du temps: analyse par TLC et GC-MS, Institut de Police Scientifique, Lausanne University, 1999.

[45] N.E. Archer, Y. Charles, J.A. Elliott, S. Jickells, Changes in the lipid composition of latent fingerprint residue with time after deposition on a surface, Forensic Science International, 154 (2005) 224-239.
[46] C. du Preez, L. Xiao, X. Spindler, P. Maynard, C. Weyermann, C. Lennard, C. Roux, A transfer study of fingermark material by GC-MS, 20th International Symposium on the Forensic Sciences, Sydney, Australia, 2010.
[47] C. Weyermann, C. Roux, C. Champod, Initial results on the composition of fingerprints and its evolution as a function of time by GC/MS analysis, Journal of Forensic Sciences 56 (2011) 102-108.
[48] K. Koenig, A. Girod, C. Weyermann, Identification of wax esters in fingermark residues by GC/MS and their potential use as aging parameters, Journal of Forensic Identification, 61 (2011) 652-676.
[49] K.G. Asano, C.K. Bayne, K.M. Horsman, M.V. Buchanan, Chemical composition of fingerprints for gender determination, Journal of Forensic Sciences, 47 (2002) 805-807.
[50] K.M. Antoine, S. Mortazavi, A.D. Miller, L.M. Miller, Chemical differences are observed in children's versus adults' latent fingerprints as a function of time, Journal of Forensic Sciences, 55 (2010).
[51] R. Wolstenholme, R. Bradshaw, M.R. Clench, S. Francese, Study of latent fingerprints by matrix-assisted laser desorption/ionisation mass spectrometry imaging of endogenous lipids., Rapid communications in mass spectrometry, 23 (2009) 3031-3039.
[52] G.M. Mong, C.E. Petersen, T.R.W. Clauss, Advanced Fingerprint Analysis Project: Fingerprint Constituents, Pacific Northwest National Laboratory, 1999.
[53] D.K. Williams, R.L. Schwartz, E.G. Bartick, Analysis of latent fingerprint deposits by infrared microspectroscopy, Applied Spectroscopy, 58 (2004) 313-316.
[54] A. Hemmila, J. McGill, D. Ritter, Fourier transform infrared reflectance spectra of latent fingerprints: a biometric gauge for the age of an individual., Journal of Forensic Science, 53 (2008) 369-376.
[55] K.A. Mountfort, H. Bronstein, N. Archer, S.M. Jickells, Identification of oxidation products of squalene in solution and in latent fingerprints by ESI-MS and LC/ APCI-MS, Analytical Chemistry, 79 (2007) 2650-2657.
[56] H.W. Tang, W. Lu, C.M. Che, K.M. Ng, Gold nanoparticles and imaging mass spectrometry: double imaging of latent fingerprints, Analytical Chemistry, 82 (2010) 1589-1593.
[57] R.D. Olsen, Chemical dating techniques for latent fingerprints: a preliminary report, The Identification News, (1987) 10-12.
[58] Advances in MALDI and laser-induced soft ionization mass spectrometry., Springer2016.
[59] D.R. Ifa, N.E. Manicke, A.L. Dill, R.G. Cooks, Latent fingerprint chemical imaging by mass spectrometry, Science . 321 (2008) 805.
[60] National Institute of Standards and Technology US, NIST Chemistry WebBook, NIST Standrad Reference Database Number 69.
[61] Q. Du, R. Superfine, E. Freysz, Y.R. Shen, Vibrational spectroscopy of water at the vapor/water interface, Physical Review Letters, 70 (1993) 2313-2316.
[62] G. Verkerk, J.B. Broens, P.A.M. de Groot, W. Kranendonk, J.L. Sikkema, J.J. Westra, I.M. Wevers-Prijs, Binas, Wolters-Noordhoff B.V. , Groningen, The Netherlands, 1998.
[63] Y. Furukawa, F. Ueda, Y. Hyodo, I. Harada, T. Nakajima, T. Kawagoe, Vibrational spectra and structure of polyaniline, Macromolecules 21 (1988) 1297-1305.
[64] Z. Ping, In situ FTIR-attenuated total reflection spectroscopic investigations on the base-acid transitions of polyaniline. Base-acid transition in the emeraldine form of polyaniline Journal of the Chemical Society, Faraday Transactions, 92 (1996) 3063-3067.
[65] H. Kato, O. Nishikawa, T. Matsui, S. Honma, H. Kokado, Fourier transform infrared spectroscopy study of conductlng polymer polypyrrole: higher order structure of electrochemically syntheslzed film, Journal of Physical Chemistry, 95 (1991) 6014-6016.

[66] M. Ahson Habib, S.P. Maheswari, Electrochromism of polyaniline: an in situ FTIR study, Journal of The Electrochemical Society, 136 (1989).
[67] G. Socrates, Infrared and raman characteristic group frequencies, Third ed., John Wiley & Sons, LtD, Chinester, 2001.
[68] Perkin Elmer, Polymer identification using mid infrared spectroscopy, Application Note Infrared Spectroscopy, 2011.
[69] E.T. Kang, K.G. Neoh, K.L. Tan, Polyaniline: a polymer with many interesting intrinsic redox states, Progress in Polymer Science, 23 (1998) 277-324.
[70] R. Pang, X. Hu, S. Zhou, C. Sun, J. Yan, X. Sun, S. Xiao, P. Chen, Preparation of multi-shelled conductive polymer hollow microspheres by using Fe_3O_4 hollow spheres as sacrificial templates, Chemical Communications, 50 (2014) 12493-12496.
[71] H. Xie, M. Yan, Z. Jiang, Transition of polypyrrole from electroactive to electroinactive state investigated by use of in situ FTIR spectroscopy, Electrochimica acta, 42 (1997) 2361-2367.
[72] N.V. Blinova, J. Stejskal, M. Trchová, J. Prokeš, M. Omastová, Polyaniline and polypyrrole: a comperative study of the preparation, European Polymer Journal 43 (2007) 2331-2341.
[73] H. Xu, J. Wu, C. Li, J. Zhang, J. Liu, Investigation of polyaniline films doped with Fe^{3+} as the electrode material for electrochemical supercapacitors, Electrochimica Acta, 165 (2015) 14-21.
[74] P.S. Rao, J. Anand, S. Palaniappan, Effect of sulphuric acid on the properties of polyaniline-HCl salt and its base, European Polymer Journal, 36 (2000) 915-921.
[75] C. Gravalidis, A. Laskarakis, S. Logothetidis, Fine tuning of PEDOT electronic properties using solvents, The European Physical Journal-Applied Physics, 46 (2009).
[76] S. Mohanapriya, K. Tintula, P. Sridhar, S. Pitchumani, A. Shukla, MWNTs-poly (3, 4-ethylenedioxy thiophene) and polystyrene sulphonic acid nanocomposite as a catalyst support for PEFCs, ECS Transactions, 33 (2010) 461-471.
[77] S. Kulandaivalu, Z. Zainal, Y. Sulaiman, Influence of monomer concentration on the morphologies and electrochemical properties of PEDOT, PANI, and PPy prepared from aqueous solution, International Journal of Polymer Science, 2016 (2016) 1-12.
[78] C. Kvarnström, H. Neugebauer, S. Blomquist, H.J. Ahonen, J. Kankare, A. Ivaska, In situ spectroelectrochemical characterization of poly(3,4-ethylenedioxythiophene), Electrochimica Acta, 44 (1999) 2739-2750.
[79] National Institute of Advanced Industrial Science and Technology (AIST), N. Wasada, Spectral Database for Organic Compounds SDBS, https://sdbs.db.aist.go.jp/sdbs/cgi-bin/cre_index.cgi.
[80] NIST National Institute of Standards and Technology, Mass Spectrometry Data Center, https://chemdata.nist.gov/.
[81] F.W. McLafferty, Mass spectrometry of organic ions, Academic Press 1963.
[82] F.W. McLafferty, F. Turecek, Interpretation of mass spectra, University science books 1993.
[83] N.T. Samuel, M. Wagner, K. Dornfeld, D.G. Castner, Analysis of poly (amino acids) by static time-of-flight secondary ion mass spectrometry (TOF-SIMS), Surface Science Spectra, 8 (2001) 163-184.
[84] M. Urbini, V. Petito, F. de Notaristefani, F. Scaldaferri, A. Gasbarrini, L. Tortora, ToF-SIMS and principal component analysis of lipids and amino acids from inflamed and dysplastic human colonic mucosa, Analytical and Bioanalytical Chemistry, 409 (2017) 6097-6111.
[85] S. Muramoto, D.J. Graham, M.S. Wagner, T.G. Lee, D.W. Moon, D.G. Castner, ToF-SIMS analysis of adsorbed proteins: principal component analysis of the primary ion species effect on the protein fragmentation patterns, The Journal of Physical Chemistry C, 115 (2011) 24247-24255.
[86] B. Tyler, C. Bruening, S. Rangaranjan, H. Arlinghaus, TOF-SIMS imaging of adsorbed proteins on topographically complex surfaces with Bi3+ primary ions, Biointerphases, 6 (2011) 135-141.

[87] S. Sole-Domenech, B.r. Johansson, M. Schalling, J. Malm, P. Sjövall, Analysis of opioid and amyloid peptides using time-of-flight secondary ion mass spectrometry, Analytical chemistry, 82 (2010) 1964-1974.
[88] J.M. Khreis, J. Reitshammer, V. Vizcaino, K. Klawitter, L. Feketeová, S. Denifl, High-energy collision-induced dissociation of histidine ions [His+ H]+ and [His− H]− and histidine dimer [His2+ H]+, Rapid Communications in Mass Spectrometry, 32 (2018) 113-120.
[89] D.R. Bush, V.H. Wysocki, P.Y. Scaraffia, Study of the fragmentation of arginine isobutyl ester applied to arginine quantification in Aedes aegypti mosquito excreta, Journal of mass spectrometry, 47 (2012) 1364-1371.
[90] O. Weeks, M. Francesconi, Occurrence of squalene and sterols in Cellulomonas dehydrogenans (Arnaudi 1942) comb. nov. Hester 1971, Journal of bacteriology, 136 (1978) 614-624.
[91] C. Ghumman, A. Moutinho, A. Santos, A. Tolstogouzov, O. Teodoro, TOF-SIMS study of cystine and cholesterol stones, Journal of Mass Spectrometry, 47 (2012) 547-551.